LEVEL

TRASANA

DTIC
ELECTE
AUG 1 3 1981

C
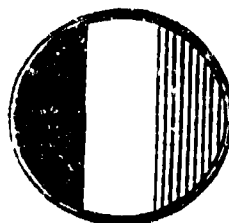
AD A102322
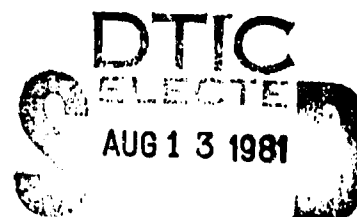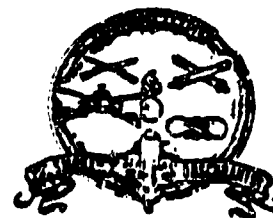
DTIC FILE COPY
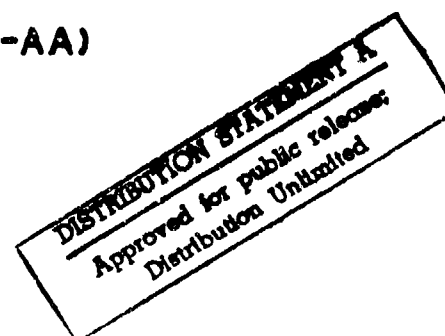
BATTLEFIELD ENVIRONMENT OBSCURATION HANDBOOK

UNCLASSIFIED EDITION

DECEMBER 1980

FINAL REPORT
CONTRACT DAAK11-80-C-0004

(SAI REPORT NO. SAI-80-009-AA)

VOLUME 1

81 8 13 030

DISPOSITION

Destroy this report when no longer needed. Do not return it to the originator.

DISCLAIMER

The findings in this report are not to be construed as an official Department of the Army position unless so specified by other official documentation.

WARNING

Information and data contained in this document are based on the input available at the time of preparation. The results may be subject to change and should not be construed as representing the DARCOM position unless so specified.

TRADE NAMES

The use of trade names in this report does not constitute an official endorsement or approval of the use of such commercial hardware or software. The report may not be cited for purposes of advertisement.

REPORT DOCUMENTATION PAGE		READ INSTRUCTIONS BEFORE COMPLETING FORM
1. REPORT NUMBER	2. GOVT ACCESSION NO. AD-A102 822	3. RECIPIENT'S CATALOG NUMBER
4. TITLE *(and Subtitle)* BATTLEFIELD ENVIRONMENT OBSCURATION HANDBOOK Volume I.		5. TYPE OF REPORT & PERIOD COVERED FINAL REPORT Dec 1979 — Dec 1980 6. PERFORMING ORG. REPORT NUMBER UNCL Edition SAI-80-009-AA-V
7. AUTHOR(s) Robert E. Turner, Paul G. Eitner, Carl D. Leonard, D.C.S. Snyder		8. CONTRACT OR GRANT NUMBER(s) DAAK11-80-C-0004
9. PERFORMING ORGANIZATION NAME AND ADDRESS Science Applications, Inc. 15 Research Drive Ann Arbor, Michigan 48103		10. PROGRAM ELEMENT, PROJECT, TASK AREA & WORK UNIT NUMBERS DA Project # 1R765706M541
11. CONTROLLING OFFICE NAME AND ADDRESS Director, US Army Materiel Systems Analysis Act ATTN: DRXSY-GP (Mr. Walter W. Clifford) Aberdeen Proving Ground, MD 21005		12. REPORT DATE December 1980 13. NUMBER OF PAGES 438
14. MONITORING AGENCY NAME & ADDRESS*(if different from Controlling Office)* Commander, US Army Materiel Development & Readiness Command 5001 Eisenhower Avenue Alexandria, VA 22333		15. SECURITY CLASS. *(of this report)* UNCLASSIFIED 15a. DECLASSIFICATION/DOWNGRADING SCHEDULE

16. DISTRIBUTION STATEMENT *(of this Report)*

APPROVED FOR PUBLIC RELEASE; DISTRIBUTION UNLIMITED

17. DISTRIBUTION STATEMENT *(of the abstract entered in Block 20, if different from Report)*

18. SUPPLEMENTARY NOTES
Contract Project Officer: Mr. Sidney Gerard
Project PM SMOKE/OBSCURANTS
DRCPM-SMK-T
Aberdeen Proving Ground, MD 21005

19. KEY WORDS *(Continue on reverse side if necessary and identify by block number)*

Aerosol	Dust	Radiation Models
Atmospheric Optics	Meteorology	Sensors
Contrast	Obscurants	Smoke
Climatology	Path Radiance	Thermal Emission Transmittance

20. ABSTRACT *(Continue on reverse side if necessary and identify by block number)*

An investigation has been performed to review an extensive number of technical reports, papers, and books and then to produce a manual for obscurant community use. The title of the assemblage is the Battlefield Environment Obscuration Handbook and is composed of data, models, and other information on the performance of visible and infrared sensors and imaging devices under battlefield conditions characterized by various kinds of environmental obscurants.

DD FORM 1473 EDITION OF 1 NOV 65 IS OBSOLETE

20. Abstract - continued

Included in the Handbook are: natural obscurants such as rain, snow, haze, and fog as well as obscuring materials which arise from anthropogenic sources. The latter include smoke and dust. The data presented are in the form of spectral attenuation coefficients, production rates, precipitation rates, and various other forms for use in models or analytical studies. Also included in the Handbook are the results and description of field tests related to battle-field obscurants and sensor performance test data. A list is provided of the basic input and output parameters for the mathematical models included in the Handbook.

Classified and unclassified material were reviewed for information to be included in the Handbook. As a result, there are two large parts of the Handbook. This one contains the unclassified sections of the Handbook in a loose-leaf form for the easy inclusion of additional information as it becomes available. The classified version contains sections and subsections which have classified and unclassified information.

The information contained here is not to be considered conclusive since it is a result of a period of research conducted and completed in an area where results and findings are still emerging.

PREFACE

The original intent of the Battlefield Obscuration Handbook effort was to assemble, in one document, the "state-of-the-art" in obscuration knowledge, to support this information via theory and data, and furthermore suggest methods of applying this knowledge to analysis of system performance on the battlefield.

Due to the time required to obtain and conduct the contractual effort and the magnitude of changes in the state-of-the-art during that time, it became apparent that our intended document would have to be modified at a rate which exceeded its preparation. The idea of a true "handbook" evolved into more of a manual, in that the basic knowledge has been emphasized rather than emphasizing the emerging field trials data and their application.

Various organizations responsible for the information presented in each of the chapters presented in this document, have accepted the mission of updating their material when significant issues were developed and exploited. At present, these modifications are to be coordinated and disseminated under the auspices of the Smoke and Aerosol Working Group (SAWG) under the JMEM tri-service office.

The information contained herein is not to be considered conclusive since it is a result of a period of research conducted and completed in an area where results and findings are still emerging.

SUMMARY

Obscurant material in the battlefield environment can have
a deleterious effect on the performance of electro-optical
sensors. The natural weather environment consists of haze, fog,
rain, snow, and similar atmospheric particulates which can cause
a loss of contrast in a military scene. In addition, the
battlefield induced contaminants such as dust, smoke, and for-
eign gases can degrade the atmospheric medium between a target
and sensor.

This report, entitled Battlefield Environment Obscuration
Handbook, is a detailed compilation of laboratory data, field
data, mathematical models, studies, and other information
pertaining to the natural and anthropogenic sources of obscur-
ants which can be found in the modern battlefield. In the
creation of this handbook we obtained over one hundred reports
and documents, some of which contained many articles relevant
to the Handbook material.

Dr. Robert E. Turner, of Science Applications, Inc., was
the principal investigator for the project. In the course of
this work, the authors would like to acknowledge the help and
guidance of many people in the military community, and in
particular, Mr. Sidney Gerard of Aberdeen Proving Ground, Md.
who was the technical monitor for the project.

TABLE OF CONTENTS

---

*"C" designates Classified Sections.

*"C" designates Classified Sections.

---

*"C" designates Classified Sections.

ix

*"C" designates Classified Sections.

---

*"C" designates Classified Sections.

*"C" designates Classified Sections.

SECTION 1
USE OF THE HANDBOOK

1.1 CRITERIA FOR SEGREGATION OF THE DATA AND MODELS

In the modern battlefield environment there are many effects
which can limit the capability of an observer to detect and/or
recognize enemy forces. First, there is the presence of terrain,
vegetation, or solid man-made objects which lie within the line
of sight; and second, there is the presence of natural and/or
anthropogenic material such as gases and particulates in the
atmosphere. In fact, the definition of line of sight which we
shall use in this Handbook is the following: "A point is said
to be within the line of sight of a sensor (or equivalently, a
sensor is said to have a line of sight to a point), if and only
if, the energy to which the sensor reacts can travel from the
point to the sensor unobstructed by terrain, vegetation, or
solid man-made objects." In strict terms this definition would
exclude anthropogenic smoke because it includes solid man-made
particles. In this sense the line of sight definition is some-
what arbitrary, but we shall interpret it to refer to solid
man-made objects which, if projected into the atmosphere, do
not reach their terminal speed. Therefore, we shall consider
as battlefield obscurants, natural and anthropogenic gases and
particulates semi-permanently suspended in the atmosphere be-
tween a target and sensor.

This Handbook consists of models and data which are primarily
of use to investigators of the response of electro-optical
systems in the course of battlefield activity. A structured
way of presenting this large and growing body of knowledge is to
segregate the various models and data according to the origin
and means of production of the obscuring material and the
systems involved. In this Handbook we have therefore organized

the data and models in the following way:

Section 3.   Natural Battlefield Environmental Conditions for
              Specific Geographic Locations. This section contains
              general information which is necessary to characterize
              electro-optical system degradation for four geographic
              regions.

Section 4.   Intentionally Induced Battlefield Environmental Con-
              ditions. This section contains information on battle-
              field environmental conditions which may be intention-
              ally induced to impair the performance of electro-
              optical or visual systems.

Section 5.   Unintentionally Induced Battlefield Environmental Con-
              ditions. This section includes battlefield environ-
              mental conditions which can degrade electro-optical or
              visual system performance as a by product of their
              primary functions.

Section 6.   Models. This section includes models which deal with
              sources of environmental degradation only. These
              include the models of natural and induced extinction.

Section 7.   Tests and Studies. This section includes tests, which
              are defined as those projects or activities which in-
              volve field measurements, whether they are for the
              battlefield environment only, sensor, or combat level.
              Studies are those projects which are more analytical
              in nature or are paper simulations rather than field
              measurements. The latter includes laboratory data
              because these data must be extrapolated or modeled to
              be applied to realistic field conditions.

Section 8.   Description of Basic Characteristics of U.S. Army
              Electro-Optical Systems (Classified Section). This
              section includes the basic electro-optical (E-O)
              characteristics of the various Army E-O systems.

Section 9.   Performance Data of Sensor (Systems) in Battlefield
             Environment Conditions (Classified Section).   This
             section summarizes the available performance data on
             specific sensor (system) performance in the battlefield
             environment.

1.2   GENERAL USE OF THE DATA AND MODELS

Depending upon which test, model, or system one is interested
in there is a section of the Handbook which is applicable.   The
user of this Handbook may be concerned with the performance of
a particular E-O sensor at a specific location under well-
defined meteorological conditions. The user should be able to
specify what his performance criteria are (i.e. contrast loss,
transmission loss, etc.) or if necessary he can learn what
specific criteria have been used by the E-O community by referring
to the definition of relationships between battlefield environ-
mental conditions and their significant parameters in Section 2
of the Handbook.   In addition, the user can refer to the models
and data given in Sections 8 and 9 to learn which performance
criteria have been used for current E-O sensors and systems.   It
should be noted that this Handbook can be used in a variety
of ways.   For example, it is applicable not only for the analysis
of specific sensors and systems but also for more theoretical
or analytical studies of the effects of the atmosphere on
electromagnetic radiation in a military environment.   Thus,
one can take parts of one section and use them with formulas,
equations, charts, tables, or graphs from another section to
perform whatever analysis one is interested in.   Also, the
looseleaf binding of the Handbook and the positioning of the
sections allows one to update the Handbook in a convenient
manner by merely inserting new sections or subsections.

1.3 TYPICAL EXAMPLES OF HOW DATA AND MODELS ARE USED

Here we shall present some examples of how one can use the Handbook in a practical way.

Example 1. Copperhead Sensor Performance Model

As a user one might want to perform a series of analytical studies to determine the effects of degraded atmospheric conditions on the performance of the Copperhead sensor. The Copperhead seeker passively homes in on the 1.06 μm laser radiation which is reflected from a target which is designated by a laser. The series of studies might include the determination (by calculation) of the target acquisition range R_{TS}, for the target T, and the Copperhead seeker S, for a light fog condition during the daytime in midwinter for southern Germany. First, the user should go to Section 8 of the Handbook to find a description of basic characteristics of US Army E-O systems. This particular sensor description is found in Subsection 8.3. Here the model provides one with the working formula for the target acquisition range, i.e.

$$R_{TS}^2 = \frac{\rho}{\pi} A \frac{P_T}{P_{Th}} T_{TS} T_{TD} \cos \chi \qquad (1.1)$$

where ρ is the diffuse target reflectance, A is the area of the collecting optics of the Copperhead seeker, P_T is the power incident on the target, P_{Th} is the threshold power required at the seeker for acquisition, T_{TS} is the line of sight (LOS) transmittance between the target and sensor, T_{TD} is the LOS transmittance between the target and the laser designator, and χ is the angle between the two lines of sight. It is assumed that the user can easily specify the geometric and design parameters of the study because the specification of parameters such

1-4

as reflectances of targets and laser designator power are beyond the scope of this Handbook.

The user can now refer to Section 2 of the Handbook to find the correct formula for laser transmittance. In the case of fog, the transmittance is given by

$$T(\lambda,S) = \exp\left[-\int_0^S \kappa(\lambda,s')\,ds'\right] \qquad (1.2)$$

where $\kappa(\lambda,S)$ is the volume extinction coefficient for fog conditions at a wavelength λ and at a point S along the path from one point to another. The next step to follow is to refer to Section 6 on Models, and for this particular case to the Subsection 6.1.1.2, i.e., Fog extinction models. In this subsection the user will find the correct fog extinction model for his case. This model, in turn, will depend upon the meteorological and climatological information relevant to the geographic region to be considered. The user should then refer to Section 3 and appropriate subsections for information on visibility, temperature, and other meteorological and climatological data which are typical of the geographic region of interest.

Example 2. Copperhead Sensor Performance Analysis

Rather than doing a study of models as they relate to the performance characteristics of a sensor, the user of this Handbook might want to analyze the Copperhead sensor's performance under actual test conditions. As in example 1, the user should refer to Section 8 for the description of the basic characteristics of US Army E-O systems for information on the Copperhead sensor. He should then go to Section 9 on the performance data of sensors in battlefield conditions, and, in particular to the Subsection 9.1.3 on homing seekers. In this example the

1-5

data are specific and exist for a particular set of conditions.
If the user would like to have performance data on the Copper-
head sensor for mid-winter daytime foggy conditions in northern
Italy and the actual data do not exist in Section 9 then this
represents a gap or void in the data for this example. It is
then suggested that the user apply the methods of example 1 if
he desires information on the performance of a sensor for which
no specific tests have been performed.

Example 3. Carmonette Analysis

A user may be interested in the simulaticn of ground combat.
In this case the user should refer to Section 6 on Models, and,
in particular to Subsection 6.3 on combat models in which he
will find a description of the stochastic, battalion level,
computer program called Carmonette. One part of this large
computer program involves visioility degradation mechanisms.
This requires as. part of the input parameters for the visual
detection routine the scattering and absorption cross sections
of the atmosphere. The user then has the capability of applying
the routine with a variety of possible degraded atmospheric
conditions. For example, if one wishes to perform a study to
simulate conditions in which smoke is present in a battlefield
then one should refer to Subsection 4.1 on smokes. Here he
will find the particular smoke of interest and the appropriate
scattering and absorption cross sections, or, if the cross
sections are not available then attenuation coefficients will be
available. Using Section 2 one can then relate cross sections,
attenuation coefficients and other quantities which are appropriate
for the analysis. In addition, this handbook with its data and
associated algorithms allows one the flexibility of implementing
new subroutines in existing codes. For example, if the user
would like to update the Carmonette model to include a new pro-
cedure for the calculation of smoke attenuation he can do so by
obtaining the Carmonette computer program, locating the section

1-6

or subroutine involving atmospheric attenuation, and then insert
the new algorithms presented in Sections 2 and 4 of the Hand-
book.

RELATIONSHIPS BETWEEN BATTLEFIELD ENVIRONMENTAL
CONDITIONS AND SIGNIFICANT PARAMETERS

2.1 MASS AND VOLUME ATTENUATION COEFFICIENTS

Radiation passing through a medium will be attenuated by two
processes, absorption and scattering. The transmittance along
a path s is given by

$$T(\lambda,s) = \exp\left[-\int_0^s \kappa(\lambda,s')ds'\right] \qquad (2.1)$$

where $\kappa(\lambda,s)$ is the volume extinction (scattering plus absorption)
coefficient at point s in the medium for radiation of wave-
length λ. The units of $\kappa(\lambda,s)$ are reciprocal length, usually
km^{-1}, and it represents the total cross section per unit volume.
Likewise, the total cross section per unit mass, $\kappa_m(\lambda,s)$, with
units of $meter^2/gm$ is referred to as the mass extinction
coefficient. The spectral transmittance, using this coefficient,
is then

$$T(\lambda,s) = \exp\left[-\int_0^s \kappa_m(\lambda,s')\rho(s')ds'\right] \qquad (2.2)$$

when $\rho(s)$ is the density at a point s along the path. It should
be noted that expressions 2.1 and 2.2 are general definitions of
spectral transmittance, i.e. for the transmittance at a particu-
lar wavelength λ. If the spectral transmittance is known then
the transmittance over some wavelength band can be determined by
using the following:

$$T(s) = \frac{\int_{\lambda_i}^{\lambda_f} T(\lambda, s) \, d\lambda}{\lambda_f - \lambda_i} \qquad (2.3)$$

where λ_i and λ_f are the initial and final wavelengths respectively. For homogeneous paths the integral expressions simplify to the following:

$$T(\lambda, s) = \exp\left[- \kappa(\lambda) s\right] \qquad (2.4)$$

and

$$T(\lambda, s) = \exp\left[- \kappa_m(\lambda) X(s)\right], \qquad (2.5)$$

or

$$T(\lambda, s) = \exp\left[- \kappa_m(\lambda) \rho s\right], \qquad (2.6)$$

where

$$X(s) = \int_0^s \rho(s') \, ds'. \qquad (2.7)$$

2-2

Equation (2.4) is to be used if the volume extinction coefficient
is independent of path and equation (2.5) is to be used if the
mass extinction coefficient is independent of path but the density
is not. Finally, equation (2.6) is to be used if the mass extinc-
tion coefficient and the density are constant along the path.

All of these equations include the combined effects of
scattering and absorption by both gases and solid or liquid
particulates in the atmosphere. The individual effects of
scattering and absorption by gases and particulates are quite
different, however, and there are a number of models which treat
these cases in detail, some of which are given in Section 6.

For the definition of terms to be used in this handbook
we use the following:

$$\kappa(\lambda,s) = \alpha(\lambda,s) + \beta(\lambda,s) \qquad (2.8)$$

where $\alpha(\lambda,s)$ is the volume absorption coefficient and $\beta(\lambda,s)$ is
the volume scattering coefficient. Furthermore,

$$\alpha(\lambda,s) = \alpha_G(\lambda,s) + \alpha_A(\lambda,s) \qquad (2.9)$$

where the subscript G refers to the gaseous component of the
atmosphere and the subscript A refers to the particulate or
aerosol component. Likewise, the corresponding terms for the
volume scattering coefficients are

$$\beta(\lambda,s) = \beta_G(\lambda,s) + \beta_A(\lambda,s). \qquad (2.10)$$

2-3

As in the case of the mass extinction coefficients the mass
absorption and mass scattering coefficients can be defined
in a similar manner, i.e. by dividing the volume coefficients
by the density.

2.2 SKY AND PATH RADIANCE

The loss of radiation by scattering and absorption is im-
portant for transmittance but the gain of radiation by scattering
and emission is important for contrast studies. Five different
effects are possible for photons as they progress from one point
to another in a scattering, absorbing, emitting medium. These
processes are illustrated in Figure 2.1. First, a photon can
survive without interaction; second, it can be absorbed; third,
it can be scattered out of the direction of travel. Fourth,
radiation from outside the original path can be scattered into
the direction from target to sensor; and fifth, radiation can
be emitted by the medium. The general equation which relates
these terms is the following:

$$\frac{dL}{ds} = - \alpha(\lambda,s)L(\lambda,s) - \beta(\lambda,s)L(\lambda,s)$$

$$+ \beta(\lambda,s)L_{SCAT}(\lambda,s) + \alpha(\lambda,s)Q(\lambda,s) \qquad (2.11)$$

where $L(\lambda,s)$ is the amount of electromagnetic energy per unit
area per unit time per unit solid angle per unit wavelength
falling on a surface perpendicular to the direction of the
radiation. This quantity is called the spectral radiance at
point s in the medium and often has the units of milliwatts
per square centimeter per steradian per micrometer. The term
$L_{SCAT}(\lambda,s)$ in equation (2.11) is the radiance resulting from
process four, i.e. the gain in radiation due to scattering, and
$Q(\lambda,s)$ is the radiance arising from thermal emission.

2-4

FOV

SENSOR
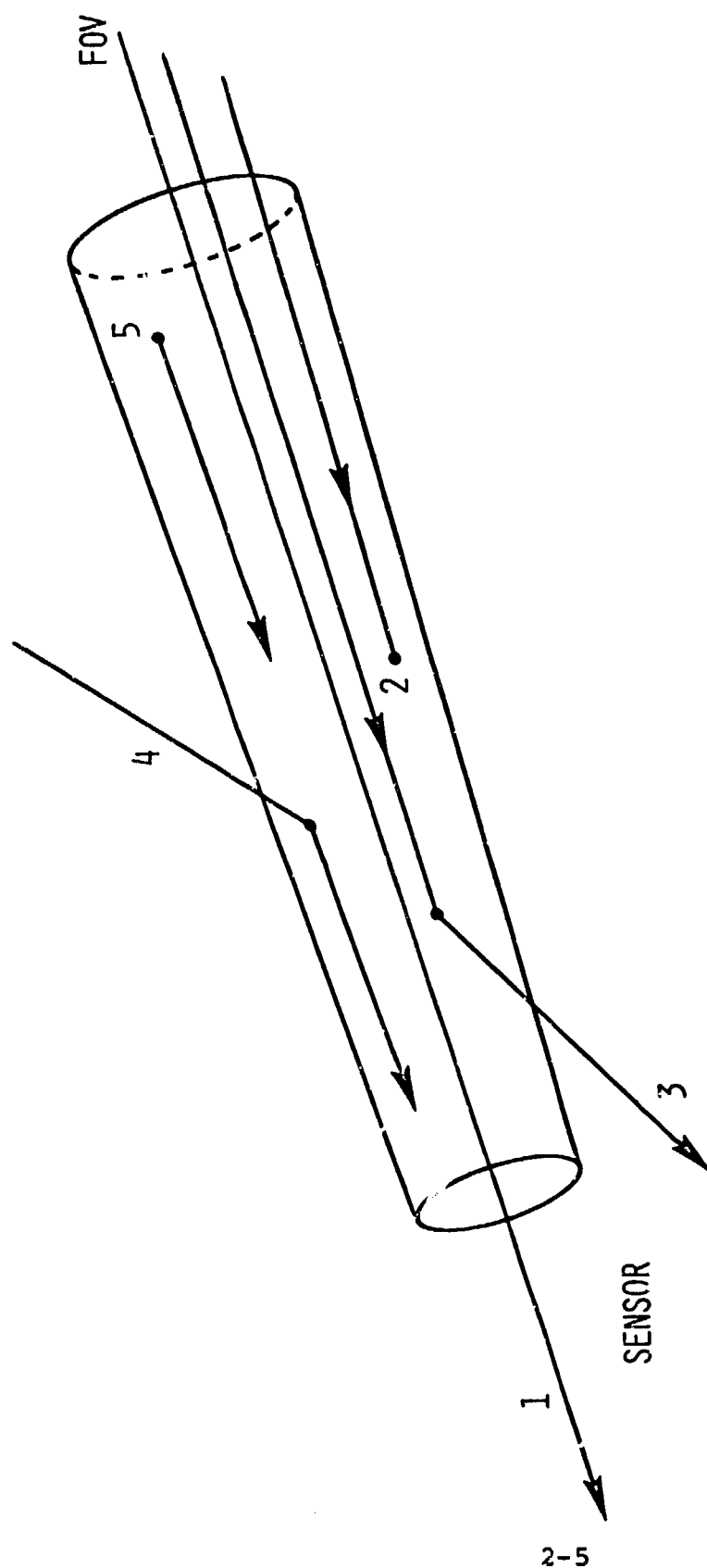
1. NON-INTERACTING RADIATION (NO GAIN, NO LOSS)
2. ABSORBED RADIATION (LOSS)
3. SCATTERED RADIATION (LOSS)
4. SCATTERED RADIATION (GAIN)
5. EMITTED RADIATION (GAIN)

FIGURE 2.1.   INTERACTION MECHANISMS

The angular dependence of radiance is not specifically denoted in equation (2.11) because the equation takes on different forms depending upon the geometry. The solution of equation (2.11) can be quite difficult to obtain especially for complicated geometries and for multiply scattered radiation. Models which describe the radiance for various geometries, atmospheric conditions, and spectral regions are treated in Section 6. Models and measurements are used to determine the radiance due to singly and multiply scattered radiation from the sky, background terrain, clouds, haze, smoke, and other obscurants. Usually the radiance for an upward-looking observer is referred to as the sky radiance. For a military scene as in Figure 2.2 the various radiation components are illustrated. The radiance at the E-O sensor can be written as

$$L_{EO}(\lambda,s) = L_t(\lambda,0)T(\lambda,s) + L_p(\lambda,s) \qquad (2.12)$$

where $L_t(\lambda,0)$ is the target radiance, $T(\lambda,s)$ is the transmittance between the target and sensor along the path s, and $L_p(\lambda,s)$ is the path radiance. The last quantity is usually quite difficult to calculate because it depends not only on the physical properties of the medium but on the specific geometry. Models have been developed which take into account the path radiance because it is of major importance in contrast studies. In the illustration of Figure 2.2 the visible and near IR path radiance arises from the singly and multiply scattered radiation along the path from the target to the E-O sensor. For the thermal infrared region scattering is less important and the path radiance arises primarily from the thermal emission of radiation by the gases and particulates along the path.

The sky radiance, $L_s(\lambda,s)$, is usually thought of as the radiance on a target which arises from singly or multiply
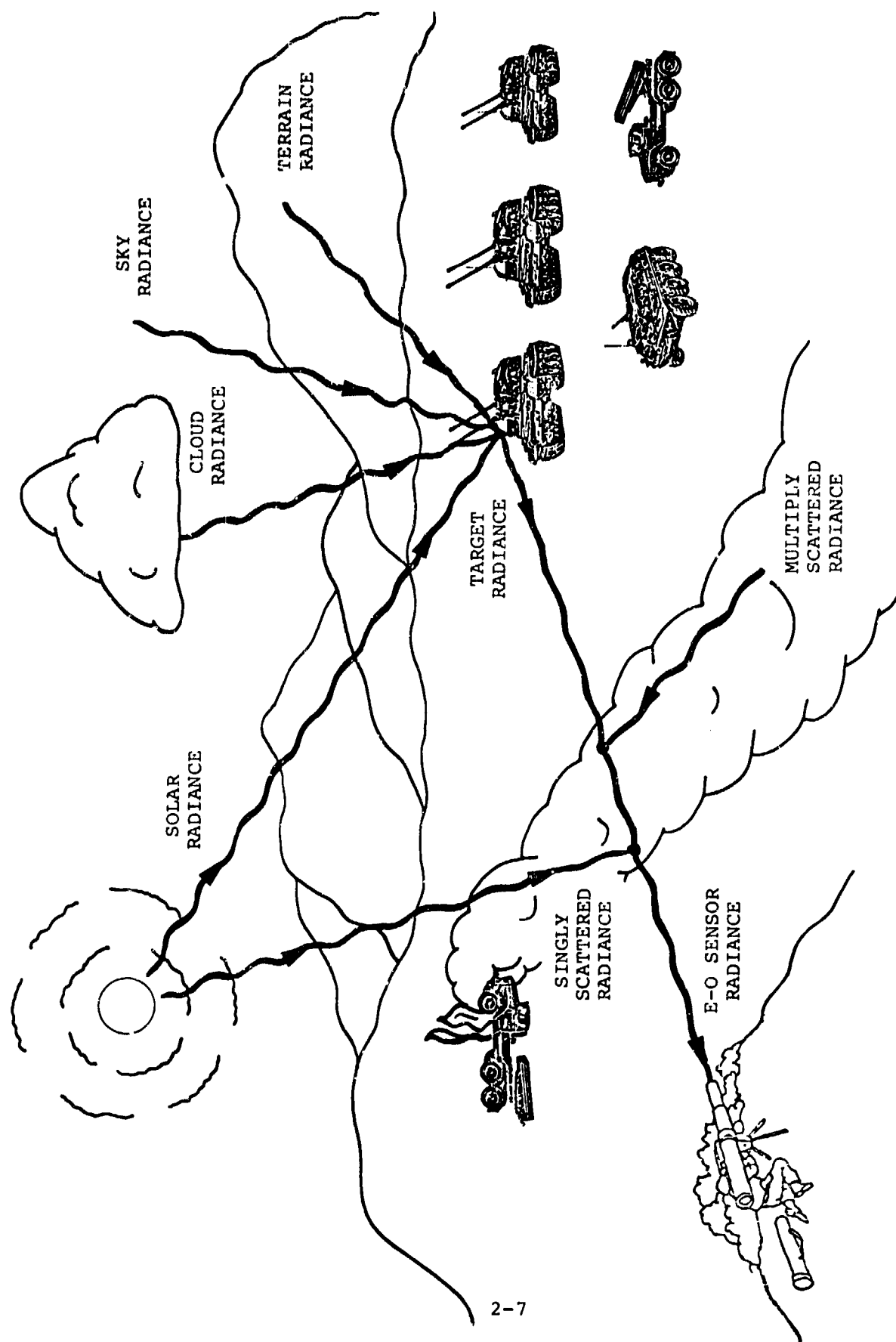
FIGURE 2.2. RADIATION COMPONENTS FOR A PASSIVE MILITARY ELECTRO-OPTICAL SENSOR

scattered or emitted radiation from the atmosphere. It is an important component of the input radiation to a target.

The target radiance, $L_t(\lambda,0)$, is the radiance at the target in the outgoing direction to the sensor. For the military scene in Figure 2.2 we can write the reflected target radiance as

$$L_t(\lambda,0) = \int_{\hat{\Omega}_T} \hat{n}\cdot\hat{\Omega}'\rho(\lambda,\hat{\Omega},\hat{\Omega}')L_{SUN}(\lambda,0,\hat{\Omega}')d\hat{\Omega}'$$

$$+ \int_{\hat{\Omega}_T} \hat{n}\cdot\hat{\Omega}'\rho(\lambda,\hat{\Omega},\hat{\Omega}')L_{CL}(\lambda,0,\hat{\Omega}')d\hat{\Omega}'$$

$$+ \int_{\hat{\Omega}_T} \hat{n}\cdot\hat{\Omega}'\rho(\lambda,\hat{\Omega},\hat{\Omega}')L_S(\lambda,0,\hat{\Omega}')d\hat{\Omega}'$$

$$+ \int_{\hat{\Omega}_T} \hat{n}\cdot\hat{\Omega}'\rho(\lambda,\hat{\Omega},\hat{\Omega}')L_B(\lambda,0,\hat{\Omega}')d\hat{\Omega}' \qquad (2.13)$$

where $L_{SUN}(\lambda,0,\hat{\Omega})$ is the solar radiance at the target facet with normal directional vector $\hat{n}$; $L_{CL}(\lambda,0,\hat{\Omega})$ is the cloud radiance at the target; $L_S(\lambda,0,\hat{\Omega})$ is the sky radiance at the target; and $L_B(\lambda,0,\hat{\Omega})$ is the background radiance (terrain, buildings, vehicles, etc.) at the target. The quantity, $\rho(\lambda,\hat{\Omega},\hat{\Omega}')$ is the bidirectional reflectance of the target which is a function of wavelength and the incoming radiation direction vector $\hat{\Omega}'$ and the outgoing radiation direction vector $\hat{\Omega}$. Thus, it is necessary to integrate these radiance components and the bidirectional reflectance over

2-8

all the incoming directions in order to determine the target
radiance. The total solid angle $\hat{\Omega}_T$ is usually 2π steradians
but if the target is below the flat terrain it can be less
than 2π. For the simple case of a horizontal Lambertian
(perfectly diffuse) target the target radiance becomes

$$L_t(\lambda,0) = \frac{\rho}{\pi}\left[E_{SUN}(\lambda) + E_{CL}(\lambda) + E_S(\lambda) + E_B(\lambda)\right] \qquad (2.14)$$

where ρ is the target reflectance and the E's are the spectral
irradiances on the target arising from the four sources. It
should be noted that spectral irradiance is the amount of
energy falling upon a surface per unit time per unit area per
unit wavelength regardless of direction. It is usually given
in units of milliwatts per square centimeter per micrometer.
It is related to radiance by the following equation:

$$E(\lambda,s) = \int_{2\pi} \hat{n}\cdot\hat{\Omega}'L(\lambda,s,\hat{\Omega}')\,d\hat{\Omega}'. \qquad (2.15)$$

Therefore, the irradiance at some point s in a medium is the
integral of the input radiation weighted by the cosine of the
angle between each radiance component and the normal to the
surface. If there is no attenuation mechanism the radiance is
independent of distance between a source and sensor whereas the
irradiance does depend upon the distance.

For a medium which is in local thermodynamic equilibrium
(LTE) the source term $Q(\lambda,s)$ in equation (2.11) is just given by
the Planck radiation function, i.e.

2-9

$$Q(\lambda,s) + B(\lambda,s) = \frac{2hc^2}{\lambda^5 \left[\exp(hc/\lambda kT_e) - 1 \right]} \qquad (2.16)$$

where h is Planck's constant, c is the speed of light (in the medium), λ is the wavelength of the radiation, k is Boltzmann's constant, and T_e is the temperature of the medium at point s. The thermal radiation is isotropic and depends only on the wavelength and temperature.

For the radiance along some path s in an absorbing, emitting medium we have the formula

$$L(\lambda,s) = L(\lambda,0)T(\lambda,s) +$$

$$T(\lambda,s) \int_0^s \alpha(\lambda,s')T^{-1}(\lambda,s')B[\lambda,T_e(s')]ds' \qquad (2.17)$$

where $T_e(s')$ is the temperature at point s' along the path from 0 to s; $T(\lambda,s')$ is the transmittance at point s' and $\alpha(\lambda,s')$ is the volume absorption coefficient. For the simple case where the temperature is constant along the path, the radiance at point s becomes

$$L(\lambda,s) = L(\lambda,0)T(\lambda,s) + [1 - T(\lambda,s)]B[\lambda,T_e] \qquad (2.18)$$

In equation (2.17) or (2.18) the first term represents the attenuated or beam radiance whereas the second term represents the sky or path radiance.

2.3   AEROSOL AND GAS TYPES

In order to calculate the effects of obscuration due to gases and particulates it is necessary to identify the type of gases and particulates. For gases the problem is to specify the type as, for example, CO_2, H_2O, H_2S, C_3, etc. throughout the region of interest. Knowing the gas, its temperature, and the wavelength of the radiation one can find the spectroscopic parameters which are needed for the calculation of absorption.

For particulates the problem is more complicated. One needs to know the complex index of refraction $m(\lambda)$ of the particles, and the shape, structure, and size distribution of the particles in order to calculate the scattering, absorption, and total cross sections. Smoke, dust, fog, haze, and other atmospheric obscurants have particles characterized by a complex refractive index $m(\lambda)$, where

$$m(\lambda) = m_1(\lambda) + i\, m_2(\lambda). \qquad (2.19)$$

The real part is responsible for the scattering and the imaginary part is responsible for the absorption. They are related by the following dispersion relations:

$$m_1(\lambda) = 1 + \frac{2}{\pi}\lambda^2 \int_0^\infty \frac{m_2(\lambda')\,d\lambda'}{\lambda'(\lambda^2 - \lambda'^2)} \qquad (2.20)$$

$$m_2(\lambda) = -\frac{2\lambda}{\pi} \int_0^\infty \frac{m_1(\lambda') - 1}{\lambda^2 - \lambda'^2}\,d\lambda'. \qquad (2.21)$$

2-11

Thus, if one has the real or imaginary part of the index then the other part is determined.

The structure or the degree of inhomogeneity of the particles is very difficult to determine and at the present time only with the collection and laboratory analysis of samples can this be determined. The same thing is true with the shape of the particulates.

Particle size distribution is important for the calculation of cross sections and attenuation coefficients. Many times it is given by a formula such as

$$\psi(r) = ar^c \exp[-br^\gamma] \tag{2.22}$$

where the parameters a, c, b, γ are not all independent but are related to the mode radius and total number of particles.

2.4 AEROSOL AND GAS CONTENT

The gaseous absorption coefficient can be subdivided into two parts, that due to line absorption and that due to continuum absorption, i.e.

$$\alpha_G(\lambda) = \alpha_{CON}(\lambda) + \sum_n \sum_\ell \alpha_{n\ell}(\lambda) \tag{2.23}$$

where $\alpha_{n\ell}(\lambda)$ is the absorption coefficient for the ℓth line of the nth absorbing gas constituent. To calculate $\alpha_G(\lambda)$ one needs to know the concentration of the gas, the partial pressure of the gas, the temperature, the total atmospheric pressure, and the spectroscopic parameters such as line position $\lambda_{n\ell}$, line

2-12

width $\gamma_{n\ell}$, and the strength $S_{n\ell}$ of each line for each gas.

The gaseous or molecular scattering coefficient is given by the Rayleigh formula. The Rayleigh cross section (in cm^2) is

$$\sigma_{Ray}(\lambda) = 1.3522 \times 10^{-21} \frac{(n_s^2 - 1)^2}{\lambda^4} \qquad (2.24)$$

where n_s is the refractive index of air at 15°C and 1013.250 mb pressure and λ is the wavelength in μm. The corresponding scattering coefficient is

$$\beta_G(\lambda) = \sigma_{Ray}(\lambda) N \qquad (2.25)$$

where N is the number of molecules per unit volume. Compared to the normal aerosol component in the atmosphere the Rayleigh coefficient is usually small and especially so for the longer wavelengths in the infrared part of the spectrum.

The differential scattering cross section is important for the calculation of path and sky radiance. It is related to the total scattering cross section by the following formula:

$$\sigma_s(\lambda) = \int_{4\pi} \sigma_s(\lambda, \hat{\Omega}) d\hat{\Omega} \qquad (2.26)$$

The quantity most often used is the single-scattering phase function, which is defined as

2-13

$$p(\lambda, \hat{\Omega}) = \frac{\sigma_s(\lambda, \hat{\Omega})}{\sigma_s(\lambda)} \qquad (2.27)$$

and is therefore a dimensionless quantity. For gases the phase function is given by

$$p(\lambda, \hat{\Omega}) = 3/4(1 + \cos^2\chi) \qquad (2.28)$$

where the solid angle Ω is

$$\Omega = 2\pi(1 - \cos\chi) \qquad (2.29)$$

χ being the angle from the forward position ($\chi = 0°$).

The absorption and scattering by particulates is a much more difficult problem than for gases. Exact calculation of cross sections have only been performed for spheres, cylinders, and ellipsoids, based on the scattering theory developed by Mie and Lorentz. This is presently a very active field of research and many attempts are being made to calculate cross sections for particles of unusual shape. Even for uniform spheres the formulas for the cross sections must be evaluated on computers because of the slowly decreasing terms in a series expansion. The general relationships which exist between cross sections and attenuation coefficients are as follows:

2-14

$$\alpha_A(\lambda, s) = \int_0^\infty N(s,r)\, \sigma_{A,a}(\lambda, r, s)\, dr \qquad (2.30)$$

$$\beta_A(\lambda, s) = \int_0^\infty N(s,r)\, \sigma_{A,s}(\lambda, r, s)\, dr \qquad (2.31)$$

$$\kappa_A(\lambda, s) = \int_0^\infty N(s,r)\, \sigma_{A,t}(\lambda, r, s)\, dr \qquad (2.32)$$

where $\sigma_{A,a}(\lambda, r, s)$, $\sigma_{A,s}(\lambda, r, s)$, and $\sigma_{A,t}(\lambda, r, s)$ are the absorption, scattering, and total cross sections respectively and $N(s,r)$ is the particle number density for a particle of radius r at position s in the medium. A scattering phase function can also be calculated for a polydisperse system of particles. It is usually quite peaked in the forward direction as opposed to the almost isotropic Rayleigh distribution in the molecular case. It should be noted that a simplification in the above formulas occurs if the particles are much larger ($r \gg \lambda$) then the wavelength of the radiation. In this case the attenuation coefficients become

$$\alpha_A(s) = \pi \int_0^\infty r^2 N(s,r)\, dr \qquad (2.33)$$

2-15

$$\beta_A(s) = \pi \int_0^\infty r^2 N(s,r)\,dr \qquad (2.34)$$

$$\kappa_A(s) = 2\pi \int_0^\infty r^2 N(s,r)\,dr \qquad (2.35)$$

In the case of a monodisperse distribution of particles, i.e. one in which all particles are the same size the attenuation coefficients become

$$\alpha_A(\lambda,s) = N(s)\sigma_{A,a}(\lambda,s) \qquad (2.36)$$

$$\beta_A(\lambda,s) = N(s)\sigma_{A,s}(\lambda,s) \qquad (2.37)$$

$$\kappa_A(\lambda,s) = N(s)\sigma_{A,t}(\lambda,s) \qquad (2.38)$$

for whatever size particle exists in the distribution. The quantity $N(s,r)$ is the number of particles per unit volume per size range Δr whereas $N(s)$ is the total number of particles per unit volume. They are connected by the following:

$$N(s) = \int_0^\infty N(s,r)\,dr \qquad (2.39)$$

$$= N(s) \int_0^\infty \psi(s,r)\,dr \qquad (2.40)$$

where $\psi(s,r)$ is the fraction of particles in the distribution.

For approximate calculations of particulate attenuation coefficients one can use the relations for the limiting case, $r \gg \lambda$, i.e.

$$\alpha_A(s) = N(s)\sigma_g \qquad (2.41)$$

$$\beta_A(s) = N(s)\sigma_g \qquad (2.42)$$

$$\kappa_A(s) = 2N(s)\sigma_g \qquad (2.43)$$

where σ_g is the geometric cross section of the particle.

Everything given so far for the volume attenuation coefficients is also true for the mass attenuation coefficients which are defined as

$$\alpha_m(\lambda,s) = \frac{\alpha(\lambda,s)}{\rho(s)} \qquad (2.44)$$

2-17

$$\beta_m(\lambda, s) = \frac{\alpha(\lambda, s)}{\rho(s)} \qquad (2.45)$$

$$\kappa_m(\lambda, s) = \frac{\kappa(\lambda, s)}{\rho(s)} \qquad (2.46)$$

where $\rho(s)$ is the density of the gas or particles at point s in the medium. The density, $\rho(s)$ is given by

$$\rho(s) = \int_0^\infty N(s, r) \rho_p v(r) dr \qquad (2.47)$$

where ρ_p is the density of a particle and $v(r)$ is the volume. For spherical particles in the "geometric" limit of large radii we get very simple formulas for the mass attenuation coefficients, i.e.

$$\alpha_m = \frac{3}{4\rho_p r} \qquad (2.48)$$

$$\beta_m = \frac{3}{4\rho_p r} \qquad (2.49)$$

$$\kappa_m = \frac{3}{2\rho_p r} \quad . \qquad (2.50)$$

Another quantity which is quite useful in radiation studies is the single-scattering albedo defined as

$$\omega_0(\lambda,s) = \frac{\beta(\lambda,s)}{\kappa(\lambda,s)} \, . \qquad (2.51)$$

It is a dimensionless ratio and is indicative of the relative amount of scattering which takes place in a medium.

2.5 CONTRAST

If we denote the radiance from a target by $L_t(s)$*, where s is the distance of the sensor from the target, and the radiance from the background by $L_b(s)$, then the contrast is defined as

$$C(s) = \frac{L_t(s) - L_b(s)}{L_b(s)} \, . \qquad (2.52)$$

The contrast ranges from -1 for black targets at zero range and increases without bound as the background radiance decreases to zero. In the daytime typical contrasts lie between -1 and 10 whereas at night the contrast can be much greater.

Using the general relationship (Eq. 2.12) which connects the radiance at distance s to the radiance at the origin we get

$$C(s) = C(0) \left[\frac{L_b(0)}{L_b(s)} \, T(s) \right] \qquad (2.53)$$

---

*We can eliminate the symbol λ for wavelength since everything is assumed to be spectral.

where $C(0)$ is the inherent contrast or the contrast at zero range. The ratio of the contrast $C(s)$ to the inherent contrast $C(0)$ is called the contrast transmittance $T_c(s)$, i.e.

$$T_c(s) \equiv C(s)/C(0) \qquad (2.54)$$

or

$$T_c(s) = \frac{L_b(0)}{L_b(s)} T(s). \qquad (2.55)$$

Thus, the contrast transmittance is equal to the actual transmittance, $T(s)$ multiplied by the ratio of the background radiances at zero range and at range s. Equation (2.55) is deceptively simple. In actual practice it is quite difficult to evaluate the ratio of the background radiances. Using the relationship

$$L_b(s) = L_b(0)T(s) + L_p(s) \qquad (2.56)$$

we obtain for the contrast transmittance, $T_c(s)$

$$T_c(s) = \frac{1}{1 + \dfrac{L_p(s)}{L_b(0)T(s)}} . \qquad (2.57)$$

2-20

It should be noted that if there is no scattering or emission into the field of view then the contrast transmittance is unity and no loss of contrast results. Hence, it is not attenuation but rather the scattering and/or emission into the field of view which causes a loss in contrast. Since some scattering always exists in a medium there will always be a loss of contrast. Even in an atmosphere composed of large black particles there will be diffraction scattering and a loss of contrast.

To the ordinary observer the concept of visual range or visibility has greater meaning than atmospheric optical depth or turbidity. For this reason it is useful to relate the visual range to specific atmospheric optical parameters. For the case of horizontal vision, i.e. for an observer looking at the horizon, in which case $L_b(0) = L_b(S)$, the contrast transmittance is given by

$$T_c(s) = \exp\left[-\int_0^s \kappa(s')ds'\right] \qquad (2.58)$$

If we use the assumption that the atmosphere is horizontally homogeneous then $\kappa(s) = \kappa$ and equation (2.58) becomes

$$T_c(s) = e^{-\kappa s} . \qquad (2.59)$$

One can now introduce the Koschmieder assumption that the limiting contrast transmittance for sizeable objects seen in daylight is 0.02. Equation (2.59) can then be solved for the range $s = V$ for which this $T_c(s)$ is equal to 0.02. It is

$$V = \frac{3.912}{\kappa} \qquad\qquad (2.60)$$

where κ is the volume extinction coefficient for a human observer, i.e. the value of κ is to be the average over the response of the human eye at daytime. For most situations it is sufficient to take the value of κ at the peak of the human eye response curve, i.e. at a wavelength of 0.55 µm. A graph of equation (2.60) is illustrated in Figure 2.3 for a large range of visibilities. The upper limit of visual range for the Earth's atmosphere at sea level is determined by the scattering and absorption in an aerosol-free atmosphere. This value is about 336 km but depends slightly on the amount of ozone present.

The visual range for terrestrial backgrounds is of importance for many military situations but it is also more complicated to evaluate because of the variability in the reflectance and emissivity of the surface materials. For such cases one must consider the fact that the background radiance at the target is not equal to the background radiance at the horizon but, rather, it depends upon the non-sky background radiance. A detailed treatment of this problem must depend upon the further development of contrast transmittance models.
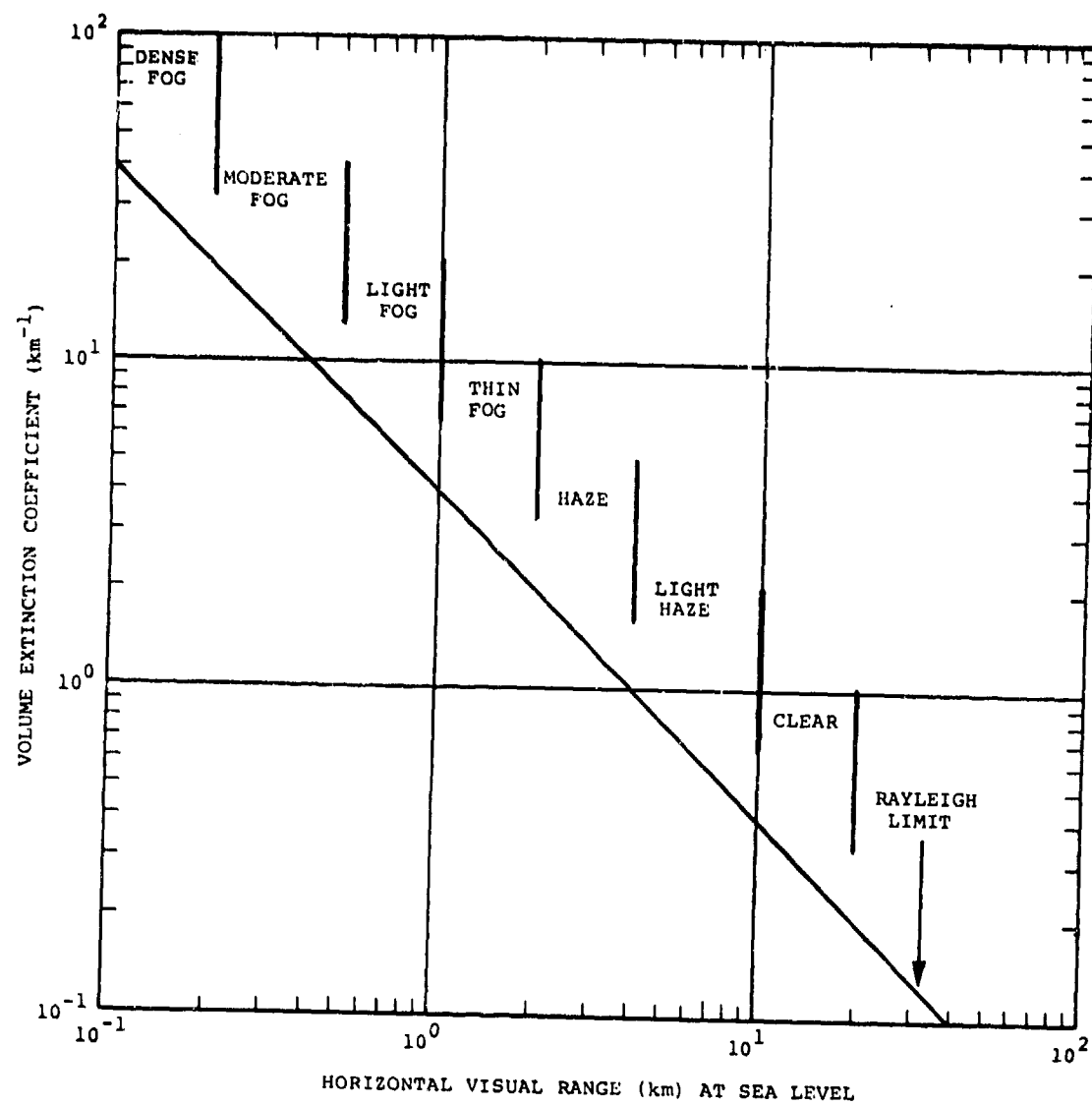
FIGURE 2.3   VARIATION OF VOLUME EXTINCTION COEFFICIENT WITH
HORIZONTAL VISUAL RANGE AT SEA LEVEL FOR A
WAVELENGTH OF 0.55 µm.

2-23

2.6 DISPERSION OF GASES AND PARTICULATES

The goal of this section is to provide tools for the reader who wishes to make rough dispersion estimates for a chemically inert cloud of gases or particulates. The equations that follow are based on Sutton's theory of turbulent diffusion as described in references 1 and 2. For a complete theoretical discussion, including derivation of these formulas from the diffusion equation, the reader is referred to Seinfeld [3].

Equation (2.61) describes local concentration $C(x,y,z,t)$ in a cloud at time t as a result of an instantaneous point source release:

$$C(x,y,z,t) = \frac{Q}{(2\pi)^{3/2}\sigma_1\sigma_2\sigma_3} \exp\left[-\frac{1}{2}\left(\frac{x^2}{\sigma_1^2} + \frac{y^2}{\sigma_2^2} + \frac{z^2}{\sigma_3^2}\right)\right]. \quad (2.61)$$

This equation is appropriate for clouds from shell burst and also some types of smoke munitions. The spatial coordinates (x,y,z) are with reference to a coordinate system moving with the cloud centroid, at mean wind speed u; Q is the total mass release at t = 0.

The values for the σ_i are given according to the relations

$$\sigma_i^2 = \frac{1}{2} c_i^2 (ut)^{2-p} \quad (2.62)$$

In the absence of detailed meteorological information, the values of c_i and p can be obtained from Table 2.1. Reference 1 contains formulas based on theory for c_i and p in terms of more complex meteorological observables:

2-24

TABLE 2.1 (from [1])

p and c^2 at Various Source Height Values h; h in Meters

$$(c_i^2 = c^2 \text{ for } i = 1,2,3)$$

	p	h=25	h=50	h=75	h=100
Large lapse rate	0.20	0.043	0.030	0.024	0.015
Zero or small temperature gradient	0.25	0.014	0.010	0.008	0.005
Moderate inversion	0.33	0.006	0.004	0.003	0.002
Large inversion	0.50	0.004	0.003	0.002	0.001

$$u = u_0 (z/z_0)^{p/(2-p)} \qquad (2.63)$$

and

$$c_i{}^2 = \frac{4\nu^p}{(1-p)(2-p)u^p} \left(\frac{s_i{}^2}{u^2} \right)^{(1-p)} . \qquad (2.64)$$

Equation (2.63) is the wind power scaling law, giving wind velocity at height z in terms of its velocity u_0 at a reference height z_0. The $S_i{}^2$ are the mean square values of the wind speed fluctuations in the i-th coordinate directions. ν is the kinematic viscosity of air, given by

$$\nu = 145.8 \times 10^{-8} \frac{T^{3/2}}{\rho(T + 110.4)} \text{ (kg/m-sec)} \qquad (2.65)$$

where T is air temperature and ρ is air density. The values of $S_1{}^2$ and $S_2{}^2$ can be obtained from anemometer readings; $S_3{}^2$ is more difficult to measure. Reference 1 derives formulas approximating S_2 and S_3 for the case of isotropic turbulence, and also gives a modification to (2.64) for surfaces where the surface roughness parameter is non-negligible.

Equation (2.66) gives steady state, local concentration $C(x,y,z)$ for a continuous point source, with a wind of average speed u in the x direction:

$$C(x,y,z) = \frac{Q}{2\pi\sigma_y\sigma_z u} \exp\left[-\frac{1}{2}\left(\frac{y}{\sigma_y}\right)^2\right]$$

$$\times \left\{\exp\left[-\frac{1}{2}\left(\frac{z-H}{\sigma_z}\right)^2\right] + \exp\left[-\frac{1}{2}\left(\frac{z+H}{\sigma_z}\right)^2\right]\right\}. \qquad \cdot \quad (2.66)$$

Q is the mass emission rate (g/sec), H is the height at which the plume centroid stabilizes and σ_y and σ_z can be obtained from Figures 2.4 from reference 2. Here the coordinate system is assumed to have origin fixed at the source, and total reflection of the plume at the ground is assumed.

Equations 2.61 and 2.66 both give a Gaussian distribution for the plume spread, with standard deviations given by the appropriate σ's. Because of the statistical nature of these formulations, even if the σ's are given by accurate meteorological data, C(x,y,z,t) may underpredict or overpredict the concentration by more than an order of magnitude at a particular point and time.

Equation (2.66) uses a principle known as the principle of total reflection. This assumes that the cloud of gases or particulates, as it diffuses outward, is totally reflected by the ground, with no deposition or reaction at the surface. This principle is not applied to (2.61), and in the case of a ground source with total reflection the value for C(x,y,z,t) should be doubled. Some sources write equations with terms for reflection from an inversion layer as well. In addition, the principle of linear superposition allows one to assess the effect of several sources by addition of their effects individually. Table 2.2 allows for determination of atmospheric stability categories from simple observations, when meteorological measurements are not available.
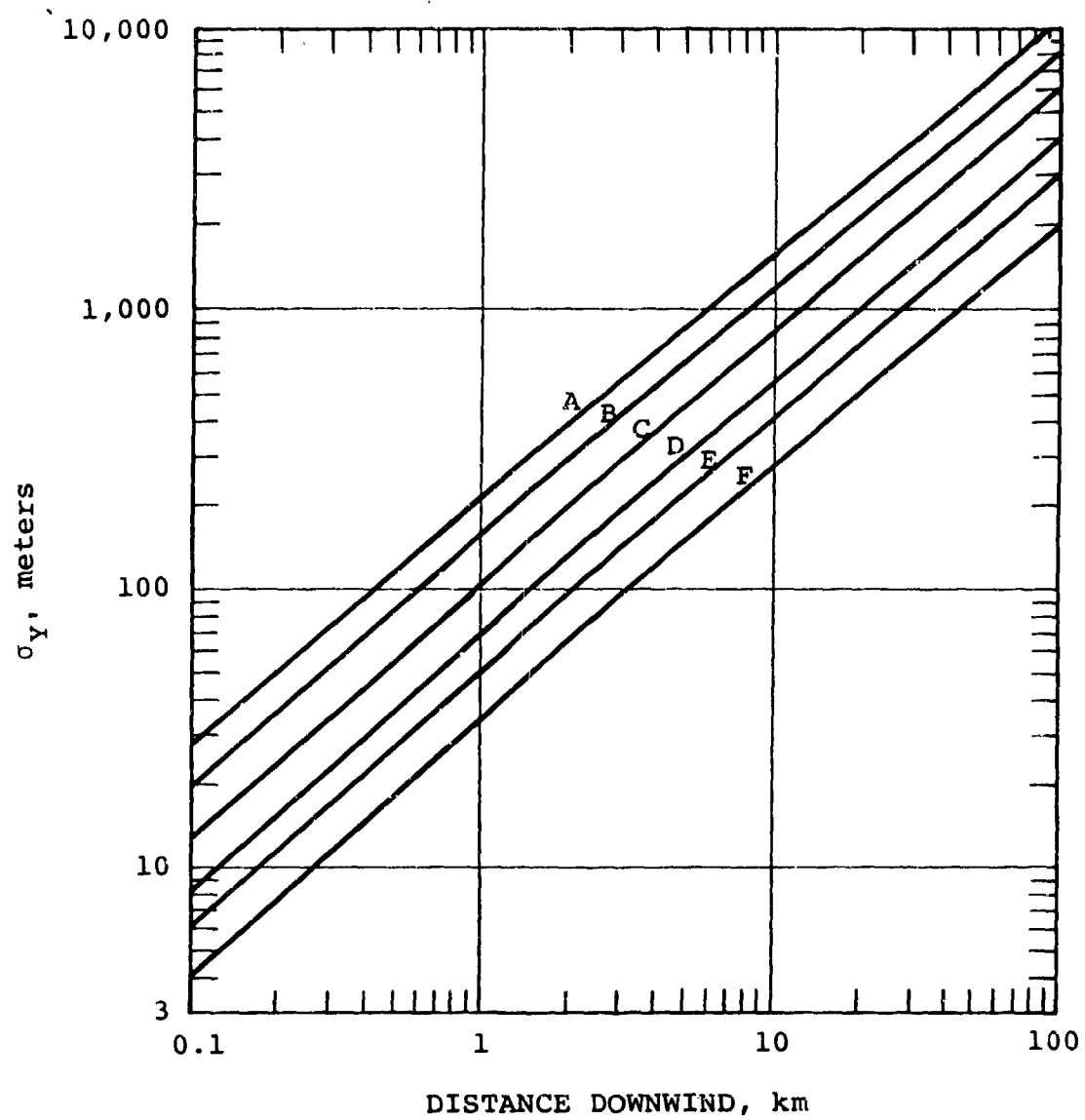
FIGURE 2.4 (a).   HORIZONTAL DISPERSION COEFFICIENT AS A
                  FUNCTION OF DOWNWIND DISTANCE FROM THE
                  SOURCE
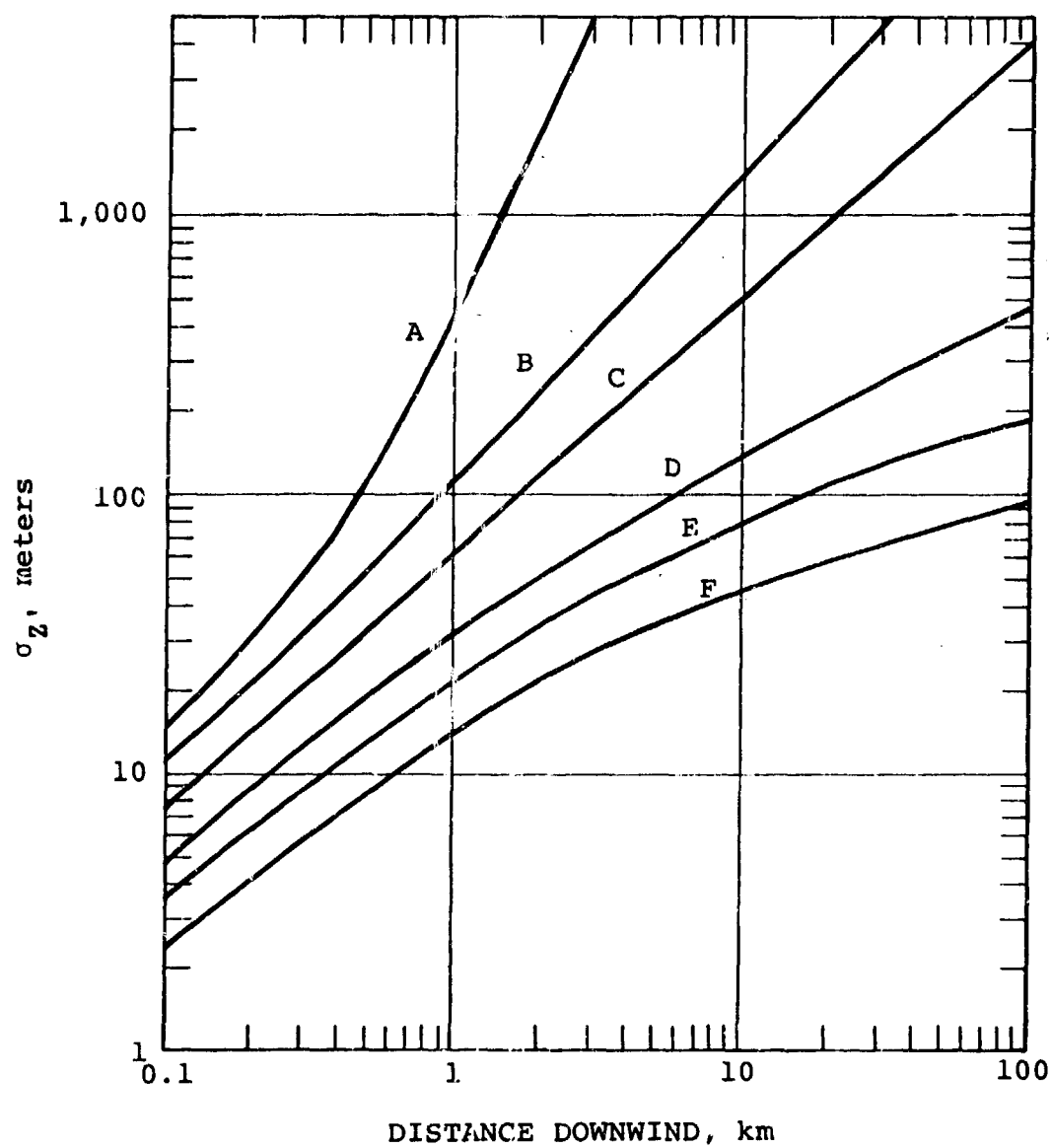
FIGURE 2.4 (b). VERTICAL DISPERSION COEFFICIENT AS A
FUNCTION OF DOWNWIND DISTANCE FROM THE
SOURCE

2-29

TABLE 2.2 (from [2])

KEY TO STABILITY CATEGORIES

Surface Wind Speed (at 10m), m/sec	Day Incoming Solar Radiation			Night	
	Strong	Moderate	Slight	$\geq \frac{4}{8}$ Cloud	$\leq \frac{3}{8}$ Cloud
< 2	A	A-B	B		
2-3	A-B	B	C	E	F
3-5	B	B-C	C	D	E
5-6	C	C-D	D	D	D
> 6	C	D	D	D	D

The neutral class, D, should be assumed for overcast conditions during day or night.   A → F are in order of increasing stability.

2.7 SURFACE CONDITIONS

A kno··ledge of the surface conditions is important in atmospheri. obscuration studies because the radiatioⅇ in the atmosphere is partially determined by the surface reflectance. Also, in contrast studies one needs to know the reflectance and emittance of the surface which can serve as a background. In this section we consider only the radiometric properties of the surface whereas in another section we consider the physical properties of the soil.

The general expression for the reflectance of a surface is given by

$$\rho(\lambda, \theta, \phi, \theta', \phi') \tag{2.67}$$

when the primed angles refer to the spherical coordinates of the incoming radiation and the unprimed angles refer to the spherical coordinates of the outgoing radiation. This quantity is called the bidirectional reflectance distribution function (BRDF) of the surface and is a function of wavelength and the four angles. The outgoing spectral radiance from a surface is given by

$$L_r(\lambda, \theta, \phi) = \int_0^{2\pi} \int_0^{\pi/2} \sin\theta' \cos\theta' \rho(\lambda, \theta, \phi, \theta', \phi') L_i(\lambda, \theta', \phi') d\theta' d\phi' \tag{2.68}$$

where $L_i(\lambda, \theta', \phi')$ is the incoming radiance and $L_r(\lambda, \theta, \phi)$ is the outgoing or reflected radiance. A reciprocity theorem exits for the bidirectional function, i.e.

2-31

$$\rho(\lambda,\theta,\phi,\theta\acute{},\phi\acute{}) = \rho(\lambda,\theta\acute{},\phi\acute{},\theta,\phi). \qquad (2.69)$$

If one integrates the BRDF over all angles θ,ϕ one obtains the directional-hemispherical spectral reflectance, i.e.

$$\rho(\lambda,\theta\acute{},\phi\acute{}) = \int_0^{2\pi}\int_0^{\pi/2} \sin\theta\ \cos\theta\rho(\lambda,\theta,\phi,\theta\acute{},\phi\acute{})d\theta d\phi \quad (2.70)$$

which defines how much of the radiant energy incident from one direction will be reflected into all directions.

For a diffuse surface the BRDF is independent of the angular coordinates and therefore the reflected radiance is

$$L_r(\lambda) = \rho(\lambda)E(\lambda) \qquad (2.71)$$

where $E(\lambda)$ is the irradiance on the surface and $\rho(\lambda)$ is the BRDF. If one now integrates the reflected radiance over all angles θ,ϕ we get by definition the radiant exitance, i.e.

$$M(\lambda) = \int_0^{2\pi}\int_0^{\pi/2} L_r(\lambda,\theta,\phi)\sin\theta\ \cos\theta d\theta d\phi \qquad (2.72)$$

$$= \pi\rho(\lambda)E(\lambda).$$

2-32

The surface albedo $\overline{\rho}(\lambda)$ is defined as the ratio of the exitance to the irradiance so that

$$\overline{\rho}(\lambda) = \frac{M(\lambda)}{E(\lambda)} \qquad (2.73)$$

For many applications in military investigations it is the surface spectral albedo which is important and which is also most commonly given in references on surface reflectances. For a Lambertian (diffuse) surface then, the spectral radiance is given by

$$L(\lambda) = \frac{\overline{\rho}(\lambda)}{\pi} E(\lambda). \qquad (2.74)$$

For the purposes of this Handbook these relations are of greatest significance. Many additional formulas can be defined for surfaces with varying degrees of symmetry but a complete discussion of these is beyond the scope of this Handbook.

Another quantity which is important for military studies is the emissivity of a surface. Unlike the emission of radiation from a blackbody the emission from a real surface depends upon the direction. The general directional emissivity of a surface is given by

$$\varepsilon(\lambda,\theta,\phi,T_e) = \frac{L(\lambda,\theta,\phi,T_e)}{B(\lambda,T_e)} \qquad (2.75)$$

where $L(\lambda,\theta,\phi,T_e)$ is the thermal radiance emitted by the surface

2-33

and $B(\lambda,T_e)$ is the thermal radiance emitted by a blackbody of the same temperature T_e. The hemispherical spectral emissivity can be defined by integrating the directional emissivity over the hemisphere, i.e.

$$\epsilon(\lambda,T_e) = \frac{M(\lambda,T_e)}{\pi B(\lambda,T_e)} \tag{2.76}$$

$$= 1/\pi \int_0^{2\pi}\int_0^{\pi/2} \sin\theta\,\cos\theta\,\epsilon(\lambda,\theta,\phi,T_e)\,d\theta d\phi$$

where $M(\lambda,T_e)$ is the radiant exitance of the surface. Finally, one can define the hemispherical total (integrated over wavelength) emissivity as

$$\epsilon(T_e) = \frac{\int_0^\infty \epsilon(\lambda,T_e)B(\lambda,T_e)\,d\lambda}{\sigma T_e^4} \tag{2.77}$$

where $B(\lambda,T_e)$ is the Planck function and σ is the Stefan-Boltzmann constant.

These relations for emissivity are of importance in thermal radiation models and especially for models of thermal contrast.

2.8 OPTICAL WEATHER

Besides the semi-permanent suspensoid called an aerosol the atmosphere contains hydrometeors classified as rain, snow, sleet, hail, drizzle, and other forms of precipitation. As in the

2-34

case of aerosols the volume extinction coefficient is given by

$$\kappa(\lambda) = \int_0^\infty n(r)\sigma(\lambda,r)\,dr.$$ (2.78)

The particle flux is given by

$$\Phi = \int_0^\infty n(r)u(r)\,dr$$ (2.79)

where $u(r)$ is the terminal speed of a particle of radius r. For large particles, i.e. those for which $r \gg \lambda$ the total cross section is

$$\sigma(\lambda,r) \approx 2\pi r^2$$ (2.80)

and the speed is proportional to r^2. Thus, both the particle flux and the extinction coefficient are proportional to the second moment of the particle number density distribution and one can write

$$\kappa = k\Phi$$ (2.81)

where k is a constant. Unfortunately, it is not easy to measure particle flux but it is relatively easy to measure the rate of precipitation, given by

$$R = \frac{\displaystyle\int_0^\infty n(r)m(r)u(r)\,dr}{\displaystyle\int_0^\infty n(r)m(r)\,dr} \qquad (2.82)$$

where the integral in the numerator is the mass flux and the integral is the denominator is the density of the particles. For size distributions which are exponential, i.e.

$$n(r) = n_0 e^{-ar} \qquad (2.83)$$

the volume extinction coefficient and the precipitation rate become

$$\kappa \propto a^{-3} \qquad (2.84)$$

$$R \propto a^{-2} \qquad (2.85)$$

so that

$$\kappa = AR^{1.5}. \qquad (2.86)$$

For a monodisperse distribution, on the other hand we have

$$\kappa = AR .$$ (2.87)

A variety of semi-empirical data indicate that the form for the relationship which connects the volume extinction coefficient and the precipitation rate is therefore

$$\kappa = AR^C$$ (2.88)

where A and c are parameters which depend upon the type of precipitation and the conditions which occur.

Another quantity of use to military studies is the mass content of smoke, dust, or in the case of precipitation and fogs, the total water content. It is given by

$$\rho = \int_0^\infty n(r) m(r) dr$$ (2.89)

and has the dimensions of mass per unit volume. Related to this is the liquid water column density, X, given by

$$X = \int_0^\infty \rho(z) dz$$ (2.90)

2-37

where $\rho(z)$ is the density of the water at some altitude z.
Thus, X has the dimensions of mass per unit area.

2.9 SUMMARY

In this section we summarize the basic relationships which
connect environmental conditions and significant parameters.

1. Transmittance

$$T(\lambda,s) = \exp[-\kappa(\lambda)s]$$

2. Mass content

$$X(s) = \int_0^s \rho(s')ds'$$

3. Extinction coefficient

$$\kappa(\lambda,s) = N(s)\sigma_t(\lambda,s)$$

4. Absorption coefficient

$$\alpha(\lambda,s) = N(s)\sigma_a(\lambda,s)$$

5. Scattering coefficient

$$\beta(\lambda,s) = N(s)\sigma_s(\lambda,s)$$

6. Spectral radiance at
    sensor

$$L = L_t T + L_p$$

7. Target radiance

$$L_t = \frac{\rho}{\pi} E(irradiance)$$

8. Path radiance
    (scattering)

L_p(complicated function of angles
and medium parameters)

9. Path radiance
    (emission)

$$L_p = (1 - T)B$$

10. Particle size
    distribution

$$\psi(r) = ar^c\exp[-br^\gamma]$$

11. Rayleigh cross section

$$\sigma_R(\lambda) \propto \frac{1}{\lambda^4}$$

12. Rayleigh phase function $\quad p(\chi) = \dfrac{3}{4}(1 + \cos^2\chi)$

13. Aerosol phase function $\quad$ (strongly peaked in forward direction)

14. Mass extinction coefficient $\quad \kappa_m(\lambda, s) = \dfrac{\kappa(\lambda, s)}{\rho(s)}$

15. Mass absorption coefficient $\quad \alpha_m(\lambda, s) = \dfrac{\alpha(\lambda, s)}{\rho(s)}$

16. Mass scattering coefficient $\quad \beta_m(\lambda, s) = \dfrac{\beta(\lambda, s)}{\rho(s)}$

17. Single-scattering albedo $\quad \omega_0(\lambda, s) = \dfrac{\beta(\lambda, s)}{\kappa(\lambda, s)}$

18. Contrast $\quad C(s) = \dfrac{L_t(s) - L_b(s)}{L_b(s)}$

19. Contrast transmittance $\quad T_c(s) = C(s)/C(0)$

20. Visual range $\quad V = \dfrac{3.912}{\kappa}$

21. Particle concentration (diffusion) (point source) $\quad C = C_0 \exp\left[-\dfrac{1}{2}\left(\dfrac{x^2}{\sigma_1^2} + \dfrac{y^2}{\sigma_2^2} + \dfrac{z^2}{\sigma_3^2}\right)\right]$

2-39

22. Particle concentration
(diffusion)
(line source)
$$C = C_0 \exp\left[-\frac{1}{2}\left(\frac{z}{\sigma_3}\right)^2\right]$$

23. Reflected radiance
$$L_r = \int \cos\theta\, \rho\, L_i\, d\Omega$$

24. Exitance
$$M = \int L_r \cos\theta\, d\Omega$$

25. Irradiance
$$E = \int L_i \cos\theta'\, d\Omega'$$

26. Surface albedo
$$\overline{\rho}(\lambda) = \frac{M(\lambda)}{E(\lambda)}$$

27. Directional emissivity
$$\varepsilon(\lambda,\Omega) = \frac{L(\lambda,\Omega)}{B(\lambda)}$$

28. Total emissivity
$$\varepsilon(T_e) = \frac{\pi \int \varepsilon(\lambda,T_e) B(\lambda,T_e)\, d\lambda}{\sigma T_e^{\,4}}$$

29. Flux (precipitation)
$$\Phi = \int_0^{\infty} n(r)\, u(r)\, dr$$

30. Extinction
(precipitation)
$$\kappa = AR^C$$

REFERENCES FOR SECTION 2

1. Nawrocki and Papa, <u>Atmospheric Processes</u>, Prentice-Hall, Inc., 1963.

2. D.B. Turner, <u>Workbook of Atmospheric Dispersion Estimates</u>, NTIS Publication PB-191 482, 1970.

3. J.H. Seinfeld, <u>Air Pollution: Physical and Chemical Fundamentals</u>, McGraw-Hill, Inc., 1975.

SECTION 3
NATURAL ENVIRONMENTS

3.0 INTRODUCTION

Climatology and topography play an important role in strategic and tactical decisions. Environmental factors can point to the need to select one type of E-O system over another for a particular application. Consequently, in designing, testing, and using systems, an assessment of the operational effects of potential environments is of first magnitude importance.

For every region of the electromagnetic spectrum the range of meteorological conditions under which systems will operate effectively must be determined. Fog or dust regimes can degrade the performance of IR systems significantly while millimeter-wave devices may be only slightly affected. Conversely, rain may affect systems operating in the infrared much less than devices employing millimeter wavelengths. Topographic features including surface roughness and vegetation type influence the choice between active and passive systems. An active system can not be expected to be effective in a heavily forested area or an area with much terrain clutter because of the spurious signals that would be returned to the detector.

In this part of the Handbook an overview of natural environments will be presented. Typical natural environments will be outlined in terms of their weather and topography, and guidance will be provided to the reader who wants further data on environmental factors.

3.1 DATA TYPES, SOURCES, AND FORMATS

This section describes the sources of data on natural environments and the type of information that is available. It should be noted that routinely recorded meteorological parameters may not be directly applicable in E-O systems studies. The parameters are derived quantities whose derivation from the standard meteorological quantities is subject to some uncertainty.

For an example application of real weather data to a system study one should consult the work of Biberman and du Mais [1].

3.1.1 WEATHER DATA

Vast quantities of local weather data are reported daily from thousands of stations in inhabited and uninhabited portions of the world. Much of this data is routinely subjected to some form of quality control, and much is available that has already been statistically analyzed. Weather data types are fundamentally distinguished by the scales of weather which they describe, ranging from local descriptions of present weather to data which includes spatial and temporal weather trends.

Surface measurements consist of aviation and synoptic observations. Aviation measurements are made on an hourly basis and more frequently in cases of bad weather to aid aviation interests. Synoptic observations contain more detailed information, including information about weather trends. These are made at three or six hour intervals, for use by weather forecasters and climatologists.

Upper air observations are mainly derived from radiosondes and PIBAL (balloon borne) measurements. PIBAL measurements for the most part yield the vertical profiles of horizontal wind velocity. Radiosonde measurements are made at designated stations at twelve-hour intervals, and provide vertical profiles of the quantities listed in Table 3.1.

Surface observations are reported much more frequently and for more locations than upper air data. For example, in the continental United States, about 550 stations report hourly surface data, while only 75 report upper air data. These data are available in real time via teletype and are also archived by the National Oceanic and Atmospheric Administration (NOAA). Sources for weather data in various formats are given in Table 3.2.

3-2

Table 3.1

WEATHER DATA OBSERVATIONS

AVIATION OBSERVATIONS

1. Cloud coverage and heights

2. Horizontal visibility

3. Air temperature

4. Dew point temperature

5. Real and equivalent sea level pressure

6. Present weather

7. Obstructions to visibility (e.g. dust, haze)

8. Horizontal wind velocity

SYNOPTIC OBSERVATIONS

Everything included under aviation observations and:

9. Past weather

10. Pressure change and pressure tendency

11. 6 and 24 hour precipitation totals

12. Time precipitation began

13. Snow depth

14. Wave information

15. Minimum and maximum temperatures

16. Spectral phenomena

UPPER AIR OBSERVATIONS

Vertical profiles of:

1. Pressure

2. Temperature

3. Humidity

4. Horizontal wind velocity

5. Geopotential height of pressure surface

SATELLITE OBSERVATIONS

1. Spatially resolved spectral data, usually including at least visible and 6.3 μm (H_2O) wavelength bands

TABLE 3.2

WEATHER DATA SOURCES

Statistically Analyzed Data

1. NOAA National Meteorological Center
    Suitland, Maryland

2. Rand Corporation Weather Data Bank
    (described in reference [2])

Archived Observational Data

1. NOAA National Weather Record Center
    Asheville, North Carolina

2. USAF Environmental Technical Application Center
    Scott Air Force Base, Illinois

Satellite Data

1. NOAA National Environmental Satellite Service
    Suitland, Maryland

Special Data Bases

1. OPAQUE European Weather Data Base [3] (includes data
    on atmospheric optical properties in addition to
    weather).

Satellite data have recently become an important source of
the most global weather data. Cloud motions yield important
information about global weather patterns. Also much information
about the vertical structure of the atmosphere can be inferred
using remote sounding methods. Currently, pictorial output is
available from satellites in real time; however, the inferred
temperature and moisture profiles are not yet routinely available.

3.1.2 DATA FOR PARTICULAR REGIONS

Four regions have been selected, because they are repre-
sentative of several of the world's major climatic regimes.
Germany was selected in Europe. The countries bordering the
Caribbean in Central and South America were chosen as examples
of tropical climates and Panama was emphasized. A Syrian desert
area was chosen to be representative of a hot, dry climate.
Alaska constitutes a large land mass, where the climate varies
from nearly temperate in the south to nearly polar along its
northern coast. We have chosen the Tanana River Basin and more
particularly Fairbanks which is located in the Basin to provide
an example of a Subarctic climate.

For each of these areas we will present a general description
of the climate and topography from an empirical point of view,
i.e. we will focus more on climatic data than causative factors.
We will also present weather statistics from a few stations
within each region, and discuss the effects that these conditions
have on operation of E-O systems.

3.2 CENTRAL EUROPEAN REGION (COLD, WET): THE CLIMATE AND TOPOGRAPHY OF GERMANY

3.2.1 CLIMATOLOGICAL DATA

The German climate to a large extent is determined by Atlantic air coming in over the northern lowlands. The Alps along Germany's southern boundary form an effective barrier against the warmer southern Mediterranean air, although Mediterranean air does enter the region in the springtime bringing mild rains. In winter the Siberian high pressure zone brings snow into the region from the northeast. Our source of qualitative information on the German climate is Kays, Seagraves, Monahan, and Sutherland [4]. The following is a brief summary of climatic conditions. There is a need for more detailed climatic characterization, which is currently being met in part by data from the NATO OPAQUE Program and ongoing work at the Atmospheric Sciences Laboratory, White Sands, New Mexico.

Winter weather over Germany results in frequent total cloud cover with low cloud ceilings, less than 1,000 feet for 20 to 30% of the time. This is interspersed with occasional good visibility, partly cloudy skies, and showers. Springtime is associated with light rains and Mediterranean air. The summer brings the period of fairest skies and warmest weather, with frequent afternoon thunderstorms. Autumn is pleasant and mild, with early morning fog occurring often.

Satellite statistics over central Germany show cloud cover in summer to be from zero to three-tenths roughly 30% of the time, from four-tenths to six-tenths around 20% of the time, and from seven-tenths to total during 50% of the time. For winter, seven-tenths to total cloud cover occurs 70-80% of the time, zero to three-tenths occurs 10% of the time, and cloud cover is from four- to six-tenths the remaining 10-20% of the time.

Haze and fog develop often, and this process is aided by soot and waste particles in the air from heavy industry. In the central

region, the fog is usually radiative in origin, and occurs most frequently in the morning. The north coast sees advective fog formation, especially in late winter and early spring when temperature differences between water and land are greatest. Autumn is in general the foggiest season in the central portion, while in late spring fog decreases until its incidence is only in the early morning. Table 3.3 shows seasonal frequency of occurrence of fog by hour of the day for Frankfurt. These data bear out that late autumn is the foggiest season, and that fogs occur mostly in the early morning during the warmer months.

Tables 3.4, 3.5, and 3.6 provide monthly temperature, pressure and precipitation statistics for five German cities. Winter sees frequent freezing temperatures, and summer temperatures are low on the average also with no monthly values exceeding 20°C. These numbers are unweighted means of observations spaced at equal time intervals throughout the day and night.

Precipitation is for the most part frequent but not excessive, averaging 20-40" annually. Summer is the wettest season, with rain occurring on around half the days, for a seasonal amount of 8-12". Winter is the season with least precipitation, with a total seasonal amount ranging from 5-8". A detailed discussion and bibliography on snow occurrence can be found in reference 15. The highest peaks in the Bavarian Alps encounter as much as 100" of precipitation per year. Thunderstorms occur on 2 to 6 days/ month in the interior in late spring. Relative humidity is mostly moderate, ranging from 50-60% in the summer months to 70-85% in the winter, for both Berlin and Frankfurt (see Table 3.7).

A substantial effort is under way at the Atmospheric Sciences Laboratory to characterize German weather. The source document for most of the above discussion is a product of this effort [4], as is the German climatology module of E-O SAEL [5].

The E-O SAEL climatology module provides comprehensive climatological data for Germany. Data are presented as averaged

3-7

for six climatic subregions of the country. The data include averages, standard deviations, and estimated probability of occurrence of the following parameters:

1. cloud cover and height of cloud base
2. horizontal visibility
3. temperature and dew point
4. sea level pressure
5. wind speed and direction
6. weather conditions (rain, snow, fog, etc.)
7. relative and absolute humidity
8. Pasquill stability category

The data base from 168 observation stations was divided into six nonoverlapping regions principally on the basis of terrain and general weather patterns. The data are presented for each hour of a standard day for each month of the year, for each of the six climatic regions. Figure 3.1 shows output from a typical computer run using this module. The means and standard deviations can be used in analytical formulas or for Monte Carlo simulations of the effects of weather on E-O systems.

TABLE 3.3

PERCENT FREQUENCY OF OCCURRENCE OF FOG AT FRANKFURT, GERMANY
(from [4]: hours are Greenwich Mean Time,
period of record 1966-1976)

	00	03	06	09	12	15	18	21
Jan.	18.3	19.5	20.4	25.0	16.0	13.1	16.5	18.1
Apr.	5.0	9.3	13.0	3.1	0.4	0.1	0.5	1.1
July	5.1	12.3	15.6	1.4	0.6	0.2	0.7	1.7
Oct.	24.5	27.5	31.3	24.2	8.2	6.3	15.6	20.0

TABLE 3.4

AVERAGE MONTHLY TEMPERATURE
STATISTICS FOR FIVE GERMAN CITIES
(Period of record in parentheses - from reference 6)

	Berlin (1951-1960)	Kassel (1953-1960)	Frankfurt (1951-1960)
Jan.	0.2°C	-0.1°C	1.3°C
Feb.	-0.4	-0.2	1.6
Mar.	3.7	4.6	6.3
Apr.	8.6	8.0	10.3
May	13.8	12.8	14.5
June	17.5	16.1	17.6
July	19.0	17.5	19.4
Aug.	18.3	16.5	18.2
Sept.	14.6	13.8	14.8
Oct.	9.9	9.6	10.1
Nov.	4.7	5.0	5.7
Dec.	2.3	2.8	3.4

	Hamburg (1951-1960)	Hannover (1951-1960)
Jan.	0.6°C	0.7°C
Feb.	-0.4	-0.2
Mar.	3.2	3.5
Apr.	7.2	7.7
May	11.8	12.4
June	15.2	15.6
July	16.8	17.2
Aug.	16.2	16.6
Sept.	13.2	13.4
Oct.	9.3	9.4
Nov.	5.0	5.1
Dec.	2.9	3.0

TABLE 3.5

AVERAGE MONTHLY PRESSURE
STATISTICS FOR FIVE GERMAN CITIES
(period of record in parentheses - from reference 6)

	Berlin (1951-1960)	Kassel (1953-1960)	Frankfurt (1951-1960)
Jan.	1007 mb	996 mb	1003 mb
Feb.	1008	995	1002
Mar.	1010	995	1002
Apr.	1010	997	1003
May	1010	998	1004
June	1009	997	1004
July	1008	995	1003
Aug.	1008	995	1002
Sept.	1010	998	1004
Oct.	1010	998	1005
Nov.	1010	999	1004
Dec.	1007	994	1002

	Hamburg (1951-1960)	Hannover (1951-1960)
Jan.	1011 mb	1007 mb
Feb.	1012	1008
Mar.	1014	1009
Apr.	1014	1010
May	1015	1010
June	1014	1010
July	1012	1008
Aug.	1011	1008
Sept.	1014	1010
Oct.	1014	1010
Nov.	1013	1009
Dec.	1010	1006

TABLE 3.6

AVERAGE MONTHLY PRECIPITATION AMOUNTS FOR FIVE GERMAN CITIES
(period of record in parentheses - from reference 6)

	Berlin (1951-1960)	Kassel (1953-1960)	Frankfurt (1951-1960)
Jan.	41 mm	61 mm	55 mm
Feb.	31	43	46
Mar.	26	35	40
Apr.	36	48	36
May	42	73	54
June	76	74	70
July	73	95	63
Aug.	60	83	78
Sept.	54	63	58
Oct.	48	65	55
Nov.	40	33	46
Dec.	46	67	64

	Hamburg (1951-1960)	Hannover (1951-1960)
Jan.	60 mm	47 mm
Feb.	37	37
Mar.	38	40
Apr.	33	37
May	52	52
June	73	71
July	78	89
Aug.	107	83
Sept.	60	48
Oct.	57	55
Nov.	51	50
Dec.	68	57

MEAN NUMBER OF DAYS WITH PRECIPITATION GREATER THAN 0.1 INCHES [4]

	Hamburg	Hannover	Kassel	Munich
Jan.	7	6	6	7
Feb.	6	5	5	6
Mar.	6	5	5	6
Apr.	6	5	5	7
May	6	6	6	10
June	7	7	6	11
July	8	7	7	11
Aug.	8	7	7	9
Sept.	7	5	6	7
Oct.	7	6	6	5
Nov.	6	5	5	6
Dec.	8	6	6	6

3-11

TABLE 3.7

AVERAGE RELATIVE HUMIDITY BY MONTH (%)

	Jan.	Feb.	Mar.	Apr.	May	Jun.	Jul.	Aug.	Sep.	Oct.	Nov.	Dec.
Berlin	81	73	63	56	50	53	55	58	60	68	79	84
Frankfurt	79	70	60	52	50	51	53	54	60	69	77	82

MEAN WATER VAPOR PRESSURE (mb) FOR SIX GERMAN STATIONS [14]

	Jan.	Feb.	Mar.	Apr.	May	Jun.	Jul.	Aug.	Sep.	Oct.	Nov.	Dec.
Hamburg/ Fuhlsbuttel	5.7	5.7	6.4	8.4	10.3	12.7	15.2	15.2	12.9	10.1	8.0	6.5
Hannover	5.7	5.7	6.4	8.1	10.5	13.1	15.1	14.9	12.8	10.0	7.9	6.4
Berlin/ Tempelhof	4.9	5.1	5.7	7.6	10.0	12.3	14.7	14.5	12.0	9.3	7.3	5.6
Kassel	5.5	5.6	6.4	7.9	10.3	12.8	14.7	14.5	12.5	9.6	7.5	6.0
Potsdam	5.2	5.3	5.9	7.6	10.1	12.7	14.9	14.7	12.4	9.6	7.5	6.0
Leipzig/ Mockau	5.2	5.3	6.3	7.9	10.7	12.8	14.8	14.4	12.4	9.5	7.2	6.1

CLIMATOLOGY DATA FOR REGION I - LOWLANDS
DURING MAY AT 1200 GMT

METEOROLOGICAL PARAMETER	MEAN	STANDARD DEVIATION	PERCENT OCCURRENCE
CLOUD COVER - LAYER 1 (OCTAS)	3	2	
CLOUD HEIGHT - LAYER 1 (KM)	1.18	1.50	
CLOUD COVER - LAYER 2 (OCTAS)	5	2	
CLOUD HEIGHT - LAYER 2 (KM)	2.43	2.41	
VISIBILITY (KM)	12.7	8.2	
TEMPERATURE (C)	14.8	4.5	
DEW-POINT TEMPERATURE (C)	7.1	4.7	
SEA LEVEL PRESSURE (MB)	1″15.2	7.6	
PASQUILL STABILITY CATEGORY	D		
ABSOLUTE HUMIDITY (GM/CU M)	7.7		
RELATIVE HUMIDITY (PERCENT)	67.9		
WIND SPEED (MPS) FOR 015 DIR	4.2	2.3	4.2
WIND SPEED (MPS) FOR 045 DIR	4.9	2.4	8.2
WIND SPEED (MPS) FOR 075 DIR	5.3	2.4	12.8
WIND SPEED (MPS) FOR 105 DIR	5.0	2.3	8.9
WIND SPEED (MPS) FOR 135 DIR	4.3	1.9	5.5
WIND SPEED (MPS) FOR 165 DIR	4.0	1.9	4.3
WIND SPEED (MPS) FOR 195 DIR	4.8	2.2	5.5
WIND SPEED (MPS) FOR 225 DIR	5.4	2.5	9.9
WIND SPEED (MPS) FOR 255 DIR	5.7	2.6	14.4
WIND SPEED (MPS) FOR 285 DIR	5.6	2.6	11.9
WIND SPEED (MPS) FOR 315 DIR	5.1	2.4	7.5
WIND SPEED (MPS) FOR 345 DIR	4.6	2.2	3.8
WIND SPEED (MPS) FOR VREL DIR	1.0	1.6	3.0
WIND SPEED (MPS) FOR ALL DIR	5.0	2.6	100.0
NO WEATHER OBSCURATION			73.8
SMOKE			.4
HAZE			3.3
LIGHT DUST			.0
MODERATE DUST			.0
HEAVY DUST			.0
FOG OR MIST			2.3
LIGHT DRIZZLE			1.2
MODERATE DRIZZLE			.0
HEAVY DRIZZLE			.0
LIGHT RAIN			15.7
MODERATE RAIN			1.3
HEAVY RAIN			.0
LIGHT SNOW			.0
MODERATE SNOW			.0
HEAVY SNOW			.0
LIGHT THUNDERSTORMS			1.5
MODERATE THUNDERSTORMS			.0
HEAVY THUNDERSTORMS			.0
LIGHT HAIL			.3
MODERATE OR HEAVY HAIL			.0

VISIBILITY
12.70 KM

FIGURE 3.1   OUTPUT FROM E-O SAEL GERMAN CLIMATOLOGY MODULE

3.2.2 TERRAIN CHARACTERISTICS

3.2.2.1 Topographic Description

Much of the topography of Germany has already been described in section 3.1.1, as it relates to climate. Germany is bounded on the northwest by the North Sea and on the northeast by the Baltic. The northern region consists of rolling lowlands. The central highlands consist of low mountains interspersed with river valleys, forming local regions each of which has its own micro-climatology. The Upper Rhine Valley is a basin in the southwest of the central highlands, where fog and pollution occur frequently. The Alpine forelands and Alps in the southern portion receive much precipitation due to northerly flow of air and orographic effects. The entire country is well forested, with abundant water from the many rivers.

3.2.2.2 Typical Albedo

No data were found on this subject.

3.2.3 CIVILIAN ACTIVITIES

3.2.3.1 Industrial Activities

The Federal Republic of Germany is one of the most industrial regions in Europe and, in fact, in the world. Steel production, coal and oil burning, general industry, and the transportation network required to convey the products of industry result in heavy pollution of the atmosphere in many regions, especially the basin of the Upper Rhine Valley.

Coal burning results in soot particulates, and also SO_2 from sulfur impurities found in the coal. This SO_2 has been blamed for the formation of "acid rain", i.e. rain containing sulfuric acid. In the region just west of Detroit, Michigan, rain pH's of

around 4 have been found, though no information was found on the
corresponding quantity in Germany. Other typical pollutants due
to industrial activity and presumably to be found in Germany are
ammonium sulfate particulates, hydrocarbons, carbon monoxide,
and various oxides of nitrogen. In general we have found that
typical emission rates are too low to provide significant attenua-
tion, unless one is very near to the pollutant source or unless
meteorological conditions favor haze formation and stasis.

3.2.3.2 Agricultural Activities

No data were found on this subject.

3.2.3.3 Population Density

The population of the Federal Republic of Germany in 1970 was
60,650,599 according to the 1977 U.N. Demographic Yearbook [7] ,
compared with 17,068,318 people living in the German Democratic
Republic. Extrapolations to 1977 indicate 61,396,000 people
in the F.R.G. and 16,765,000 in the G.D.R., resulting in popula-
tion densities of 247 and 155 persons per square kilometer
respectively. The percentage of people in the G.D.R. living
in urban areas was estimated at 75.5% in 1976; this percentage
is unknown for the F.R.G.. In the G.D.R. there were only
14 cities with populations greater than 100,000 in 1976, where
in the F.R.G. there were 66 such cities at around the same time,
including West Berlin.

3.3 DESERT REGION (HOT, DRY): THE CLIMATE OF SYRIA

3.3.1 CLIMATOLOGICAL DATA

The climate of Syria reflects to a great extent its geo-
graphical location. With the Mediterranean Sea along Syria's
western coast, and a northern boundary with mountainous Turkey,
the rainfall amount decreases inland from a maximum value greater
than 40" per year in the northwest corner to amounts less than 10"
per year in the interior.

The majority of rainfall, and cooler temperatures, occur in
the winter, with Damascus at 2,362 feet elevation experiencing
occasional freezing temperatures in the winter months. The
diurnal range of temperature is fairly wide in Damascus, as shown
in Table 3.8. Monthly average maximums of greater than 90° F occur
four months out of the year. Relative humidity is quite low,
ranging from 19% in July to 59% in December.

Tables 3.9, 3.10, and 3.11 show monthly average temperature,
uncorrected pressure, and rainfall amount statistics for six of
Syria's largest cities. These numbers, from the World Weather
Record [6], are unweighted averages of observations taken at
regular intervals through the day and night.

Average monthly temperatures in excess of 25° C for the most
part make Syria a very hot country in the summer months. The
annual rainfall amounts bear out the trend of decreasing as one
goes inland; however, even cities near the coast experience some
months with no rainfall in the summer.

3.3.2 TERRAIN CHARACTERISTICS

The groundwater situation mostly follows the pattern of
decreasing inland, like the rainfall amounts. Syria is mountainous
along its coast and in the north, and the "Fertile Crescent" also

3-17

TABLE 3.8

TEMPERATURE AND RELATIVE HUMIDITY
STATISTICS FOR DAMASCUS

	Jan.	Feb.	Mar.	Apr.	May	June
Average Max. Temperature (°F)	53	57	65	75	84	91
Average Min. Temperature	36	39	42	49	55	61
Extreme Max. Temperature	69	86	83	95	101	102
Extreme Min. Temperature	21	23	28	33	44	48
Relative Humidity (%)	57	53	42	32	26	22

	July	Aug.	Sep.	Oct.	Nov.	Dec.
Average Max. Temperature (°F)	96	99	91	81	67	56
Average Min. Temperature	64	64	60	54	47	40
Extreme Max. Temperature	108	113	102	93	86	69
Extreme Min. Temperature	55	55	50	42	28	23
Relative Humidity (%)	19	21	24	31	46	59

TABLE 3.9

MONTHLY MEAN TEMPERATURE
STATISTICS FOR SYRIAN CITIES
(Period of record in parentheses - from reference 6)

	Aleppo (1952-1960)	Damascus (1951-1960)	Deir Ezzor (1952-1960)
Jan.	6.3°C	7.7°C	7.6°C
Feb.	8.0	9.1	10.3
Mar.	10.5	11.9	12.8
Apr.	15.9	16.6	19.0
May	21.2	21.4	23.9
June	25.9	25.1	29.7
July	28.6	27.2	32.8
Aug.	28.9	27.6	32.6
Sept.	24.8	24.4	28.2
Oct.	20.0	20.6	21.9
Nov.	12.5	13.5	13.7
Dec.	7.4	8.7	8.5

	Hama (1956-1960)	Lattakia (1952-1960)	Palmyra (1955-1960)
Jan.	7.4°C	12.2°C	7.9°C
Feb.	8.4	13.1	9.5
Mar.	11.7	14.3	12.9
Apr.	16.7	17.4	18.3
May	21.9	20.3	23.6
June	26.0	23.9	28.4
July	28.3	26.1	29.5
Aug.	28.9	27.1	30.1
Sept.	25.1	25.6	25.8
Oct.	20.4	22.5	20.8
Nov.	13.5	17.6	12.9
Dec.	8.2	13.5	8.6

TABLE 3.10

MONTHLY MEAN PRESSURE
STATISTICS FOR SYRIAN CITIES
(Period of record in parentheses - from reference 6)

	Aleppo (1952-1960)	Damascus (1951-1960)	Deir Ezzor (1955-1960)
Jan.	971 mb	933 mb	996 mb
Feb.	969	932	995
Mar.	967	930	990
Apr.	965	929	988
May	966	930	987
June	963	928	984
July	960	925	979
Aug.	960	926	981
Sept.	965	929	986
Oct.	969	933	992
Nov.	971	934	995
Dec.	973	935	997

	Hama (1955-1960)	Lattakia (1952-1960)	Palmyra (1956-1960)
Jan.	980 mb	1015 mb	971 mb
Feb.	980	1014	971
Mar.	976	1011	967
Apr.	975	1011	966
May	974	1010	966
June	972	1007	963
July	968	1004	959
Aug.	969	1004	962
Sept.	973	1007	965
Oct.	978	1013	970
Nov.	981	1015	972
Dec.	982	1016	974

TABLE 3.11

MONTHLY MEAN PRECIPITATION STATISTICS FOR SYRIAN CITIES

	Aleppo (1951-1960)	Damascus (1951-1960)	Deir Ezzor (1951-1960)
Jan.	63 mm	54 mm	35 mm
Feb.	46	39	34
Mar.	36	30	33
Apr.	35	15	20
May	14	6	7
June	4	0.4	1.7
July	0.3	0	Tr
Aug.	1.5	Tr	Tr
Sept.	0.3	Tr	0.4
Oct.	18	5	3
Nov.	27	26	12
Dec.	74	60	33

	Hama (1951-1960)	Lattakia (1952-1960)	Palmyra (1955-1960)
Jan.	69 mm	158 mm	16 mm
Feb.	61	94	11
Mar.	41	74	15
Apr.	28	41	12
May	12	25	9
June	2.2	4	1.8
July	0	Tr	0
Aug.	0	0.4	0
Sept.	0.3	15	0
Oct.	7	32	0.7
Nov.	29	87	15
Dec.	50	134	20

includes the northern and western parts of the country [8]. The
inland segment is flatter and more arid, though it does not consist
of sandy desert but rather, rocky soil and scrub brush. No part of
Syria is much more than 300 miles from a large body of water, with
the Mediterranean on the west, the Black Sea across Turkey to the
north, and the Caspian Sea across Iran to the northeast.

3.3.3 CIVILIAN ACTIVITIES

3.3.3.1 Industrial Activity

No data were found on this subject.

3.3.3.2 Agricultural Activity

Estimates in [8] show approximately 35% of Syria's available
78,700 square miles are cultivated, only 10% of which are irrigated.
The area around Latakia in the northwest is heavily farmed, with
little farming in the inland section.

3.3.3.3 Population Density

The Syrian Arab Republic's population as of the 1970 census
was 6,304,685. Extrapolations in the 1977 U.N. Demographic Year-
book [7] give the 1977 population as 7,845,000, a 3.3% annual
rate of increase, for an effective population density of 42 people
per square km. This makes Syria ten times more densely populated
than Saudi Arabia, but only one-fourth as densely populated as
Israel. The cities with populations greater than 100,000 and
their populations are shown in Table 3.12. Around 45-50% of the
population is estimated to live in urban areas. The west coast
is dense with cities, with a rural and sedentary population along
the coast and a nomadic population inland.

TABLE 3.12

MAJOR CITIES OF SYRIA
AND THEIR POPULATIONS
AS OF MID-1977 [7]

City	1977 Population
Damascus	1,097,205
Aleppo	842,606
Homs	292,280
Latakia	191,329
Hama	173,459

3.4 TROPICAL REGION (HOT, WET): THE CLIMATE OF CENTRAL AND NORTHERN SOUTH AMERICA

The countries of Northern South America and Central America bordering the Caribbean Sea uniformly represent the tropical climate. By this is meant that:

1.   the mean annual temperature is relatively high ($\geq 25°C$);

2.   the diurnal range of temperature is greater than the annual range (defined as the difference between the mean temperatures for the warmest and coolest months); and

3.   the annual range of temperature is low ($< 5°C$).

In addition, high relative humidity conditions prevail and most areas get great amounts of rain. Our source for descriptive data on this region is the comprehensive World Survey of Climatology [9]. Already it can be noted that a limiting factor for some systems' performance will be water vapor absorption due to the high relative humidity.

A characteristic of this region is that the seasons are differentiated by rainfall amounts, and not by temperature changes. Most areas have two annual periods each of minimum and maximum rainfall. The seasonal variation of rainfall amount at a given location is often determined by the relative positions of the equatorial trough, also known as the Inter-Tropical Convergence Zone (ITCZ). The north-south passage of this region of low pressure explains the prevalence of two annual "wet" and "dry" seasons, since the trough passes over a particular area twice, once during its northern and once during its southern passage.

Data on rainfall amounts in Figure 3.2 show that most stations in Northern South America receive between 2000 and 2500 mm/year, while the mode in Central America is somewhat less, 1500 - 2000 mm/year. Outstanding exceptions include Cuba, which is relatively dry (Camaguey in the east-central portion reports an annual rainfall averaging less than 1400 mm/year), and Jaque
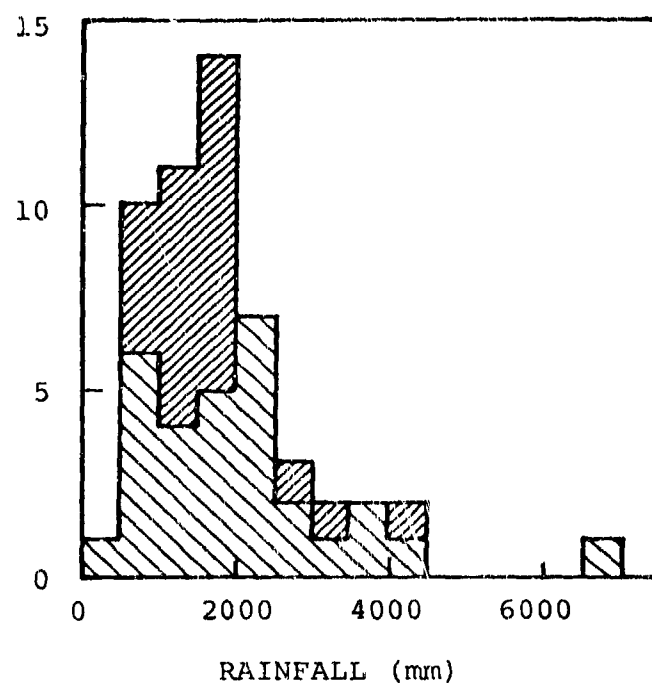
RAINFALL (mm)

Number of Stations Reporting a
Given Amount of Rain

South America

Central America
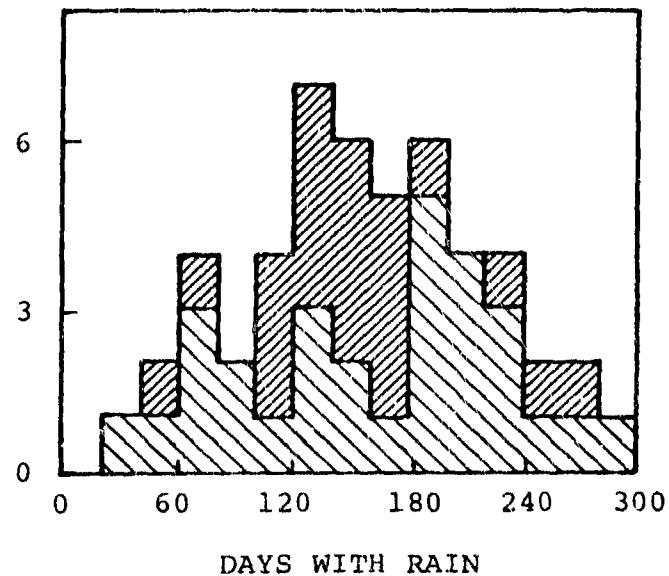
DAYS WITH RAIN

Number of Stations Reporting a
Given Number of Days with Rain

FIGURE 3.2. ANNUAL RAINFALL STATISTICS
FOR NORTHERN SOUTH AMERICA
AND CENTRAL AMERICA (reference [9])

in Panama where the mean annual rainfall exceeds 4300 mm/year. Nearly all stations in this region report measurable precipitation on more than one third of the days in a year. The distribution of days with rain shows strong seasonal variation in most places due to local geography and the relative position of the equatorial trough.

Fog is a rare occurrence, especially at low altitudes, the average number of days per year with fog at stations in Central America being around two. Cloud cover averages around 50% over Central America, and is somewhat higher, 60% or more, for most reporting stations in Northern South America. Haze is a frequent phenomenon in Central America in the dry season, resulting in decreased visibility. In general, the visibility increases in going from east to west.

The relative humidity as noted above averages quite high, in the 70% to 90% region, decreasing inland. Wind speed exhibits a strong negative correlation with moisture, resulting in frequent periods of absolute calm. Tropical storms, while accompanied with winds in excess of 30 meters/second, are a fairly rare occurrence for any particular location.

Topography influences the local climate considerably. In general, more precipitation can be expected on the windward side of mountains than on the leeward side. The land-sea interface causes temperature gradients which influence wind velocity and precipitation amount. Vegetation in Northern South America ranges from the low grass and bush of the steppes to tropical rain forest, i.e. jungle. Much of Central America is also covered with dense jungle.

Tables 3.13, 3.14, and 3.15 show meteorological data for three specific sites. More detailed information on climatological variables at these sites can be found in Tables XXXIII, XXXIV, and XLIX of reference 9. All three sites experience the dual annual rainfall maxima and minima. The annual temperature

3-26

TABLE 3.13

TEMPERATURE STATISTICS FOR CENTRAL AND SOUTH AMERICAN STATIONS
(period of record in parentheses - from reference 6)

	Balboa, Panama (1951-1960)	Cristobal, Panama (1951-1960)	Paramaribo, Surinam (1951-1960)
Jan.	26.7°C	26.3°C	26.5°C
Feb.	27.1	26.4	26.4
Mar.	27.8	26.8	26.8
Apr.	28.3	27.2	27.0
May	27.2	27.1	26.7
Jun.	26.8	27.0	26.7
Jul.	26.8	26.6	27.0
Aug.	26.8	26.6	27.7
Sep.	26.5	26.8	28.4
Oct.	26.1	26.6	28.3
Nov.	26.3	26.2	27.7
Dec.	26.6	26.5	26.9

TABLE 3.14

MEAN MONTHLY PRESSURE

	Balboa, Panama (1951-1960)	Cristobal, Panama (1951-1960)	Paramaribo, Surinam (1951-1960)*
Jan.	1007.0 mb	1007.9 mb	1011.2 mb
Feb.	1006.7	1007.6	1011.3
Mar.	1006.5	1007.6	1011.4
Apr.	1005.9	1006.8	1011.3
May	1005.7	1005.9	1011.5
Jun.	1006.0	1006.1	1012.3
Jul.	1006.2	1006.5	1012.4
Aug.	1005.9	1006.3	1011.8
Sep.	1005.8	1006.0	1011.2
Oct.	1006.3	1006.1	1010.5
Nov.	1006.0	1006.1	1009.9
Dec.	1006.1	1006.6	1010.4

*corrected to sea level

TABLE 3.15

PRECIPITATION DATA FOR CENTRAL AND SOUTH AMERICAN STATIONS
(period of record in parentheses - from reference 6)

	Balboa, Panama (1951-1960)	Cristobal, Panama (1951-1960)	Paramaribo, Surinam (1951-1960)
Jan.	47.8 mm	120.5 mm	152.0 mm
Feb.	24.7	45.4	172.9
Mar.	9.5	50.8	143.9
Apr.	62.6	113.0	224.2
May	238.8	330.5	336.5
Jun.	179.9	285.2	292.9
Jul.	199.2	405.5	194.9
Aug.	216.2	377.5	148.3
Sep.	199.8	291.4	93.3
Oct.	304.6	411.8	80.8
Nov.	268.5	571.4	116.4
Dec.	151.0	349.2	150.8

range in all cases is low, $\geq 2.2°C$. The data for Panama reveal
the variation in annual precipitation that can occur over a short
distance. The prevailing wind directions indicate offshore winds,
with a low mean wind speed, and generally moderate amounts of
clouds. Preliminary data from [10] indicate that the probability
of at least cirrus clouds at Howard AFB in the Canal Zone is 50%,
whereas it is stated in [9] that cirrus cloud coverage occurs in
Central America around 70% of the time.

3.5 COLD REGIONS (COLD, DRY): THE TANANA RIVER BASIN OF CENTRAL ALASKA (FAIRBANKS, ALASKA)

The cold, clear, calm polar air mass forms a background for
most discussions of Arctic and Subarctic climate. Strong seasonal
variations are brought about by the variable solar input which
results in the short days and long nights of the Arctic winter
and the long days and short nights of summer.

The Polar and Subpolar regions are under frequent temperature
inversions, which are usually based at the surface during cold
months and at higher elevations during the summer months [13].
This results in a marked stability of the air, with very little
turbulent exchange occurring. The low moisture content of the
air brought about by cold temperatures results in a long but
light snow season. Annual totals around 1.3 m. are common in the
central Tanana River Basin [11], as contrasted with, for example,
the 5 m. that can occur annually in the Upper Peninsula of Michi-
gan.

Figure 3.3 illustates two major points made in the above
discussion and simultaneously reveals two important factors for
E-O systems performance. The low water vapor content can
create a benevolent environment as far as molecular absorption
is concerned, and it also inhibits aerosol growth. However, the
strong temperature inversions and resulting stable air masses
cause weakened dispersion, and so the obstructions to visibility
which form naturally or due to battlefield activity may tend to
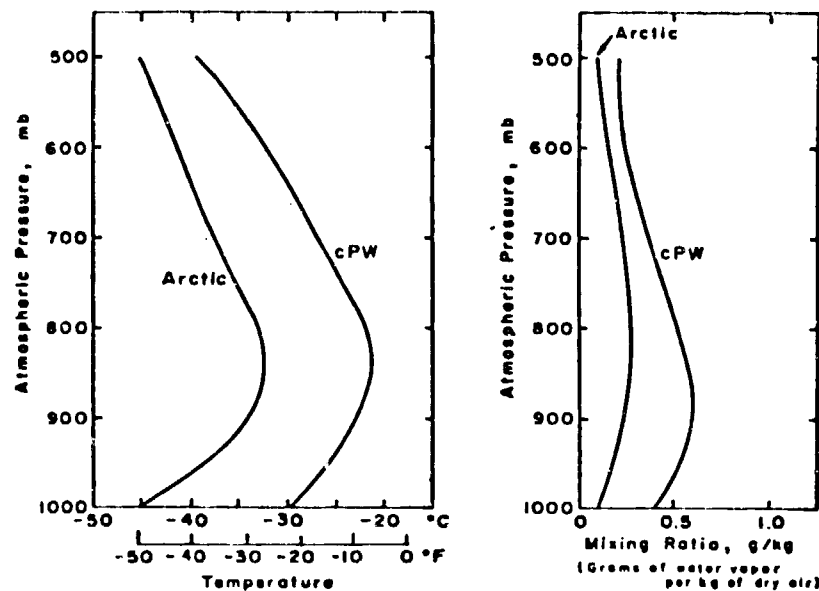
FIGURE 3.3   TYPICAL WINTER PROFILES OF TEMPERATURE AND WATER
VAPOR IN ARCTIC AND POLAR CONTINENTAL AIR MASSES
(AFTER PETTERSSEN 1969). [11]

be relatively stronger in the downwind direction.

Natural obstructions to visibility are fairly common,
expecially in winter. Blowing snow, defined as snow entrained
in the air by the wind to a height of six feet or more, occurs
more frequently with loose snow than packed snow: higher winds
are required to produce drifts in cases of hard snow. Water
droplet or ice fogs form and persist in populated areas where
products of combustion provide condensation nuclei. In addition,
the water vapor content of the air is enhanced by exhaust from
automobiles, power plants, and household chimneys, aiding fog
formation [11].

The ranges of visibility expected with various forms of
fog and precipitation are shown in Table 3.16.

3-30

TABLE 3.16

AVERAGE VISIBILITY DURING WATER DROPLET FOGS, ICE FOGS, SNOW-
STORMS, BLOWING-SNOW STORMS AND ICE CRYSTAL OCCURRENCES, BIG
DELTA AIRPORT, ALASKA, OCTOBER THROUGH APRIL, 1957-1968. [11]

Miles	<1	1 to 3	4 to 5	6 to 10	>10
During water droplet fogs					
% of time	29	51	19	1	0
During ice fogs					
% of time	30	27	26	12	5
During snowfall					
% of time	9	26	16	28	21
During blowing-snow storms					
% of time	12	31	25	18	14
During ice crystal occurrences					
% of time	3	15	14	28	40

The climate of the Tanana River Basin in Central Alaska is
continental and characterized by wide temperature variations,
especially in winter. This region is surrounded on all sides
by mountains which shelter it from maritime influences, and the
base of the valley acts as a cold air sink so that the temperature
inversions common in the Subarctic are emphasized (Figure 3.4).
Figure 3.5 shows a 32-year average of temperature for Fairbanks,
in the northeast corner of the Tanana Valley. These records
bear out the wide winter temperature fluctuations referred to
above. The average temperature in the summer months is somewhat
above zero, while in the winter months it is perhaps 15° below
zero (°C). This area gets 18 to 21 hours of sun in June and
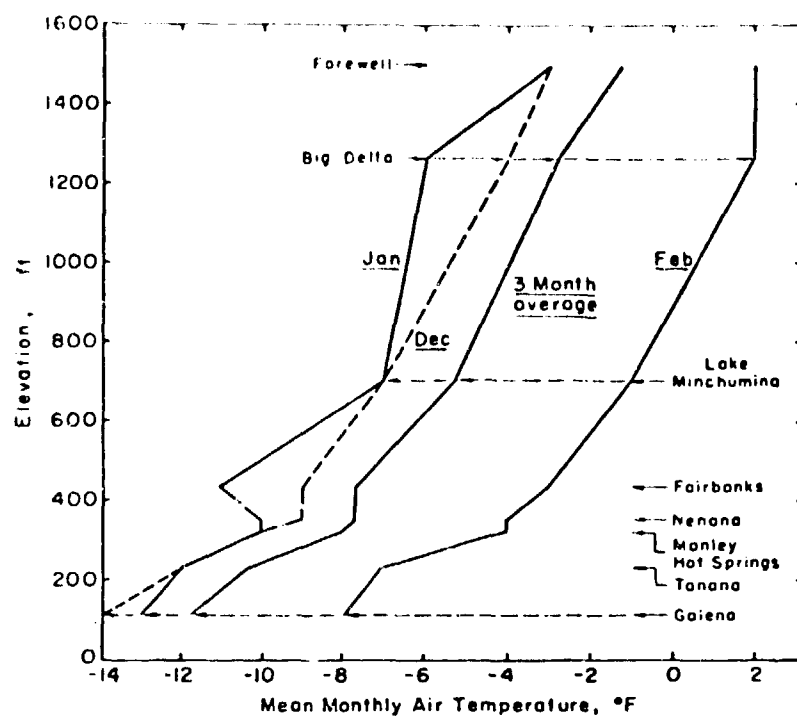
FIGURE 3.4   AIR TEMPERATURE AND ELEVATION RELATIONSHIPS FOR
INTERIOR BASIN WEATHER STATIONS. [11]
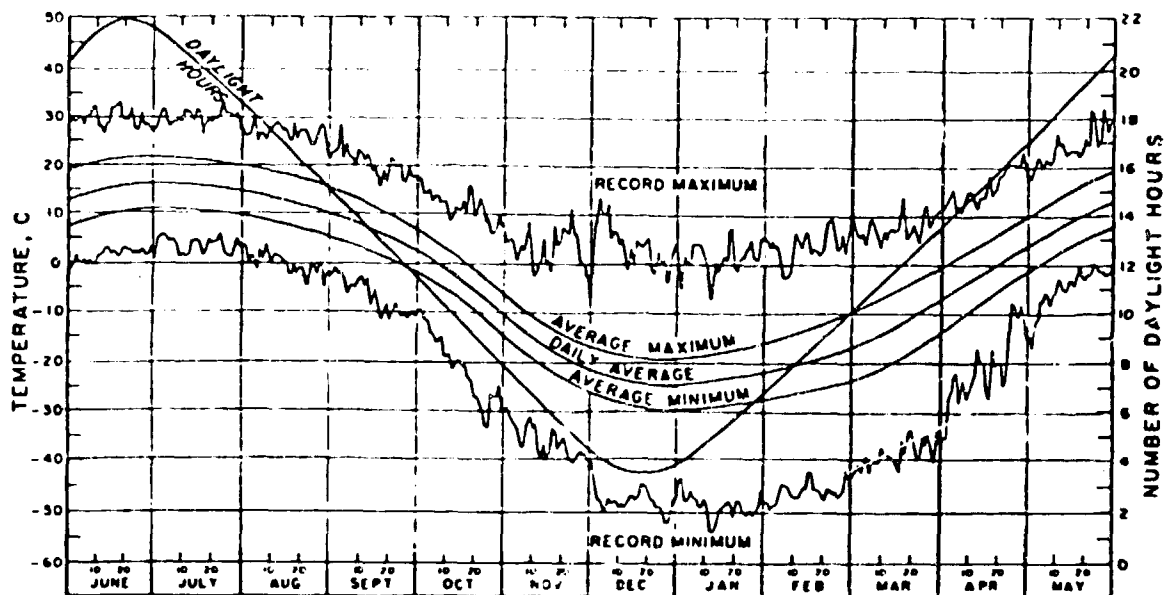
FIGURE 3.5   TEMPERATURES AND DAYLIGHT HOURS AT FAIRBANKS, ALASKA. [12]

July, and 4 to 6 hours of sun in midwinter, when temperatures can drop to -60°F.

Precipitation, as shown in Table 3.17, is mostly light. The primary source of precipitation is warmer maritime air from the south and southwest. It can be seen from Table 3.18 that the strongest winds also come from the south or southwest, with mean local winds being very light.

The remaining data in this section concern frequency and persistence of conditions yielding obstruction to visibility. Reference [11] discusses in detail the meteorological correlates of these conditions, including wind speed and temperature. Ice fog was found to occur rarely at temperatures >-20°F, but was nearly always present at -50°F if any water vapor was available from the air. The temperature ranges yielding the highest frequency of the different fog types are:

1.   10° to 19°F   - highest occurrence of water droplet fogs

2.   -20° to -11°F - airborne ice crystals

3.   -40° to -31°F - highest frequency of ice fogs

Ice fogs are associated with calm or southerly winds, while water fogs occur with winds >5 knots from the west. In general, temperature exhibits a negative correlation with visibility. Most of these fogs are caused by radiative cooling and occur in populated areas. Radiation fog formation is favored by:

1.   cloud cover during the day, so that moisture is held near the ground;

2.   clear skies at night allowing rapid terrestrial cooling;

3.   an excessively cool surface layer; and

4.   calm or light surface winds.

Conditions favorable to the formation of water droplet fogs occur mostly in late fall or early winter when sources of water

3-33

aren't yet frozen. Figure 3.6 summarizes the frequency of occurrence of some obstruction to vision, showing that some obstruction occurs, on the average, around 200 hours per month in the wintertime, or about 25 to 30% of the time.

TABLE 3.17

CLIMATIC COMPARISON OF INTERIOR BASIN STATIONS, 1951-1960. [11]

Station	Elevation (ft)	J	F	M	A	M	J	J	A	S	O	N	D	Ann
a. Mean temperature (°F)														
Big Delta Airport	1268	- 6	2	10	31	47	58	60	56	43	24	10	- 4	27
Galena	120	-13	-8	6	25	45	58	59	55	43	24	6	-14	24
Tanana FAA	232	-12	-7	4	25	45	57	58	54	41	22	2	-12	23
Fairbanks Airport	436	-11	-3	9	28	48	58	60	55	44	26	3	- 9	26
Farewell FAA	1499	- 3	2	9	26	42	52	55	51	40	23	10	- 3	25
Lake Minchumina FAA	701	- 7	-2	9	28	46	58	59	55	43	24	6	- 7	26
Manley Hot Springs	325	-10	-4	7	27	45	57	59	53	42	25	2	-10	24
Nenana FAA	356	-10	-4	5	27	46	57	58	54	42	23	5	- 9	25
b. Total precipitation (in.)														
Big Delta Airport		0.37	0.41	0.25	0.12	1.01	2.22	2.20	1.93	1.32	0.62	0.36	0.58	11.23
Galena		0.61	0.86	0.57	0.28	0.63	0.97	2.11	2.61	1.71	0.64	0.87	0.50	12.36
Tanana FAA		0.53	0.64	0.50	0.14	0.75	1.21	1.98	2.80	1.75	0.73	0.58	0.63	12.31
Fairbanks Airport		0.63	0.51	0.28	0.12	0.58	1.38	1.81	1.56	1.39	0.62	0.41	0.58	9.87
Farewell FAA		0.55	0.73	0.46	0.39	0.97	2.16	3.24	3.75	2.01	0.87	0.65	0.50	16.24
Lake Minchumina FAA		0.65	0.63	0.36	0.25	0.75	1.49	2.15	2.80	1.37	0.54	0.58	0.45	12.02
Manley Hot Springs		0.79	0.73	0.58	0.16	0.52	1.41	2.48	3.45	1.84	0.65	0.61	0.75	14.00
Nenana FAA		0.70	0.67	0.26	0.15	0.62	1.45	1.87	1.94	1.57	0.56	0.49	0.46	10.74
c. Total snowfall (in.)														
Big Delta Airport		5.4	5.3	3.9	1.3	1.4	T	0	0	2.0	7.2	4.6	6.2	37.3
Galena		6.3	9.0	6.5	2.3	0.7	T	0	0	0.6	6.6	9.0	5.7	46.7
Tanana FAA		7.7	7.8	10.0	1.2	0.1	T	0	1	1.1	7.2	7.4	9.7	52.2
Fairbanks Airport		12.0	9.5	5.0	1.7	0.4	T	T	T	0.8	7.5	8.7	9.3	54.9
Farewell FAA		7.0	10.8	6.9	5.8	1.4	T	T	T	1.9	9.8	9.4	8.0	61.0
Lake Minchumina FAA		8.9	9.4	5.5	2.6	0.3	T	0	0	1.3	4.9	8.7	7.2	48.8
Manley Hot Springs		9.9	8.9	7.5	1.7	0.4	T	0	T	0.8	6.1	9.2	9.5	54.0
Nenana FAA		8.5	8.5	3.5	1.4	0.2	T	0	T	0.9	5.9	7.0	6.4	42.3

FAA - Federal Aviation Administration.

T - Trace

TABLE 3.18

WIND DIRECTION AND SPEED IN WINTER AT FAIRBANKS. [12]

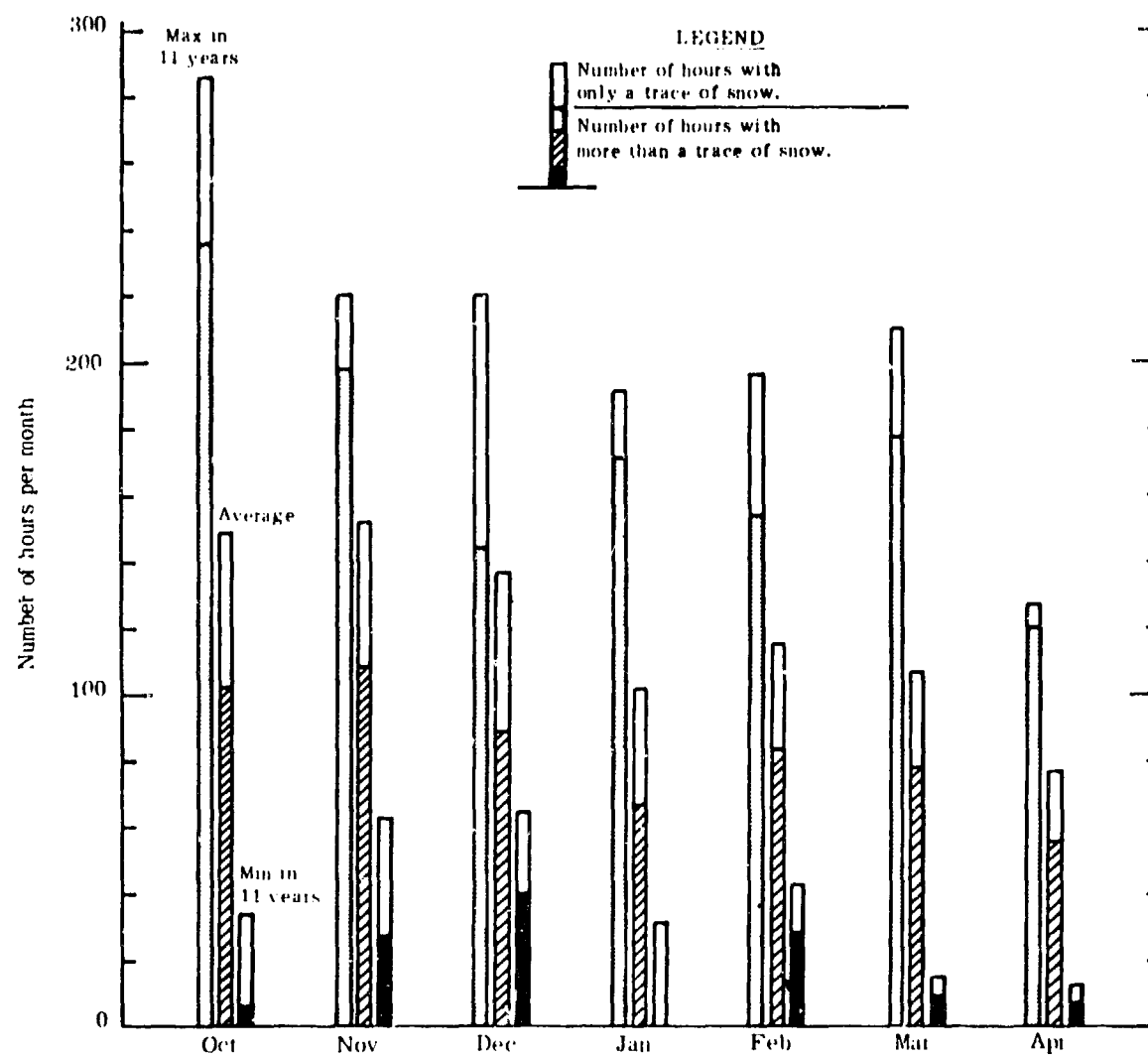| Month	Prevailing direction	Hourly average wind		Maximum wind		
		Hourly average speed		Direction	Speed	
		m/sec	mph		m/sec	mph
October	NE	2.3	5.2	S	12.0	26.2
November	N	1.7	3.8	S	12.9	28.8
December	N	1.4	3.1	SW	12.0	26.2
January	N	1.4	3.1	SW	15.0	33.6
February	N	1.7	3.8	SW	13.5	30.2
March	N	2.1	4.7	S	17.0	38.0

FIGURE 3.6 (a)   FREQUENCY OF OCCURRENCE OF OBSTRUCTIONS TO VISION AT
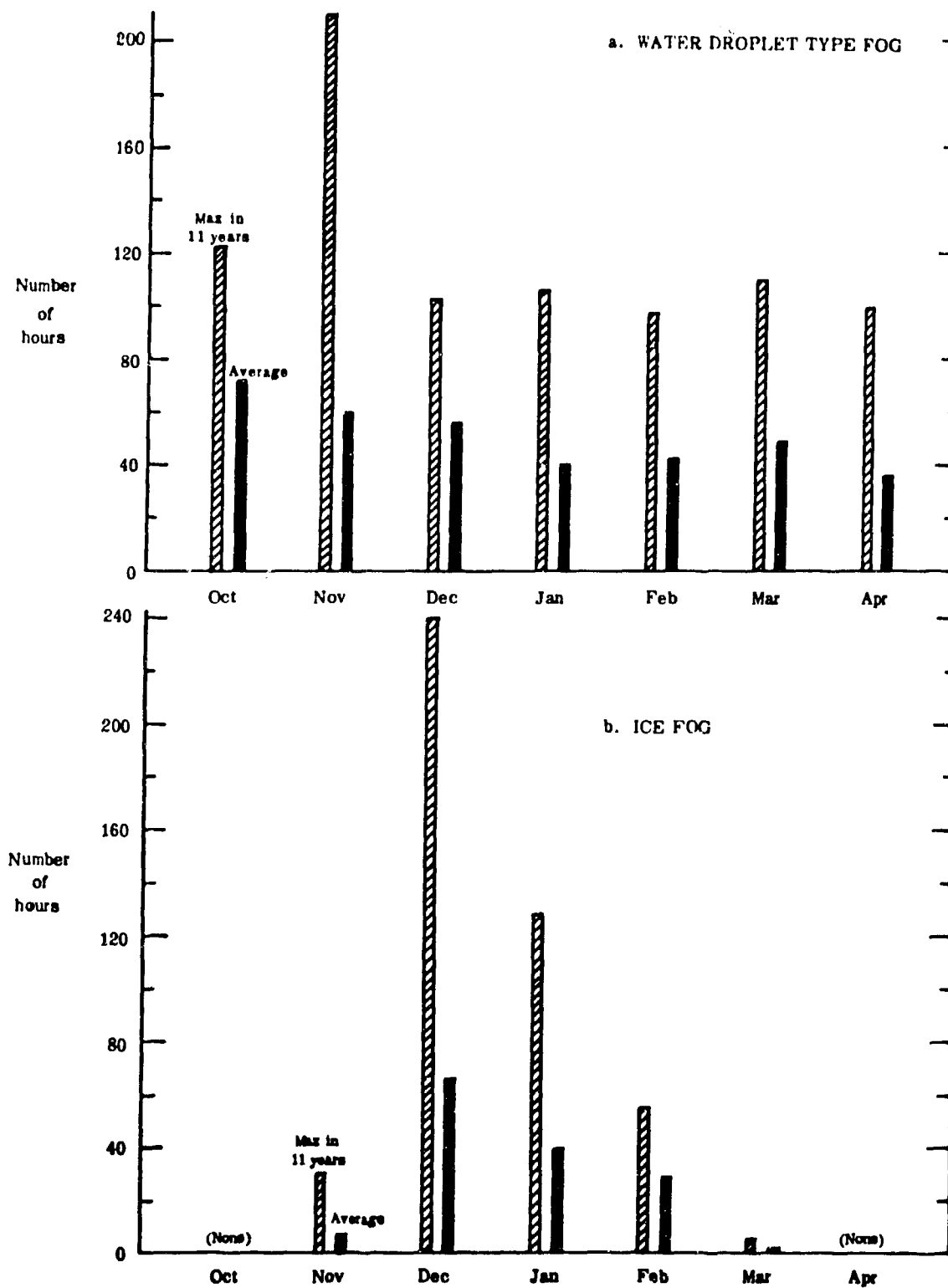
BIG DELTA AIRPORT [11]

3-36

Figure 10. Frequency of water droplet fogs and ice fogs, Big Delta Airport, Alaska, October through April, 1957-1968.

FIGURE 3.6 (b)   FREQUENCY OF OCCURRENCE OF OBSTRUCTIONS TO VISION

AT BIG DELTA AIRPORT, 1957-1968 [11]

3-37

REFERENCES FOR SECTION 3

1. L.M. Biberman and G.A. duMais, "Modeling the Effects of
    Weather on 8.5-11 μm FLIR Performance: an Analysis using Real
    Weather Data", Proceedings IRIS Volume 20 Number 2, February
    1977.

2. E. Rodriguez and R.E. Huschke, The Rand Weather Data Bank
    (RAWDAB): An Evolving Base of Accessible Weather Data, Rand
    Corporation Report R-1269-PR, March, 1974.

3. R.W. Fenn, A Measurements Program on Optical Atmospheric
    Quantities in Europe, Volume I - The NATO OPAQUE Program,
    Air Force Geophysics Laboratory Report AFGL-TR-78-0011,
    17 January 1978.

4. M.D. Kays, M.A. Seagraves, H.H. Monahan, R.A. Sutherland,
    A Qualitative Description of Obscuration Factors in Central
    Europe, Atmospheric Sciences Laboratory Draft Report,
    January 1980.

5. L. Duncan, R. Shirkey, R.A. Sutherland, E. Avara, and
    H.H. Monahan, The Electro-Optical Systems Atmospheric Effects
    Library, Vol. I: Technical Documentation, ASL-TR-0047,
    December 1979.

6. World Weather Record, published by Smithsonian Institution,
    1960.

7. U.N. Demographic Yearbook, published by the United Nations,
    1977.

8. Issues in the Middle East, Central Intelligence Agency
    Atlas, 1973.

9. H.E. Landsberg, Editor-in-Chief: World Survey of Climatolog
    Volume 12: Climates of Central and South America, Elsevier
    Publishing Co., New York, 1970.

10. F.F. Hall "A Cirrus Transmittance Subroutine for LOWTRAN V",
    Viewgraph presentation at AFGL Atmospheric Transmittance
    Review Meeting, May, 1980.

11. M.A. Bilello, Air Masses, Fronts, and Winter Precipitation
    in Central Alaska, Cold Regions Research and Engineering
    Laboratory Research Report 319, June, 1974.

12. M. Kumai and H. O'Brien, A Study of Ice Fog and Ice Fog
    Nuclei at Fairbanks, Alaska: Part II, Cold Regions Research
    and Engineering Laboratory Research Report 150, April, 1965.

13. M.A. Bilello, Survey of Arctic & Subarctic Temperature
    Inversions, Cold Regions Research and Engineering Laboratory
    Technical Report 161, October, 1966.

14. U.S. Department of Commerce, Monthly Climatic Data for the World, published by the National Oceanic and Atmospheric Administration Environmental Data Service, 1974.

15. M.A. Bilello and G. Cameron Appel, Analysis of the Midwinter Temperature Regime and Snow Occurrence in Germany, Cold Regions Research and Engineering Laboratory Report 78-21, September 1978.

SECTION 4
INTENTIONALLY INDUCED BATTLEFIELD ENVIRONMENTAL CONDITIONS

4.1 SMOKES

In this section are cataloged the basic physical and optical properties of smoke which can be intentionally induced in a battlefield environment.

4.1.1 PHOSPHOROUS SMOKE

In this section we shall describe the physical and optical properties of phosphorous smoke.

4.1.1.1 Bulk WP

In this subsection we present material on the properties of bulk white phosphorous smoke.

4.1.1.1.1 Munition Characteristics

Bulk White Phosphorous smoke usually originates in munitions such as hand grenades, 60 mm Mortars, 75 mm Rifles, 5 inch gun fire, 100-lb. smoke bombs, and in many other forms [1]. The munitions are generally characterized by their fill weights and a "weapon phase" time (t_w) as defined by Dolce and Metz [2]. This is the time interval from initial detonation of the high explosive to the time when the cloud becomes white. Typical white phosphorous munitions, the high explosive weights, the fill weights, and the weapon phase times are indicated in Table 4.1.

TABLE 4.1

WHITE PHOSPHOROUS MUNITION CHARACTERISTICS

Munition	HE (lb)	WP (lb)	t_w (sec)
60 mm	0.025	0.75	0.44
81 mm	0.08	4.0 (1.75)	0.56
4.2 in	0.73	0.75	0.87
105 mm	0.51	3.83	~0.6
155 mm	0.83	15.6	1.1

4.1.1.1.2 Yield Factor

The yield factor is defined as follows:

$$\text{Yield Factor} = \frac{\text{Final Mass}}{\text{Initial Mass available for smoke generation}}$$

According to a summary of yield factors in a report by Zirkind [3], the formula for white phosphorous is:

$$Y(WP) = 3.8 + 0.003(RH\% - 10)^{1.67} \qquad (4.1)$$

where RH% is the per cent relative humidity.

4.1.1.1.3 Environmental Effects

Water vapor can condense onto smoke nuclei and the particles
can then grow to a size which depends upon the ambient environ-
mental conditions of pressure, temperature, and relative humidity.
Presented here are a number of figures of the mass extinction
coefficients as a function of relative humidity and wavelength for
phosphoric acid. It should be noted that this study by Frickel
et al. [4] is representative only of phosphoric acid which differs
from phosphorous smoke in the infrared part of the spectrum.
Figures 4.1-4.6 provide values of the mass extinction coefficient
for phosphoric acid as a function of wavelength for various
relative humidities.

FIGURE 4.1 EXTINCTION COEFFICIENT FOR VARIOUS CONCENTRATIONS
(RELATIVE HUMIDITY LEVELS) FOR PHOSPHORIC ACID IN
THE VISIBLE. UNITS ARE m^2 PER GRAM OF AEROSOL.
FRICKEL ET AL. [4].

4-4

FIGURE 4.2   EXTINCTION COEFFICIENT FOR VARIOUS CONCENTRATIONS
             (RELATIVE HUMIDITY LEVELS, RH) FOR PHOSPHORIC ACID
             IN THE MID-IR.   UNITS ARE m^2 PER GRAM OF AEROSOL.
             FRICKEL ET AL. [4].
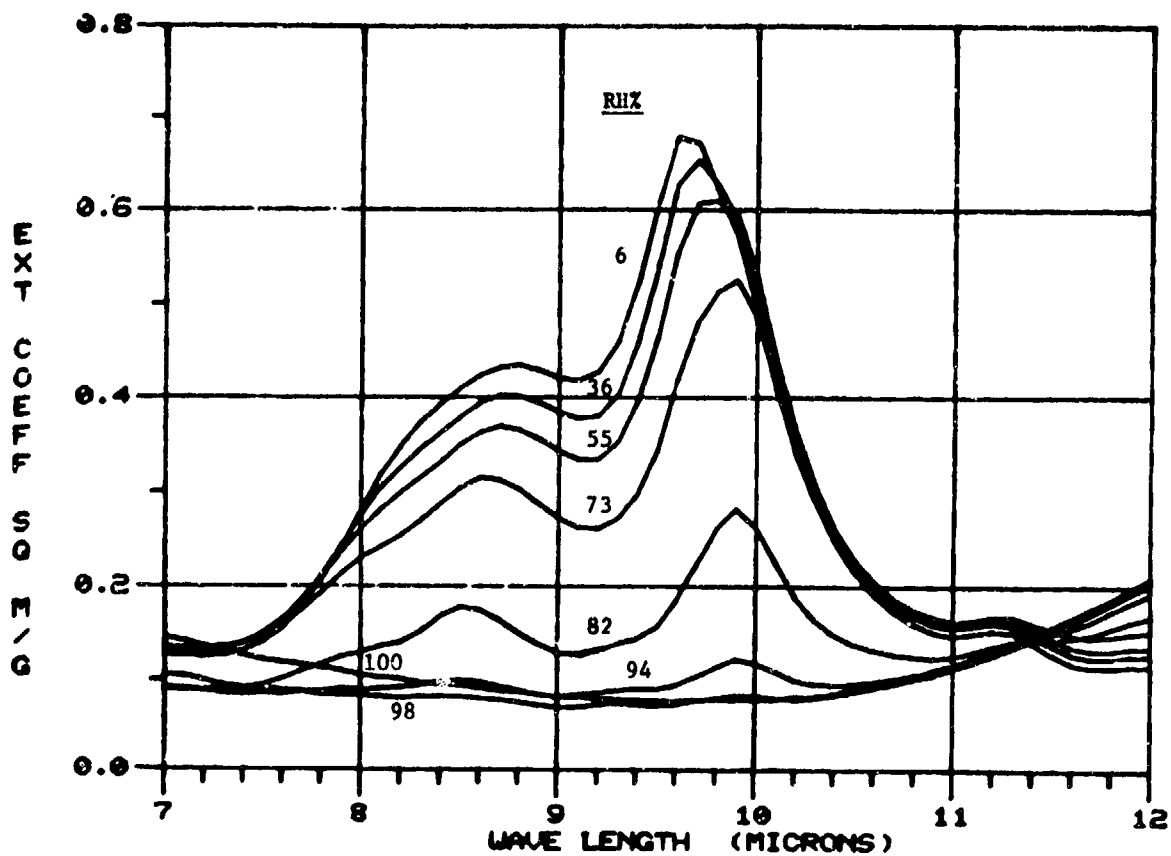
FIGURE 4.3 EXTINCTION COEFFICIENT FOR VARIOUS
CONCENTRATIONS (RELATIVE HUMIDITY
LEVELS) FOR PHOSPHORIC ACID IN THE
FAR-IR. UNITS ARE m^2 PER GRAM OF
AEROSOL. FRICKEL ET AL. [4].
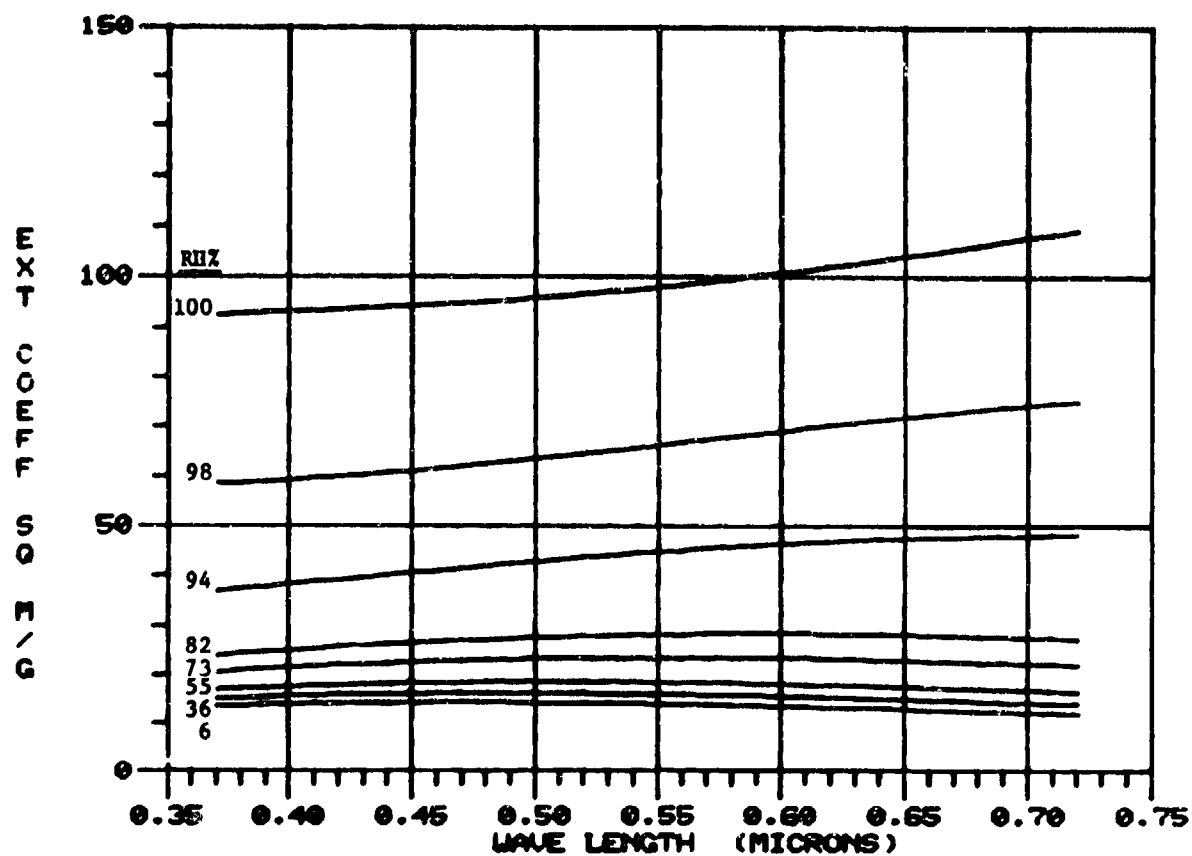
FIGURE 4.4 EXTINCTION COEFFICIENT FOR VARIOUS
CONCENTRATIONS (RELATIVE HUMIDITY
LEVELS) FOR PHOSPHORIC ACID IN THE
VISIBLE. UNITS ARE m^2 PER GRAM OF
PHOSPHORUS CONTAINED IN THE AEROSOL.
FRICKEL ET AL. [4].

4-7
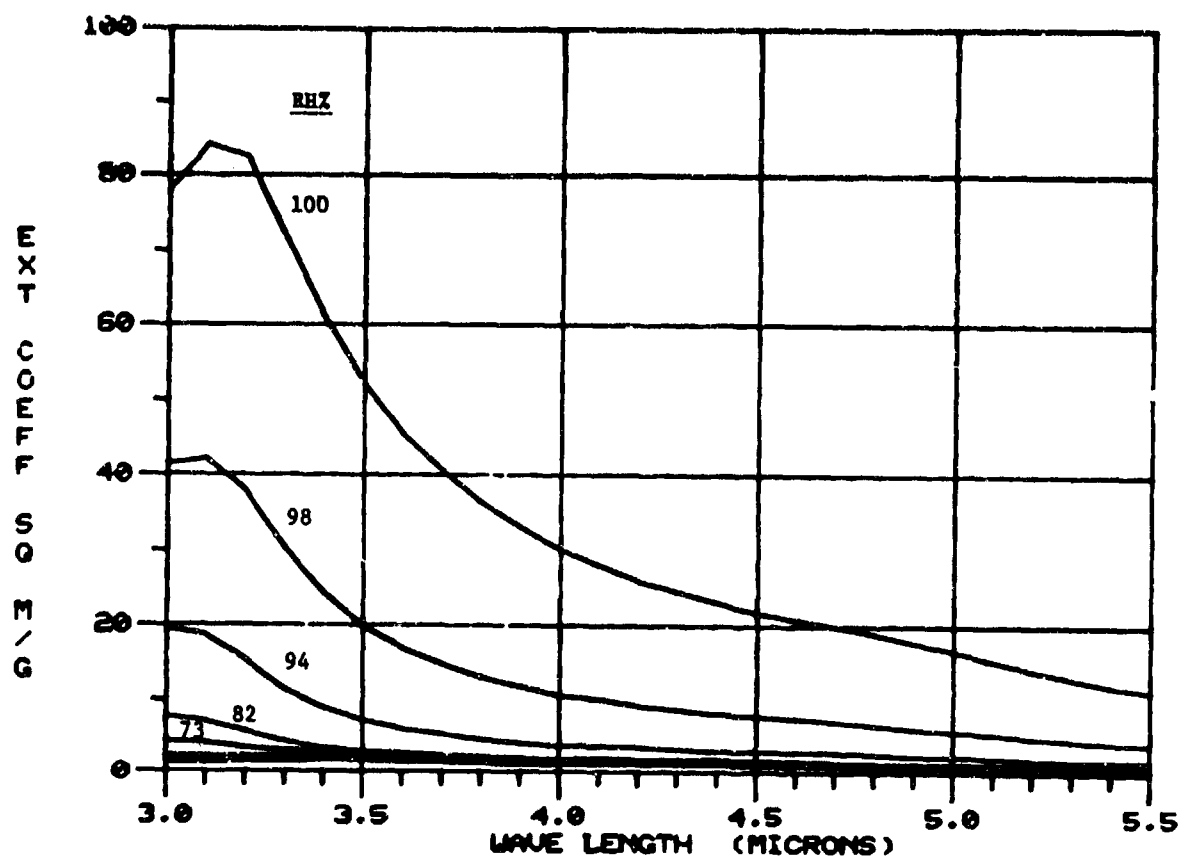
FIGURE 4.5 EXTINCTION COEFFICIENTS FOR VARIOUS
CONCENTRATIONS (RELATIVE HUMIDITY
LEVELS) FOR PHOSPHORIC ACID IN THE
MID-IR. UNITS ARE m^2 PER GRAM OF
PHOSPHORUS CONTAINED IN THE AEROSOL.
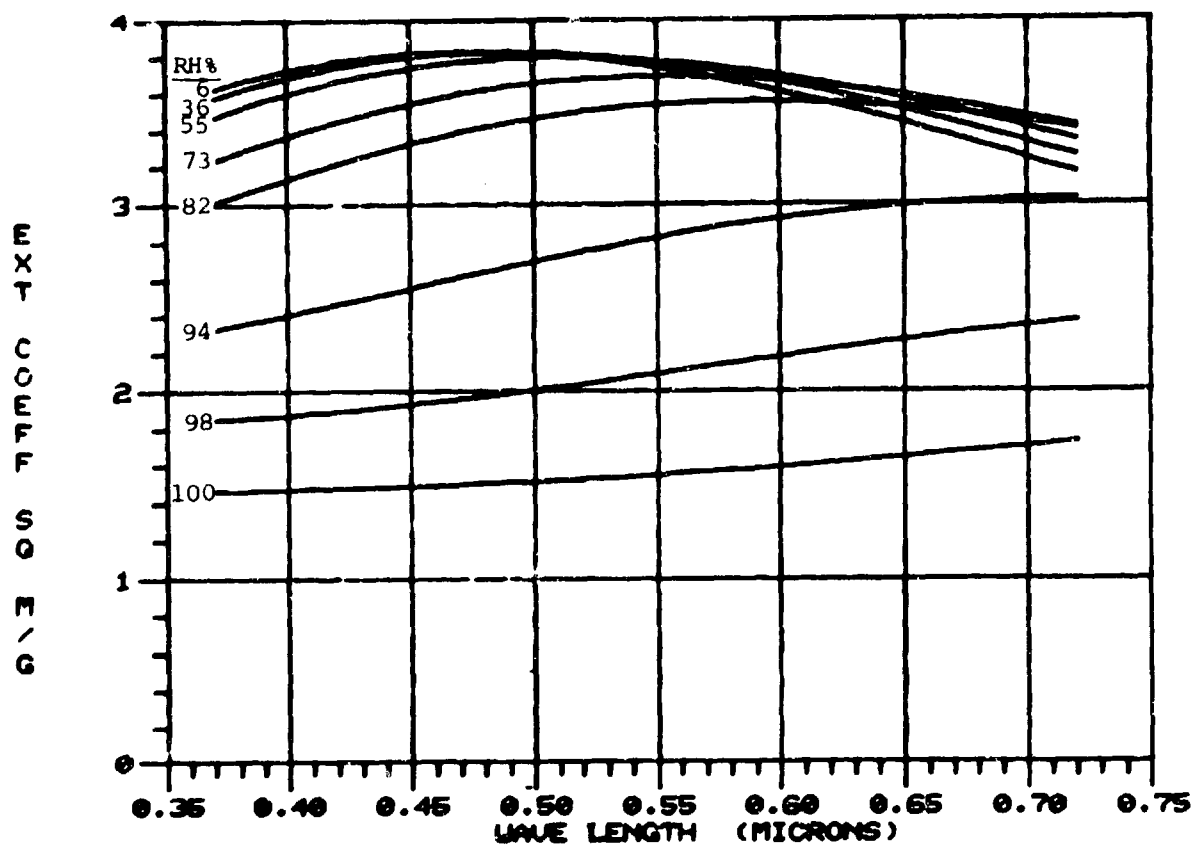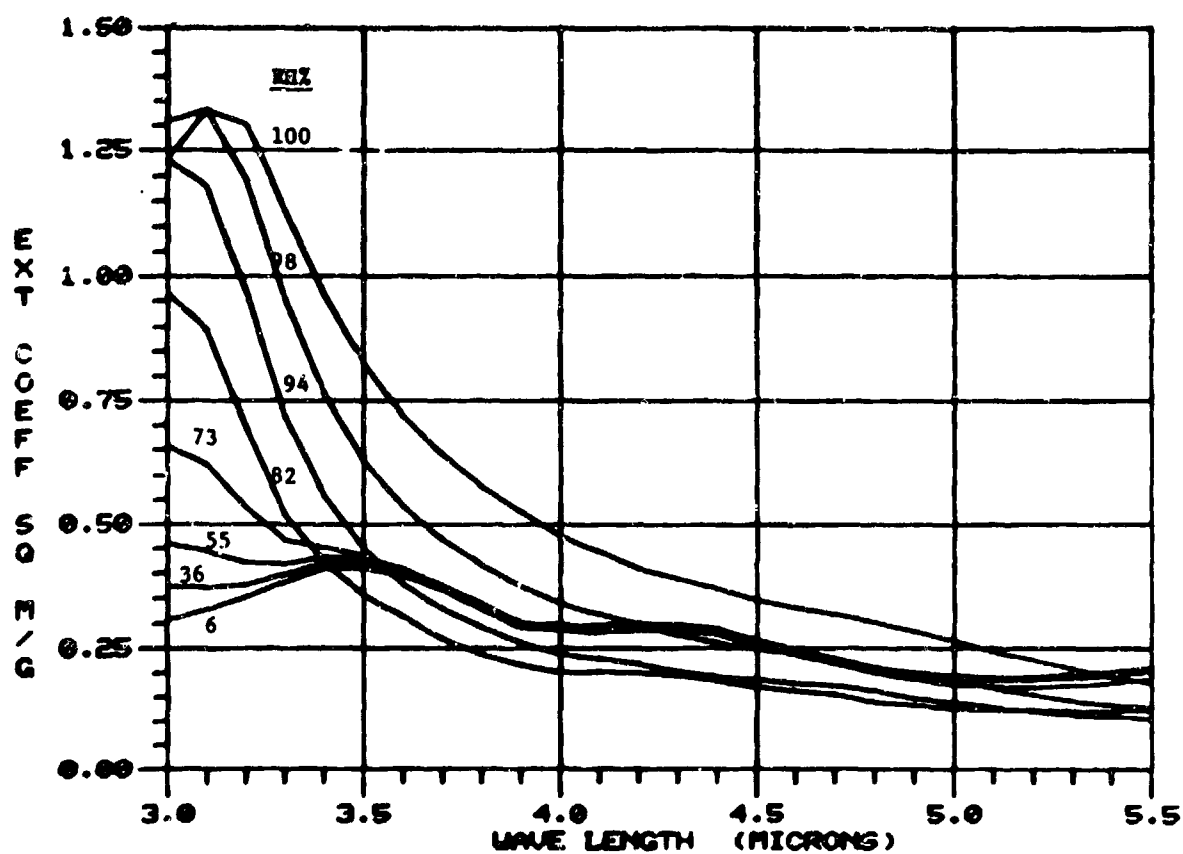FRICKEL ET AL. [4].

4-8
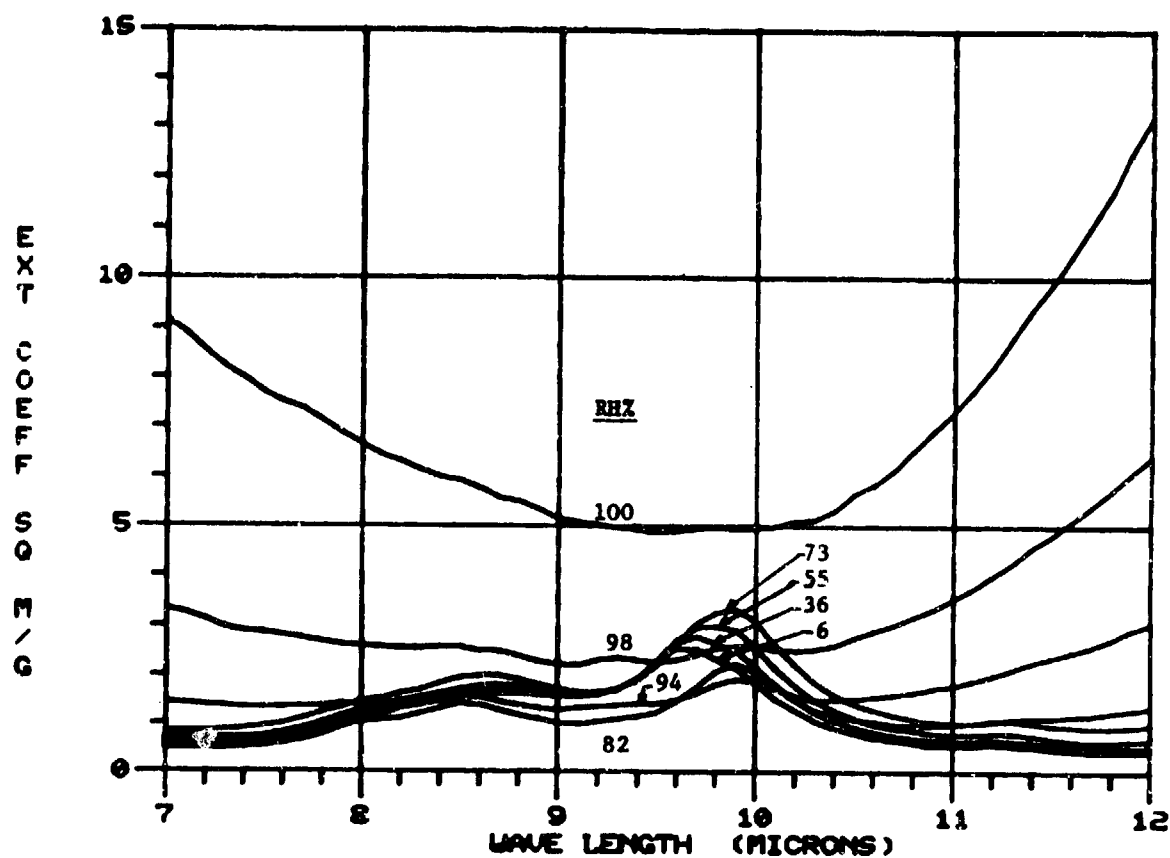
FIGURE 4.6 EXTINCTION COEFFICIENT FOR VARIOUS
            CONCENTRATIONS (RELATIVE HUMIDITY LEVELS)
            FOR PHOSPHORIC ACID IN THE FAR-IR.
            UNITS ARE m^2 PER GRAM OF PHOSPHORUS
            CONTAINED IN THE AEROSOL.   FRICKEL ET AL. [4].

The median mass diameter characterizes the particle size distribution. This is illustrated by considering the density distribution of particles, i.e. the density of particles per unit diameter,

$$\rho(D) = \frac{\rho}{D\sqrt{2\pi}\,\ln\,\sigma}\,\exp\left[-\frac{(\ln\,D - \ln\,D_m)^2}{2\,\ln^2\,\sigma}\right] \qquad (4.2)$$

in which ρ is the total particle density, σ is the standard deviation, D is the particle diameter, and D_m is the median particle diameter for this log-normal distribution. The corresponding number size distribution, i.e. the number of particles per unit volume per unit size range ΔD is given by

$$n(D) = \frac{6\rho}{\sqrt{2\pi^3}\,\rho_p\,D^4\,\ln\,\sigma}\,\exp\left[-\frac{(\ln\,D - \ln\,D_m)^2}{2\,\ln^2\,\sigma}\right] \qquad (4.3)$$

where ρ_p is the density of a particle.

Figures 4.7 through 4.14 depict the change in the mass extintion coefficient of phosphoric acid and phosphorous as a function of the relative humidity and the median mass diameter.
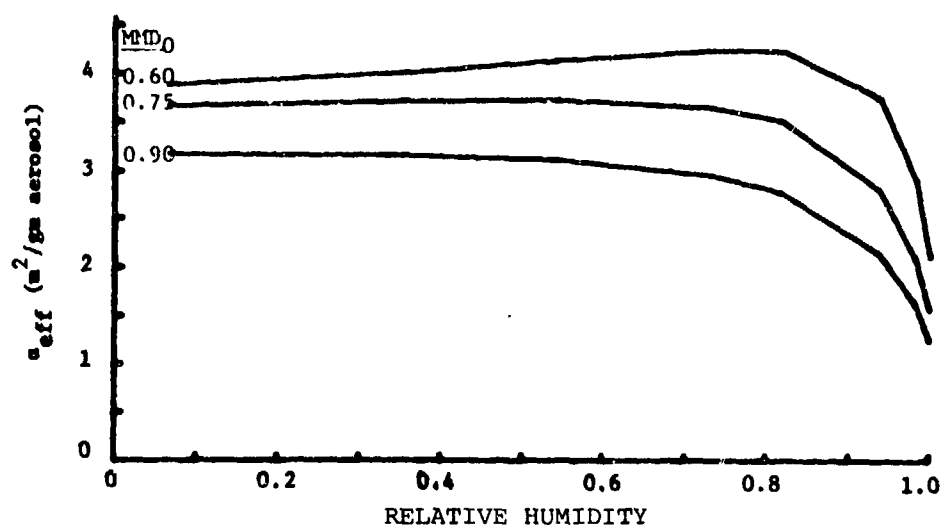
FIGURE 4.7   RELATIVE HUMIDITY DEPENDENCE OF THE
INTEGRATED EXTINCTION COEFFICIENT FOR
PHOSPHORIC ACID AEROSOL IN THE
VISIBLE.   THE REGION BETWEEN THE
PLOTTED LINES REPRESENTS THE EXPECTED
RANGE OF VARIATION OF PHOSPHORUS
SMOKES.   THESE CURVES CORRESPOND TO
AEROSOLS PRODUCED FROM LOG-NORMAL
PRIMITIVE ACID NUCLEI DISTRIBUTIONS
HAVING σ_g = 1.45 and MMD'S AS SHOWN.
α_{eff} IS CALCULATED AT $C\ell$= 5.0 g/m^2.
FRICKEL ET AL. [4].

FIGURE 4.8 RELATIVE HUMIDITY DEPENDENCE OF THE INTE-
GRATED EXTINCTION COEFFICIENT FOR PHOSPHORIC
ACID AEROSOL IN THE MID-INFRARED.   THE
REGION BETWEEN THE PLOTTED LINES REPRESENTS
THE EXPECTED RANGE OF VARIATION OF PHOSPHOROUS
SMOKES.   THESE CURVES CORRESPOND TO AEROSOLS
PRODUCED FROM LOG-NORMAL PRIMITIVE NUCLEI
DISTRIBUTIONS HAVING σ_g = 1.45 AND MMD'S AS
SHOWN. α_{eff} IS CALCULATED AT $C\ell$= 5.0 g/m^2.
FRICKEL ET AL. [4].

FIGURE 4.9 RELATIVE HUMIDITY DEPENDENCE OF THE
INTEGRATED EXTINCTION COEFFICIENT OF
PHOSPHORIC ACID AEROSOL IN THE FAR
INFRARED. THE REGION BETWEEN THE
PLOTTED LINES REPRESENTS THE EXPECTED
RANGE OF VARIATION DUE TO PARTICLE SIZE
VARIATIONS TYPICAL OF PHOSPHOROUS SMOKES.
(SEE TEXT). THESE CURVES CORRESPOND TO
AEROSOLS PRODUCED FROM LOG-NORMAL
PRIMITIVE ACID NUCLEI DISTRIBUTIONS
HAVING $\sigma_g = 1.45$ AND MMD'S AS SHOWN.
α_{eff} IS CALCULATED AT $C\ell = 5.0$ g/m^2.
FRICKEL ET AL. [4].

4-13
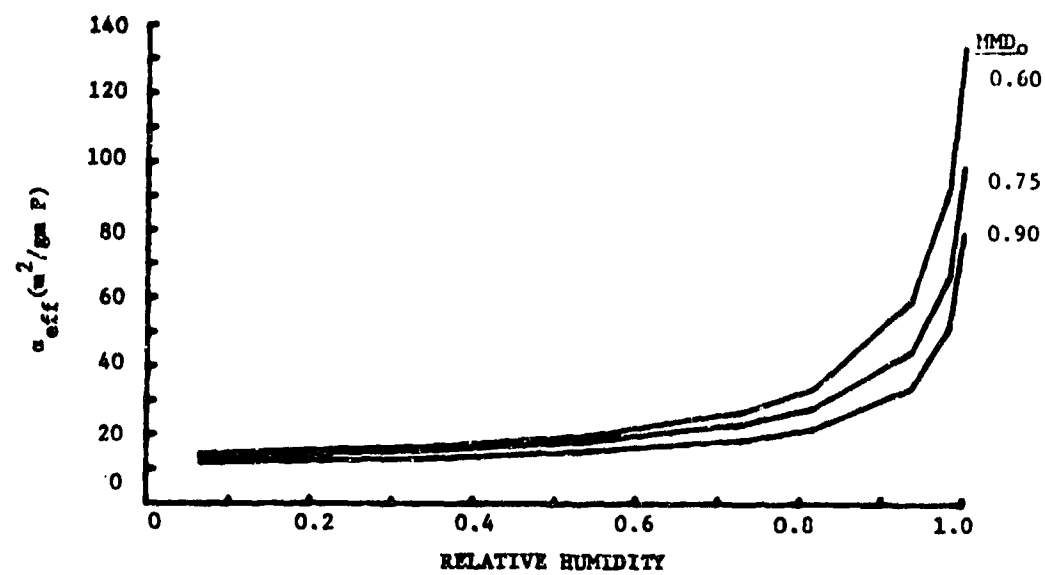
FIGURE 4.10 VISIBLE EXTINCTION REFERRED TO MASS OF
PHOSPHORUS IN THE AEROSOL. FRICKEL ET AL.
[4].
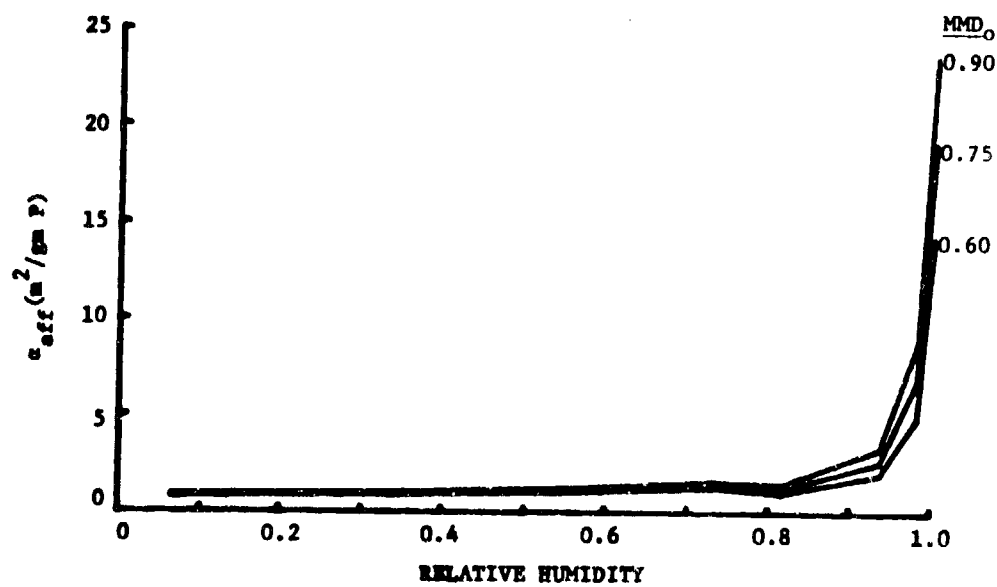
FIGURE 4.11   MID-INFRARED EXTINCTION REFERRED TO
MASS OF PHOSPHORUS IN THE AEROSOL.
FRICKEL ET AL. [4].

25

20

15

10

5

0

$\alpha_{eff}(m^2/gm\ P)$

MMD$_o$

0.9

0.6

0   0.2   0.4   0.6   0.8   1.0
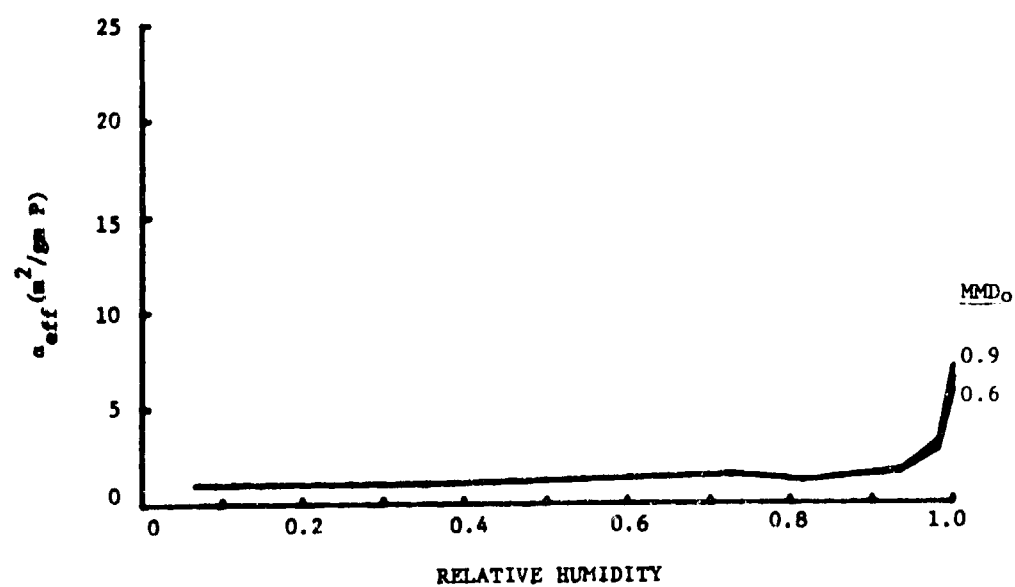
RELATIVE HUMIDITY

FIGURE 4.12 FAR-INFRARED EXTINCTION REFERRED
TO MASS OF PHOSPHORUS IN THE
AEROSOL.   FRICKEL ET AL. [4].

4-16
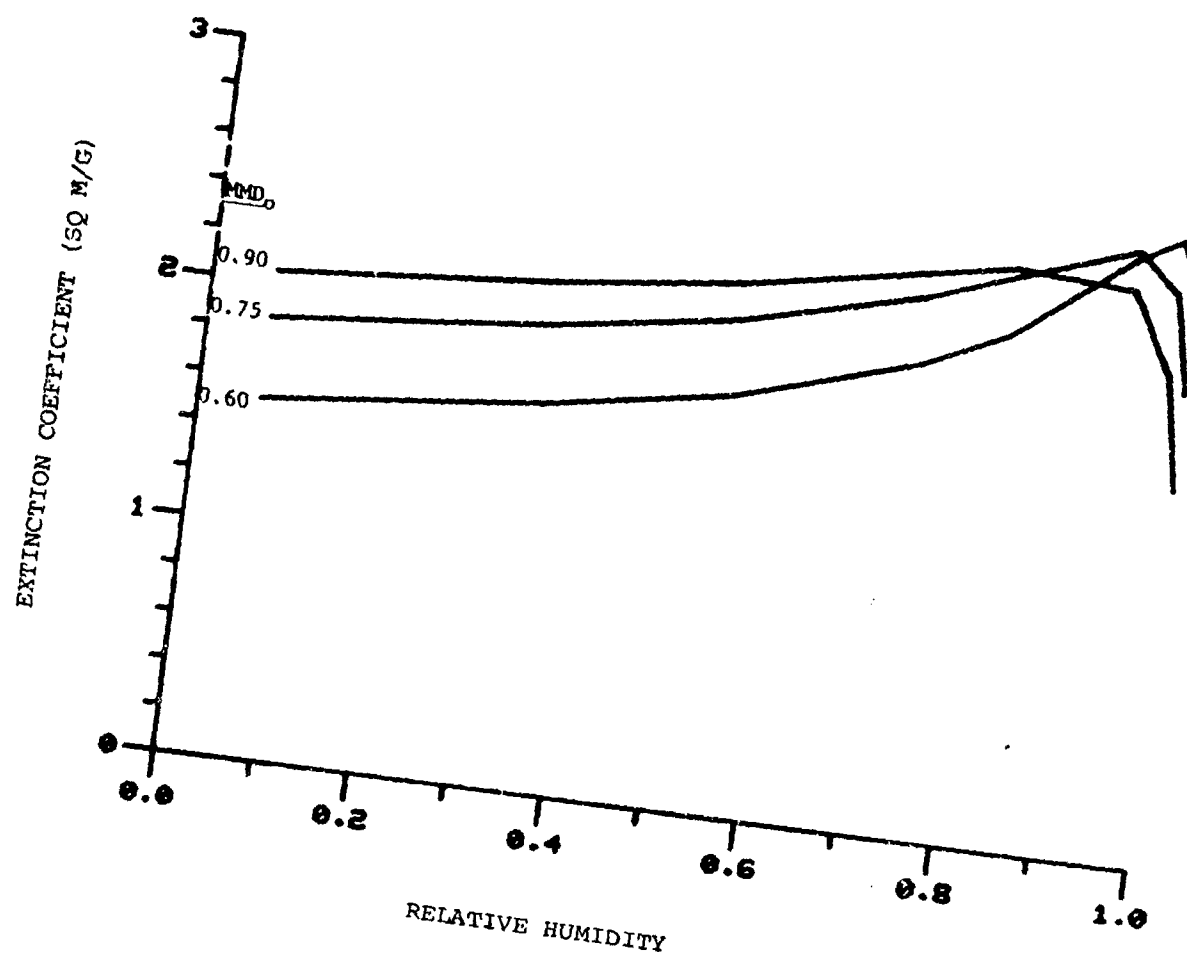
FIGURE 4.13 COMPUTED EXTINCTION COEFFICIENT FOR
PHOSPHORUS SMOKES AT 1.06 μm WAVE-
LENGTH VERSUS RELATIVE HUMIDITY.
FRICKEL ET AL. [4].

4-17
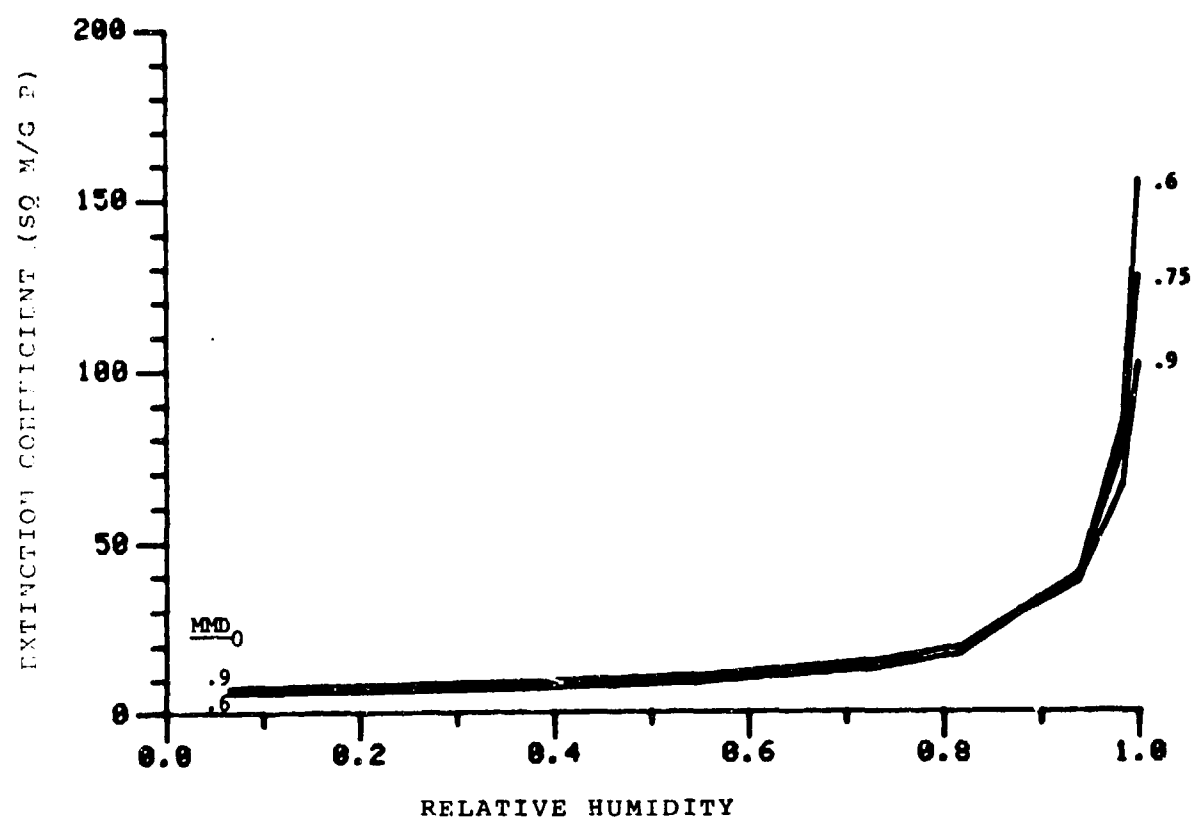
FIGURE 4.14 PHOSPHORUS SMOKE EXTINCTION CO-
EFFICIENT AT 1.06 μm REFERRED TO
PHOSPHORUS CONTENT OF THE AEROSOL.
FRICKEL ET AL. [4].

4.1.1.1.4 Attenuation Coefficients

There exist many papers and reports on field tests of
phosphorous smoke. Unfortunately, the authors of many of these
reports do not always specify the state of the original munition,
i.e. whether it is red phosphorous, or white phosphorous or in
what form (wedges, wicks, bulk) it exists. The attenuation
coefficients as defined in Section 2 will be either volume
coefficients, i.e. meter $^{-1}$, or mass coefficients, i.e. m^2/gm.
In this section are given tables and curves of the attenuation
coefficients which includes absorption and scattering.

Figure 4.15 illustrates the mass extinction coefficient of
WP smoke, taken from Salomon and Peterson [5].
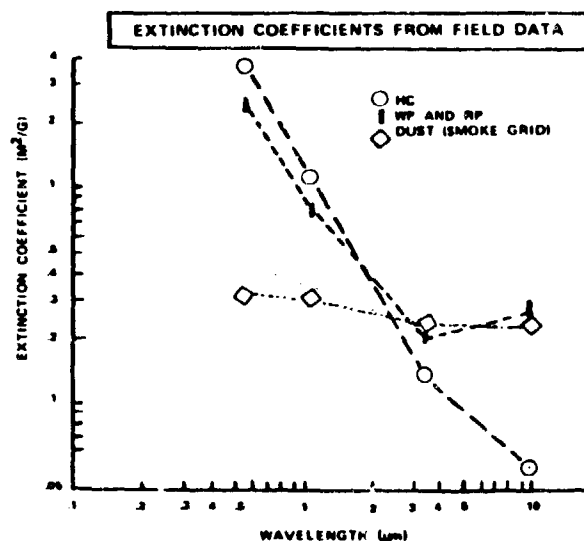
FIGURE 4.15 MASS EXTINCTION COEFFICIENTS FROM
FIELD DATA.

Although not specifically stated, the WP here probably refers to
cannisters or wicks rather than bulk WP. Nevertheless, the mass
extinction coefficients should be the same.

Figure 4.16, taken from Milham et al. [6] depicts the mass
extinction coefficient from ~ 1 μm to 9.5 μm. In a similiar
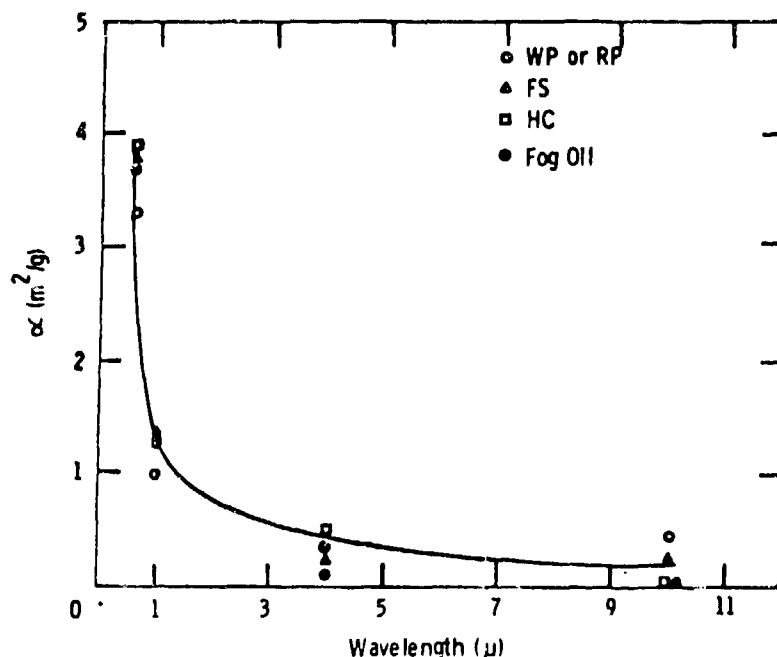
REF: Milham, et. al., ED-SP-77002, ARCSL-TR-77067, Chemical Systems Laboratory,
Aberdeen Proving Ground, MD

FIGURE 4.16   SUMMARY OF LOW RESOLUTION EXTINCTION
               COEFFICIENTS OF COMMON SMOKES FOR VISIBLE
               TO NEAR-IR RADIATION.

smoke transmission study, Carlon et al. [7] found the extinction
coefficients illustrated in Figure 4.17. It should be noted that
these values are not too different from these in Figure 4.16.
An expanded version of the spectral region from 8-12 μm is
depicted in Figure 4.18. Vervier [8] reports on the mass extinction
coefficients for various smokes. These are illustrated in
Figure 4.19 for the spectral region 0.4-12 0 μm.
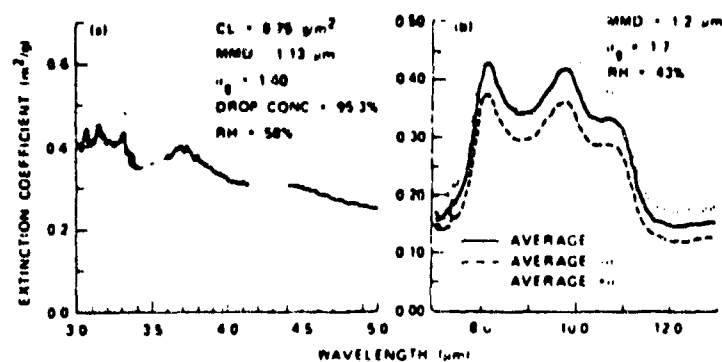
Reference: Edgewood Arsenal Report
H. R. Carlon, D. H. Anderson, M. E. Milham, T. L. Tarnove,
R. H. Frickel and I. Sindoni, Appl. Optics 16. 1598, June 1977

FIGURE 4.17   EXTINCTION COEFFICIENT FOR WHITE
PHOSPHORUS.   RAPID DROP OF EXTINCTION
BEYOND 10.5 μ WAVELENGTH IS ILLUS-
TRATED. (U)
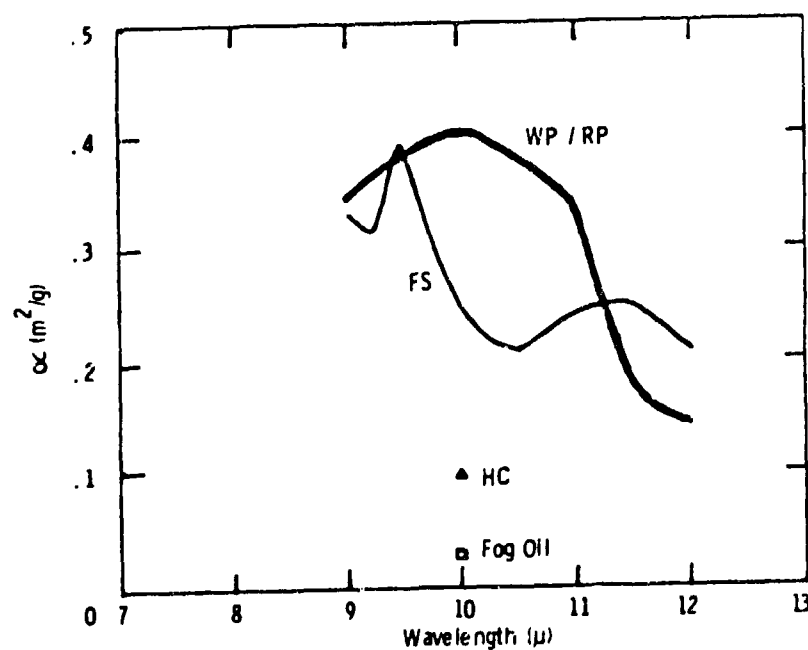
REF: Milham, et. al, ID-SP-77002, ARCSL-TR-77067, Chemical Systems Laboratory,
Aberdeen Proving Ground, MD.

FIGURE 4.18   EXPANDED SCALE OF FIGURE 4.17 EXAMINING
EXTINCTION FOR WHITE PHOSPHORUS AND FS
IN 8-12 μ WAVELENGTH REGION.   (U)

4-21
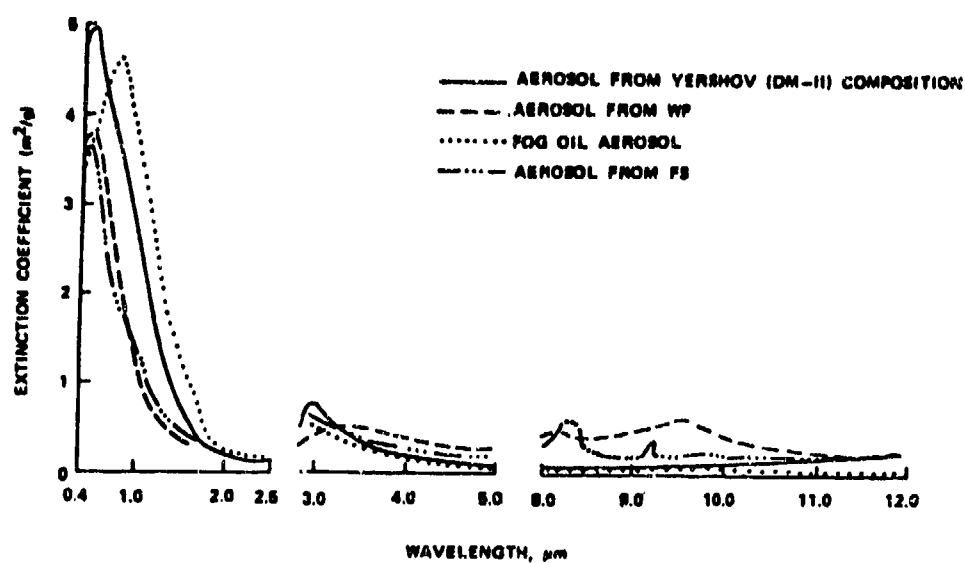
FIGURE 4.19 EXTINCTION SPECTRA-STANDARD SMOKE

Data by Stuebing [9] on phosphorous in the mid-IR and the far-IR are given in Figures 4.20 and 4.21 respectively.
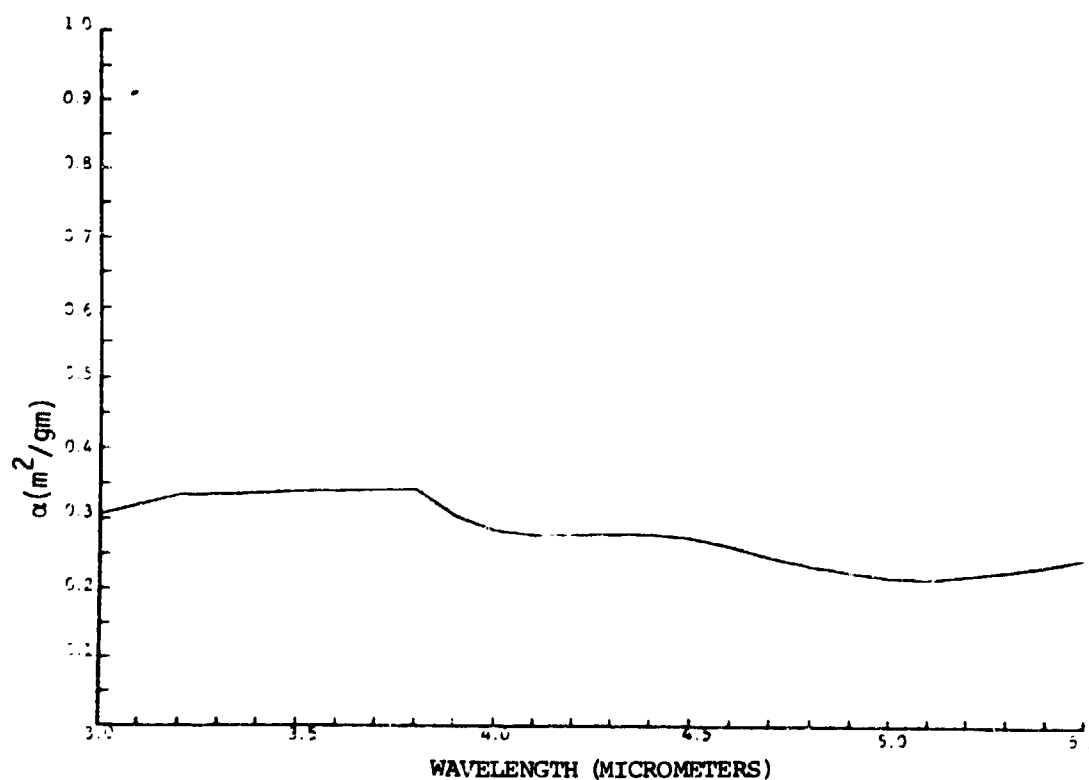
FIGURE 4.20 EXTINCTION COEFFICIENT FOR PHOSPHORUS SMOKE IN THE MID-IR. (U)
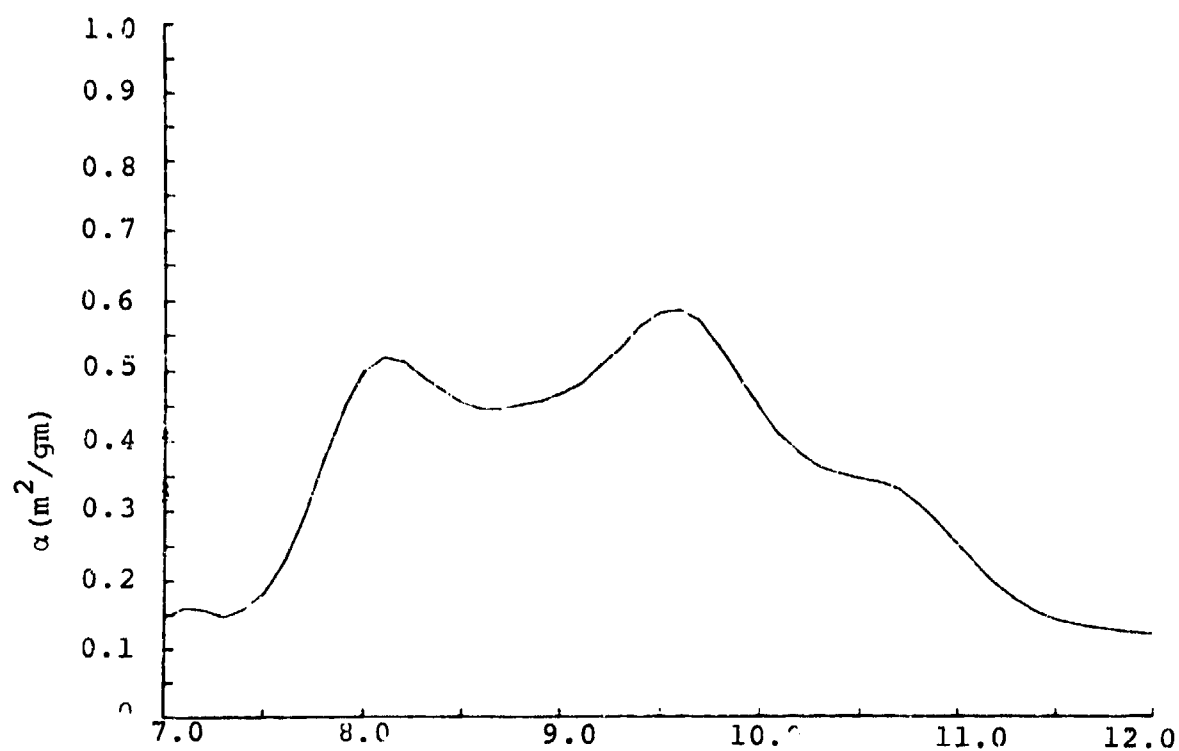
FIGURE 4.21 EXTINCTION COEFFICEINT FOR PHOSPHORUS
SMOKE IN THE FAR IR (U)

Laboratory data collected by Holst and Milham [10] are
given for WP in Figure 4.22 for the spectral region 7-13.5 μm.
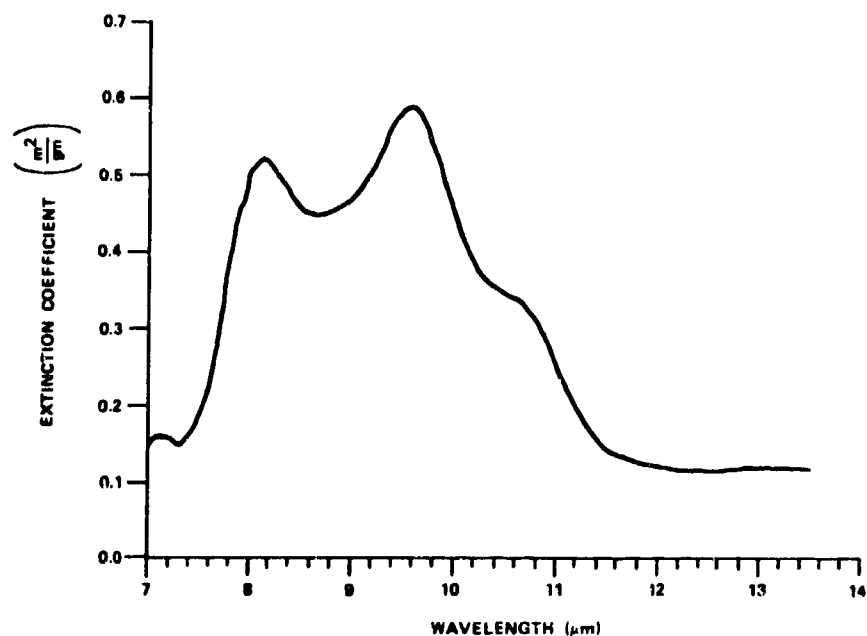
FIGURE 4.22 SPECTRAL EXTINCTION COEFFICIENT OF WP

4-23

In a classification of mass extinction coefficients for smokes, Dubinsky and Levesque [11] presented a table of values. These are given in Table 4.2 for broadband measurements.

TABLE 4.2

SUMMARY OF EXTINCTION RESULTS

Smoke	Wavelength[1]	Extinction co-efficient, $\alpha(m^2/gm)$	Relative Extinction (WP Reference)
WP (White Phosphorous)	A	5.310 (± 2.070)	1.000
	B	1.330 (± 0.194)	1.000
	C	.549 (± 0.066)	1.000
Red Castable Smoke	A	1.000 (± 2.750)	.188
Composition	B	0.306 (± 0.014)	.230
	C	0.073 (± 0.001)	.133
Grenade Hand Smoke	A	2.	2.
1330-21-861-9316	B	0.225 (± 0.120)	.169
Pains Wessex Ltd.	C	0.084 (± 0.053)	.153
Grenade Mini Smoke	A	0.460 (± 0.198)	.087
White 45 sec	B	0.433 (± 0.066)	.326
Pains Wessex Ltd.	C	0.080 (± 0.049)	.146
HC-CIAL, Lot 3-22 2521	A	0.848 (± 0.208)	.160
Hand Grenade Smoke	B	0.753 (± 0.037)	.566
C.I.L.	C	0.160 (± 0.030)	.291
Benzoyl Peroxide	A	1.050 (± 0.230)	.198
Free radical initiation	B	0.707 (± 0.060)	.532
	C	0.125 (± 0.037)	.228
Yellow Grenade Hand	A	0.800 (± 0.377)	.151
Smoke 1330-21-861-9314	B	2.	2.
Lot 4/032 Pains Wessex Ltd.	C	0.125 (± 0.025)	.228
Schermuly Smoke Grenade	A	0.225 (± 0.126)	.042
Lot 3 White 3/35	B	2.	2.
Shermuly Ltd.	C	0.041 (± 0.037)	.075
Shermuly Smoke Grenade	A	0.733 (± 0.069)	.139
Lot 1 Yellow	B	2.	2.
Shermuly Ltd. Surrey	C	0.150 (± 0.014)	.273

1. The wavelength range, optical source and detector used for the extinction measurements
   are abbreviated as follows:
   A. 0.4 µm - 0.7 µm tungsten spotlight source (1800°C) using S-11 photomultiplier detector.
   B. 0.6 µm - 14 µm tungsten spotlight source (1800°C) using $LiTaO_3$ pyroelectric detector.
   C. 0.6 µm - 14 µm 600°C black body source using $LiTaO_3$ pyroelectric detector.

2. No data available due to instrument failure or grenade shortages.

4.1.1.1.5 Scattering Parameters

Very little information exists on the angular scattering properties of smoke particles, at least insofar as field tests are concerned. The scattering properties, however, are important for contrast studies and for the investigation of the effects of the medium on visible and infrared imaging devices.

Sztankay [12] performed measurements with a dual-channel nephelometer and obtained values of the volume scattering coefficient and the backscatter coefficient. The latter is defined as $\mu(\pi)$, the power scattered per unit solid angle at an angle of π radians (180°) from the incident beam direction per unit power density per unit volume. Likewise, the single scattering phase function for that angle can be defined as:

$$F(\pi) = \frac{\mu(\pi)}{\sigma} \qquad (4.4)$$

where σ is the volume extinction coefficient. A plot of the backscatter coefficient $\mu(\pi)$ for white phosphorus smoke, cumulus or stratus clouds, and dust is given in Figure 4.23. Sztankay [12] also states that HC and P smoke distributions lie between the so-called L and M cloud models calculated by Deirmendjian [13]. WP wick most resembles the M distribution, and WP (mortar) and HC (smoke pot) more resemble the L distribution. The phase function $F(\pi)$ for 180° for these models is given in Table 4.3.
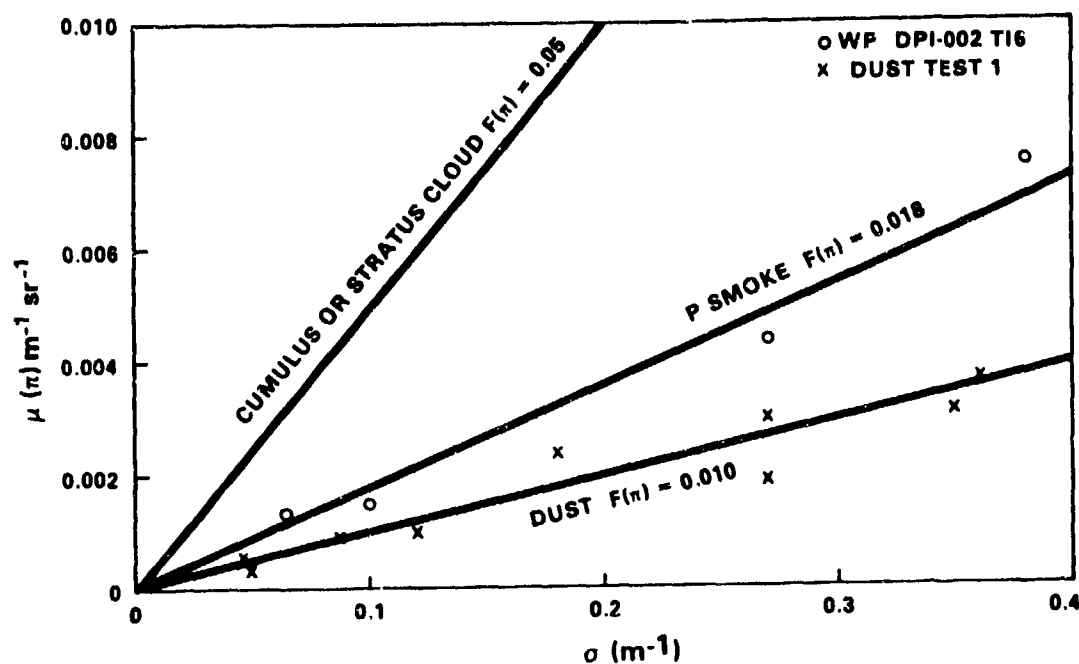
FIGURE 4.23 BACKSCATTER COEFFICIENT VS EXTINCTION
COEFFICIENT PLOT, WP SMOKE AND DUST.

TABLE 4.3

CALCULATED VALUES OF $F(\pi)$
BASED ON HAZE MODELS

AEROSOL MODEL	$F(\pi)$ (sr^{-1})
WATER HAZE H	0.014
WATER HAZE L	0.010
WATER HAZE M	0.016
WATER CLOUD C$_2$	0.05

REFERENCE: "ELECTROMAGNETIC SCATTERING ON
SPHERICAL POLYDISPERSIONS",
D. DEIRMENDJIAN, AMERICAN
ELSEVIER PUB. CO. (1969)

4-26

4.1.1.1.6 Dispersion Parameters

(Data on dispersion parameters for bulk WP are not available.)

4.1.1.2 Wick WP/Wedges

In this section we present material on the physical and optical characteristics of white phosphorous and red phosphorous in the form of wicks and wedges.

4.1.1.2.1 Munition Characteristics

Wicks and wedges can be characterized by their burn times. This is true of WP wicks and wedges as well as RP munitions which are also in the form of wicks and wedges. Solomon and Peterson [5] report on the submunition burn times for WP and RP wicks and wedges. These are listed in Table 4.4.

TABLE 4.4

SUBMUNITION BURN TIMES (Min)

	6 Inch Wick	6.5
WP	3 Inch Wick	7.8
	2.75 Inch Wedge	4.3
	81mm (Navy)	4.3
RP	81mm (German)	3.6
	155mm (Navy)	6.4

They represent the time interval required for a loss in mass from 2 to 98%. Wicks and wedges are designed to have longer and more controlled burn times than bulk-filled WP rounds. The results in Table 4.4 are from an extensive series of field tests at Dugway Proving Ground during the latter part of 1977. Another critical factor is the rate at which submunitions burn; a factor which governs the rate at which smoke is released through time. The rates for wick (WP) and a wedge (RP) are illustrated in Figures 4.24 and 4.25 respectively.
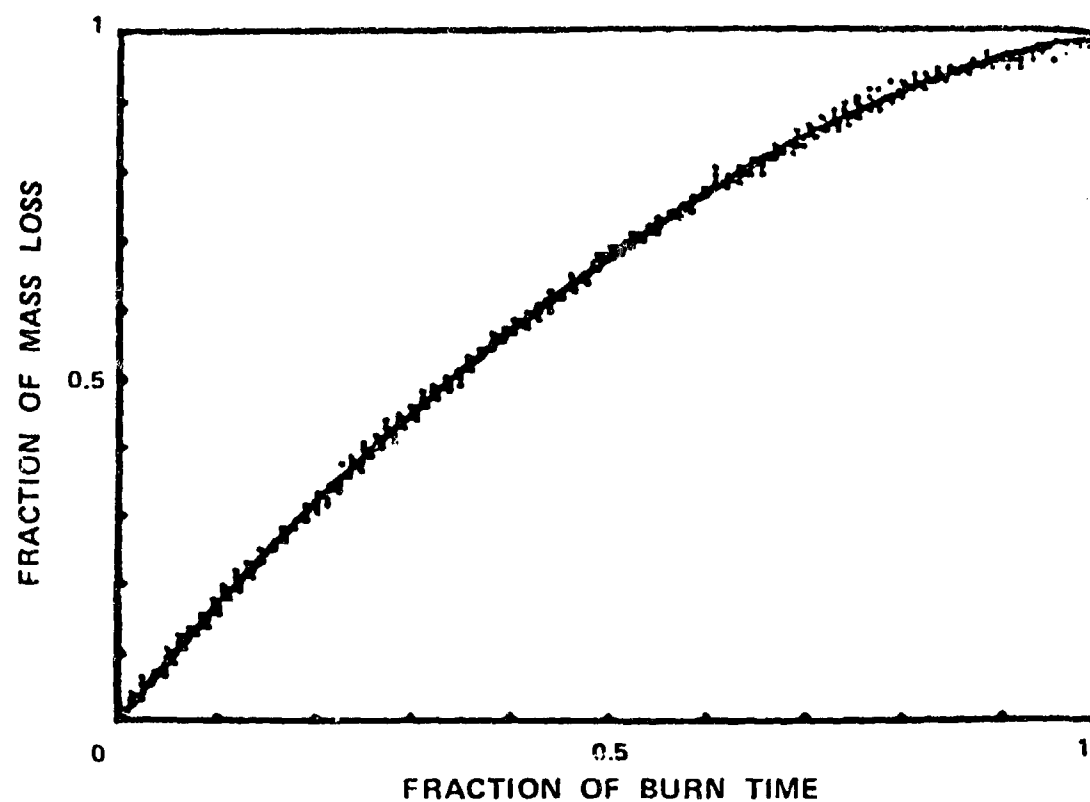
FIGURE 4.24   SUBMUNITION BURN RATE, SIX INCH WICK (WP)
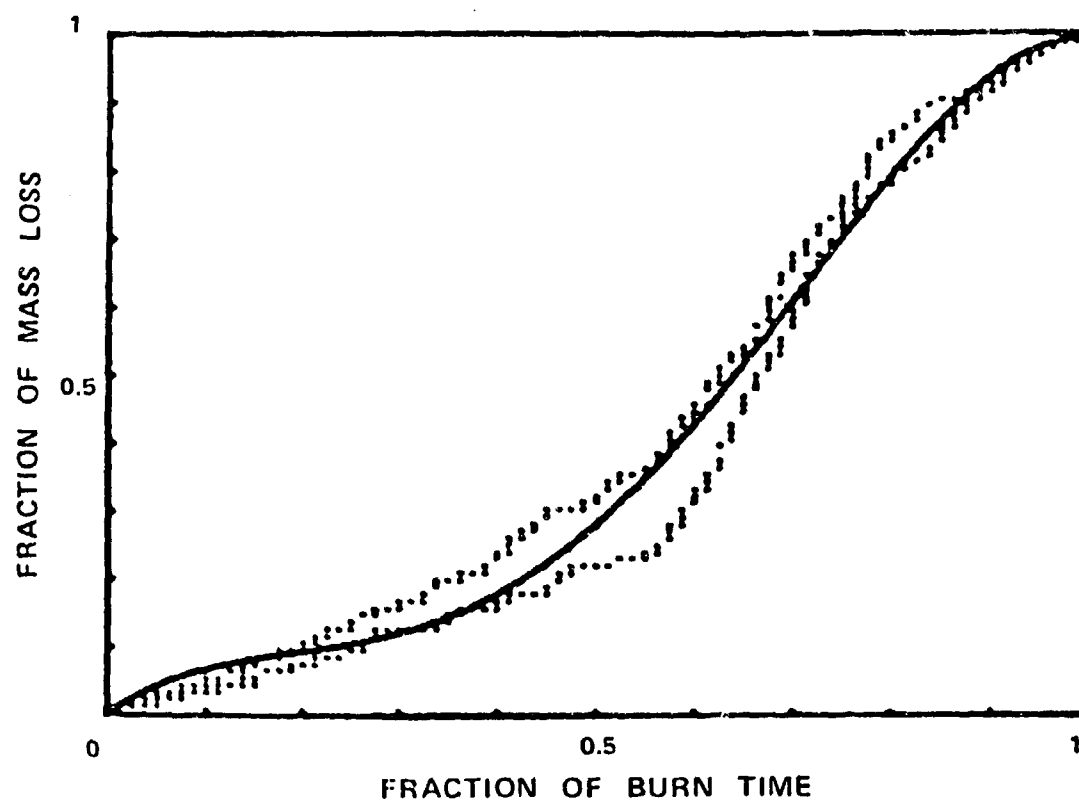
FIGURE 4.25   SUBMUNITION BURN RATE, NAVY 155MM WEDGE (RP)

4.1.1.2.2 <u>Yield Factor</u>

The yield factor for WP wicks and wedges will probably be the same as for bulk WP. See Section 4.1.1.1.2.

4.1.1.2.3 Environmental Effects

In this section are presented the variations in the mass extinction coefficients for WP wicks, WP wedges and RP grenades. Figures 4.26 through 4.31 represent data obtained during the High Humidity Hygroscopic Smoke (H^3S) Test conducted at the Edgewood area of Aberdeen Proving Ground in July, 1979. Farmer [14] analyzed the data from nineteen trials involving phosphorous dispersed as red phosphorous grenades and white phosphorous wicks and wedges. Eight trials were conducted using hexachloroethane cannisters.
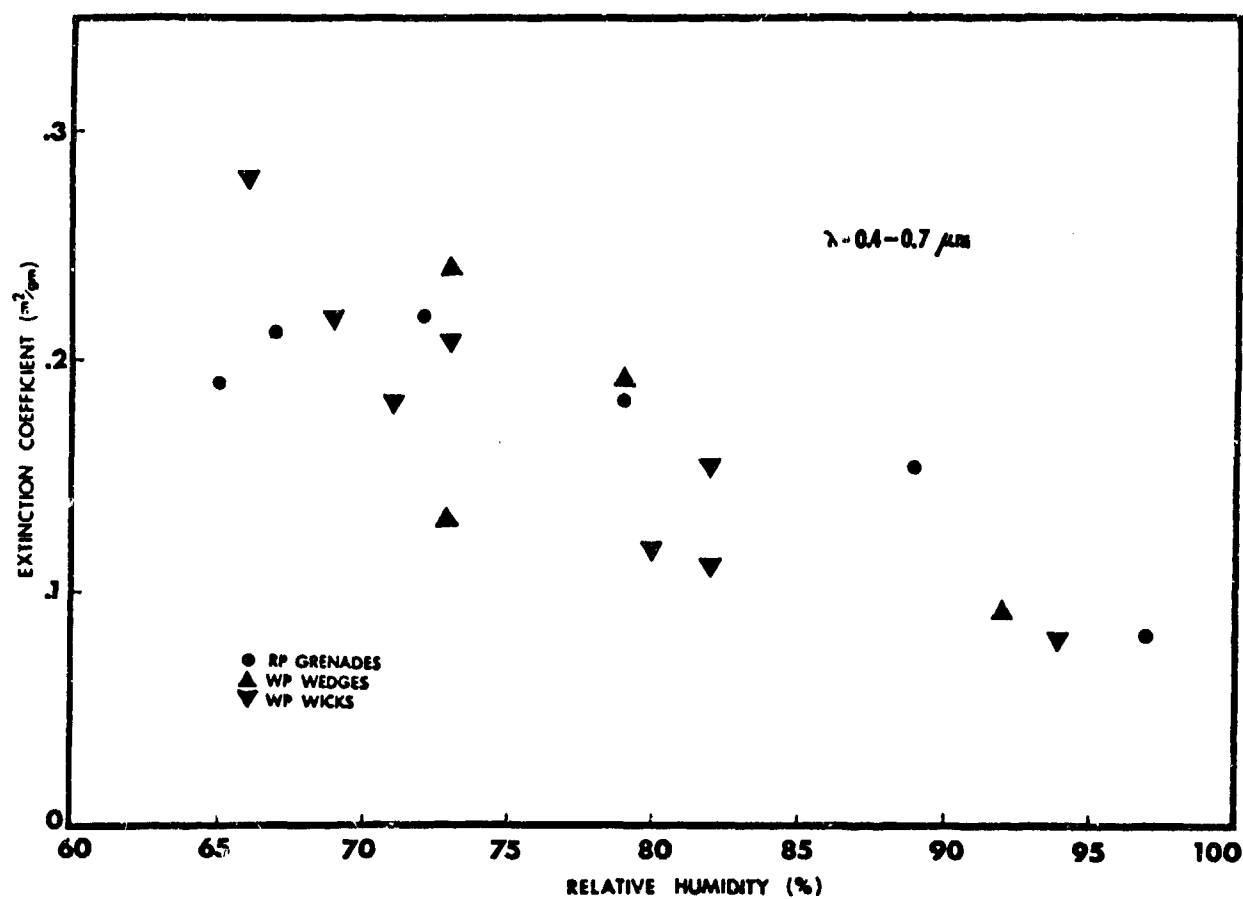
FIGURE 4.26 EXTINCTION COEFFICIENT AS A FUNCTION OF RELATIVE
HUMIDITY FOR VISIBLE WAVELENGTHS.
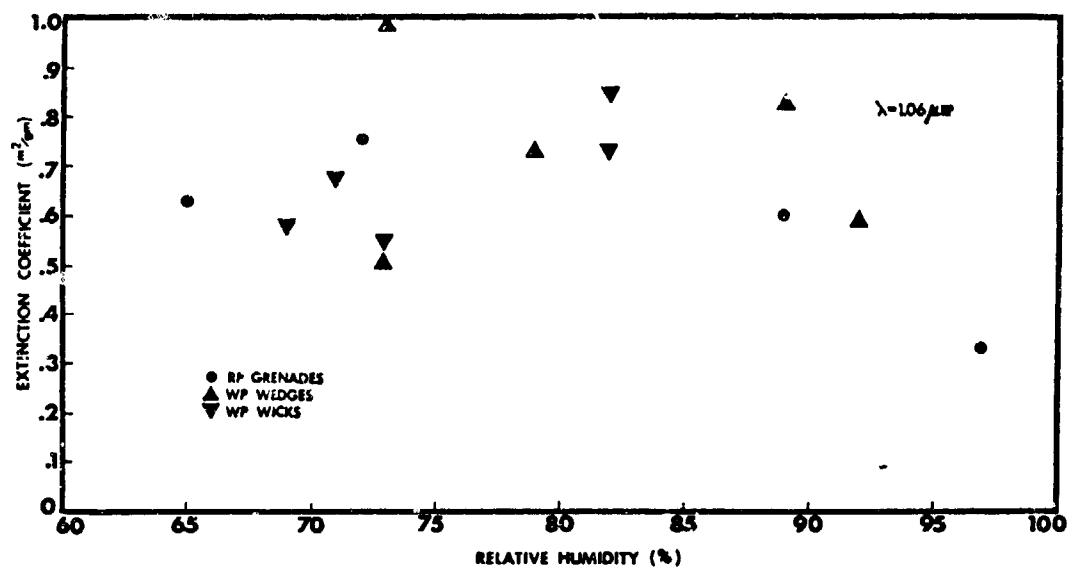
FIGURE 4.27 EXTINCTION COEFFICIENT AS A FUNCTION OF RELATIVE HUMIDITY FOR TRANSMISSION AT 1.06 MICROMETER WAVELENGTHS.
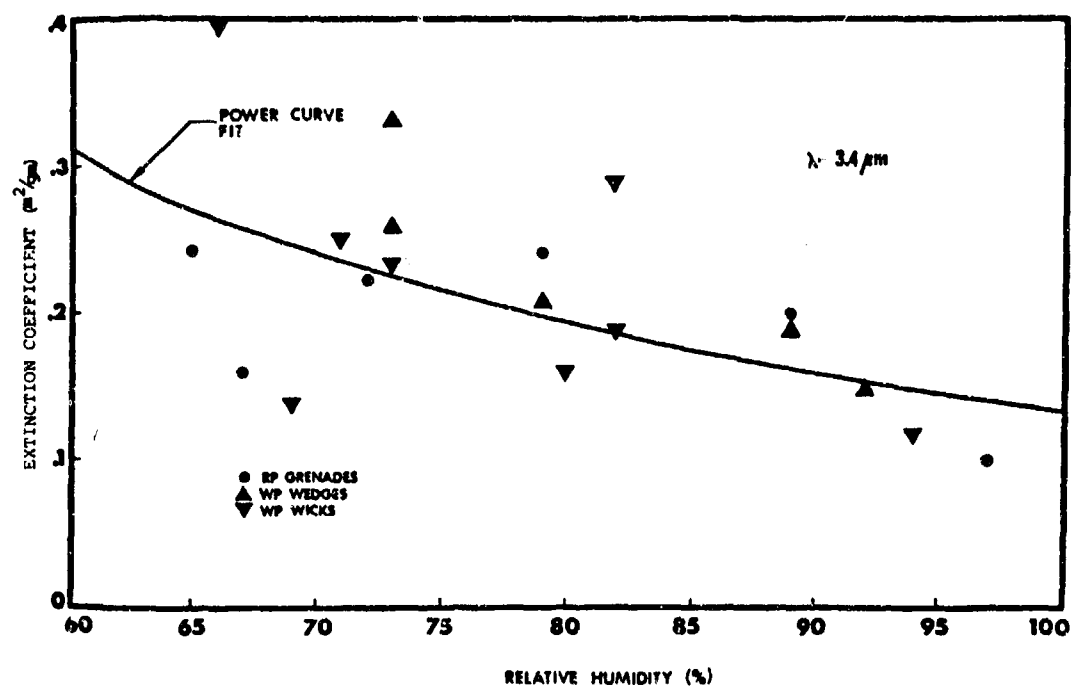
FIGURE 4.28 EXTINCTION COEFFICIENT AS A FUNCTION OF RELATIVE
HUMIDITY FOR TRANSMISSION AT 3.4 MICROMETER WAVE-
LENGTHS.

4-35
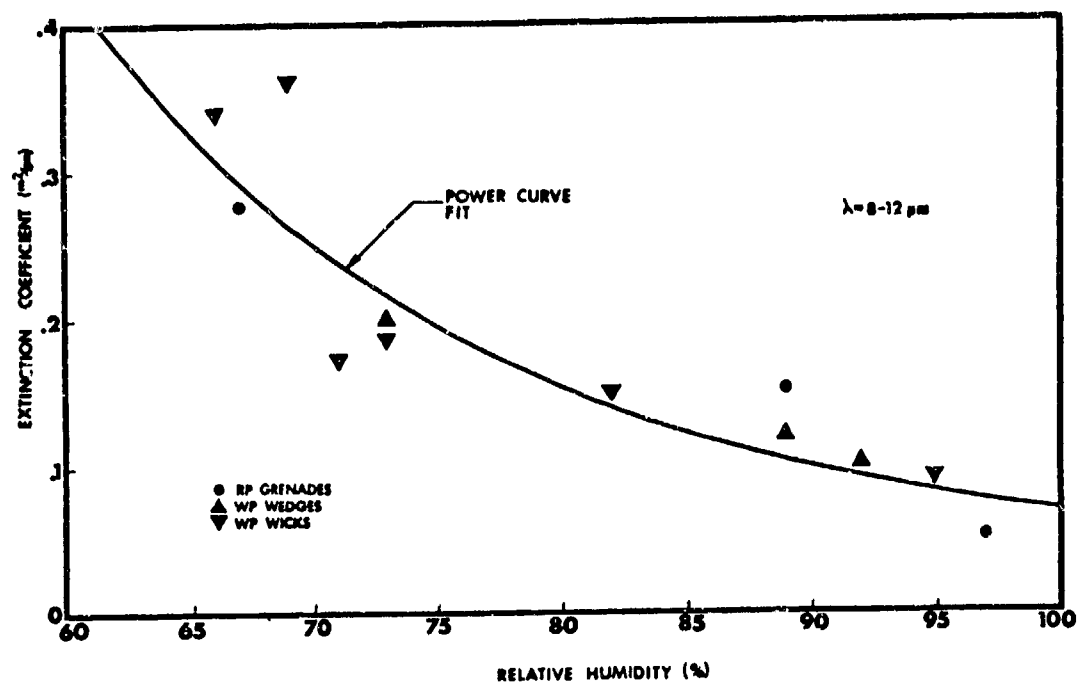
FIGURE 4.29 EXTINCTION COEFFICIENT AS A FUNCTION OF RELATIVE
HUMIDITY FOR TRANSMISSION AT 9.75 MICROMETER WAVE-
LENGTHS.

4-36
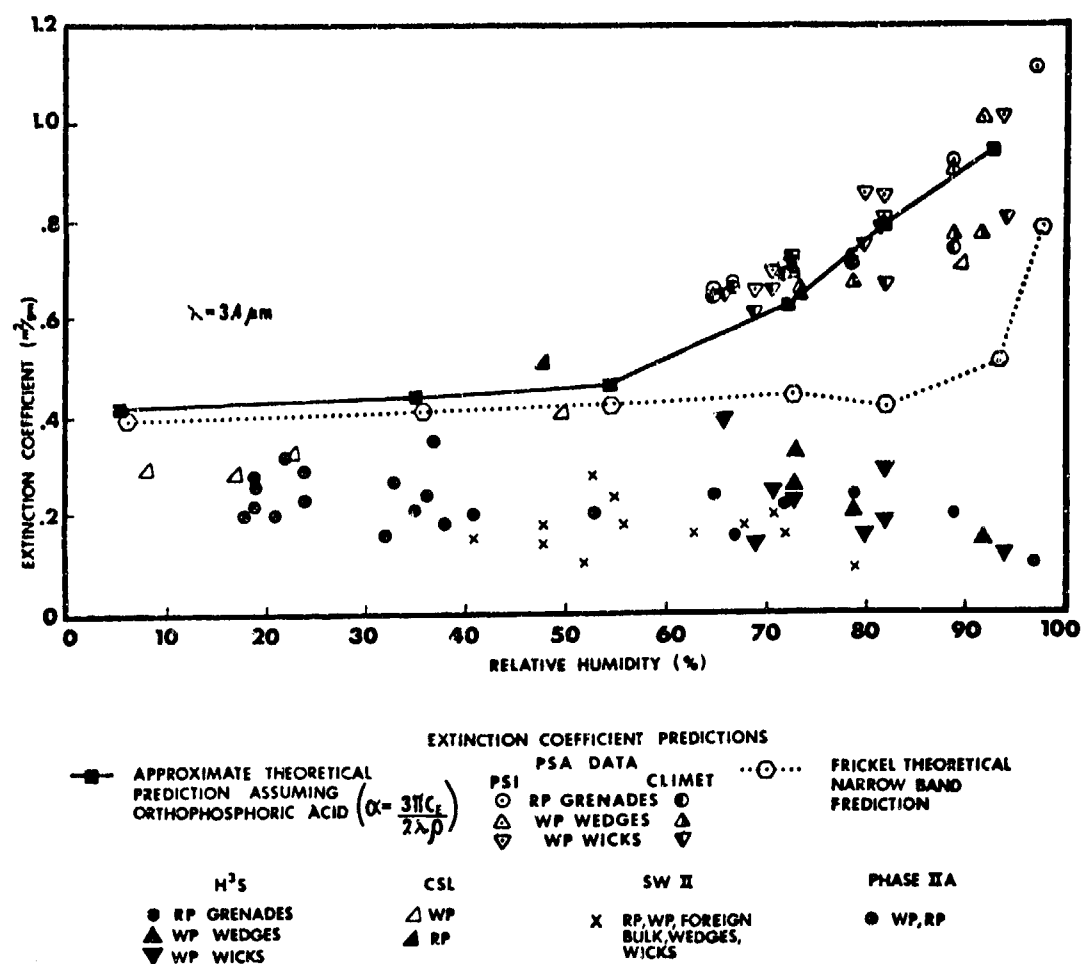
FIGURE 4.30 COMPARISON OF EXTINCTION COEFFICIENT MEASUREMENTS FOR
3.4 MICROMETER WAVELENGTHS FROM FOUR DIFFERENT TESTS
WITH APPROXIMATE THEORETICAL VALUES FOR PHOSPHORUS
SMOKES.

4-37
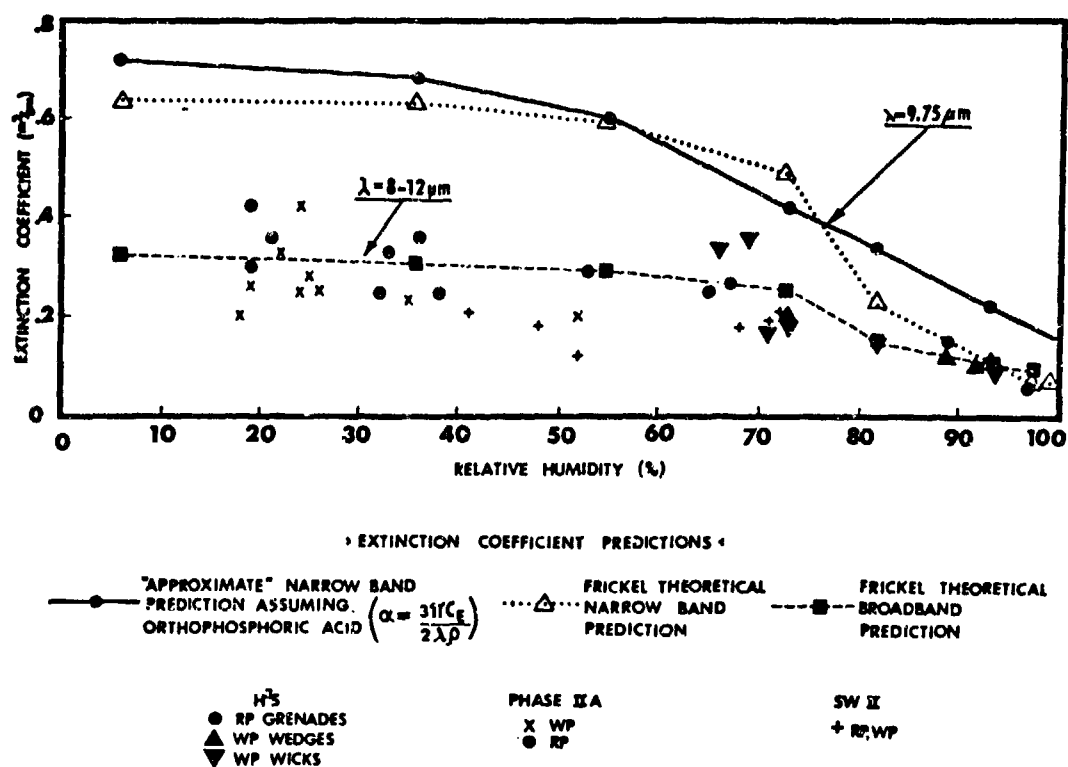
FIGURE 4.31   COMPARISON OF EXTINCTION COEFFICIENT MEASUREMENTS
FOR 9.75 MICROMETER WAVELENGTHS FROM FOUR DIFFERENT
TESTS WITH APPROXIMATE THEORETICAL VALUES FOR
PHOSPHORUS SMOKES.

4.1.1.2.4 Attenuation Coefficients

In this section are contained data on white phosphorous smoke arising from burning wicks and wedges. Because red phosphorous usually exists in this form we also include these data here especially since the attenuation properties of white and red phosphorous are really the same.

A series of field measurements by Solomon and Peterson [5] resulted in the following mass extinction coefficients for Red Phosphorous (RP) at a wavelength of 3.4 μm·

TABLE 4.5

EXTINCTION COEFFICIENTS (m^2/g) FOR RP AT 3.4 μm

0.18	
0.20	
0.24	Mean 0.22
0.16	SD $\pm$ 0.04
0.27	
0.20	
0.28	
0.22	

For other wavelengths we should refer to Figure 4.15.

A series of laboratory experiments were undertaken by Milham et al. [6] to determine the mass extinction coefficients of red

4-39

phosphorous and other smokes for the 3-5 μm and the 8-13 μm spectral region. These coefficients are given in Figures 4.32 through 4.35 for various values of CL (concentration multiplied by path length); median mass diameter (MMD), standard deviation σ_g, droplet concentration, and relative humidity (RH).

A High Humidity Hygroscopic Smoke (H^3S) Test was performed at the Edgewood area of Aberdeen Proving Ground during July 1979. Smokes from HC cannisters, RP grenades, and WP wicks and wedges were measured and the mass extinction coefficients were determined for the visible, 1.06 μm, 3.4 μm and 8-12 μm spectral regions. Farmer [14] presented these results which are given in Table 4.6.
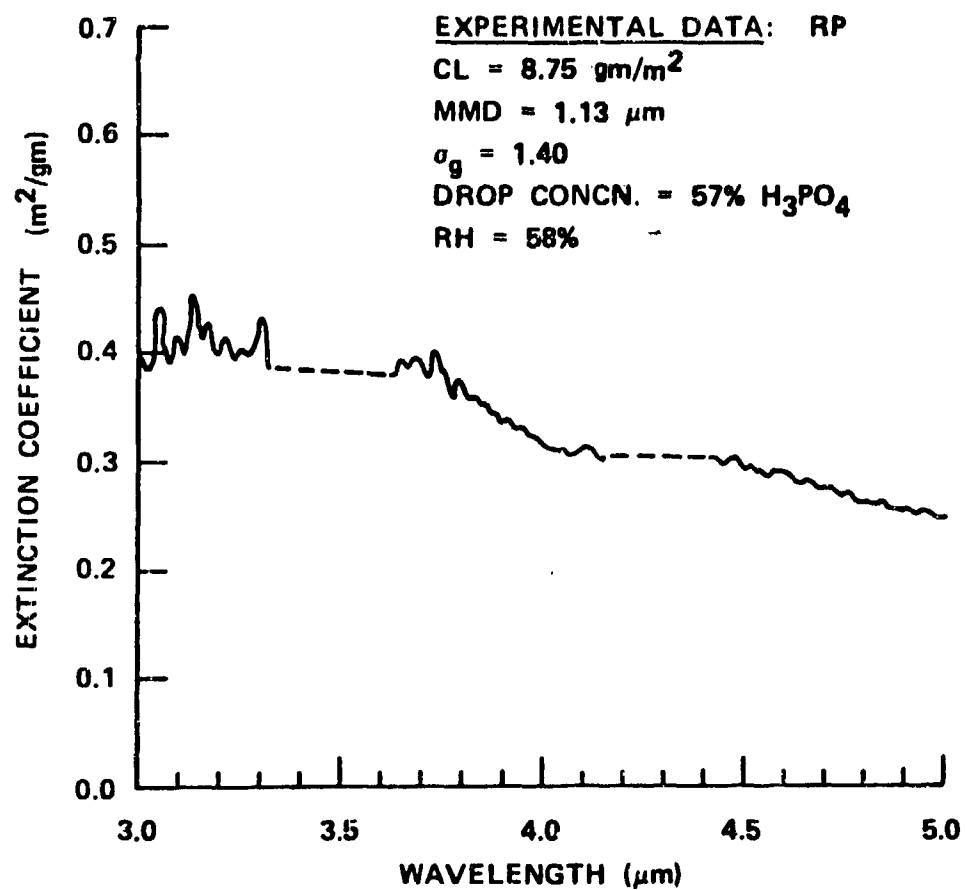
FIGURE 4.32   RED PHOSPHOROUS SMOKE 3-5 μm

4-41
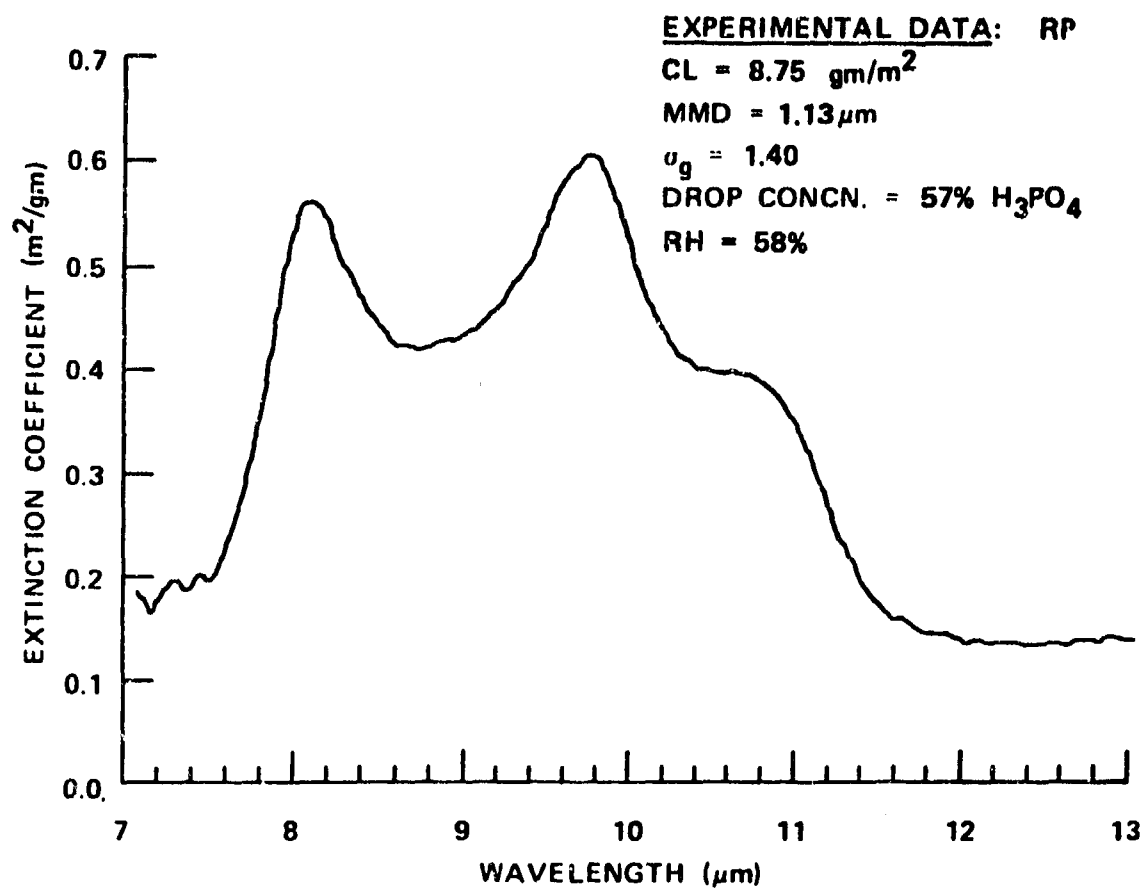
FIGURE 4.33   RED PHOSPHOROUS SMOKE 8-13 μm
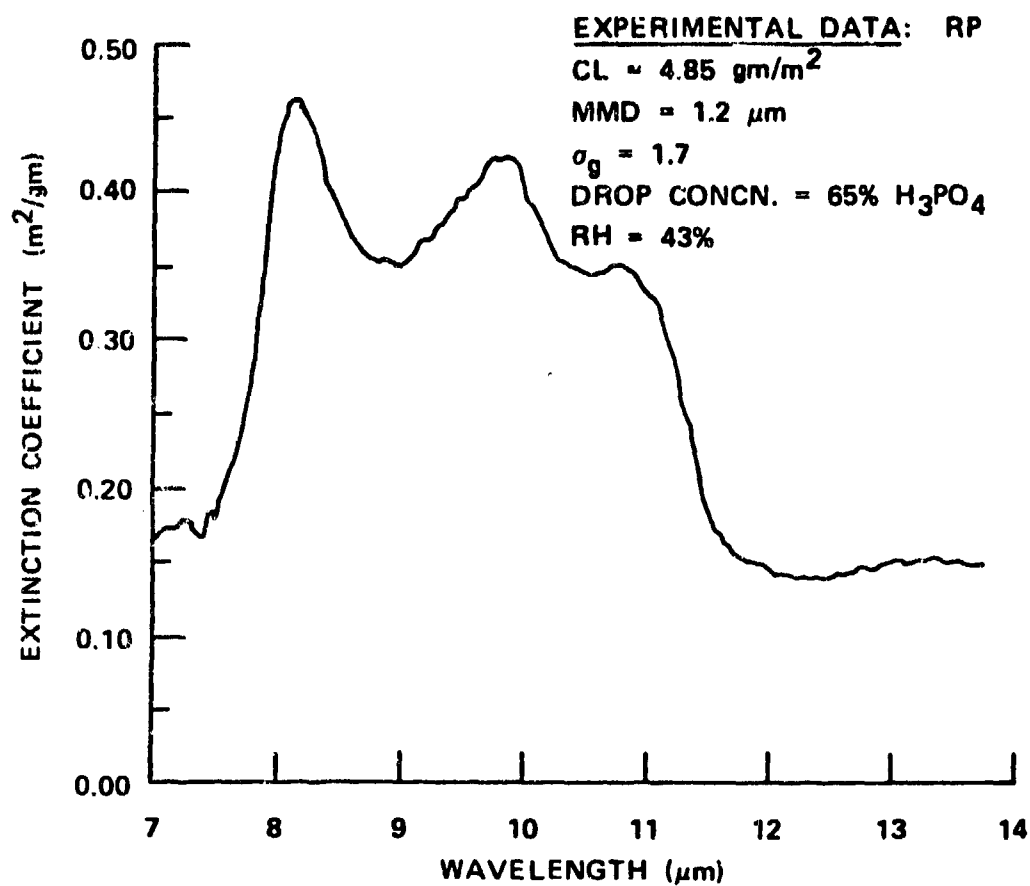
FIGURE 4.34   RED PHOSPHOROUS SMOKE 8-13 μm

4-43
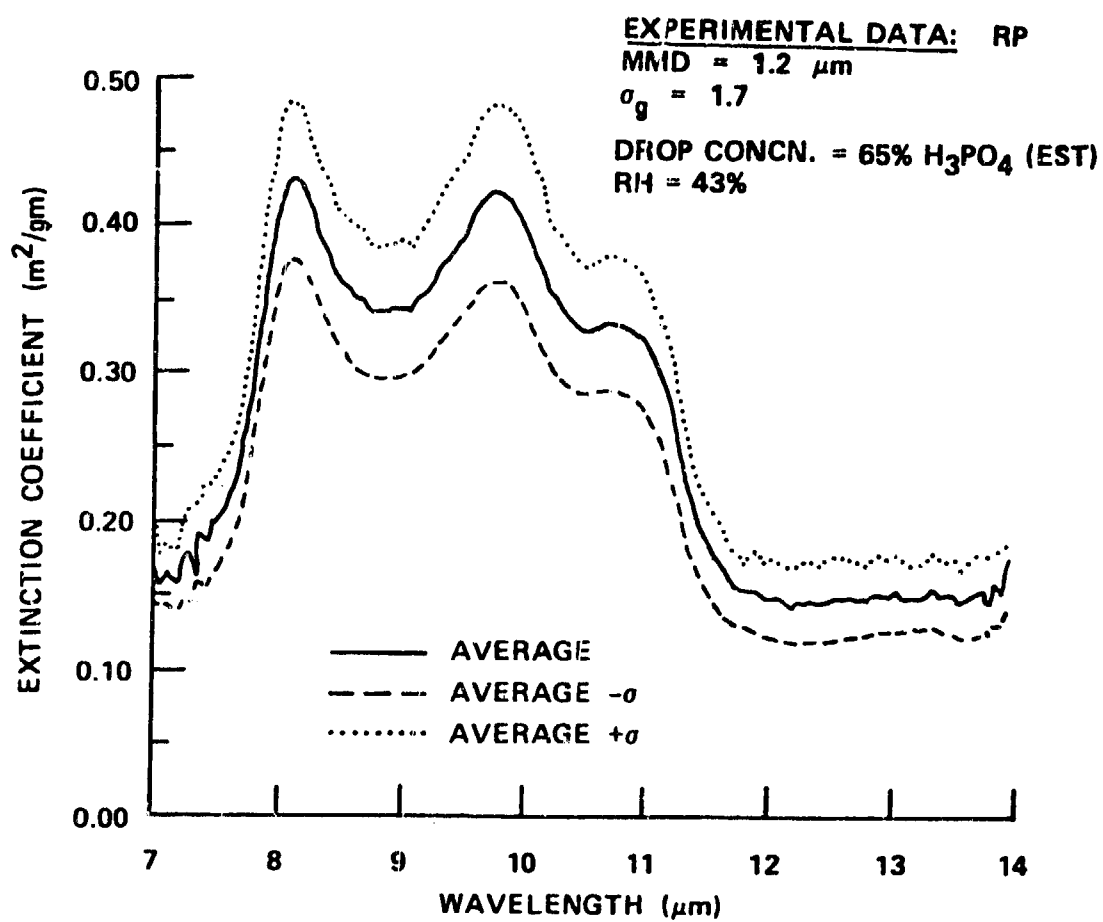
FIGURE 4.35   RED PHOSPHOROUS SMOKE 8-13 μm

TABLE 4.6

EXTINCTION COEFFICIENT AND DOSAGE PATHLENGTH MEASUREMENTS OBTAINED DURING H³S TEST

TRIAL NO.	OBSCURANT SOURCE MASS (kg)	RELATIVE HUMIDITY (%)	EXTINCTION COEFFICIENT (m^2/gm) WAVELENGTH (um)				DOSAGE x PATHLENGTH (gm·min/m^3)	DOSAGE NEAREST PSI ($\frac{mg \cdot min}{m^3}$)	SAMPLE TIME (min.)
			0.4 - 0.7	1.06	3.4	8 - 12			
	WP GRENADES								
10	2.17	97	0.64	0.33	0.10	0.05	82.20	.67	8.0
15	1.45	89	1.57	0.60	0.20	0.15	20.87	.32	10.0
3	1.45	79	1.83		0.24		12.16	.15	5.03
7	2.90	72	2.21	0.76	0.22		21.12	.40	5.23
19	1.45	67	2.16		0.16	0.27	5.68	.00	5.25
18	2.90	65	1.92	0.63	0.24		9.46	.15	3.75
	WP WEDGES								
17	6.21	92	0.94	0.59	0.15	0.10	83.24	.98	10.00
12	6.21	89		0.83	0.19	0.18	64.65	1.2	8.0
8	6.21	79	1.96	0.73	0.21		24.62	.17	11.00
4	6.21	73	2.42	0.99	0.33		46.38	.64	10.25
27	12.42	73	1.32	0.49	0.24	0.20	45.98	.48	14.0
	WP WICKS								
16	0.95	94	0.78		0.12	0.09	30.99	.02	10.25
2	2.85	82	1.56	0.74	0.29		28.11	.43	8.0
13	1.91	82	1.16	0.85	0.19	0.15	28.92	1.14	8.0
9	1.91	80	1.21		0.16		18.80	.29	10.0
28	1.91	73	2.10	0.55	0.23	0.18	8.38	.23	6.0
25	1.91	71	1.83	0.68	0.25	0.17	13.42	.3	9.0
22	.95	69	2.24	0.58	0.14	0.36	4.66	0	9.0
20	1.91	66	2.81		0.40	0.34	5.05	.11	6.5
	RC								
11	4.9	93	0.81		0.11	0.06	11.40	.49	3.0
23	4.9	87	1.49	9.00	0.05	0.01	8.92	.06	5.0
16	2.45	84	0.99		0.10	0.04	6.36	.11	3.0
26	9.8	75	2.07		0.15	0.04	8.75	.10	6.0
6R	4.9	72	1.46	0.71	0.07		12.43	.71	3.0
5	2.45	70	3.14	0.82	0.11		4.73	0	2.75
21	4.9	68	2.05	0.99	0.11	0.03	5.07	.03	3.0
18	4.9	39					19.7	.06	3.0

4.1.1.2.5 Scattering Parameters

The backscatter coefficients and phase functions for wick and wedges WP are probably the same as for bulk WP. These values are given in Section 4.1.1.1.5. Sztankay [12] gives nephelometer data for red phosphorous which we include here (Table 4.7). In Table 4.8 we present data on $F(\pi)$ by Sztankay et al. [15] from Smoke Week II.

TABLE 4.7

DUAL-CHANNEL NEPHELOMETER DATA

Run/Smoke	$\sigma (m^{-1})$	$\mu(\pi)(m^{-1}sr^{-1})$	$F(\pi)(sr^{-1})$	Average $F(\pi)$
3/RP	.16	.00095	.006	.009
(DPI-003-T2D)	.14	.0009	.006	
	.10	.0003	.003	
	.035	.0006	.017	
	.25	.003	.012	
	.035	.00064	.018	
	.04	.00027	.007	
	.01	.0001	.01	

TABLE 4.8

NEPHELOMETER DATA FOR SMOKE WEEK II

Trial Number	Aerosol	Type Munition	$F(\pi)(sr^{-1})$
15	WP	122 mm foreign	0.013
20	WP	122 mm foreign	0.008
3	WP	Wick, 2 75 in. rocket	0.008
28	WP	Wick, 2.75 in. rocket	0.013
24	WP	Wedge, 155 mm	0.017
2	PWP	5-in. Zuni	0.016

4.1.1.2.6 Dispersion Parameters

(Data on dispersion parameters for wicks and wedges not available.)

4.1.2 HC Smoke

In this section we present data on a zinc oxide, aluminum, Hexachloroethane (HC) Smoke.

4.1.2.1 Bulk HC

Hexachloroethane (HC) Smoke exists in bulk form and is dispensed in cannisters. The detailed properties of HC smoke are given in this section.

4.1.2.1.1 Munitions Characteristics

As in the case of WP and RP wicks and wedges the burn times and rates are important for HC smoke. Salomon and Peterson [5] provide these data which are included in Table 4.9 and in Figure 4.36.

TABLE 4.9

SUBMUNITION BURN TIMES (MIN) (U)

	155mm M1	2.3
HC	155mm M1	1.3
	105mm	2.0
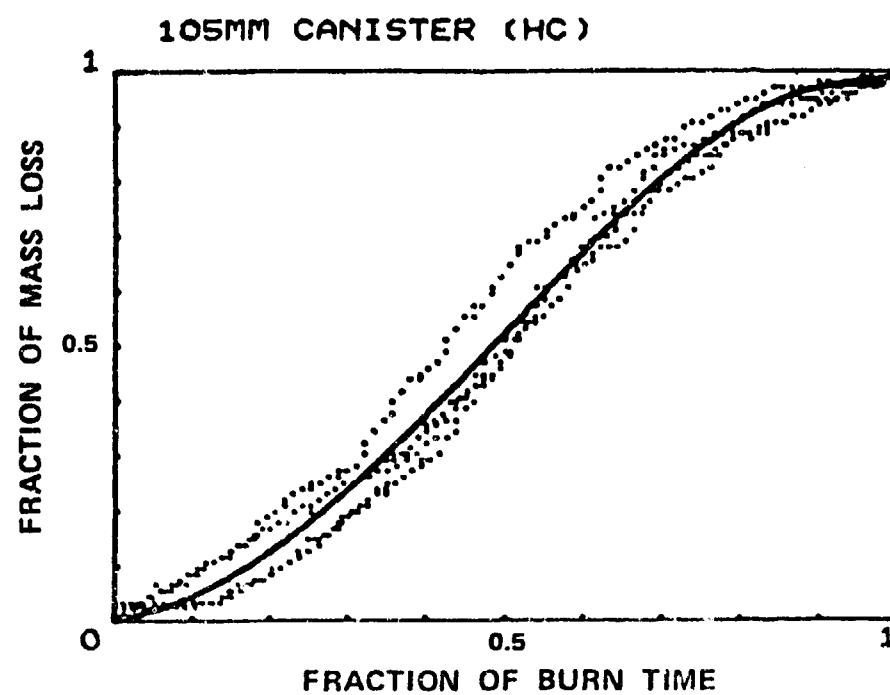
105MM CANISTER (HC)

FIGURE 4.36 SUBMUNITION BURN RATE, 105 mm CANISTER (HC)

4.1.2.1.2 Yield Factor

None available.

4.1.2.1.3 Environmental Effects

Less information is available on the relative humidity dependence of HC smoke. Figure 4.37 illustrates the dependence of the mass extinction coefficient of HC smoke on relative humidity [14].
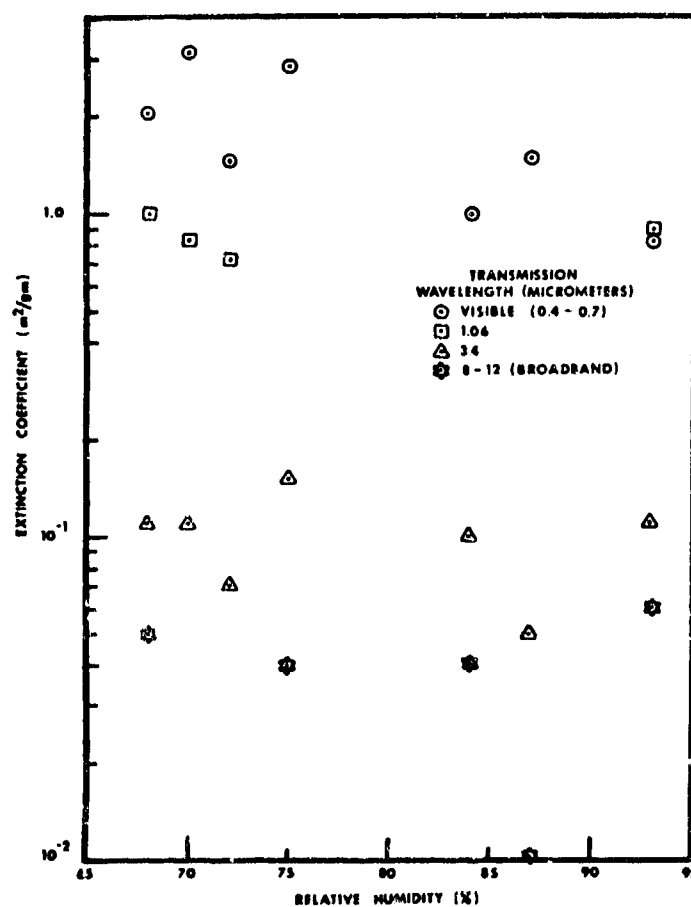
FIGURE 4.37 EXTINCTION COEFFICIENTS AS A FUNCTION OF RELATIVE HUMIDITY FOR HC.

4.1.2.1.4 Attenuation Coefficients

Experimental data on the mass extinction coefficients of HC smoke are given by Stuebing [9] for the mid infrared (Fig. 4.38) and the far infrared (Fig. 4.39).
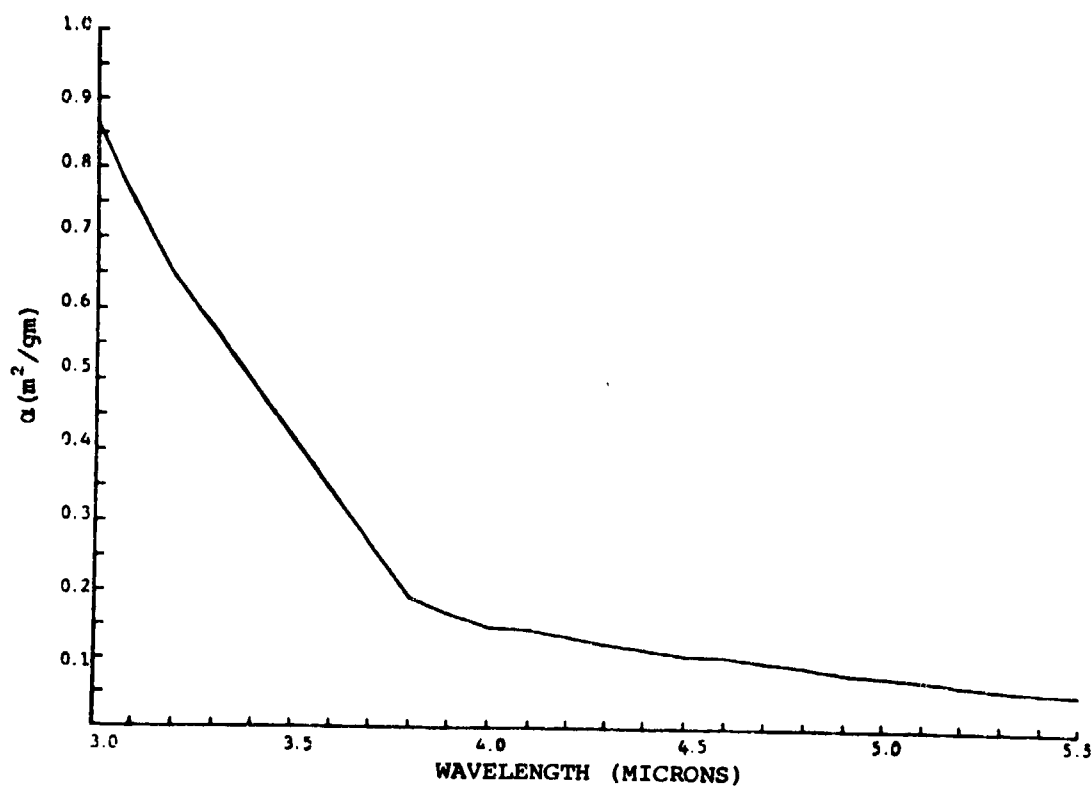
FIGURE 4.38   EXTINCTION COEFFICIENT FOR HC SMOKE IN THE MID INFRARED.

4-53
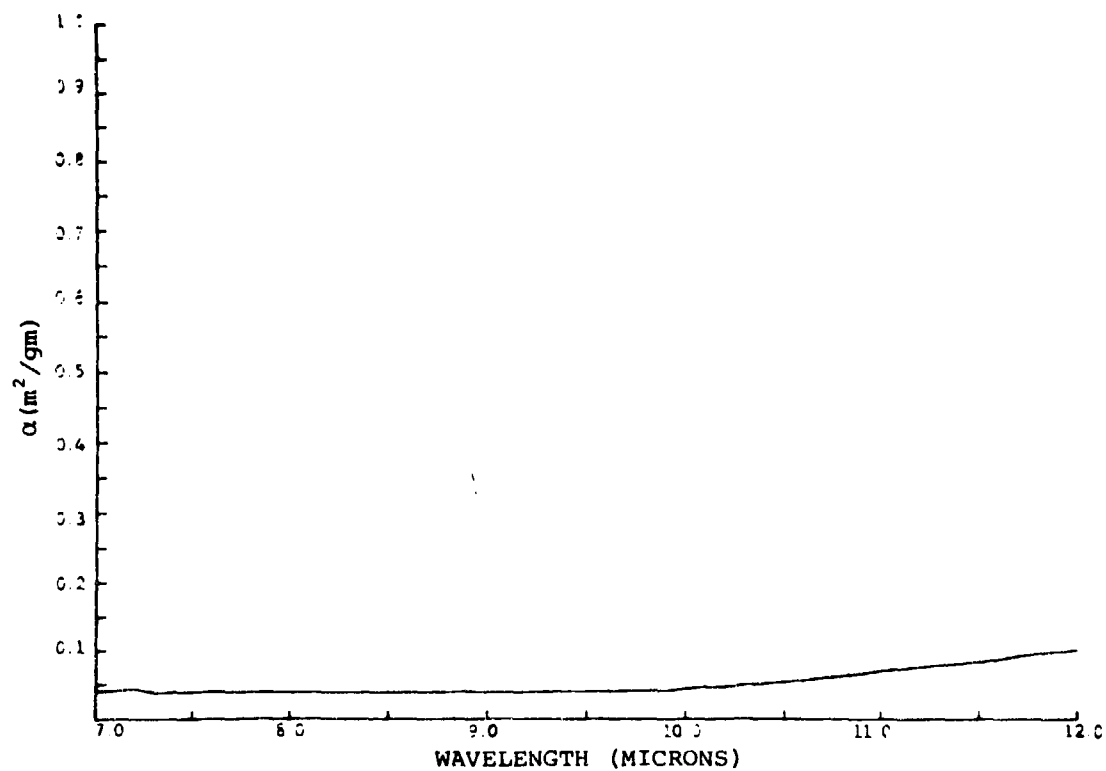
FIGURE 4.39   EXTINCTION COEFFICIENT FOR HC SMOKE
IN THE FAR INFRARED.

4-54

Hoock [16], in analyzing Dugway test results, used the following average values to evaluate the EOSAEL model:

TABLE 4.10

EXTINCTION COEFFICIENTS (m^2/gm) FOR HC SMOKE

Visible	1.06 μm	3.44 μm	9.75 μm
3.3	0.98	0.11	0.044

Other spectral data by Salomon and Peterson [5] are given in Figures 4.15 and 4.16. As in the case of Red Phosphorous, Milham et al. [6] obtained laboratory values for HC smoke. These experimental data are presented in Figures 4.40 to 4.42.
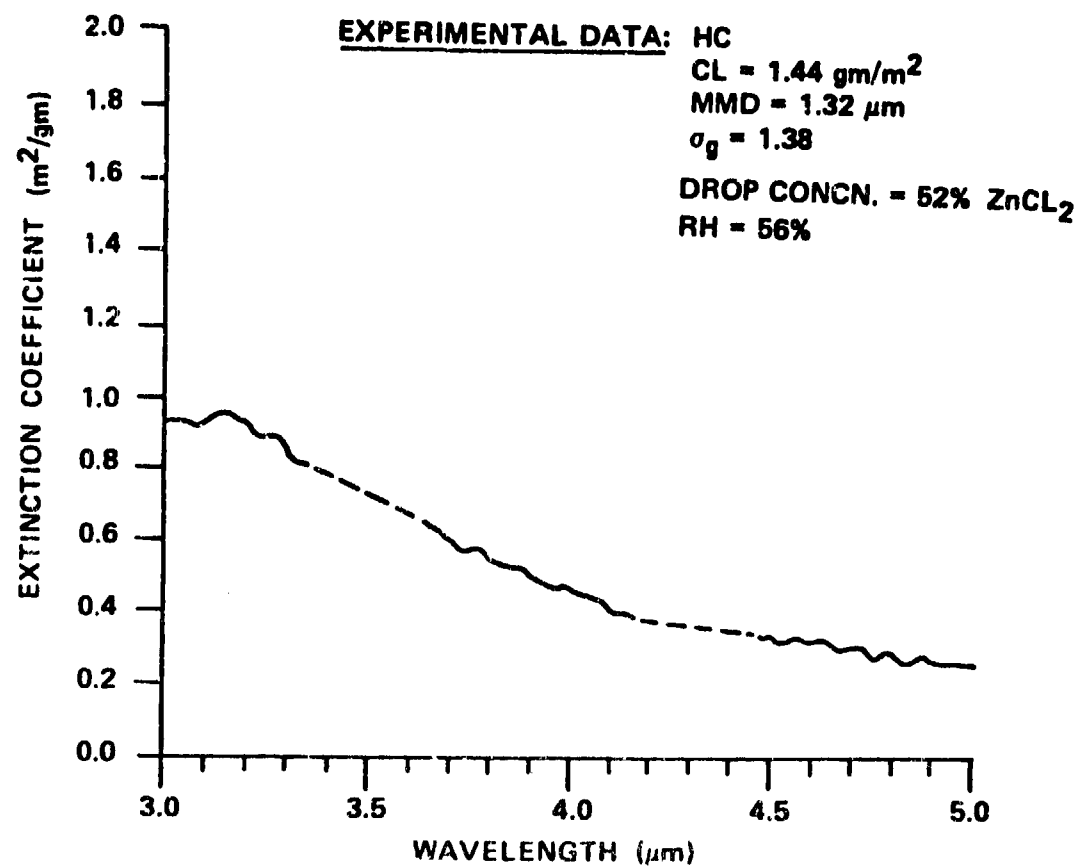
FIGURE 4.40   HC SMOKE FOR 3-5 μm REGION

EXPERIMENTAL DATA: HC
CL = 1.44 gm/m^2
MMD = 1.32 μm
σ_g = 1.38
DROP CONCN. = 52% $ZnCl_2$
RH = 56%
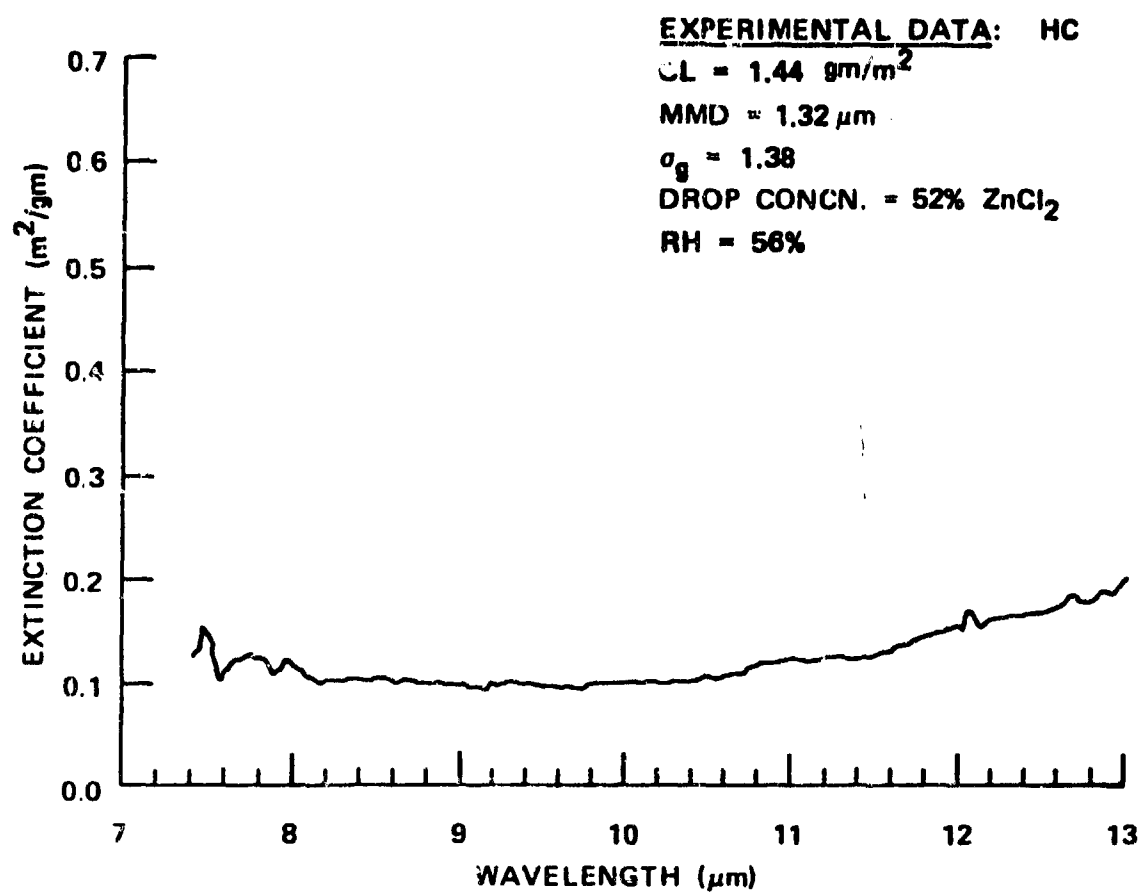
FIGURE 4.41   HC SMOKE FOR 7-13 μm REGION

4-57
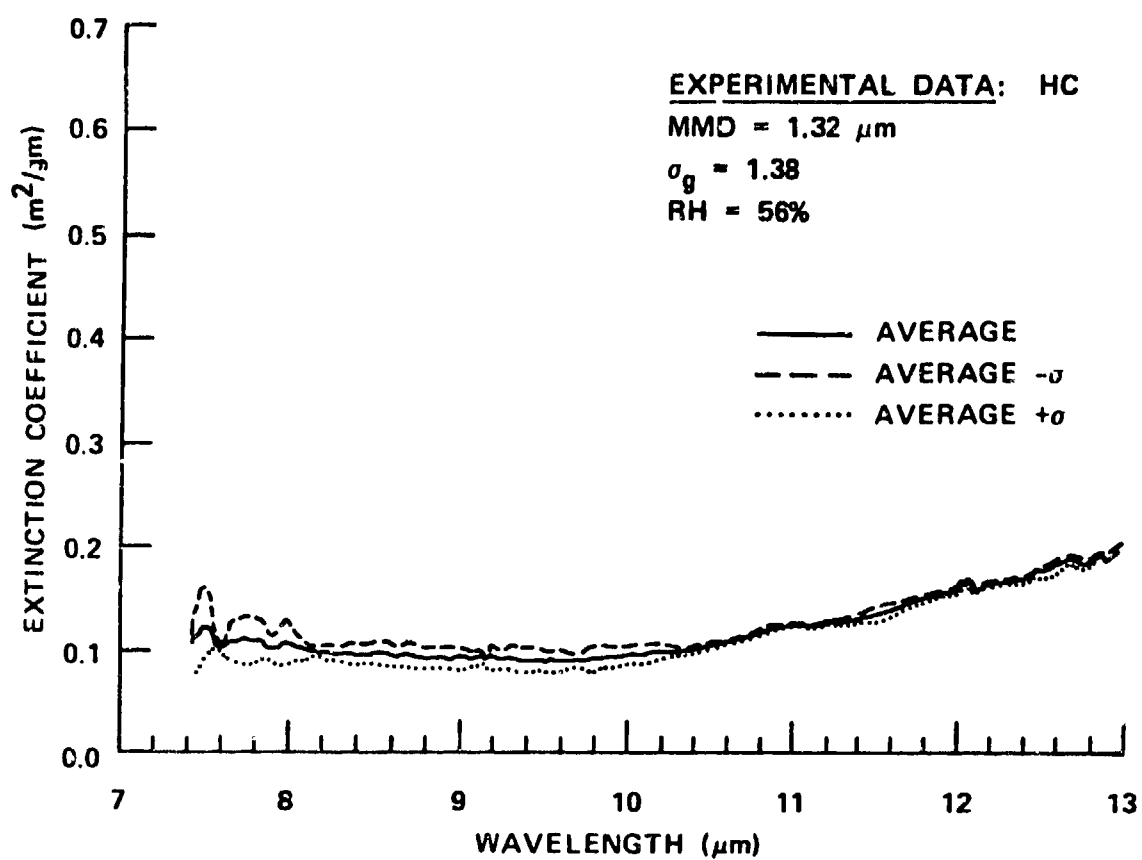
FIGURE 4.42   HC SMOKE FOR 7-13 μm REGION

4.1.2.1.5 Scattering Parameters

The scattering parameters on HC smoke were determined by Sztankay [12] & Sztankay et al. [15] and are given in Figure 4.43 and Tables 4.11 and 4.12.

4-59
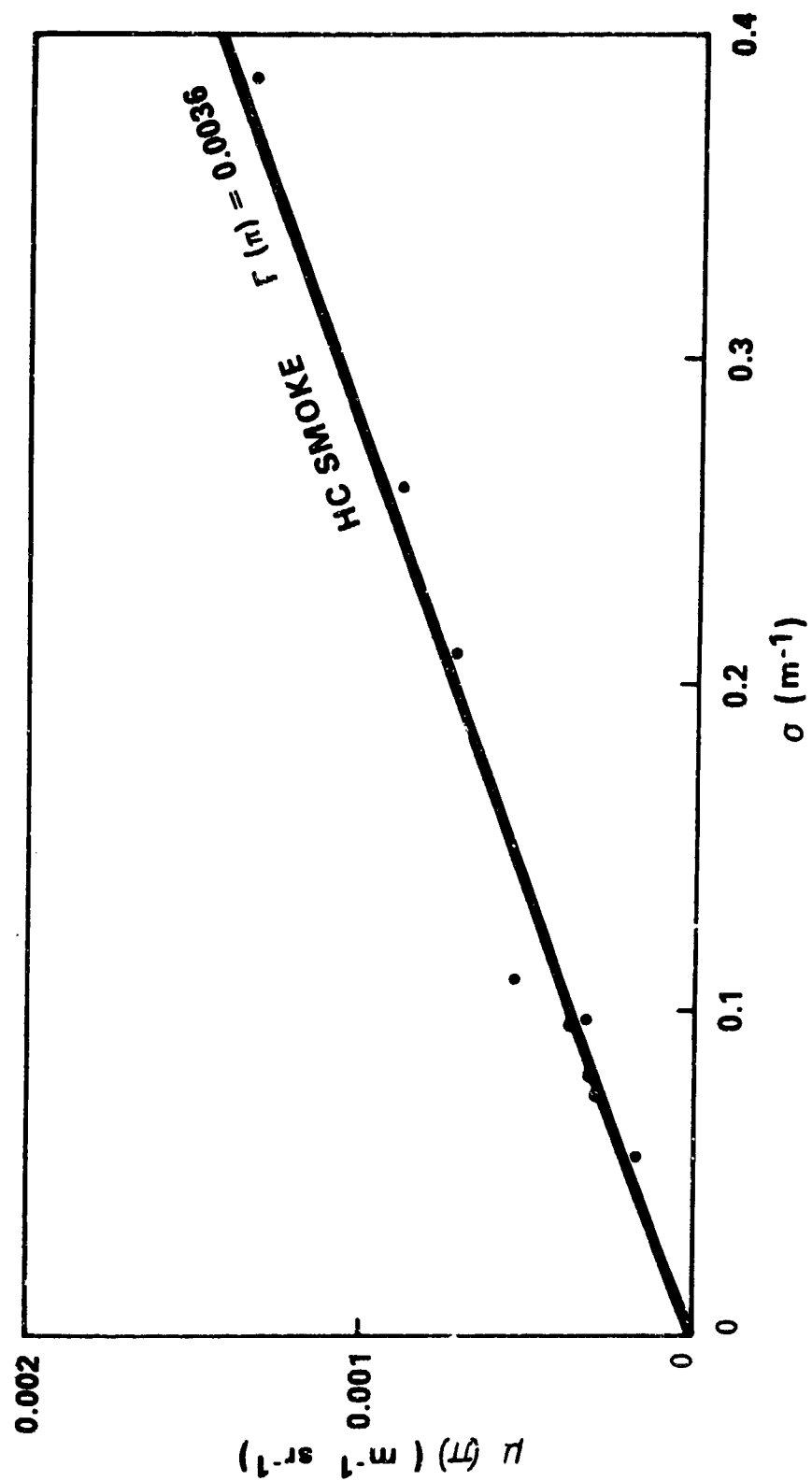
FIGURE 4.43 BACKSCATTER COEFFICIENT VS EXTINCTION COEFFICIENT PLOT, HC SMOKE (U).

TABLE 4.11

DUAL-CHANNEL NEPHELOMETER DATA

Run/smoke	σ (m^{-1})	$\mu(\pi)(m^{-1}sr^{-1})$	$F(\pi)$ (sr^{-1})	Average $F(\pi)$
1/HC (DPI-002-T33)	.05	.0004	.008	.011
	.015	.00032	.021	
	.195	.002	.010	
	.016	.0003	.019	
	.145	.0009	.006	
	.185	.0016	.007	
	.225	.0025	.011	
	.035	.00029	.008	

TABLE 4.12

NEPHELOMETER DATA FROM SMOKE WEEK II

Trial Number	Aerosol	Type Munition	$F(\pi)(sr^{-1})$
17	HC	155 mm canister	0.012

4-61

4.1.2.1.6 Dispersion Parameters

(Data on dispersion parameters for HC Smoke not available.)

4.1.3 DIESEL/FOG OIL SMOKE

In this section we present material on the generation of diesel/fog oil smoke and its physical and optical properties.

4.1.3.1 Diesel/Fog Oil Smoke Generators

In the following subsections, we describe the detailed properties of smoke which is generally characterized by diesel and fog oil.

4.1.3.1.1 Munition Characteristics

One method for the creation of diesel/fog oil smoke is the Vehicle Engine Exhaust Smoke System (VEESS), This system, designed for the M60 series Main Battle Tank, is an integral part of the engine, using the same fuel, the same supply system and the same electrical system. The VEESS components are used to inject diesel fuel into the hot exhaust manifold ahead of the turbo chargers. The fuel is flash vaporized and carried with the exhaust gases to the atmosphere where it is condensed producing a dense, billowing, white smoke cloud. The VEESS, described by Pribyl [17], is provided as a modification kit to the engine and the hull of M60A1/A3 Main Battle Tanks with AVDS-1790-2C and 2D engines. The VEESS is activated by the driver, and in so doing approximately one gallon of fuel per minute is equally divided through the right and left tube assemblers into the hot engine exhaust system just ahead of the turbochargers.

There are other methods of generating diesel/fog oil smoke. Two of them, described by Gordon [18], are the man-portable oil burner system and the high volume system. This device weighs 163 lbs. and produces fog oil smoke at a rate of 40 gallons per hour. The operation consists of a gasoline motor to provide shaft power to operate a pump for a fuel spray into the combustion chamber and

a smoke liquid spray into the vaporization section of the cylindrical chamber. The oil burner as a man-portable system weighs 50 to 60 lbs. and produces a 20 gallon per hour diesel fuel white smoke with a slight gray tint. The basic characteristics of candidate man portable smoke generators are given in Table 4.13.

Another system is the high volume smoke generator originally based on the use of a system on a vehicle-mounted helicopter engine. The helicopter system has an output of 600 to 700 gallons per hour, or 10 to 12 times that of one of the man-portable systems. A description of the characteristics of the jet engine is indicated in Table 4.14.

TABLE 4.13

CANDIDATE MAN PORTABLE SMOKE GENERATOR CONCEPTS

	M3A3	VALVELESS M3A3	ENGINE DRIVER OIL BURNER	AI-RESEARCH TO3 TURBINE
Fog oil rate, gph	40	40	60	60
Fuel rate, gph	3-4	3-4	4	4*
Total weight, no fuel, lbs	163	88*	50-70*	150*
Man transportable	Fair	Fair	Good	Fair
Power source				
Pulse jet combustor	X	X	---	---
Gasoline engine	---	---	X	---
Turbine	---	---	---	X
Diesel engine	---	---	X	---
Potential noise level, DB	High	High	Low	High
Capable of using diesel fuel	Yes	Yes	Yes	Yes
Capable of producing different liquid smokes	Yes	Yes	Yes	Yes
Capable of producing solid powder aerosols	No	No	Yes	Yes
Gasoline required for power supply engine	Yes	Yes	Yes	Possible
*Maintenance level	Moderate	Moderate	Low	Moderate
Capability of remote control	Poor	Poor	Good	Good
Simplicity of operation	Fair	Fair	Good	Fair
*Simplicity of design	Fair	Fair	Good	Fair
*Unit cost, 1000 units, $	2,600	2,600	2,600	9,000
*Cost to prototype, $(X1000)	240	450	200	2,000
*Time to prototype, mos.	19	24	18	18

*Estimated

TABLE 4.14

JET ENGINE (J33) CHARACTERISTICS IN SMOKE GENERATION AND SMOKE LIQUID PROPERTIES

ENGINE SPEED RPM	EXHAUST GAS TEMPERATURE °F	THEORETICAL MAXIMUM LIQUID VAPORIZATION			
		SGF-2 FOG OIL GPH	DIESEL FUEL GPH	PEG 200 GPH	WATER GPH
11,500	1,203	5,675	13,210	5,710	8,110
11,000	1,085	3,335	9,585	3,905	6,725
10,500	1,040	2,495	8,315	3,255	6,190
10,000	927	550	5,080	1,695	4,745
8,500	860	---	2,900	755	3,355
7,000	849	---	2,060	505	2,495
4,000	937	210	1,605	545	1,455
3,500	952	250	1,525	535	1,340
Mean Boil Pt, °F		700	510	590	212
Max Boil Pt, °F		870	650	770	212
Heat Req'd to vaporize BTU/gal		3,565	2,515	5,235	9,515

4.1.3.1.2 Yield Factor

The yield factor for fog oil according to Johnson and Forney [19] is:

$$YF = 1. \qquad (4.5)$$

4.1.3.1.3 Environmental Effects

Although there have been a number of laboratory and field measurements of fog oil, there are no references on the environmental aspects of fog oil.

4.1.3.1.4 Attenuation Coefficients

Vervier [8] presented data on various smokes. The data on Fog Oil are given in Figure 4.19. In addition, Milham et al. [6] have collected data on Fog Oil mass extinction coefficients under laboratory conditions. These are given in Figures 4.44 through 4.47 for Fog Oil smoke generated with an imbiber bead device and in Figures 4.48 through 4.52 for Fog Oil generated by the hot plate dissemination method.
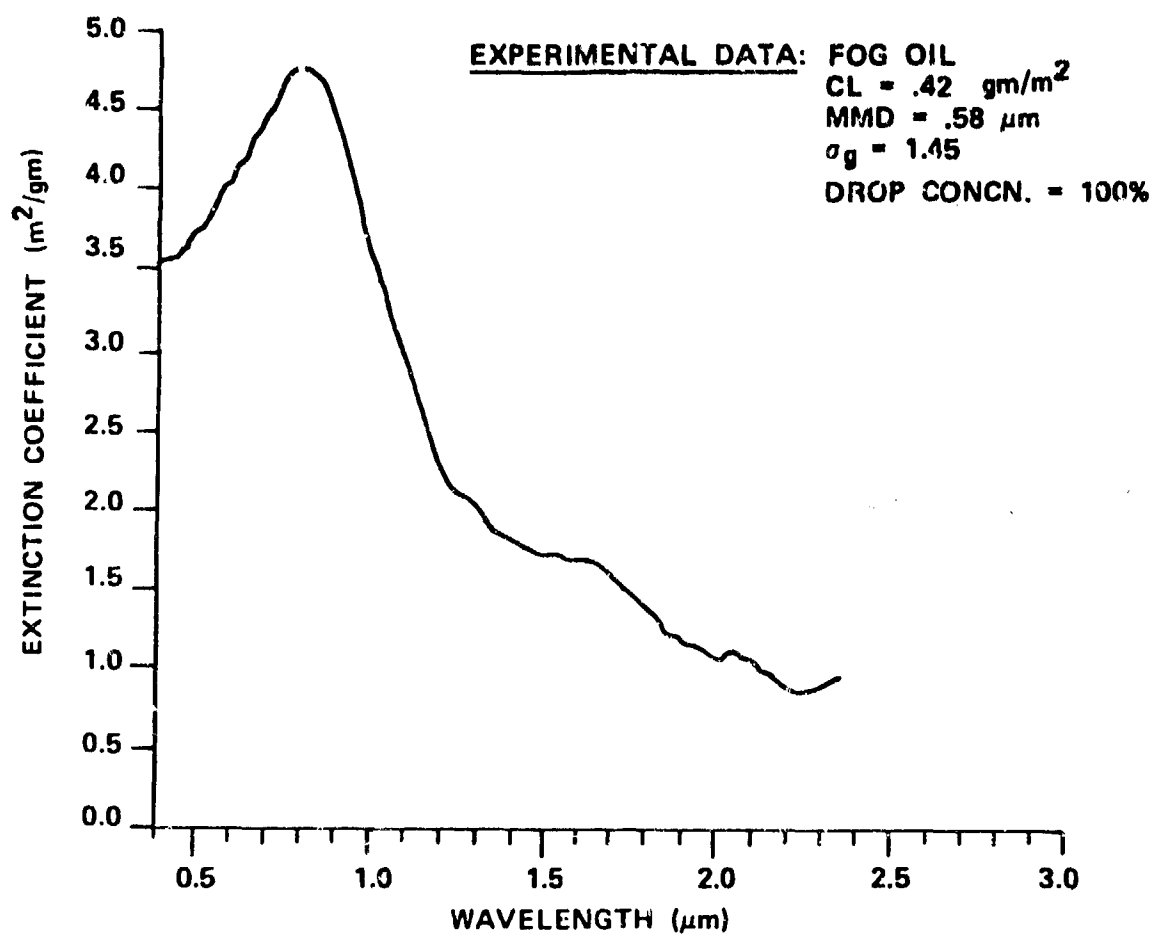
FIGURE 4.44   FOG OIL SMOKE 0.4-2.4 μm

EXPERIMENTAL DATA: FOG OIL
$CL = 2.28 \ gm/m^2$
$MMD = 0.58 \ \mu m$
$\sigma_g = 1.45$
DROP CONCN. = 100%
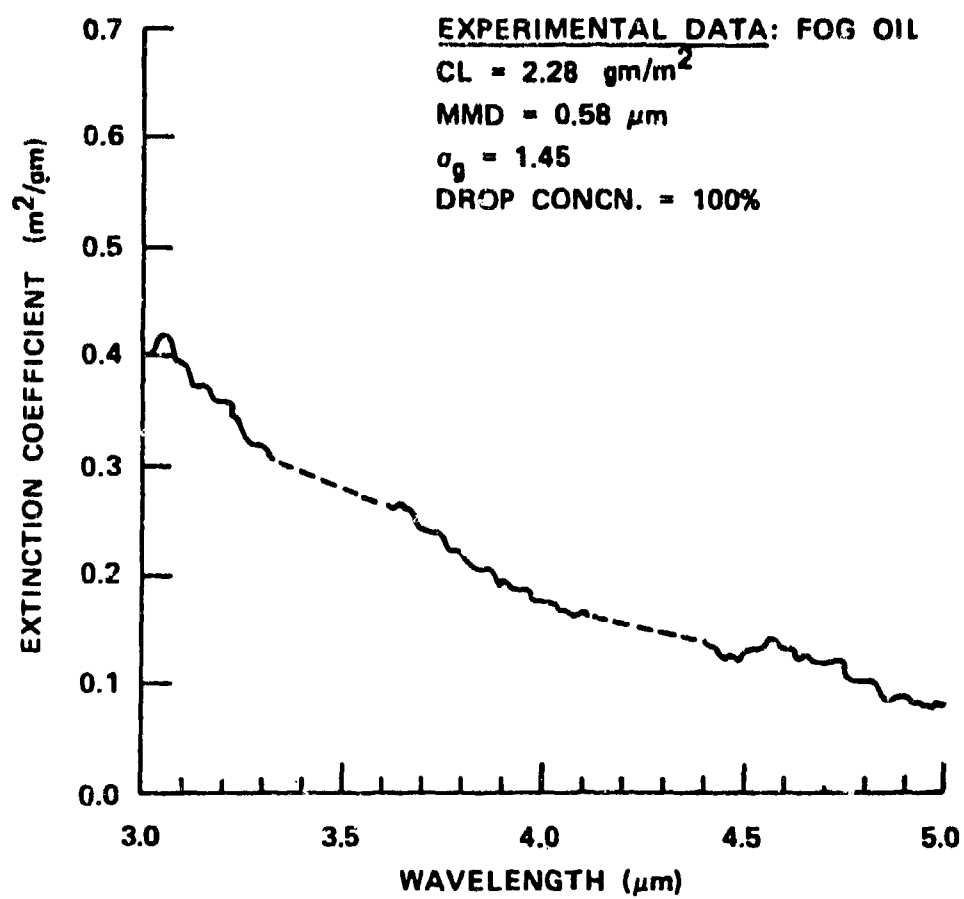
FIGURE 4.45   FOG OIL SMOKE 3-5 μm

EXPERIMENTAL DATA: FOG OIL
CL = 2.28 gm/m^2
MMD = 0.58 μm
σ_g = 1.45
DROP CONCN. = 100%
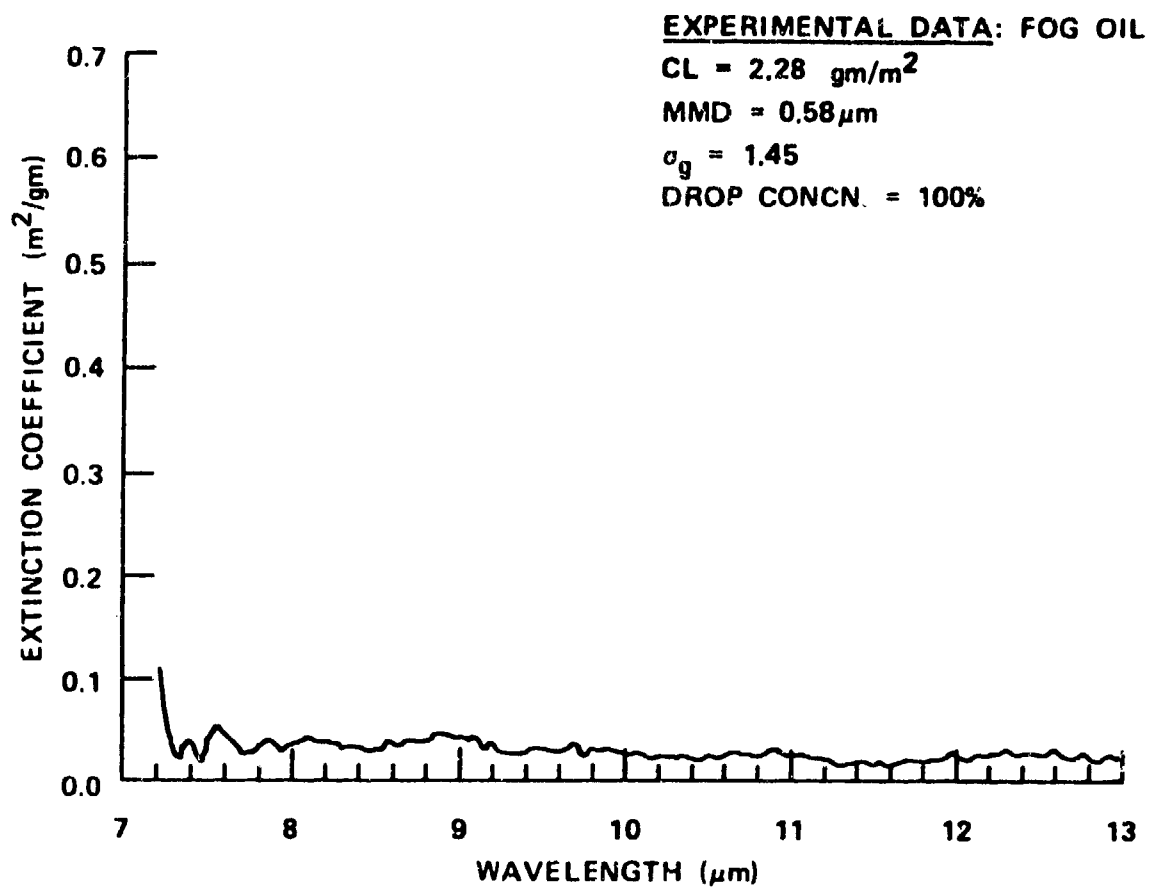
FIGURE 4.46   FOG OIL SMOKE 8-13 μm

4-72

EXPERIMENTAL DATA: FOG OIL

MMD = 0.58 μm

σ_g = 1.45

DROP CONCN. = 100%

————— AVERAGE

— — — AVERAGE -σ

·········· AVERAGE +σ
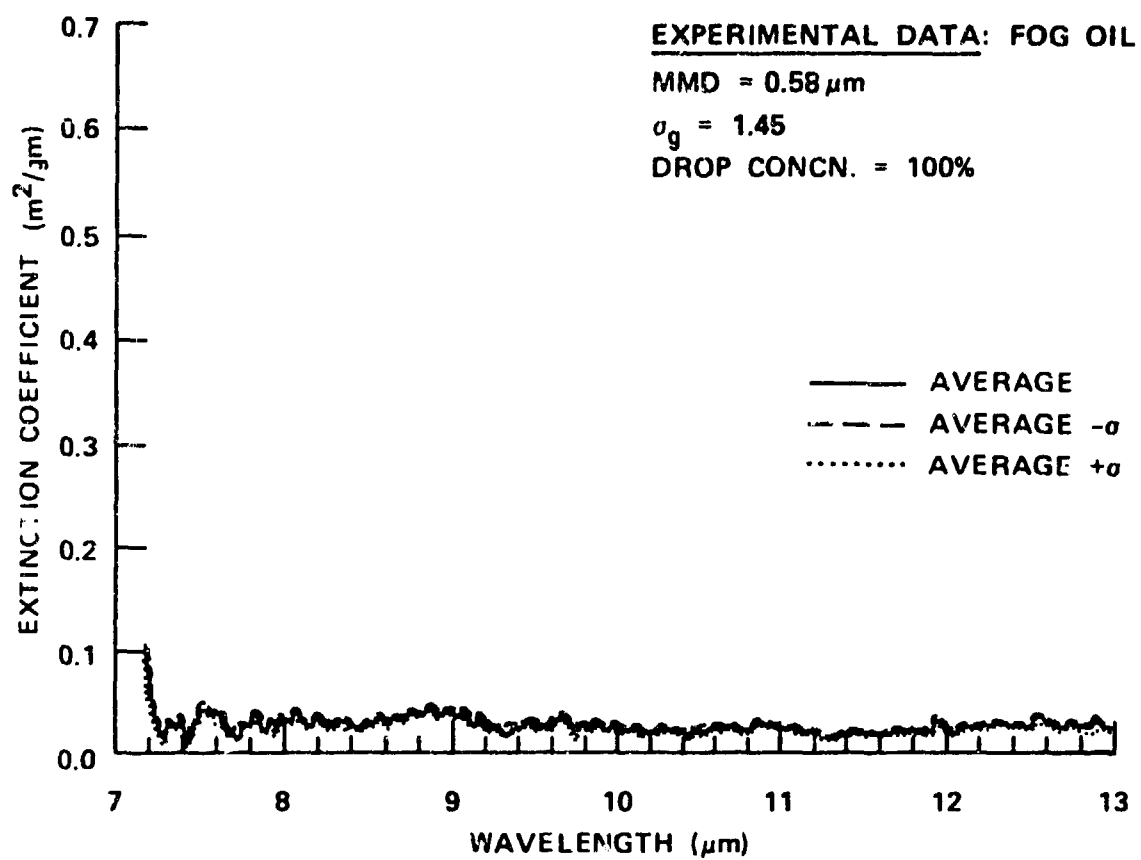
FIGURE 4.47   FOG OIL SMOKE 8-13 μm

4-73
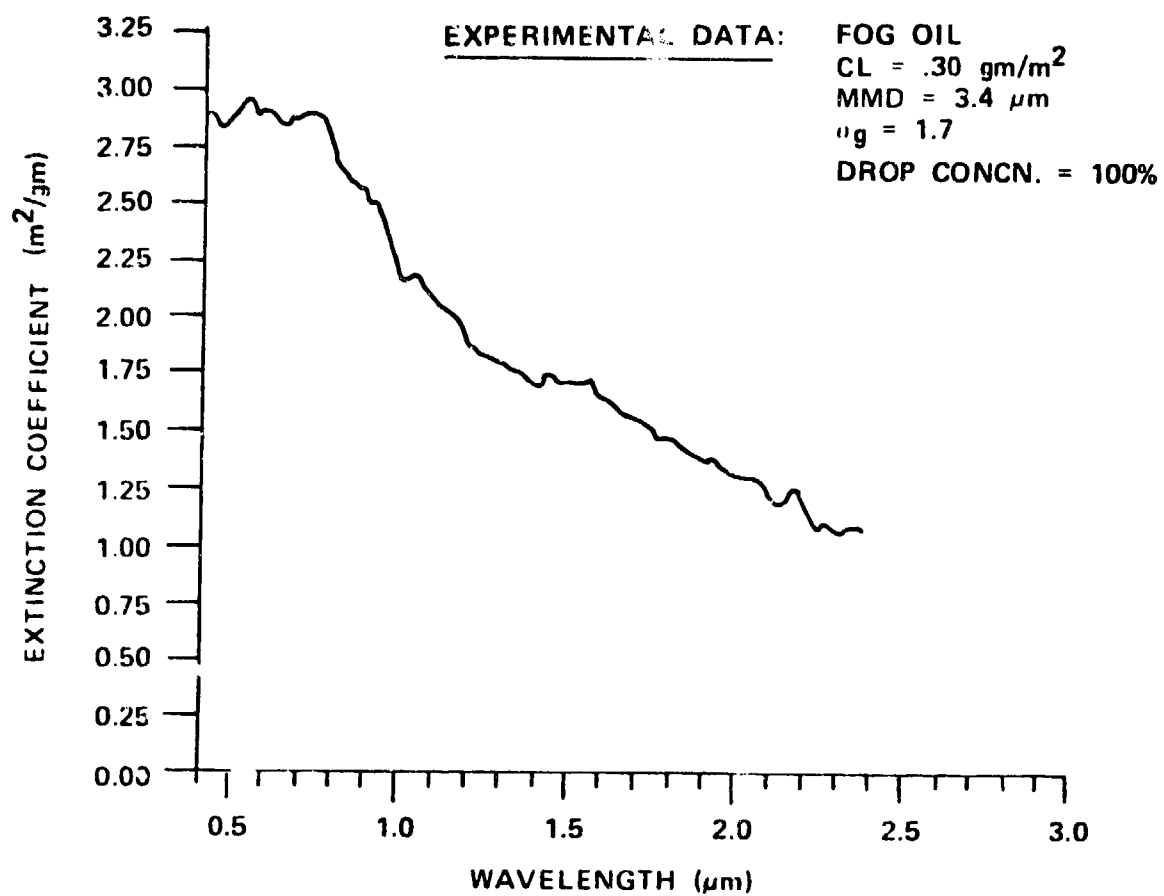
FIGURE 4.48   FOG OIL SMOKE 0.4 - 2.4 μm

4-74
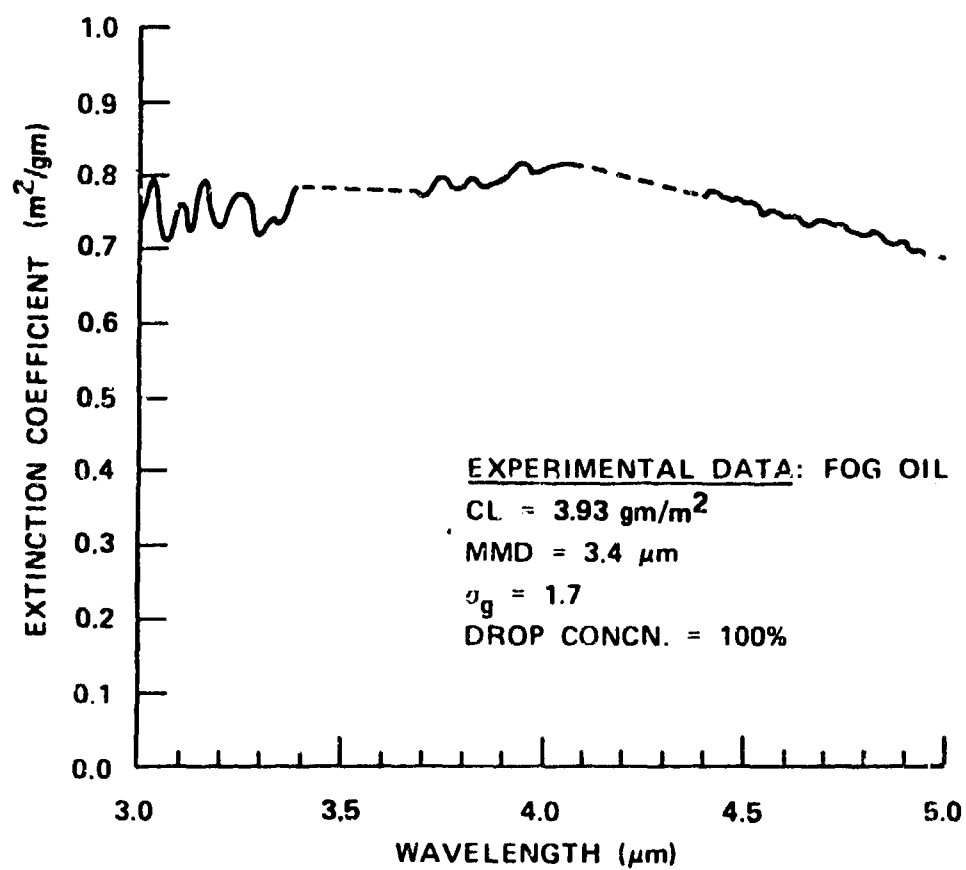
FIGURE 4.49   FOG OIL SMOKE 3-5 μm

The chart shows EXTINCTION COEFFICIENT (m²/gm) on the vertical axis versus WAVELENGTH (μm) on the horizontal axis, with the following annotations:

EXPERIMENTAL DATA: FOG OIL
CL = 3.93 gm/m²
MMD = 3.4 μm
σ_g = 1.7
DROP CONCN. = 100%
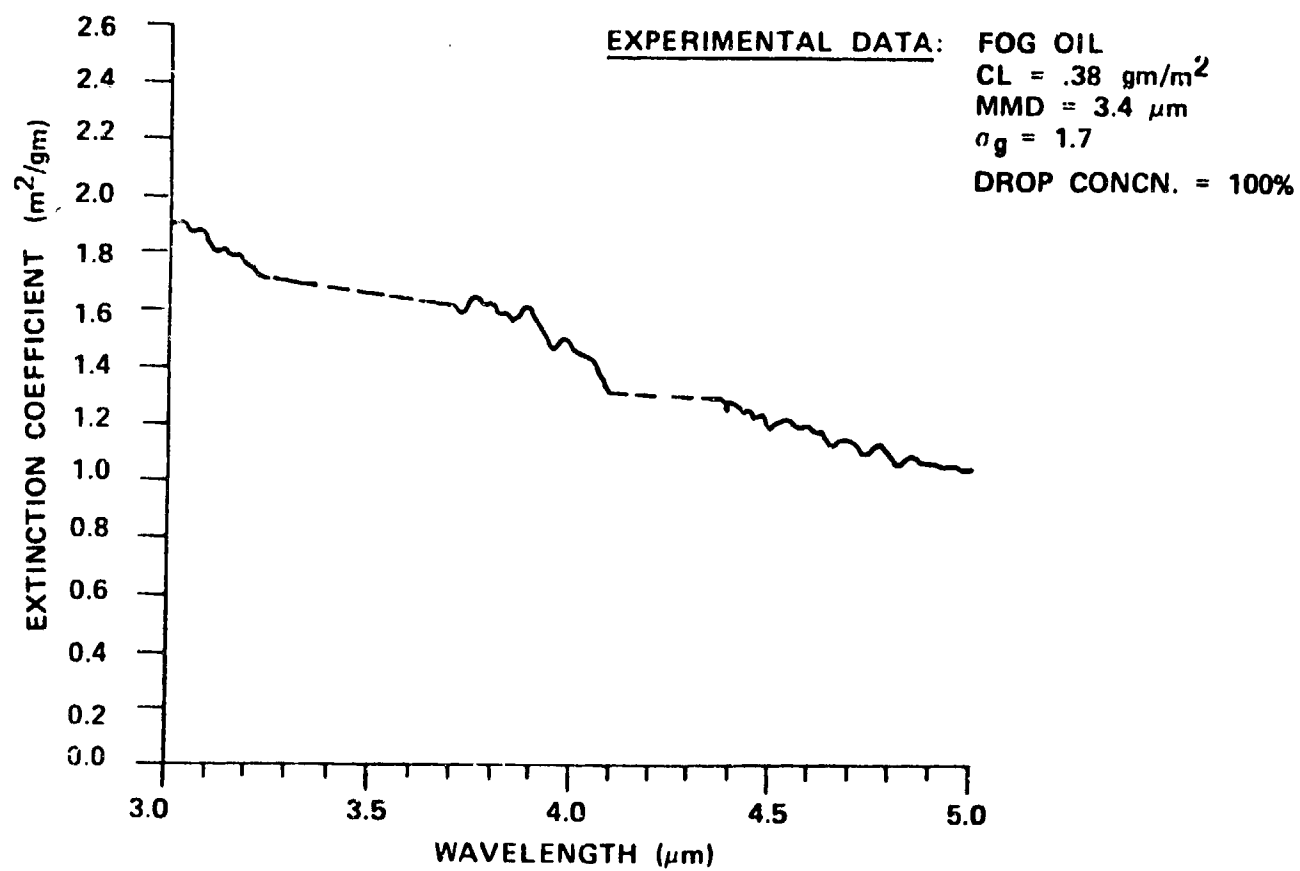
FIGURE 4.50   FOG OIL SMOKE 3-5 μm
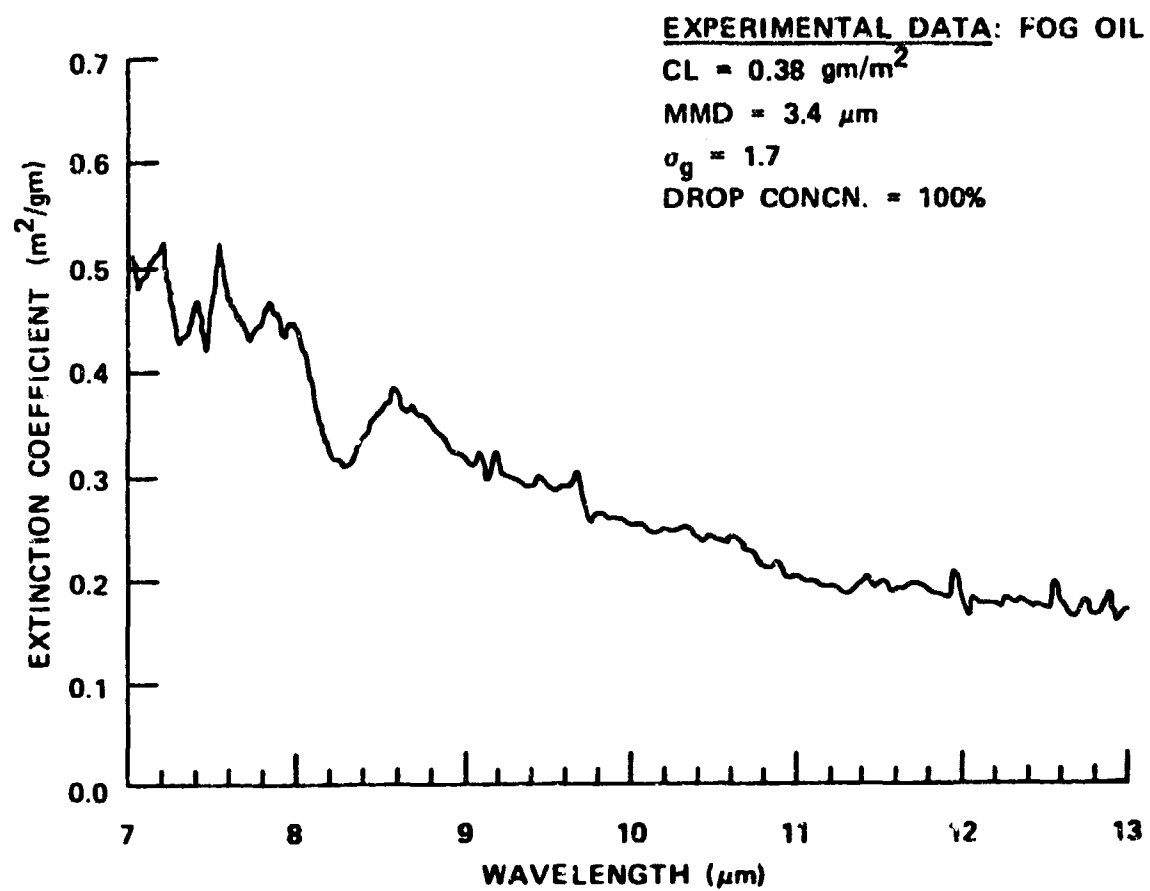
FIGURE 4.51   FOG OIL SMOKE 8-13 μm
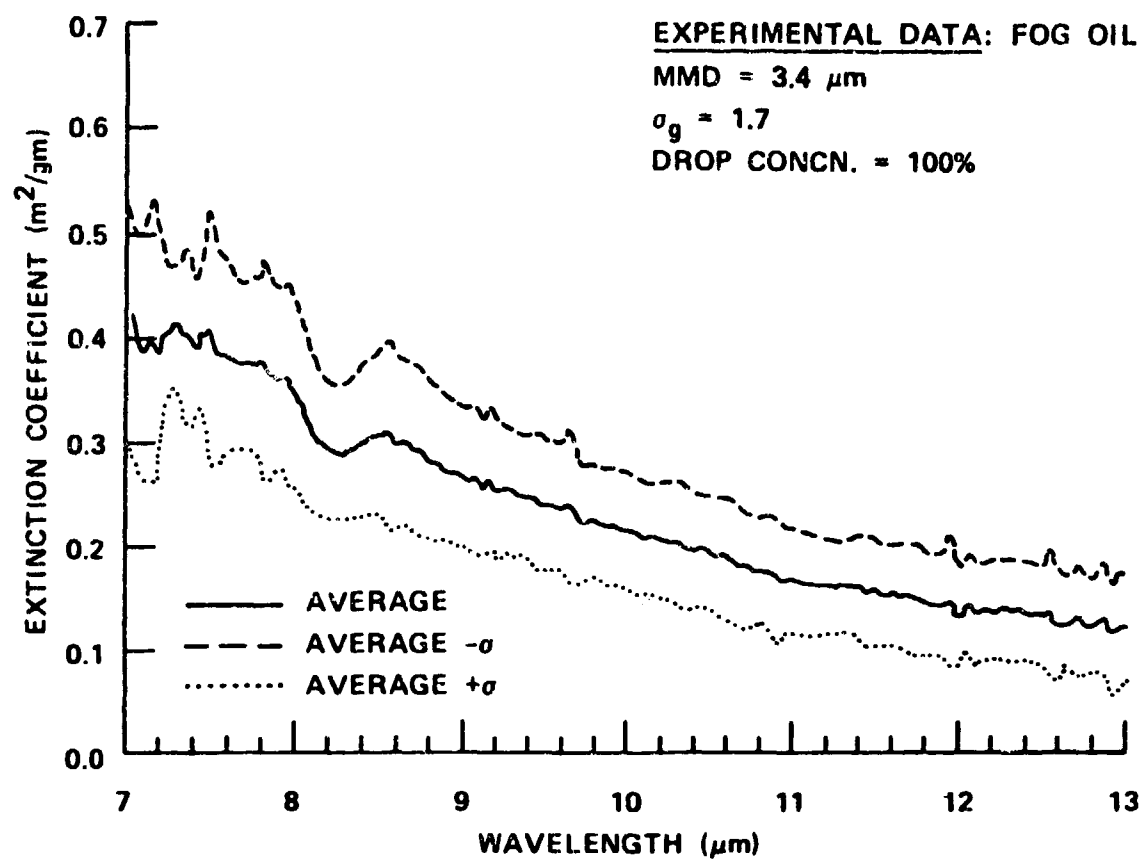
FIGURE 4.52   FOG OIL SMOKE 8-13 μm

4.1.3.1.5 Scattering Parameters

For Fog Oil the only data on scattering parameters are those of Smoke Week II by Sztankay et al. [15]. They are given in Table 4.15.

TABLE 4.15

PHASE FUNCTION AT 180° FOR FOG OIL

Trial Number	Aerosol	Type Munition	$F(\pi)(sr^{-1})$
16	Fog Oil	Generator	0.020
21	Fog Oil	Generator	0.030

4.1.3.1.6 Dispersion Parameters

(No data on dispersion parameters.)

4.1.3.1.7 Other Parameters

Some physical parameters have been measured for fog oil.
One of these is the particle number density size distribution.
The measured cumulative size distribution was done by Farmer [20]
and is illustrated in Figure 4.53 in which D_g is the geometric mean
diameter (μm) and σ_g is the logarithmic standard deviation. The
PMS device used was the Particle Measuring Systems' (SASF-100-HC).
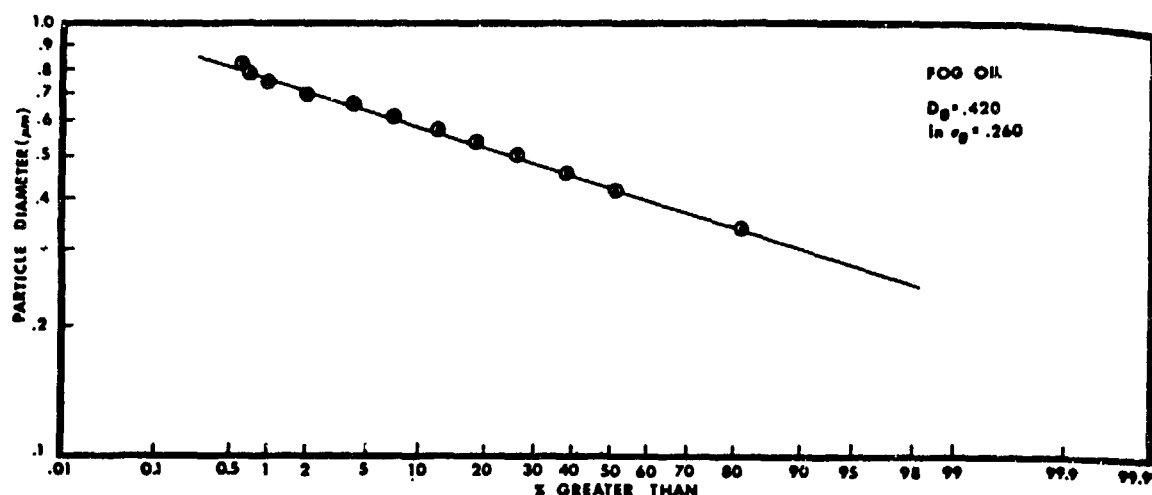
FIGURE 4.53 PMS MEASURED SIZE DISTRIBUTION FOR FOG OIL.

In a detailed theoretical analysis of the effects of high-
energy laser radiation on smoke, Gebhardt and Turner [21] present
information on the particular mass and number size distributions of
fog oil. These are illustrated in Figures 4.54 and 4.55. Fog oil
1 and fog oil 2 differ according to the standard deviation, the
median mass diameter, and the total particle density. These
properties are given in Table 4.16.

4-81
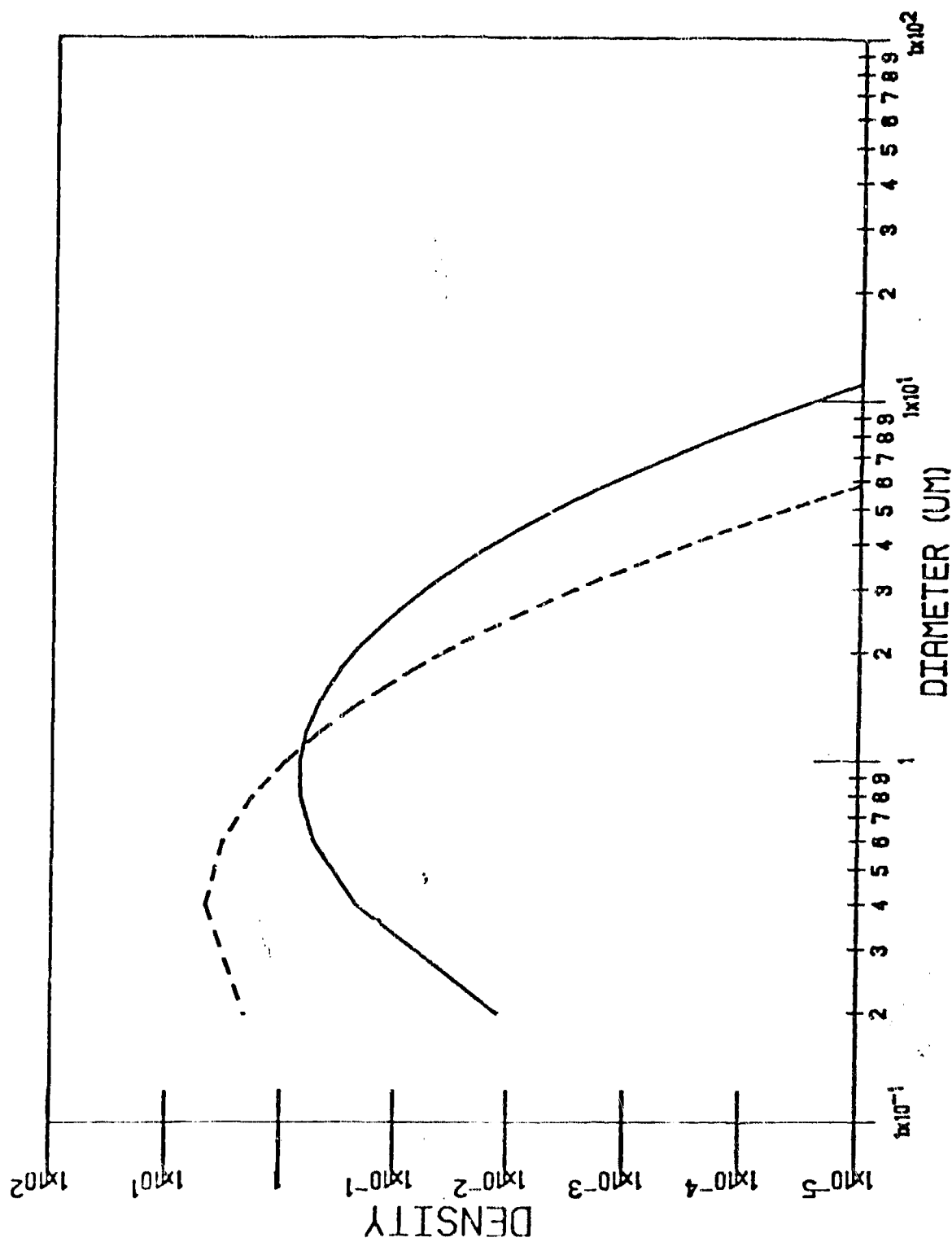
FIGURE 4.54 MASS DISTRIBUTION (G/CM^3-μM) (——) AND NUMBER DISTRIBUTION (#/CM^3-μM) (---) FOR FOG OIL 1.
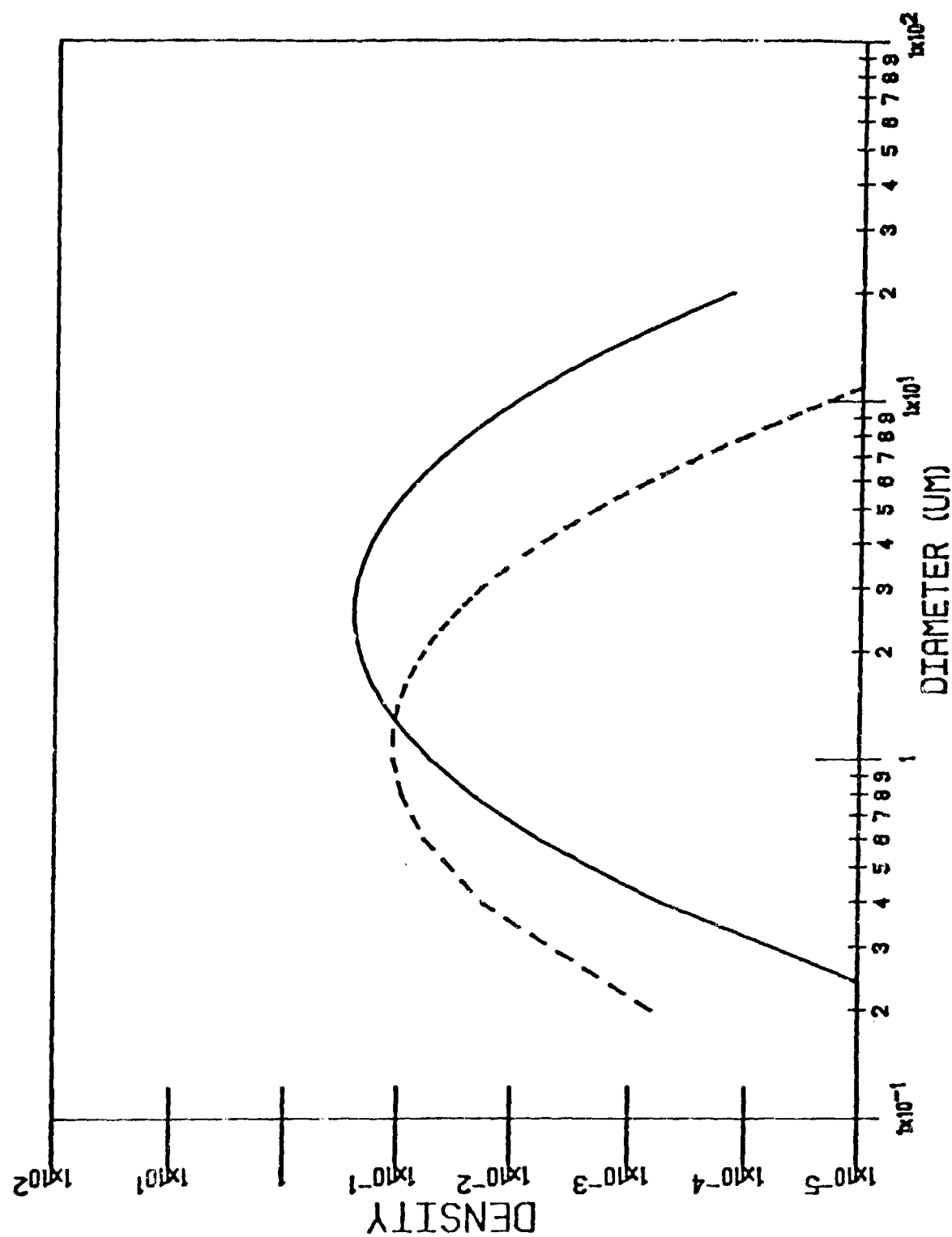
FIGURE 4.55 MASS DISTRIBUTION (G/CM^3–µM) (———) AND NUMBER DISTRIBUTION (#/CM^3–µM) (– – –) FOR FOG OIL 2.

TABLE 4.16

MASS DISTRIBUTION DATA FOR THREE SPECIFIC CASES

	Standard Deviation	Median Mass Diameter D_m (μm)	Particle Density ρ (g/m^3)
Red Phosphorous	1.7	1.2	1.45
Fog Oil 1	1.45	0.58	0.895
Fog Oil 2	1.7	3.4	0.895

4.1.4   DEVELOPMENTAL SMOKES

In this section we present information on smokes which are under development.

4.1.4.1   Deployment Characteristics

4.1.4.1.1 Yield Factor

(Information not available at present time.)

4.1.4.1.2 Dispersion

(No data available)

4.1.4.2 E-O Characteristics

(See Classified Version)

4.1.5   THREAT SMOKES

In this section we present data on the physical and optical properties of threat smokes.

4.1.5.1   Munition Characteristics

(No data available)

4.1.5.2   Yield Factor

(No data available)

4.1.5.3   Environmental Effects

(Data not available at this time)

4.1.5.4 - 4.1.5.7 Other Parameters

(See Classified Version)

REFERENCES FOR SECTION 4

1.   _Ammunition Handbook_, Dept. of the Army Field Manual FM 9-13
      Headquarters, Dept. of the Army, March 1973.

2.   T.J. Dolce and D.F. Metz, An Analysis of the Smoke Cloud Data
      from August 1975 Jefferson Proving Ground Smoke Test, AMSAA
      Technical Report 301, Sept., 1977.

3.   R. Zirkind, A Battlefield Obscuration Model (Smoke and Dust)
      Final Report, 524-02-79-CR, General Research Corporation,
      Od., 1979.

4.   R.H. Frickel, G.O. Rubel, E.W. Stuebing, Relative Humidity
      Dependence of the Infrared Extinction by Aerosol Clouds of
      Phosphoric Acid, Proceedings of the Smoke/Obscurants Symposium
      III, OPM Smoke/Obscurants Technical Report, DRCPM-SMK-T-002-
      79, Vol. II, April, 1979.

5.   L.L. Salomon and E. Peterson, Testing of Smoke Munitions
      and Submunitions, Proceedings of the Smoke Symposium-II,
      OPM Smoke/Obscurants, Technical Report, DRCPM-SMK-T 003-78,
      April, 1978.

6.   M. Milham et al. ED-SP-77002, ARCSL-TR-77067, Chemical
      Systems Laboratory, Aberdeen Proving Ground, MD.

7.   H.R. Carlon, D.H. Anderson, M.E. Milham, T.L. Tarnove,
      R.H. Frickel, and I. Sindoni, Appl. Optics 16, June 1977.

8.   J. Vervier, Update on the Spectral Properties of Inventory
      and Candidate Smokes, Proceedings of the Smoke Symposium-II,
      OPM/Obscurants, Technical Report, DRCMP-SMK-T-003-78, April,
      1978.

9.   E.W. Stuebing, Deviations from Beer's Law Which Sometimes
      Prevent Defining a Single Overall Extinction Coefficient for
      a Smoke in Each Atmospheric Window, Proceedings of the
      Smoke Symposium-II, OPM/Obscurants, Technical Report, DRCPM-
      SMK-T-003-78, April, 1978.

10.   G.C. Holst and M. Milham, Examination of the Correlation
      Between Laboratory and Field Smoke Extinction Data, Proceedings
      of the Smoke/Obscurants Symposium III, OPM Smoke/Obscurants
      Technical Report, DRCPM-SMK-T-002-79, Vol. II, April, 1979.

11.   R.N. Dubinsky and R.J. Levesque, Attenuation of IR and
      Visible Radiation by Common Military Smokes, Proceedings of
      the Smoke/Obscurants Symposium III, OPM Smoke/Obscurants,
      Technical Report, DRCPM-SMK-T-002-79, Vol. II, April, 1979.

12. Z.G. Sztankay, Measurement of the Localized Optical Characteristics of Natural Aerosols, Smoke, and Dust, Proceedings of the Smoke Symposium-II, OPM Smoke/Obscurants Technical Report, DRCPM-SMK-T-003-78, April, 1978.

13. D. Deirmendjian, Electromagnetic Scattering on Spherical Polydispersions, American Elsevier, 1969.

14. W.M. Farmer, An Evaluation of Data Obtained During the H^3S Test, Proceedings of the Smoke/Obscurants Symposium IV, OPM Smoke/Obscurants Technical Report, DRCPM-SMK-T-001-80, Vol. I, April, 1980.

15. Z.G. Sztankay, J. Nemarich, J. Griffin, Backscatter and Extinction Measurements at Smoke Week 2, Proceedings of the Smoke/Obscurants Symposium III, OPM Smoke/Obscurants Technical Report, DRCPM-SMK-T-002-79, Vol. II, April, 1979.

16. D.W. Hoock, Analysis of CL Profiles from Inventory Smoke Munitions Test (Phase II A), Proceedings of the Smoke/Obscurants Symposium IV, OPM Smoke/Obscurants Technical Report, DRCPM-SMK-T-001-80, Vol. I, April, 1980.

17. M. J. Pribyl, VEESS - Techniques and Application, Proceedings of the Smoke/Obscurants Symposium III, OPM Smoke/Obscurants Technical Report DRCPM-SMK-T-002-79, Vol. II, April 1979.

18. M. G. Gordon, Large Area Smoke Screening System Concepts, Proceedings of the Smoke/Obscurants Symposium III, OPM Smoke/Obscurants Technical Report DRCPM-SMK-T-002-79, Vol. II, April 1979.

19. M. C. Johnson and P. D. Forney, The Effectiveness of Obscuring Smokes, ORG Edgewood Arsenal, 1972.

20. W. M. Farmer, A Comparison of Data from Particle Size Analysis Used to Measure Hygroscopic Smokes, Proceedings of the Smoke/Obscurants Symposium IV, OPM Smoke/Obscurants Technical Report, DRCPM-SMK-T-001-80, Vol. , April 1980.

21. F. G. Gebhardt and R. E. Turner, Nonlinear Effects of Laser Irradiated Smoke Particles, Chemical Systems Laboratory Contractor Report ARCSL-CR-80039, Final Report, April, 1980.

4-93

SECTION 5

UNINTENTIONALLY INDUCED BATTLEFIELD ENVIRONMENTAL CONDITIONS

5.1 MUNITION EXPLOSION CONDITIONS

Exploding munitions, including primarily but not limited to artillery shells, are a source of several quantities which can degrade E-O systems performance on the battlefield. Dust and debris are raised by projectile impact and by the shock wave. The chemical process of detonation generates heat, which causes turbulence, adding to the momentum transfers resulting from the shock wave. Gases and particulates produced by the chemical decomposition of an explosive also have an effect on propagation of electromagnetic radiation. Each of these phenomena is treated in the following sections of the Handbook.

5.1.1 DUST FROM EXPLOSIONS

Of all obscuration conditions resulting from munition events, dust clouds are the most intensively measured and analyzed. Data from Smoke Weeks I and II, DIRT-I, and the Grafenwöhr test series conducted by the U.S. Army provide information about these dust clouds in realistic battlefield environments. At least four models, of varying levels of complexity, have been developed to predict obscuration due to dust clouds from munition events [1,2,3,4]. These models for the most part share a common division into phases of the history of a munition dust cloud: dust cloud loading, buoyant rise or stabilization of the dust cloud in the atmosphere, wind-driven or turbulent diffusion of the resulting plume, and prediction of optical properties. In the following sections we will attempt to develop a coherent picture of munition dust cloud phenomenology based on these models and measurements.

5.1.1.1 Yield Factors

An almost universal approach to determining the dust yield of an explosion is based on measurements of the crater volume.

The dust yield Y is assumed to be given by:

$$Y = \rho V, \qquad (5-1)$$

where ρ is average soil density and V is measured crater volume.

Around 1960, a project was undertaken by the U.S. Army Waterways Experiment Station to compile and analyze available crater data. The results of this comprehensive survey appeared in 1960 and 1961 [5,6]. Their data base consisted of nearly 1800 events and spanned a broad range of explosive types and local conditions. We will summarize their results and compare them for consistency with more recent data, notably crater measurements from the DIRT-I test series [7].

The Waterways analysis showed that the most fundamental parameters influencing crater size were charge weight W (in kg. of TNT), charge depth Z at the time of the explosion (in meters), and the soil type.

Charge weight for explosives other than TNT can be scaled to an equivalent weight of TNT, using the constants in Table 5.1 on page 5-8 from reference 8. Rather than quantifying soil hardness, the Waterways analysis yielded correlations of crater volume with W and Z for several qualitative soil types.

The fundamental scaling laws developed in [6] express the depth and radius of a crater, for a fixed soil type and burst depth, as a function of TNT weight, W:

$$d = k_d W^{3/10}$$

$$r = k_r W^{1/3}. \qquad (5-2)$$

5-2

Here k_r and k_d are constants, and d and r are crater depth and radius respectively.

Figures 5.1 and 5.2 adapted from [6] summarize the appropriate values for k_d and k_r for various soil types and burst depths. It should be noted that the abscissa λ_c is a scaled burst depth, given by

$$\lambda_c = h/W^{1/3} \qquad\qquad (5-3)$$

where h is the burst depth in feet (h>0 for burst above ground).

Crater volume can be obtained from equations (5-2) by assuming some shape factor for the crater. In [1] a cone of radius r and depth d is used; an ellipsoid with semi-axes (r,r,d) probably also gives reasonable results. In any case crater volume scales as

$$V \approx k_v W, \qquad\qquad (5-4)$$

where k_v is a constant depending on depth of burst and soil type.

Two questions arise concerning the applicability of the Waterways scaling laws (5-2):

1. What is the difference in cratering efficiency between cased and bare charges?

2. What is the difference in cratering efficiency between impacting and static rounds?

The discussion in [6] indicates that the data were not partitioned to reflect these distinct types of events.
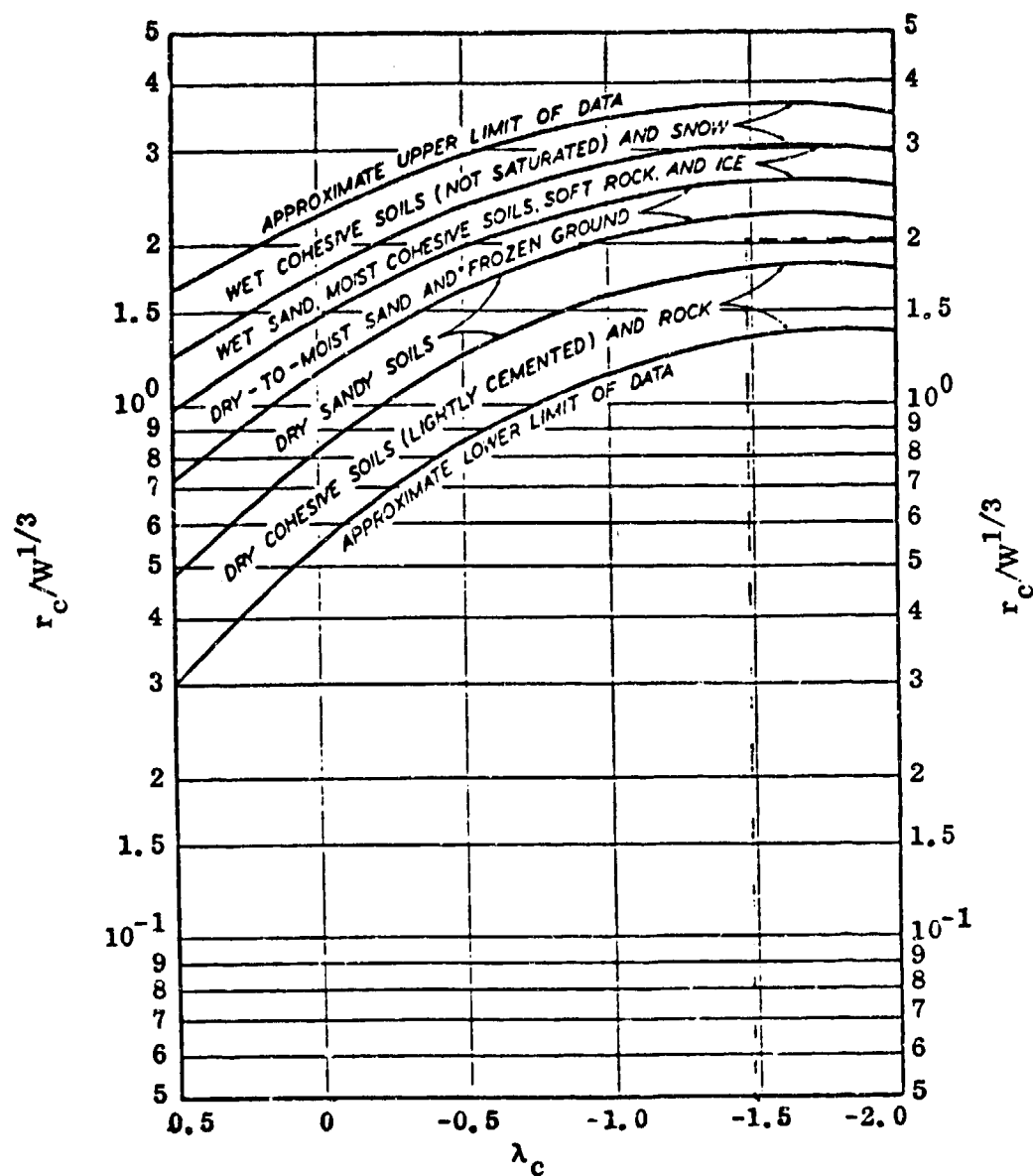
FIGURE 5.1.　MONOGRAPH FOR DETERMINING THE APPARENT
CRATER RADIUS r_c IN VARIOUS MEDIA
(Reference 6).　HERE, $\lambda_c = hW^{-1/3}$, WHERE
H IS EXPLOSION DEPTH IN FEET, AND W IS
THE CHARGE WEIGHT IN POUNDS OF TNT.
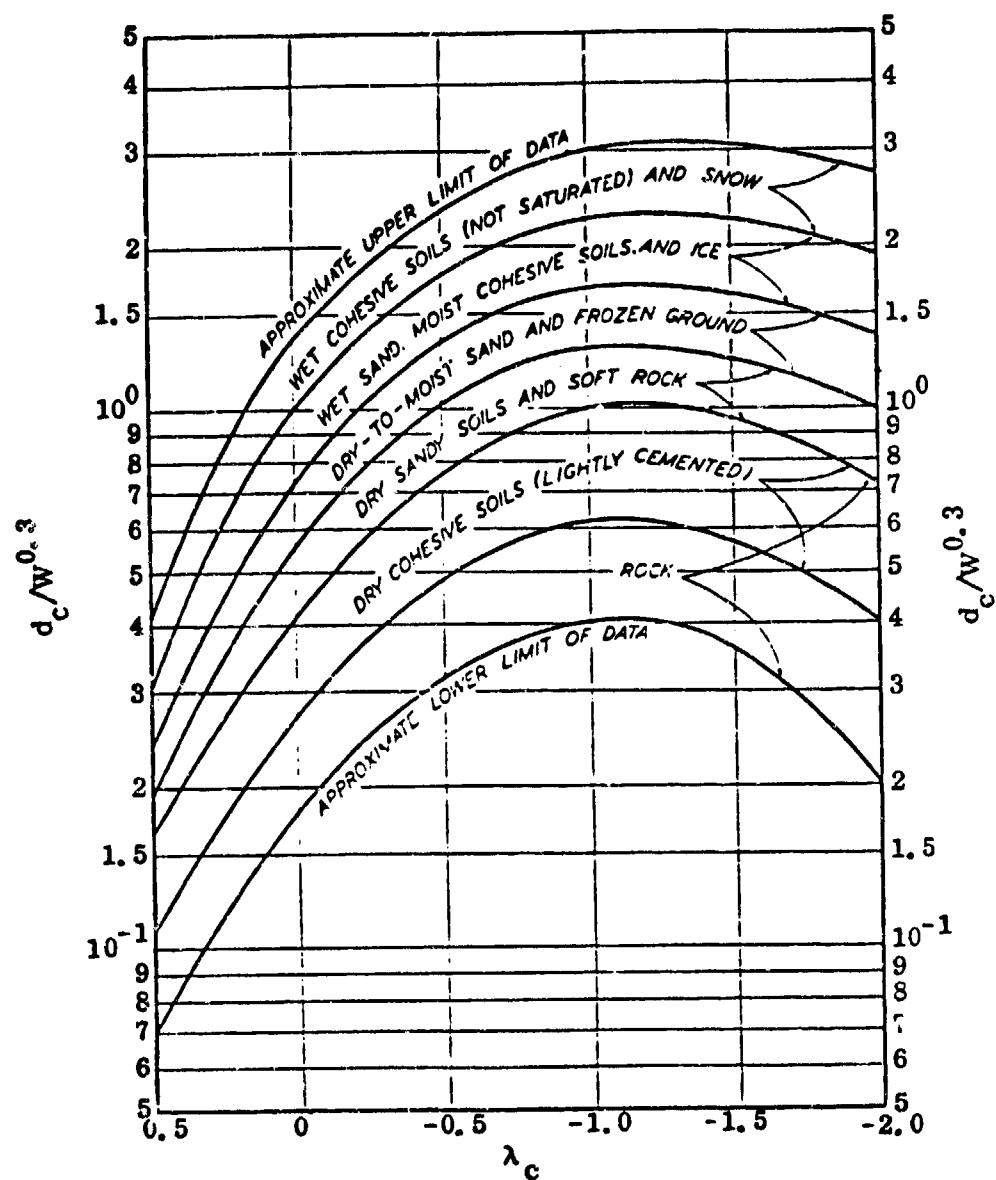
FIGURE 5.2. NOMOGRAPH USED FOR DETERMINING THE APPARENT
CRATER DEPTH d_c IN VARIOUS MEDIA. AGAIN
$\lambda_c = hW^{-1/3}$.

5-5

Measurements of crater volume have shown that cased shells yield bigger craters than bare charges of the same charge weight because of fragmentation effects. Thus the Waterways scaling laws can be regarded as somewhat overpredicting crater dimensions for bare charges and underpredicting the volume of crater due to cased shells. In [1] it is recommended that the weight of a cased charge be scaled by 60% to account for energy going into motion of shell fragments. The above discussion shows that this approach is incorrect. In addition, in reference 8, 90% of the available energy of an explosion is said to be converted into motion of shell fragments and explosion products.

With regards to question 2 above, the surprising observation made in [9] is that craters produced at DIRT-I by impacting charges were somewhat smaller than those produced by static detonations. This is explained when one takes into account the fact that the static charges were buried. Thus the Waterways formulas can be regarded as slightly underpredicting the crater size for an impacting charge and overpredicting the volume due to an equivalent static charge. In [6] a 30% uncertainty is stated for Figures 5.1 and 5.2 for crater dimension in soil, so that underprediction or overprediction using equation (5.2) is hopefully slight. In any case it seems that at least that much uncertainty could arise just from considering the variability between conditions for individual events.

The results from DIRT-I [9] yield the relationship

$$dr^2 \approx .056W \qquad (5-5)$$

for surface bursts at WSMR, on days immediately following rainstorms. (Units here are kg. for W and meters for d and r.) This is consistent with the WES data for dry-to-moist sand, which shows

5-6

$$.049 \; \tilde{<} \; \frac{dr^2}{W} \; \tilde{<} \; .094. \qquad (5\text{-}6)$$

Vortman gives a scaling law, reported in [2]:

$$V = .067W^{1.11} \qquad (5\text{-}7)$$

for surface bursts in dry lake playa in Nevada. This too is reasonably consistent with the WES data.

Table 5.2 from [3] is a tabulation of densities for several common soil types. This table, plus the Waterways data, assuming a conical or ellipsoidal shape for the crater, suffices to give estimates of initial dust cloud mass loading which are reasonable to within scatter of currently available measurements.

5.1.1.2 Environmental Effects (Hygroscopicity, etc.)

The effects of the environment on the dust cloud generated by a munition explosion influence the dynamic evolution of the cloud particle size distribution.

Particle size data were collected at DIRT-I from ground samples and airborne samples. No thorough analysis has been presented to relate ground to airborne PSD's before and during a munition event, and the extent to which the airborne PSD mimics the ground sample is not known, or if the explosion fundamentally alters the shape of the dust size distributions.

Gravitational settling has an effect on the airborne PSD's, reducing the number of particles on the large end of the distribution. References 1 and 2 present detailed solutions of the cloud rise and diffusion equations which include terms for large particle fall-out.

5-7

The effect of sod cover is to reduce the amount of airborne material [12]. As for the effect of soil moisture, it is probable that initially the dust is dried out by the thermal

TABLE 5.1

TNT EQUIVALENT WEIGHTS FOR CRATER
VOLUME COMPUTATIONS

TNT	1.0
Composition B (60% RDX, 40% TNT)	1.13
Pentolite (50% TNT, 50% PETN)	1.16
Explosive D (Ammonium Picrate)	0.85
Torpex II (Aluminized RDX-TNT mixture)	1.23
HBX-3 (Aluminized RDX-TNT mixture)	1.16

TABLE 5.2

SOIL DENSITIES FOR DUST CLOUD MASS
CALCULATION (in g/cc)

Quartz	2.67
Clay	2.0
Loose, Dry Loam	1.0
Wet Loam	1.8
Sandy Loam	1.5
Loose, Fine Sand	0.7
Wet, Compact Sand	1.8
Light Soil, Grass Roots	0.3-0.5
Rock Materials	~2.4

output of the explosive, but then is free to act hygroscopically in air.

Further effects of the atmospheric environment on a munition dust cloud will be discussed in Section 5.1.1.5, on dispersion parameters.

5.1.1.3   Attenuation Coefficients

ASL reports by Duncan and Seagraves [10] and McMillan, Rogers, Platt, Guillory, Gallagher, and Snider [11] present attenuation coefficients due to munitions events at recent Army field tests. Reference 10 considers IR and visible wavelengths while reference 11 treats the millimeter wavelength region. Both of these sources report their data in terms of the amount of time after a munition event for which transmittance remains at or below a fixed level.

Table 5.3 from [11] shows peak attenuation and system recovery times for the active 94 and 140 GHz systems at the DIRT-I test. The authors infer that the quick recovery times are due to fall-out of the large particle crater ejecta. Their theory is that the particles which are large enough to interact with millimeter waves fall out of the dust cloud fairly quickly, and that the remaining airborne dust particles are too small to hamper millimeter propagation seriously. They emphasize that their results are preliminary and describe a plan for extending this data base in the future.

Duncan and Seagraves [10] analyze visible to mid-IR transmission statistics from the Fort Sill, Smoke Week I and II, and DIRT-I tests. Their effort was to determine if one spectral region was better than another for propagation through battlefield dust. They concluded that:

1.   visible (0.55 μm) propagation was better than 10.35 μm most of the time for DIRT-I,

TABLE 5.3

SUMMARY OF RESULTS OF MILLIMETER WAVE PROPAGATION THROUGH EXPLOSIONS

DATE	EVENT	FREQUENCY (GHz)	MAXIMUM ATTENUATION (dB)	RECOVERY TIME (sec)	TIME CONSTANT (sec)	COMMENTS
10/02/78	A-1	94	-	-	1.25	Fluctuations, Equipment Problems, etc. Prevented Data Taking; Long Time Constant.
	A-2	94	-	-	1.25	Same as A-1.
	A-3	94	-	-	1.25	Same as A-T.
	A-4	94	-	-	1.25	Same as A-1.
10/03/78	B-1	94 / 140	- / 6.3	- / 10	0.400	Scintillations and Equipment Failure Hindered the 94 GHz Operation.
	B-2	94 / 140	- / -	- / -	- / -	Equipment Failure.
	B-3	94 / 140	7.5 / 7.0	15 / 5	0.400	Interesting that 140 GHz Recovered Faster than 90 GHz System; High Scintillation.
	B-4	94 / 140	8.1 / 7.5	<5 / <5	0.400	Well Defined Absorption.
	B-5	94 / 140	7.8 / 9.3	12 / 12	0.400	Secondary Absorption in Both Channels.
	B-6	94 / 140	8.7 / 8.9	13 / 13	0.400	Secondary Absorptions Present.
	B-7	94 / 140	9.8 / ~9.3	10 / -	0.400	Recorder Pen Failure on 140 GHz.
	B-8	94 / 140	10 / 13.2	10 / 18	0.400	94 GHz Signal Did Not Return to 0 dB Baseline.

TABLE 5.3 (Continued)

SUMMARY OF RESULTS OF MILLIMETER WAVE PROPAGATION THROUGH EXPLOSIONS

DATE	EVENT	FREQUENCY (GHz)	MAXIMUM ATTENUATION (dB)	RECOVERY TIME (sec)	TIME CONSTANT (sec)	COMMENTS
10/05/78	C-1	94 / 140	28 / 28	25 / 25	0	Scintillation Reduced; Integration Removed; Dynamic Range of Amplifier Insufficient to Show Attenuation Accurately > 28 dB
10/06/78	D-1	94 / 140	~30 / ~30	7 / 15	0.040	Fluctuations ~ 1 dB; Short Time Constant for D-runs.
	D-2	94 / 140	>20 / >20	11 / >20	0.040	Poor 140 GHz Results.
	D-3	94 / 140	13.9 / 22	12 / 19	0.040	
	D-4	94 / 140	25 / 25	- / -	0.040	Interpretation Difficult Due to Large Fluctuations and Drift.
10/10/78	C-2	94 / 140	>35 / -	- / -	0	Equipment Problems; Estimate on Attenuation for 94 GHz.
10/11/78	E-1	94	-	-	0.004	E-Events 94 GHz Only - No Data Because of Equipment Problems and Large Fluctuations; Estimate 35 - 40 dB.
	E-2	94	-	-	0.004	See Comments on E-1.
	E-3	94	35	5	0.004	Strong Attenuation; Both Traces for 94 GHz.
	E-4	94	-	-	0.004	See Comments on E-2.
10/12/78	F-1	94	-	-	0.040	F-Events: Howitzer Firings; Probably Missed Road.
	F-2	94	20	10-12	0.040	3 Groups of Four 155 mm Howitzer Rounds Max Attenuation is for One Round. Probably Directly in Line of Sight.

TABLE 5.3 (Continued)

SUMMARY OF REULSTS OF MILLIMETER WAVE PROPAGATION THROUGH EXPLOSIONS

DATE	EVENT	FREQUENCY (GHz)	MAXIMUM ATTENUATION (dB)	RECOVERY TIME (sec)	TIME CONSTANT (sec)	COMMENTS
10/12/78	F-3	94	3-4	10-12	0.040	Attenuation Reduced, Possibly Not Directly in Line of Sight; One Salvo of This Event Missed Road.
	F-4	94	-	-	0.040	Probably Missed Road.
10/13/78	F-5	94	10, 6	4, 1	0.040	Two Salvos of 4 Rounds Each; Second Salvo Reduced Because of Impact Region.
	F-6	94	6	3-4	0.040	Both Salvos Show Strong Absorption Inversion; Possibly Not Directly in Line of Sight.
	F-7	94	9, 8	4-5	0.040	Strongest Attenuation of Series; Probably Directly in Line of Sight.
	F-8	94	-	-	0.040	Probably Missed Line of Sight.
10/14/78	E-5	94	19	8	0.040	Tests 1 - 6: Static Firings of Howitzer Rounds at Varying Depths.
	E-6	94	13	5	0.040	Notice Reduction of Attenuation from Test 1 to Test 6 as Charges are Moved Toward Surface.
	E-7	94	8.4	4	0.040	See Comments on Test 1 and Test 2.
	E-8	94	7.8	5	0.040	See Comments on Test 1 and Test 2.
	E-9	94	6.7	3	0.040	Rounds on Surface.
	E-10	94	6.1	3	0.040	Rounds on Surface.
	G-1	94	~1	-	0.040	Total Attenuation Small, but Very Large ($>$ 5 dB) Scintillation.

2. transmission at the 9.75 μm wavelength excelled over 3.443 μm, 1.06 μm, and visible* wavelengths at Fort Sill and the Smoke Week tests, and

3. the 3.443 μm system performed better than the Nd:YAG laser at 1.06 μm and also better than the visible* region for low transmission values at DIRT-I.

Table 5.4 from [10] shows the average fraction of time that transmission was less than fixed thresholds for the duration of these tests.

Figure 5.3 from the TAPATS (Threat Artillery Preparation Against Tank Sights) barrages at Fort Knox, Kentucky shows that transmission can be essentially zero for the duration of an artillery barrage and can remain less than 10% for more than 60 seconds after the end of the barrage. In [12] it is noted that the conditions of the test range at Fort Knox were such that loose dirt was easily swept up, and for areas with thick sod cover as that for GRAF-II, an even more intense barrage resulted in significantly less attenuation.

---

*Here, visible means 0.4-0.7 micrometers.

TABLE 5.4

STATISTICS FOR TNT TRIALS OF DIRT-I (9 CASES). HERE
K IS THE TRANSMISSION THRESHOLD, AND THE TABULATED
VALUES ARE THE MEANS AND STANDARD DEVIATIONS OF THE
FRACTION OF THE TIME DURING THE ENTIRE MEASUREMENT
THAT THE TRANSMISSION WAS LESS THAN K, IN EACH WAVE-
LENGTH BAND.

	Means		Standard Deviations	
K	0.55	10.35	0.55	10.35
0.1	0.122	0.105	0.137	0.109
0.2	0.146	0.151	0.154	0.155
0.3	0.159	0.167	0.157	0.157
0.4	0.184	0.195	0.162	0.166
0.5	0.210	0.215	0.177	0.180
0.6	0.225	0.230	0.189	0.190
0.7	0.243	0.254	0.203	0.212
0.8	0.270	0.315	0.221	0.242
0.9	0.375	0.406	0.255	0.269

STATISTICS FOR 155 mm TRIALS OF DIRT-I (12 CASES)

	Means		Standard Deviations	
K	0.55	10.35	0.55	10.35
0.1	0.212	0.171	0.140	0.136
0.2	0.228	0.207	0.141	0.127
0.3	0.247	0.243	0.144	0.134
0.4	0.270	0.269	0.155	0.134
0.5	0.292	0.312	0.172	0.148
0.6	0.323	0.362	0.183	0.184
0.7	0.361	0.410	0.209	0.231
0.8	0.387	0.460	0.234	0.231
0.9	0.418	0.515	0.275	0.233

TABLE 5.4   (Continued)

STATISTICAL TEST RESULTS FOR COMBINED SINGLE ROUND DUST DATA (16 CASES)

K	Means				Standard Deviations			
	9.75	3.443	1.06	Visible	9.75	3.443	1.06	Visible
0.1	0.026	0.039	0.064	0.061	0.031	0.037	0.044	0.032
0.2	0.050	0.081	0.102	0.105	0.037	0.036	0.044	0.038
0.3	0.082	0.112	0.126	0.131	0.032	0.033	0.046	0.043
0.4	0.111	0.134	0.148	0.153	0.030	0.038	0.046	0.044
0.5	0.131	0.159	0.175	0.178	0.036	0.041	0.051	0.053
0.6	0.155	0.180	0.191	0.199	0.039	0.047	0.055	0.067
0.7	0.180	0.211	0.223	0.225	0.048	0.057	0.066	0.077
0.8	0.223	0.249	0.259	0.291	0.064	0.069	0.075	0.167
0.9	0.288	0.305	0.317	0.396	0.079	0.093	0.090	0.213

STATISTICS FOR COMBINED MULTIPLE ROUND DUST DATA (14 CASES)

K	Means				Standard Deviations			
	9.75	3.443	1.06	Visible	9.75	3.443	1.06	Visible
0.1	0.215	0.254	0.275	0.282	0.111	0.130	0.133	0.132
0.2	0.272	0.301	0.321	0.324	0.132	0.129	0.137	0.137
0.3	0.310	0.331	0.350	0.350	0.124	0.129	0.131	0.133
0.4	0.338	0.362	0.378	0.377	0.124	0.131	0.126	0.129
0.5	0.370	0.398	0.422	0.422	0.125	0.124	0.126	0.129
0.6	0.408	0.435	0.452	0.456	0.127	0.122	0.127	0.128
0.7	0.448	0.469	0.487	0.488	0.124	0.126	0.141	0.140
0.8	0.488	0.501	0.521	0.536	0.134	0.136	0.137	0.142
0.9	0.567	0.583	0.602	0.624	0.151	0.155	0.159	0.156

FIGURE 5.3.   NV&EOL TAPATS BARRAGE

5-16

5.1.1.4 Scattering Parameters

Data on scattering alone for dust from explosions are more difficult to obtain than total extinction coefficients. Scattering parameters are functions of the particle size distribution and refractive index, as described in Chapter 2. Data on refractive index of various soils and dusts are presented by Volz [13]. Particle size distributions from sampling at munitions events are available from DIRT-I [14]. Thompson presents heuristic justification for a special hybrid particle size distribution for munition-generated dust clouds [2]. However, one is not justified at this point to report scattering coefficients for typical munition dust clouds. More work needs to be done on this problem.

5.1.1.5 Dispersion Parameters

Most discussions of dispersion of munition dust clouds assume dispersion coefficients which are related empirically to the Pasquill stability categories, as in Table 2.2. It is possible that during sustained barrages, the energy released by munition explosions may affect the value of these coefficients by making the atmosphere more unstable. There is no empirical evidence to suggest this or to rule it out at this point.

5.1.2 GASEOUS/HEAT EMISSION FROM EXPLOSIVES

The gases and heat we consider here are direct products of chemical decomposition of a detonating explosive. Heat and unusual gases generated by the passage of the blast wave through the ambient air are not treated since they are assumed to be second order effects in comparison with those associated with the detonation. Ozone and NO_x compounds are formed in significant amounts by the passage of the blast wave through air but the reaction

$$O_3 + NO \rightarrow NO_2 + O_2 \qquad (5-8)$$

5-17

causes these molecules to dissipate rapidly, in 0.1 to 1
second [15]. The results in [15] can be considered to be pre-
liminary, but there is nothing there to indicate that air-
blast generated battlefield gases would be of primary importance.
So we confine our discussion to detonation products.

5.1.2.1   Yield Factors

Table 5.5 shows amounts of gases generated by detonation
of the condensed explosives TNT, RDX, and HMX. These three
are members of the CHNO family of explosives (the molecular
formulas of TNT, RDX, and HMX are $C_7H_5N_3O_6$, $C_3H_6N_6O_6$, and
$C_4H_8N_8O_8$ respectively). Most military explosives include one
or more of these three compounds. There are explosives outside
the CHNO family which produce unusual gases with strong infrared
absorption bands (especially halogenated explosives such as
FEFO, $C_5H_6N_4O_{10}F_2$, which produces large quantities of HF). The
CHNO explosives however, are easiest to produce and handle and
are, therefore, the ones of most military interest. Military
explosives involving non-TNT, RDX, HMX ingredients include amatol
(TNT plus ammonium nitrate) and pentolite (TNT plus PETN).
Amatol was used extensively in World War I and is still common
in non-NATO nations [16].

The measured data in Table 5.5 are from laboratory
calorimeter experiments rather than field tests. Some sources
report traces of gases with important absorption bands (for
example, methanol [17]) but the gases in Table 5.5 are the ones
generally thought to be present in significant quantities. C(S)
is the amount of solid carbon present in detonation products,
whose optical properties will be considered in Section 5.1.3.2.

Knowledge of the quantity of explosives delivered to a given
area and an idea of the subsequent diffusion of the detonation
products enables one to compute in principle the concentrations
of these gases along an arbitrary line of sight. This was done
in references 18 and 19. A discussion of these results follows.

TABLE 5.5

DETONATION PRODUCTS OF TNT, RDX, AND HMX (IN moles/kg OF EXPLOSIVE)

	TNT	RDX	HMX
CO_2	5.5	6.4	6.5
CO	8.7	5.0	3.6
H_2O	7.0	9.2	10.7
H_2	2.0	1.6	1.0
N_2	5.8	13.1	12.4
NH_3	.71	.77	1.3
CH_4	.44	.80	.13
HCN	.09	--	.03
C(S)	16.1	1.3	3.3

The behavior of explosions in air is often modeled by assuming an instantaneous point source release of thermal energy and detonation products [20,21]. The theory allows one to track the centroid and spread of the plume of detonation products as they expand into a possibly inhomogeneous atmosphere. The Morton - Taylor - Turner model [20] assumes that the cloud of detonation products is buoyant because of the thermal energy released by the explosion. The plume rises, entraining air, until it is at pressure and temperature equilibrium with its surroundings.

The partitioning of energy into momentum, via the shock wave, and heat is a subject of current research, but the Morton-Taylor - Turner model has been shown to give results for dust cloud rise that are consistent with field tests [1]. Their equation for cloud rise, according to Dumbauld [22], is:

$$h(t) = h_0 + \left\{ \frac{3H}{C_p \pi \rho \alpha^3 s} \left[1 - \cos\left(\sqrt{\frac{gs}{T}}t\right) \right] \right\}^{1/4}. \qquad (5-8)$$

where

$h(t)$ = height of the plume centroid at time t

h_0 = initial source height

g = gravitational constant = 9.8 m/sec^2

H = total heat released by the explosion

C_p = specific heat of air at constant pressure

ρ = ambient air density

T = ambient air temperature

α = entrainment coefficient $\approx$ 0.6

s = $\frac{d\theta}{dz}$ = stability parameter, vertical gradient of potential temperature.

5-20

Equation (5-8) is assumed to be valid for $t < t_f \left(= \pi(gs/T)^{-1/2}\right)$. At $t = t_f$, the plume has reached its buoyant height

$$h(t_f) = h_0 + \left(\frac{6H}{C_p \pi \rho \alpha^3 s}\right)^{1/4} \qquad (5-9)$$

which remains as the height of the centroid for $t > t_f$.

Combining the Morton - Taylor - Turner model with Sutton's atmospheric dispersion model (described in Section 2.6 of this Handbook) results in Figure 5.4, which indicates CO concentration as a result of detonation of a single 25 lb. TNT charge in the middle of a 1 km. line of sight. Concentration drops rapidly along the line of sight and remains low due to the buoyant plume rise. This rapid decrease in concentration means that significant molecular absorption is not expected on a ground level line of sight due to products of a single artillery shell.

These calculations were extended in [18] to an intense artillery barrage, consisting of one 4 kg. round for every 10 m x 10 m square subarea of a kilometer square area, in 30 minutes time. Gases were assumed to be uniformly mixed under a 60 meter containment height, in a very stable atmosphere. Table 5.6 shows the predicted concentrations.

Thermal emissions from munition events have been measured with FLIR's at DIRT-I and GRAF-II. Figure 5.5 shows one of these images. From the literature available, these measurements have not been compared with theory. Accepted values for the total thermal emissions from munition events are 1.27 kcal/g of TNT, and 1.48 kcal/g of RDX or HMX. More information on this subject is included in a classified supplement to this chapter.

5-21
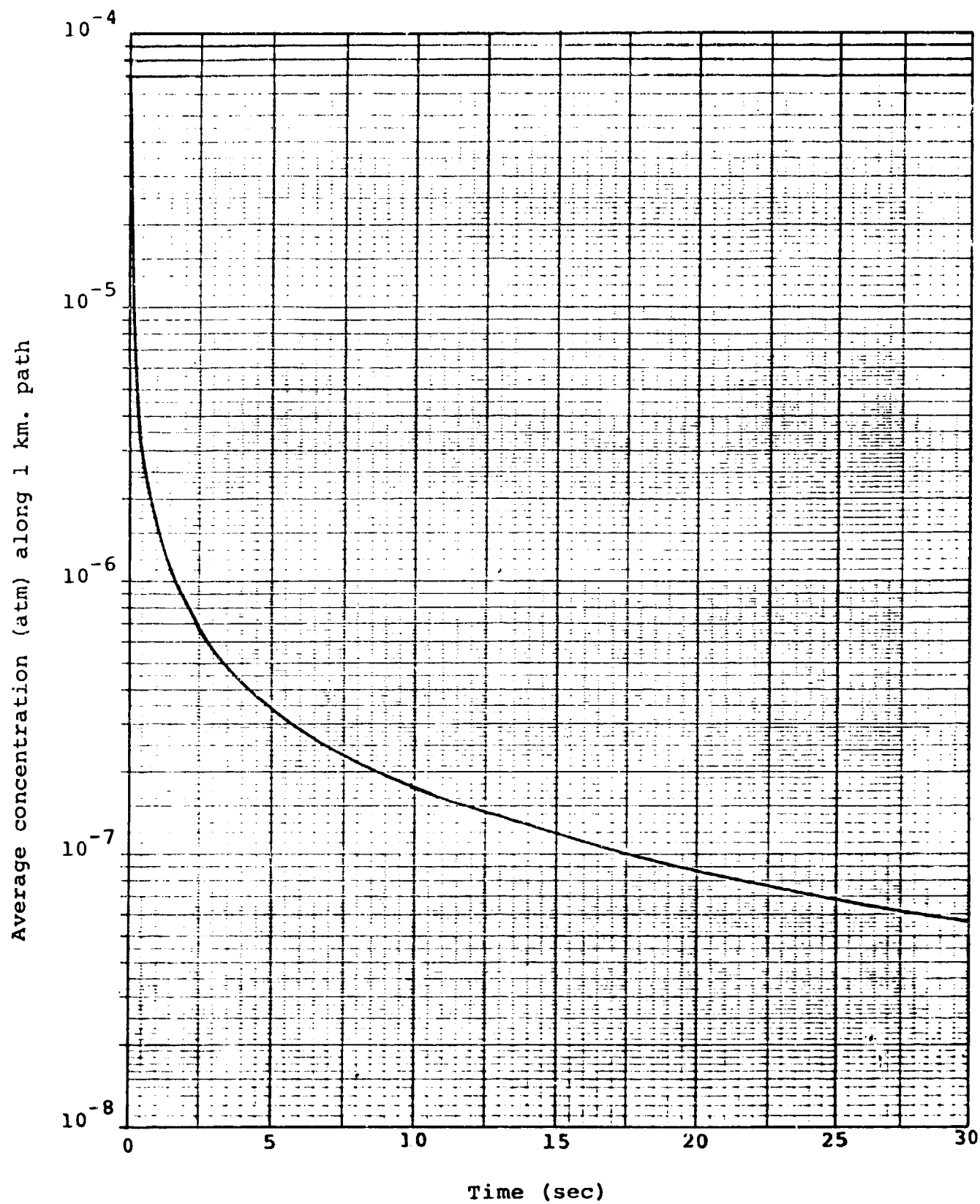
FIGURE 5.4   DIFFUSION OF CARBON MONOXIDE IN DETONATION
PRODUCTS.

5-22

FIGURE 5.5. FLIR THERMAL IMAGERY FROM GRAF-II TESTS

5.1.2.2 Attenuation Coefficients

The gases in Table 5.6 with concentrations significantly higher than ambient are CO, NH_3, and CH_4. Figures 5.6, 5.7, and 5.8 show broadband absorption due to these gases. Figure 5.8 shows that ammonia, as characterized in the AFGL Trace Gas Data Base [23], does not cause serious problems for the CO_2 laser at 10.6 μm. Likewise, methane absorption near 3.8 μm does not seriously hamper DF laser propagation. But 8-12 μm absorption by 10 ppm of NH_3 over a 1 km. path results in absorption averaging 10-20%, and CO absorption at 60 ppm averages 60% from 4.4 to 5.0 μm.

Enhanced CO concentrations were observed at WSMR during DIRT-I [14]. This is the only confirmation of the model that has been found. An NH_3 sampler was also present but significant concentrations of NH_3 were not recorded.

CO and HCN are gases from Table 5.6 which have significant absorption in the millimeter region. Figures 5.9 and 5.10 show theoretically derived spectra giving the amount of this absorption. More gas sampling at future field tests will yield potentially useful information on obscuration conditions for E-O systems.

TABLE 5.6

CONCENTRATIONS OF ABSORBING GASES PREDICTED BY DIFFUSION MODEL FOR SUSTAINED BARRAGE (IN PARTS PER MILLION BY VOLUME).

	TNT	RDX	HMX	Ambient
CO_2	82.	95.	97.	330.
CO	129.	74.	53.	.075
H_2O	104.	137.	159.	variable
NH_3	11.	11.	19.	--
CH_4	6.5	12.	1.9	1.6
HCN	1.3	--	.45	--
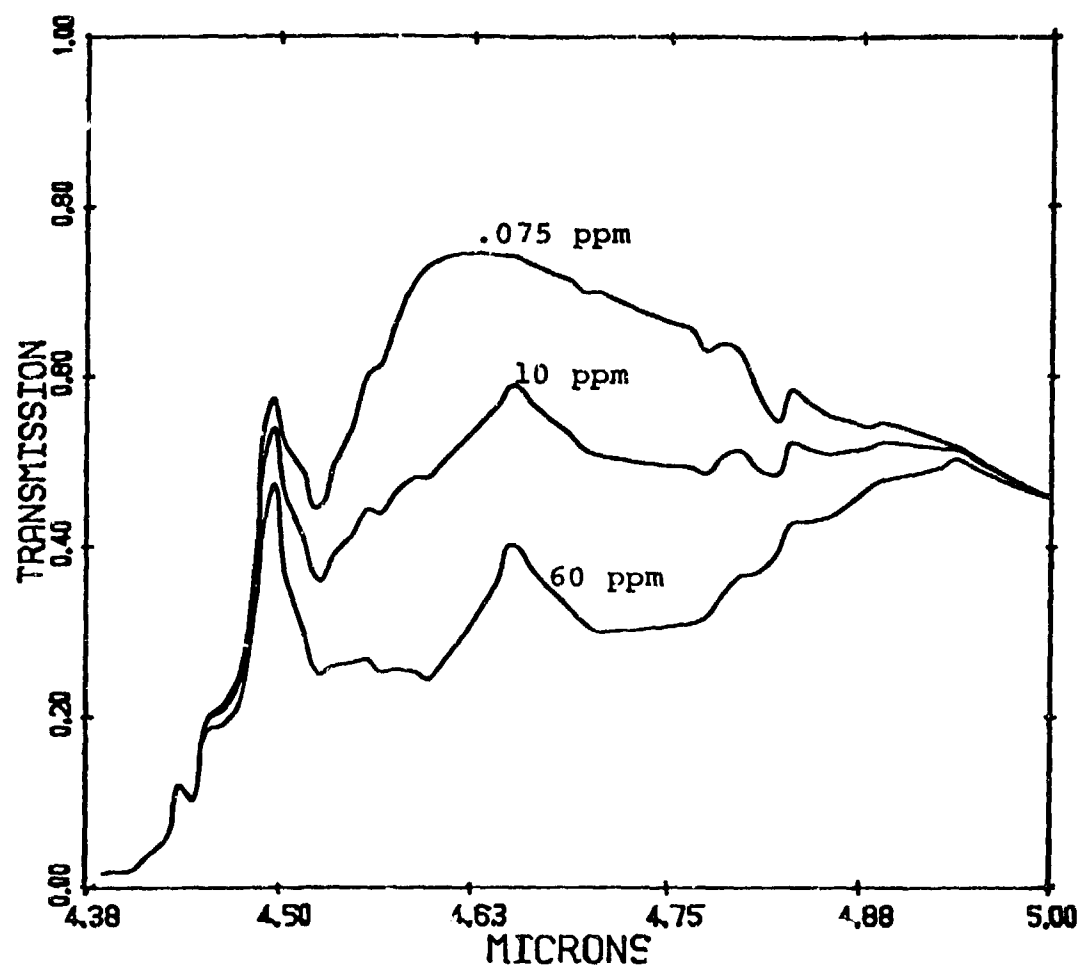
FIGURE 5.6.   TRANSMISSION FROM 4.39 to 5 μm FOR A MIDLATITUDE
SUMMER ATMOSPHERE WITH AMBIENT AND ENHANCED CO
CONCENTRATIONS
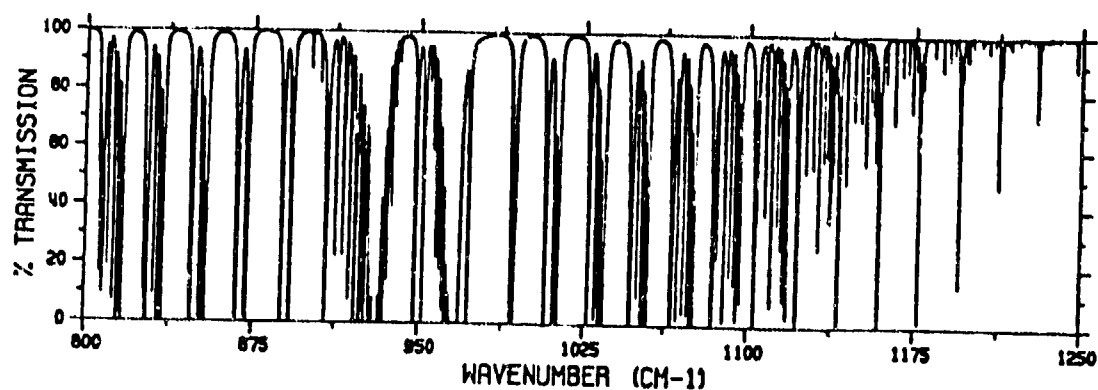
FIGURE 5.7. ABSORPTION OVER A 1 km. PATH DUE TO 10 ppm.
OF AMMONIA, 8-12 MICRON REGION.
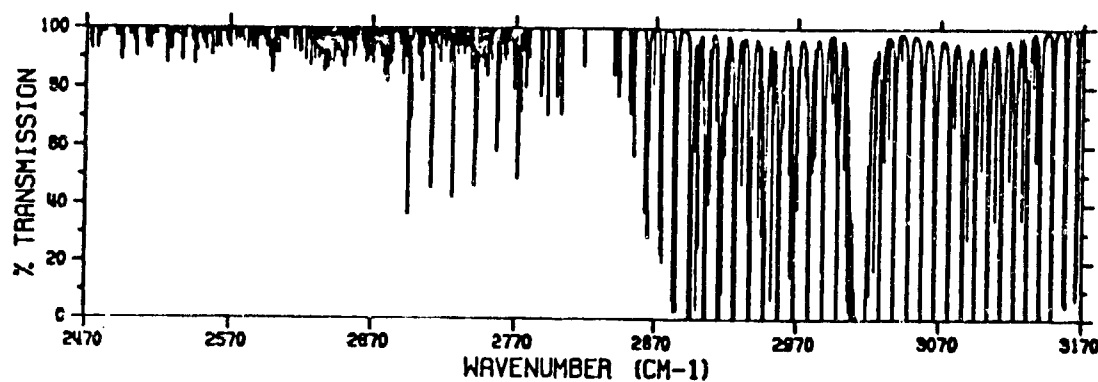
FIGURE 5.8. ABSORPTION OVER A 1 km. PATH DUE TO 30 ppm.
OF METHANE, 3.15-4.05 MICRON REGION.

5-26
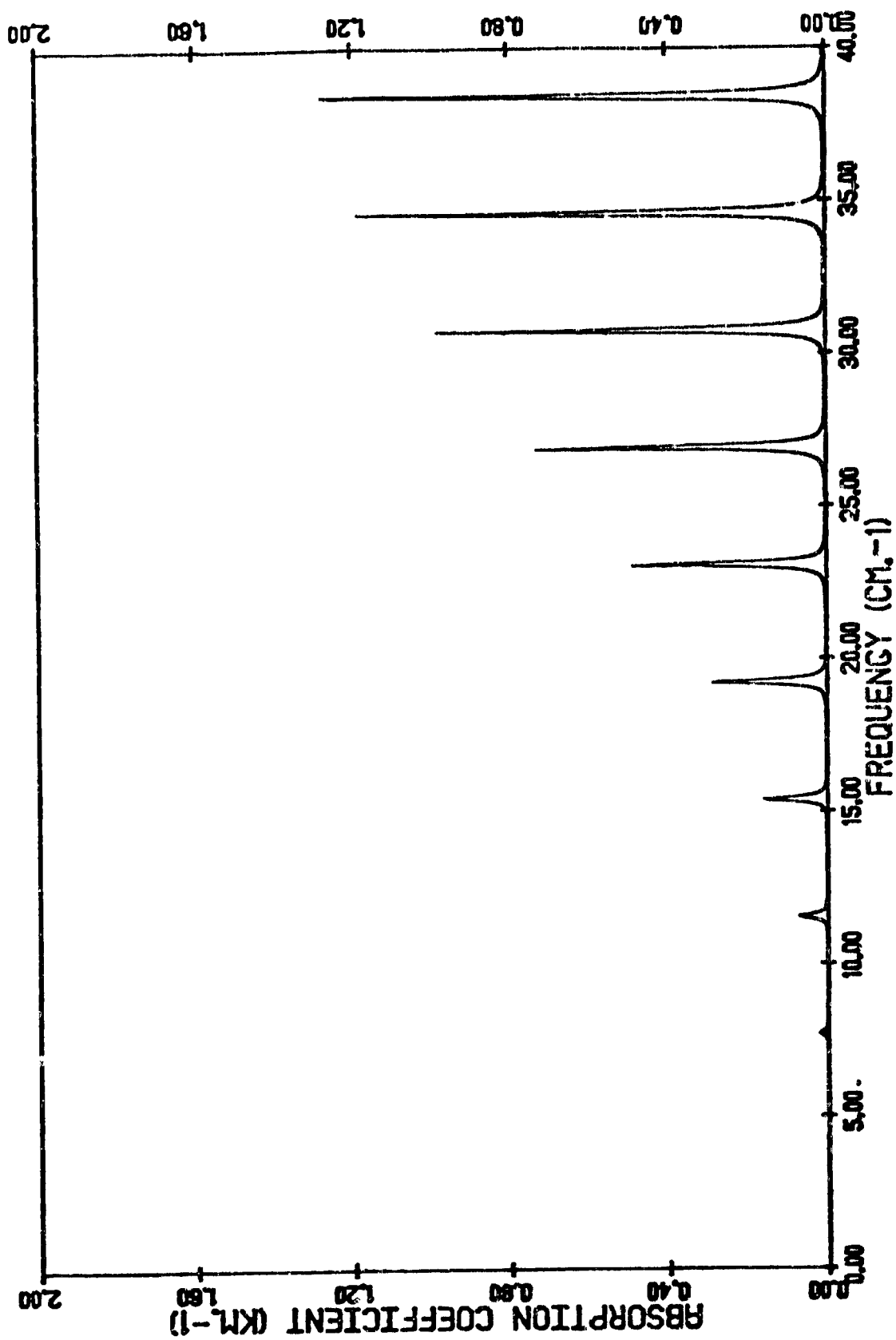
FIGURE 5.9. ABSORPTION BY 90 ppm OF CO

FREQUENCY (CM.-1)

ABSORPTION COEFFICIENT (KM-1)
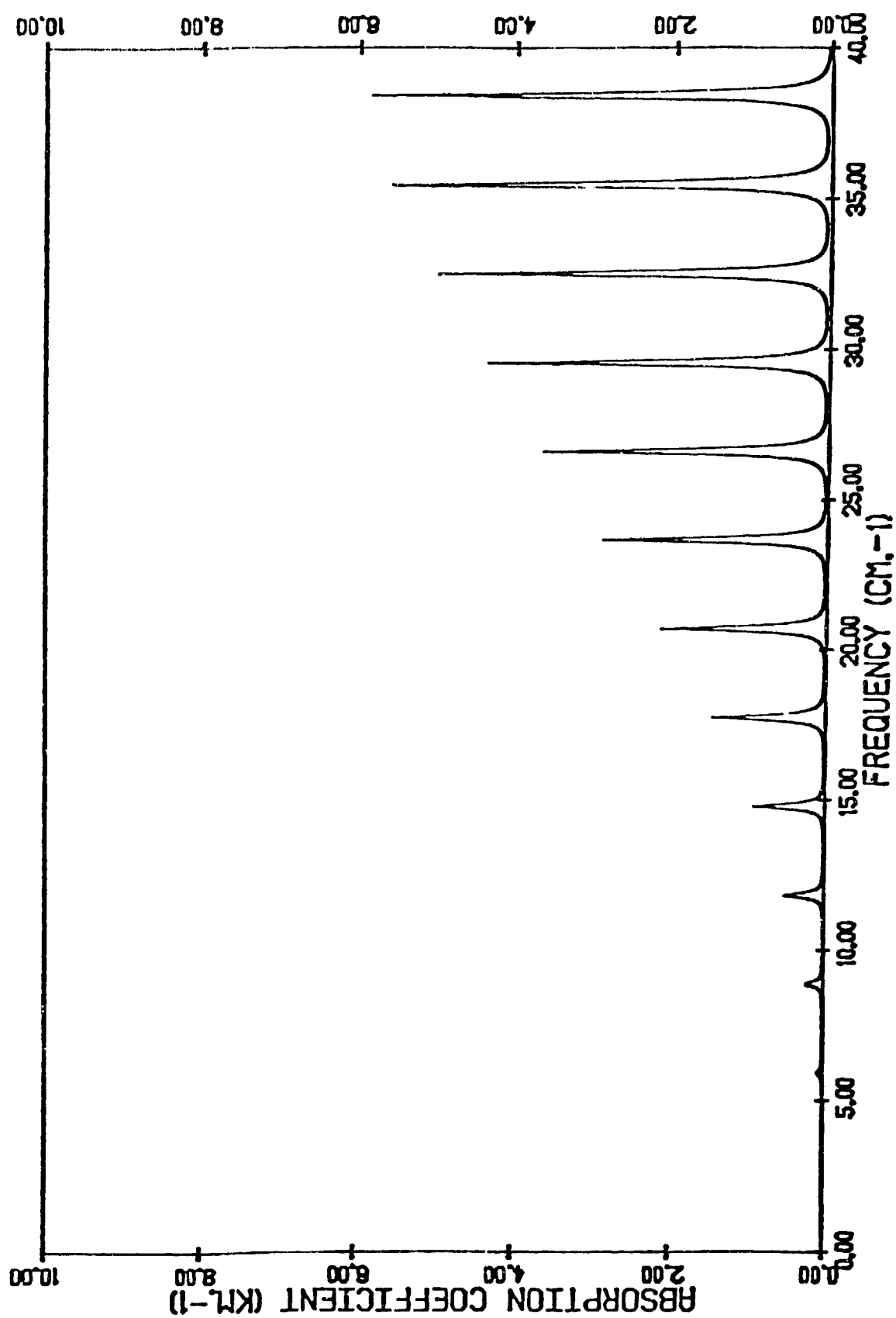
FIGURE 5.10. ABSORPTION BY 1 ppm OF HCN

5.1.3   DIRT AND DEBRIS

5.1.3.1   Free-Falling Objects

In this section we consider in more detail the theory of particle settling and its effect on the dust and smoke generated by an explosive detonation.

From [24], the drag force on a spherical particle of diameter D, moving at speed u through a fluid of density ρ_a and viscosity μ, is given by:

$$F = \frac{\pi \rho_a C_D}{8k} u^2 D^2. \qquad (5-10)$$

Here C_D is the drag coefficient, empirically related to the Reynolds number

$$Re = \frac{Du\rho_a}{\mu} \qquad (5-11)$$

by the equation

$$C_D = \frac{24}{Re} + 0.44. \qquad (5-12)$$

The constant k, known as the Cunningham factor, accounts for the fact that the assumption that the medium is continuous breaks down in the small particle limit. Its value is given by

$$k = 1 + \frac{2\lambda}{D} \left(1.257 + 0.4e^{-1.1D/2\lambda} \right) \qquad (5\text{-}13)$$

where λ = the mean free path of gas molecules ($\sim 6.62 \times 10^{-6}$ cm for a sea-level standard atmosphere). For large particles,

$$\lim_{D \to \infty} k = 1, \qquad (5\text{-}14)$$

so that for large particles this factor may be neglected. For particles 1 μm in diameter, its value is ~ 1.16, so that small particles fall faster than the continuous theory would predict.

When the drag force F equals the gravitational force $\overline{F}$ (corrected for buoyancy) the particle has attained terminal velocity. Here

$$\overline{F} = ma = \frac{4}{3}\pi \left(\frac{D}{2} \right)^3 \left(\rho_p - \rho_a \right) \qquad (5\text{-}15)$$

where $g = 980$ cm/sec^2 is the acceleration due to gravity and ρ_p is particle density. The equation $F = \overline{F}$ reduces to a quadratic equation which can be solved for u. The result for the terminal-velocity is

$$u = \frac{-b + \sqrt{b^2 - 4ac}}{2a} , \qquad (5\text{-}16)$$

5-30

where

$$a = 0.44$$

$$b = \frac{24\mu}{D\rho_a}$$

$$c = -\frac{4}{3} kDg\left(\frac{\rho_p - \rho_a}{\rho_a}\right). \tag{5-17}$$

Figure 5.11 shows the results of equation (5-16) for a range of densities appropriate for typical soils and carbon soots. For a particle of diameter 1 cm, the terminal velocity is about 20m/sec, so that such particles fall out very rapidly. For particles of diameter 1 μm, terminal velocity is $\sim 5 \times 10^{-3}$ cm/sec, so that these particles can remain airborne for hours and account for most of the long-term attenuation by solid detonation products. The Cunningham factor k is neglected in the known models [1-4] of munition dust clouds, which is the single fact making this development unique. Its effect is to increase the settling speed of the smaller particles. Thus, using these equations we predict fewer airborne particles on the small end of the particle size distribution than these models show, which can have a significant effect on propagation.

For particles of larger diameter whose density is large with respect to that of air, the equation

$$s = \frac{1}{2} gt^2 \tag{5-18}$$
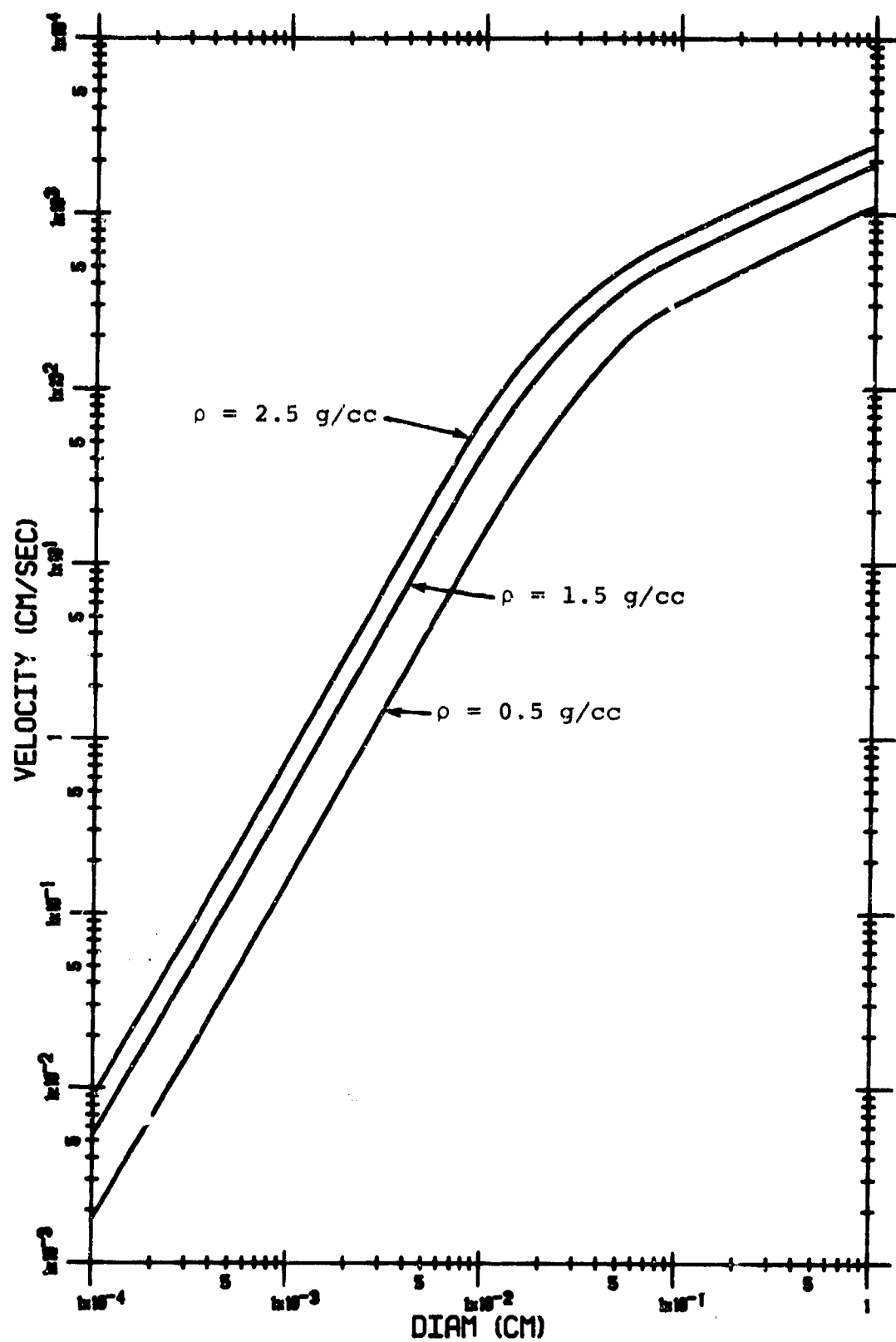
FIGURE 5.11. TERMINAL VELOCITY FOR SMALL PARTICLES OF VARYING DENSITIES.

gives the distance s which the particle falls in time t. This
equation can be used for shrapnel and other large debris objects
from explosions. If we assume that such an object is initially at
height 100 meters, it takes 4 or 5 seconds to impact the ground, and
2 or 3 seconds if falling from 30 meters. Thus, the time spent by
these objects in the field of view is fairly small. However if
there is a steady flux of such objects from explosions in rapid
succession, significant obscuration can presumably occur. In
this case the geometrical cross section in the field of view of
the system at a given time can be used to predict the total
attenuation, as defined in Section 2.

5.1.3.2   Smoke From Explosives

Table 5.5 shows the amount of solid carbon, C(S), generated by a TNT explosion. Again the units are moles solid carbon per kg of explosive: a simple calculation shows that roughly 19% by weight of the initial explosive goes into solid carbon after detonation.

Extinction due to solid carbon particles is strong, though the exact value, especially at longer wavelengths, is somewhat uncertain. Table 5.7 shows some of the values for the complex refractive index of solid carbon that can be found in the literature. Absorption due to solid carbon or soot particles is an area of active research, especially in the auto industry [25, 26, 27].

In this section we will attempt to derive practical bounds on extinction due to carbon soot from explosives. These bounds are of course limited by the extent of current knowledge of the size, shape, and composition of these soot particles, in addition to the uncertainty in optical properties.

Figure 5.12 assembled from reference 28 shows detonation product particulates viewed under an electron microscope. Experiments carried out at Lawrence Livermore Laboratory to characterize particles from high explosive detonations are described in reference 28, by A.W. Casey and A.H. Biermann. They state that detonations for the most part yield spherical, smooth particles, possibly because of the exposure of detonation products to high temperatures. Their report does not include a discussion of particle size distributions, but in a private conversation A.W. Casey indicated that most of the particles were definitely in the submicron range, with ten times as many particles in the range 0.5 - 1.0 μm diameter as in the range 5.0 - 10.0 μm diameter. In addition to spherical particles they found rough, irregular particles, and particles that looked like aggregates of fused spheres. However they did not report the chain-like aggregates found in acetlyne smoke by Roessler and Faxvog [27].

5-34

TABLE 5.7

LITERATURE VALUES FOR COMPLEX
REFRACTIVE INDEX OF CARBON SOOT
(from Reference 27)

$$m = m_1 - m_2 i$$

$\lambda = 0.5145\ \mu m$			$\lambda = 10.6\ \mu m$	
m_1	m_2		m_1	m_2
1.95	0.66		2.2-2.4	0.9-1.2
2.0	0.5		4.85	3.85
2.05-2.75	0.66-1.46		2.0-2.4	0.7-1.3
1.8-2.0	0.0-0.8		3.85	1.64
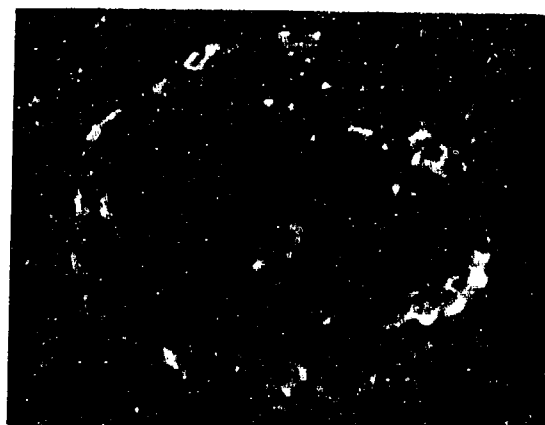
Spherical rough

Irregular

Spherical smooth

Agglomerate
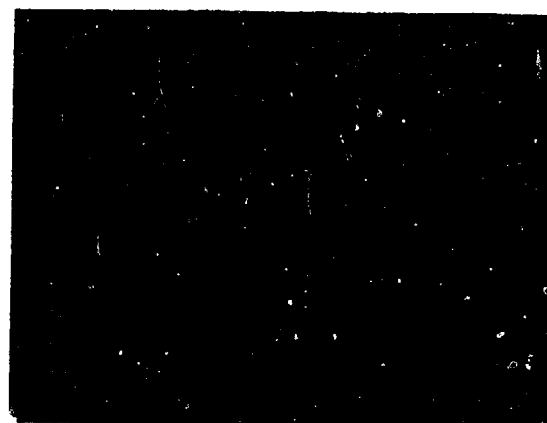
Semispherical

FIGURE 5.12.   EXAMPLES OF CATEGORIES OF SHAPE AND SURFACE MORPHOLOGY
USED TO CLASSIFY DETONATION-PRODUCT PARTICULATES [28]

Figures 5.13 and 5.14 show the Rayleigh extinction approximation
for small absorbing carbon spheres. Here refractive index data were
taken from [29] and a density of 2.0 g/cm was assumed. These
results follow from the expression for the Rayleigh approximation

$$A_{EXT} = \frac{-6\pi}{\rho\lambda} \, Im\left(\frac{m^2 - 1}{m^2 + 2}\right) + \frac{4\pi^4 D^3}{\rho\lambda^4} \left|\frac{m^2 - 1}{m^2 + 2}\right|^2 . \qquad (5-19)$$

The first term on the right hand side is the absorption component
and the second term is the scattering contribution. Here ρ is
material density (g/cm^3), m is the complex refractive index at
wavelength λ, and D is particle diameter (microns). As can be
seen by comparing Figures 5.13 and 5.14, increasing the
particle diameter D only serves to increase the scattering component
at short wavelengths; at longer wavelengths the λ^{-4} dependence
drives the scattering term to zero. Rayleigh calculations done
using the different values for the complex refractive index as
in Table 5.7 give a variation in total extinction coefficient
from 0.197 m^2/g to 0.064 m^2/g near a wavelength of 10 μm, so the
values in the figure should be taken as qualitative.

We will use the predictions of the barrage model described
in Section 5.1.2.1 to bound the extinction due to detonation –
produced carbon particulates. In this model, 40,000 kg of TNT
were delivered to a kilometer square area, with uniform mix of
detonation products under a 60 meter containment height. Since
19% by weight of the explosive goes into solid carbon, we have
a density of

$$(0.19)(40,000)/(60)(1000)(1000)(kg/m^3) =$$
$$0.00013 \ kg/m^3 =$$
$$0.13 \ g/m^3$$

5-37
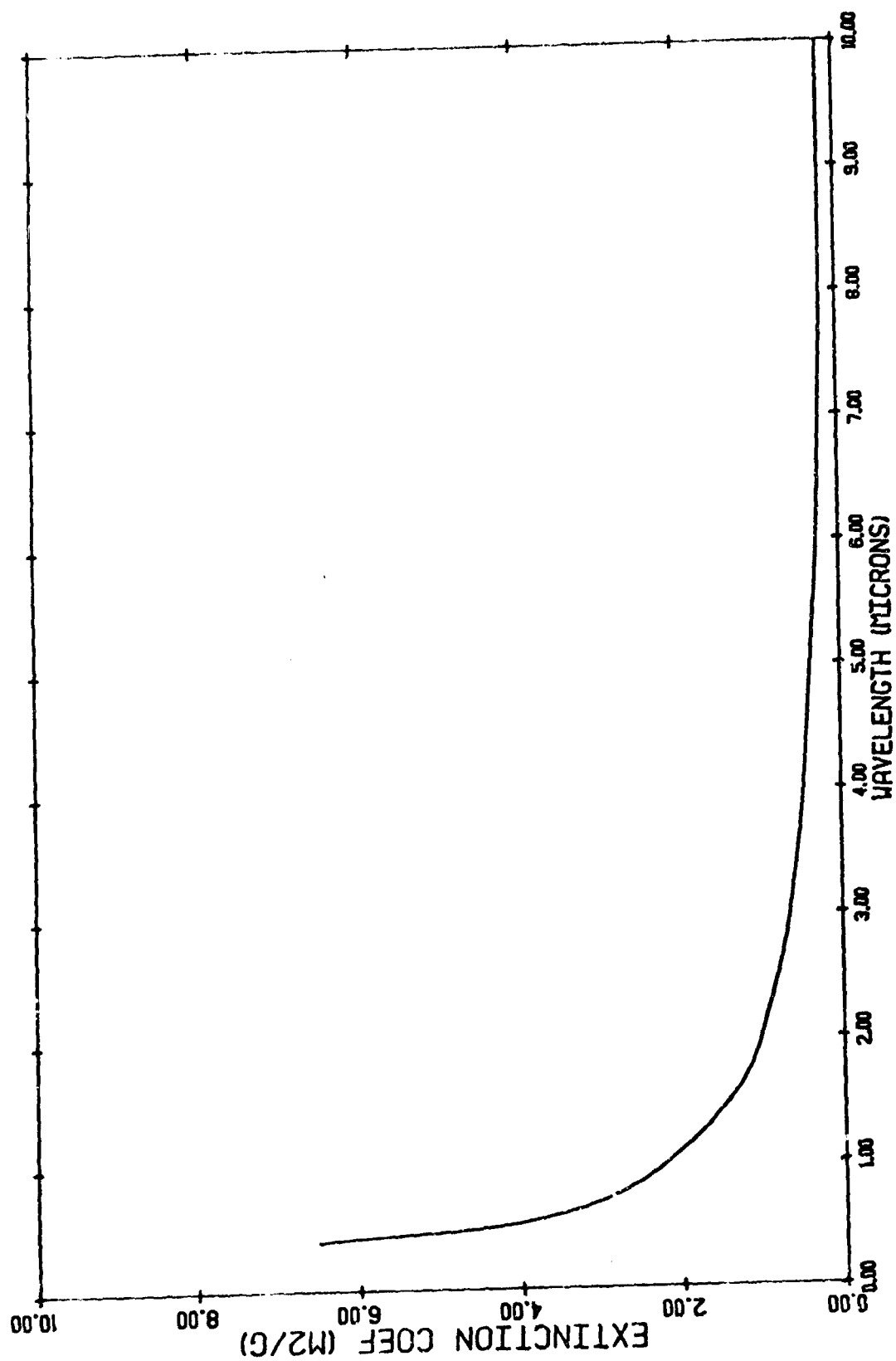
FIGURE 5.13. RAYLEIGH EXTINCTION FOR 0.02 μm DIAMETER CARBON SPHERES.
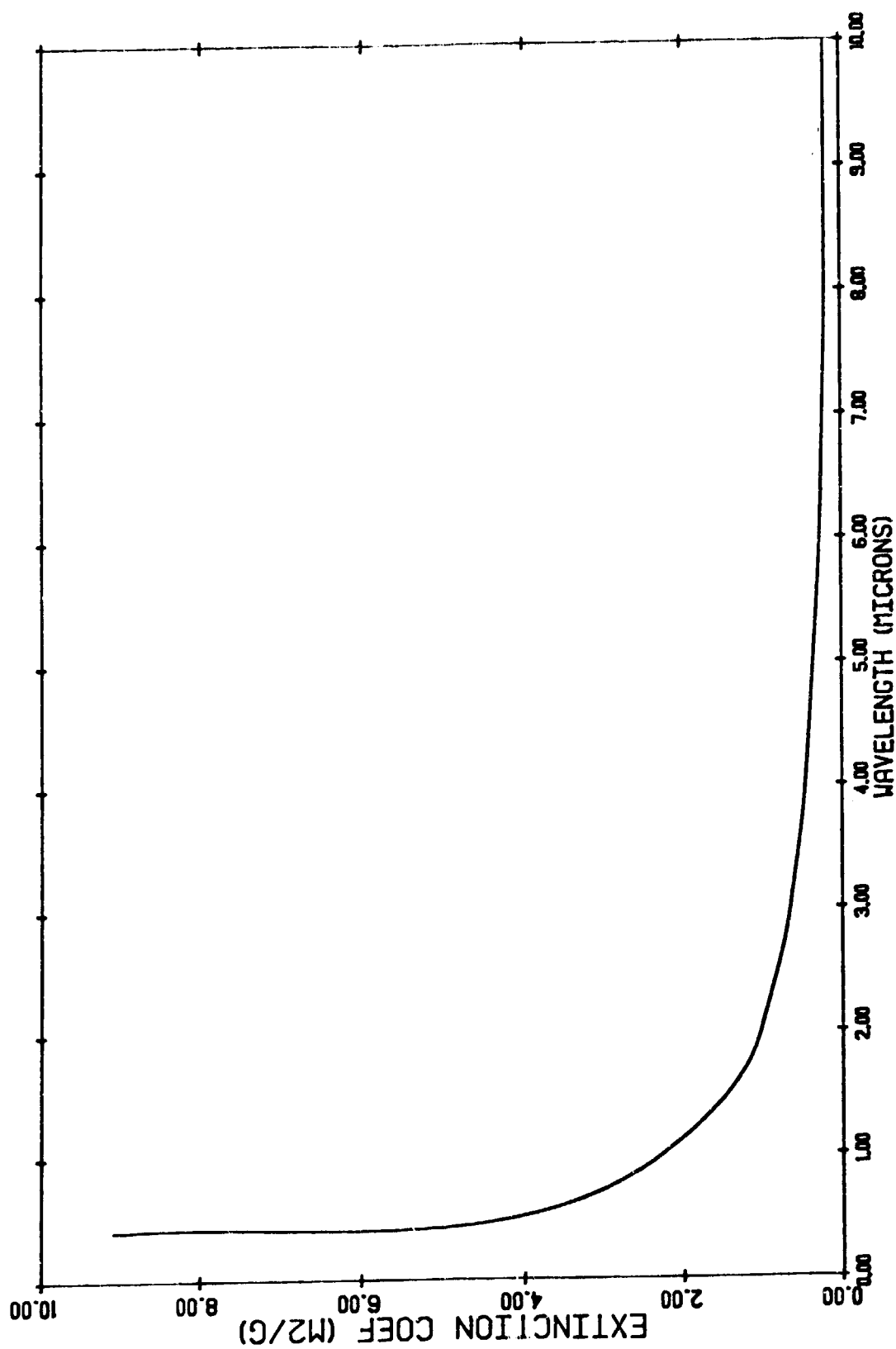
FIGURE 5.14. RAYLEIGH EXTINCTION FOR 0.1 μm DIAMETER CARBON SPHERES.

5-39

if all the solid carbon remains airborne.

Quantitative knowledge of the particle size distribution is required, in addition to the terminal velocity data developed in the preceding section, to calculate the exact quantity remaining airborne at any given time. Assume that only 1/100 of one per-cent by weight of the particles are in the Rayleigh size region and remain airborne, then the effective density at the end of the barrage is 0.13×10^{-4} g/m^3.

Multiplying this by the mass extinction coefficient over a 1 km path and applying Beer's law for the transmission we obtain

$$t_{vis} = \exp \left\{ - \left(.13 \times 10^{-4}\right)(1000) A_E (vis) \right\} \approx$$

$$\exp \left\{ - \left(.13 \times 10^{-1}\right)(5) \right\} =$$

$$0.937. \hspace{4cm} (5.21)$$

If a similar calculation is done assuming 1/10 of one percent of the material remains airborne, then

$$t_{vis} \approx 0.522. \hspace{3cm} (5.22)$$

And in this case

$$t_{3-5} \approx \exp \left\{ - (.13)(.5) \right\} = 0.937. \hspace{2cm} (5.23)$$

5-40

So, under some not unreasonable assumptions, solid carbon in detonation products can have a measurable obscuring effect on electro-optical systems. The key parameters about which more data are required to make an exact assessment are the carbon soot particle size distributions and complex refractive indices. The work of Casey and Biermann [28] shows that to a large extent the particles are spherical enough for Rayleigh - type approximations, but more measurements are required before a quantitative theory can be developed. Also note that different amounts of solid carbon are expected from non-TNT explosives; for example, composition B which contains some RDX. Also for aluminized explosives one would expect non-carbon particulates, particularly solid aluminum and aluminum oxides, to be present in the detonation products.

5.2 VEHICLE-INDUCED CONDITIONS

In this section we present those obscurants which are from vehicle traffic and battlefield conditions.

5.2.1   DUST FROM VEHICLE TRAFFIC

There exists little data on the generation of dust by vehicles. A report by Turner et al. [19] does summarize the available data on dust generation resulting from a number of field tests. Also, some data exist on the detailed physical and optical properties of dust as a result of Army tests at Ft. Sill, Oklahoma. In the following sections we present these data.

5.2.1.1   Yield Factors

Over the last few years the Environmental Protection Agency (EPA) has performed research on sources of particulate pollutants in the United States. Detailed studies were made of the amounts of dust and vehicle dust products which were produced in various parts of the country. Excellent summaries are contained in the EPA reports [30, 31]. Because of the nature of their work, investigators at EPA are primarily concerned with emissions, dosages, and other distributions integrated over extended areas and time periods. For example, they have much information on the number of tons per day of dust emitted by various sources throughout a large urban area. For military investigations one would have to have information which is differential in nature; i.e., the number of grams of dust particles per second per unit size range for a highly localized source. Much of this detailed information does not exist or it must be inferred from the integral values.

There are a number of vehicle dust emission models which have been developed. These models provide the amount of mass produced per vehicle distance; e.g., lbs/vehicle-mile in terms of various environmental factors such as the silt content of the terrain,

5-42

rainfall history, vehicle speed and number of wheels on the vehicle. Thus, for a vehicle, one can write the basic dust emission factor as:

$$E = \frac{dM}{dS} \qquad (5.24)$$

where E has units of lbs/vehicle-mile or gms/vehicle-mile.

The Puget Sound Air Pollution Control Agency Study [30] produced three emission values for three discrete vehicle speeds; these are 3.5 lbs/vehicle mile at 10 miles/hour, 7.0 lbs/vehicle mile at 20 miles/hour, and 22.2 lbs/vehicle mile at 30 miles/hour.

C. Anderson [31] found smaller values between 0.5 - 0.7 lbs/vehicle mile for a vehicle at 30 miles/hour.

University of Iowa [32] found an emission factor of 5.5 lbs/vehicle mile but no vehicle speed was given.

University of New Mexico [33] measured 0.93 lbs/vehicle mile for particles less than 6 μm in size and 0.04 lbs/vehicle mile for particles less than 3 μm in size. The vehicle speed was 25 miles per hour.

PEDCo Environmental Specialists, Inc. [34] developed a model which is dependent upon vehicle speed. It is given by:

$$E = (0.27)(1.068)^u \qquad (5.25)$$

where E is in lbs/vehicle mile and u is the vehicle speed in miles/hour. The region of validity is 15 mph $\leq$ u $\leq$ 40 mph. In the PEDCo study sampling data of particulate concentrations were taken by a beta gauge airborne dust sampling/readout instrument positioned at various distances and heights downwind of the road.

The model developed by the Midwest Research Institute [35] is the most detailed of all. They used a field sampling program to develop their emission factor. Isokinetic samples were

located at set heights and distances from the road. Hi-Vol
(high volume) samples were taken to correct for background
dust concentrations.   Their emission factor is:

$$E = 0.81 \ c \ \left(\frac{u}{30}\right) \frac{N}{4} \left(\frac{365 - w}{365}\right) \qquad (5.26)$$

where E is in lbs/vehicle mile, c is the silt content of the
surface in per cent, N is the number of wheels on the vehicle,
and w is the number of days with 0.01 inch or more rainfall.

All of these models are illustrated in Figure 5.15.   A
continuous line was drawn through the three points for the
Puget Sound Study.
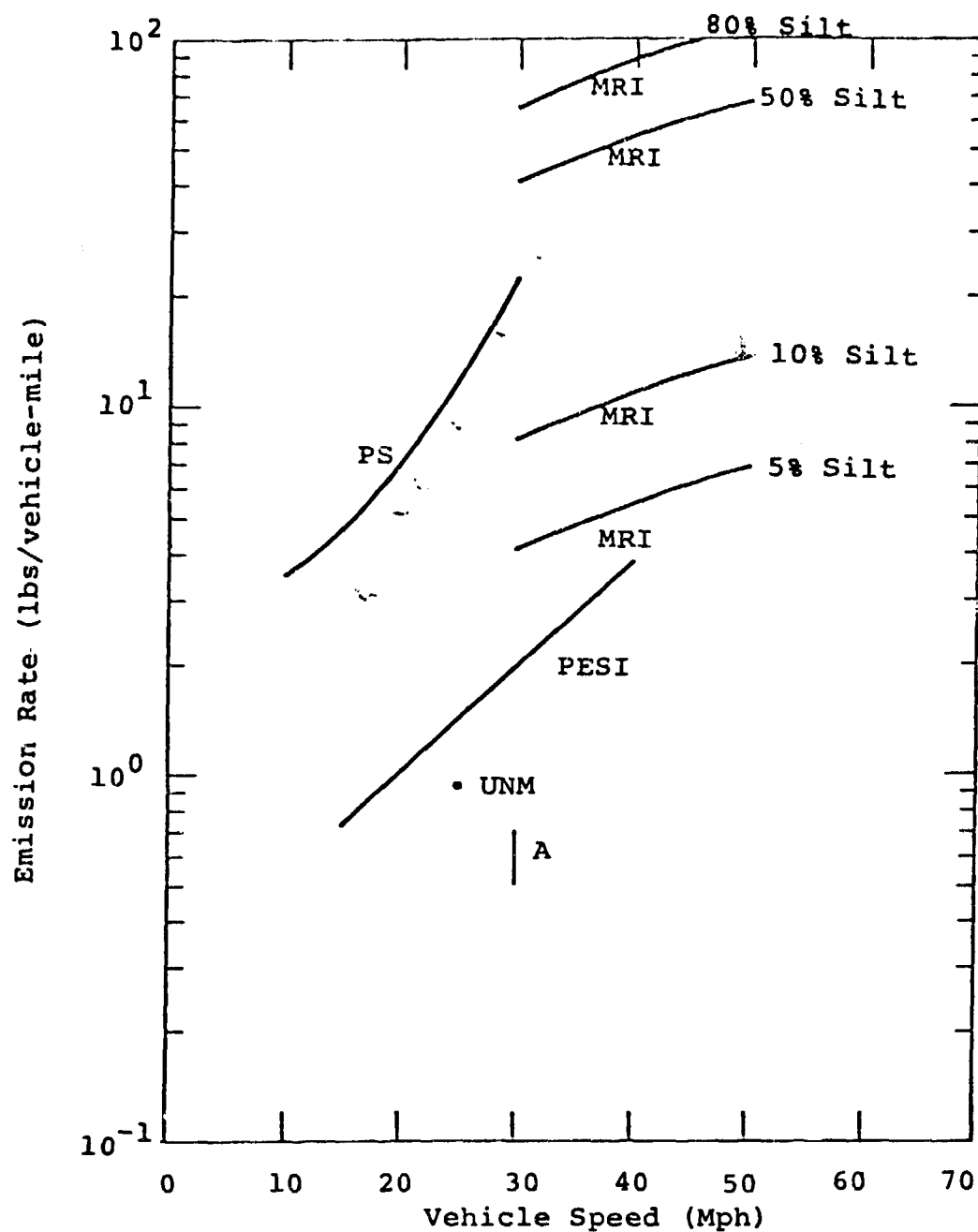
FIGURE 5.15. COMPARISON OF DUST EMISSION MODELS FOR UNPAVED ROADS
FOR FOUR WHEELED VEHICLES. (w = o)

MRI - Midwest Research Institute [35]

PESI - PEDCO Environmental Specialists, Inc. [34]

UNM - University of New Mexico [33]

A   - Anderson [31]

PS   - Puget Sound Air Pollution Control Agency [30]

5.2.1.2   Attentuation Coefficients

There are very little data on dust extinction coefficients insofar as vehicular dust is concerned.   In an analysis of the Ft. Sill data, Turner [19] calculated the mass extinction coefficients according to the formula for a monodispersion:

$$\kappa_m = \frac{3}{\rho_p D} \tag{5.27}$$

where ρ_p is the particle density and D is the median diameter, and for the "geometric limit", i.e.

$$\kappa_m = \frac{3}{\rho_p} \frac{\sum\limits_{i=1}^{N} \psi_i D_i^2}{\sum\limits_{i=1}^{N} \psi_i D_i^3} \tag{5.28}$$

where ψ_i is the particle size distribution.   The results for four separate tests at Ft. Sill are given in Table 5.8.

TABLE 5.8

MASS EXTINCTION COEFFICIENTS (m^2/gm) FT. SILL DATA

	0.4 - 0.7 μm	1.06 μm	3.4 μm	9.75 μm
E	0.24	0.19	0.16	0.13
P_1^*	0.27	0.27	0.27	0.27
P_2^*	0.26	0.26	0.26	0.26
P_3^*	0.26	0.26	0.26	0.26
P_4^*	0.29	0.29	0.29	0.29
$P_1^\dagger$	0.61	0.61	0.61	0.61
$P_2^\dagger$	0.61	0.61	0.61	0.61
$P_3^\dagger$	0.67	0.67	0.67	0.67
$P_4^\dagger$	0.62	0.62	0.62	0.62

P_1, P_2, P_3, and P_4 refer to the four separate tests.

E   ~ According to experimental dosage

P_i^* ~ According to Eq. (5.28)

$P_i^\dagger$ ~ According to Eq. (5.27) with number median diameter.

5.2.1.3 <u>Scattering Parameters</u>

As far as can be determined from the literature no tests
have been performed which provide data on scattering attenuation
coefficients or scattering phase functions for vehicular dust.

5.2.1.4 Dispersion Parameters

From the literature there are no models or information on the dispersion parameters for vehicular dust. The parameters used will probably depend upon a specific, detailed model for the generation and dispersion of vehicular dust, which in turn, depends upon the meteorology and climatology of the region.

5.2.1.5 Other Parameters

There are other parameters which are of importance in vehicular dust studies. These are the particle size distributions, the complex index of refraction of the particles, and the cross sections. Details on these parameters will be discussed in the following sections.

5.2.1.5.1 Particulate Size Distributions

According to the EPA study [36] the MRI investigators used conventional cascade impactors to determine the particle size distributions of roadway emissions. The size distribution they obtained is given in Table 5.9.

TABLE 5.9

WEIGHT PERCENT DISTRIBUTION FOR ROADWAY DUST [35]

Particle Diameter (μm)	Weight Percent
< 2	25
2 - 30	35
30 - 100	40

This function ψ (r) is given in Table 5.10 for dust arising from many sources. It is interesting to note the bi-modal nature of the distribution for motor vehicles and for off-road vehicles. Although the distributions are coarse there does seem to be a peak in the small size range of 0 - 10 μm and another in the very large size range of 30 - 70 μm. The cumulative distribution by weight is illustrated in Figure 5.16 for various sources. The size distributions for the four vehicular dust tests at Ft. Sill, Oklahoma are summarized in Table 5.11.

5-51

TABLE 5.10 PARTICLE SIZE DISTRIBUTIONS FOR VARIOUS EMISSION SOURCE CATEGORIES*

Source Category	FRACTION OF ALL PARTICLES IN STATED SIZE RANGE							
	$\leq 10\mu$	$0-10\mu$	$\leq 20\mu$	$10-20\mu$	$\leq 30\mu$	$20-30\mu$	$\leq 70\mu$	$30-70\mu$
ANTHROPOGENIC								
Motor Vehicles	.41	.41	.52	.11	.60	.08	.85	.25
Ag. Tilling	.62	.62	.74	.12	.80	.06	.93	.13
Aggregate Sto.	1.00	1.00	1.00	-	1.00	-	1.00	-
Cattle Feed Lots	.41	.40	.52	.11	.60	.08	.85	.25
Off Road Vehicles	.41	.41	.52	.11	.60	.08	.85	.25
Construction	.66	.66	.89	.23	1.00	.11	1.00	-
Resuspension	.66	.66	.89	.23	1.00	.11	1.00	-
WIND BLOWN								
Unpaved Roads	.68	.68	.90	.22	1.00	.10	1.00	-
Agriculture	.68	.68	.90	.22	1.00	.10	1.00	-
Undisturbed Desert	.68	.68	.90	.22	1.00	.10	1.00	-
Tailing Piles	1.00	1.00	1.00	-	1.00	-	1.00	-
Disturbed Soils	.68	.68	.90	.22	1.00	.10	1.00	-
CONVENTIONAL								
Motor Vehicles	.91	.91	.93	.02	.94	.01	.97	.03
Aircraft	.91	.91	.93	.02	.94	.01	.97	.03
Point Sources	.99	.99	.99	-	.99	-	1.00	.01
Area Sources	.99	.99	.99	-	.99	9.	1.00	.01
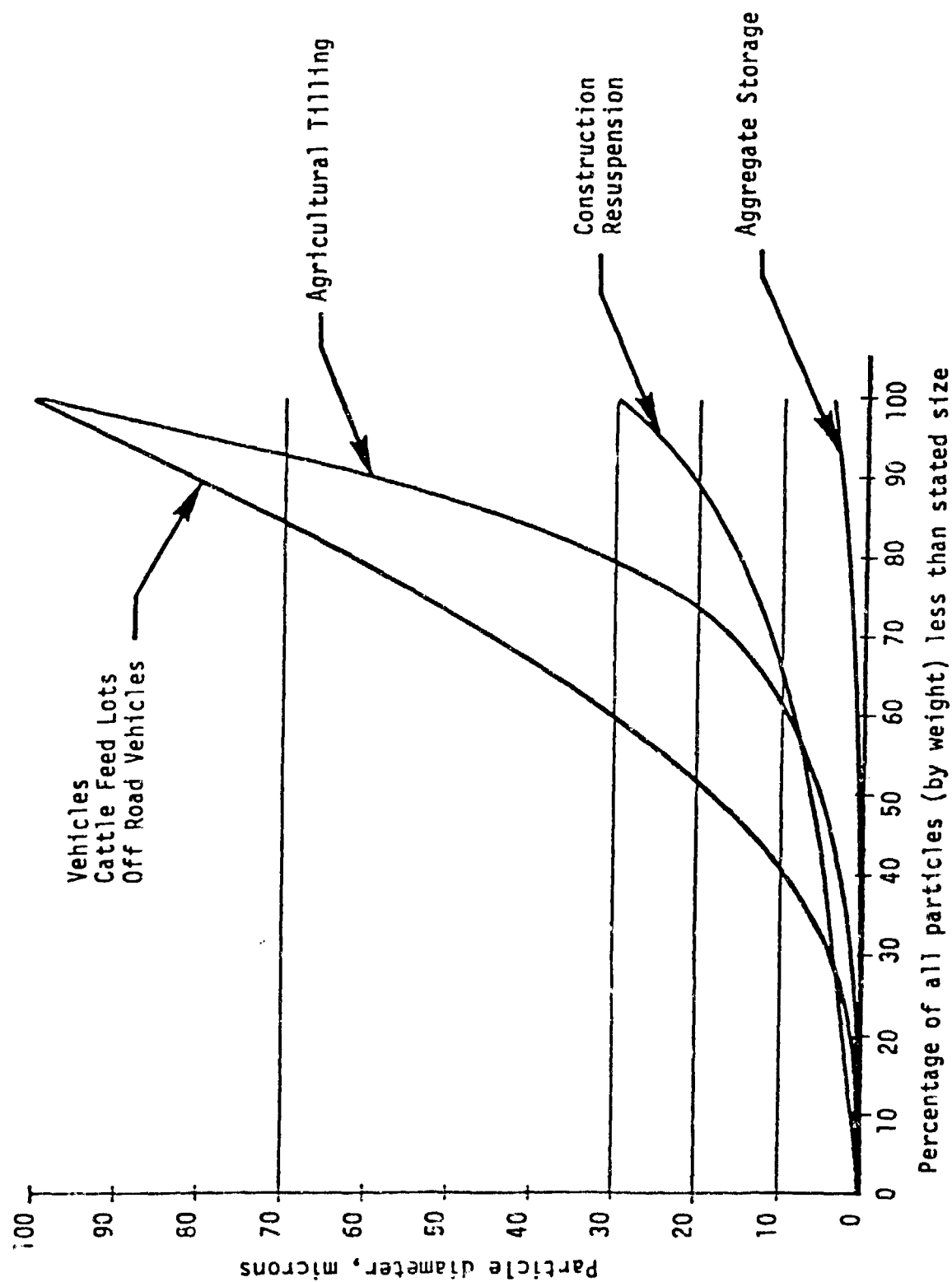
FIGURE 5.16. PARTICLE SIZE DISTRIBUTION OF ANTHROPOGENIC FUGITIVE DUST EMISSION SOURCES

TABLE 5.11

PARTICLE SIZE DISTRIBUTIONS (PER CENT) FOR
FT. SILL, OKLAHOMA VEHICULAR DUST TESTS.

Particle Diameter (μm)	P_1	P_2	P_3	P_4
0.65 - 1.3	12	14	18	13
1.3 - 2.3	17	19	20	15
2.3 - 10.0	69	66	59	71
10.0 - 15.0	1	2	2	0
15.0 - 20.0	0	0	0	0
> 20.0	0	0	0	0

Note: P_1, P_2, P_3, and P_4 refer to the four separate tests.

5.2.1.5.2 Complex Indices of Refraction

In order to calculate the total cross section one needs to know the complex index of refraction of the particle. A number of measurements [37, 38, 39, 40, 41, 42] have been made of airborne dust material and also of soil material but no experiments have been made on the dust samples representative exclusively of vehicle-generated dust. One can only make the reasonable assumption that the refractive index of the top layer of the soil is quite similar to that of the dust arising from that layer of soil.

Volz [37] analyzed Sahara dust, volcanic ash, and fly ash. The real and imaginary parts of the refractive index are illustrated in Fig 5.17 as a function of wavelength. Grams et al. [42] performed measurements of airborne soil particles and obtained a value for the complex index of 1.525 - 0.005 i.
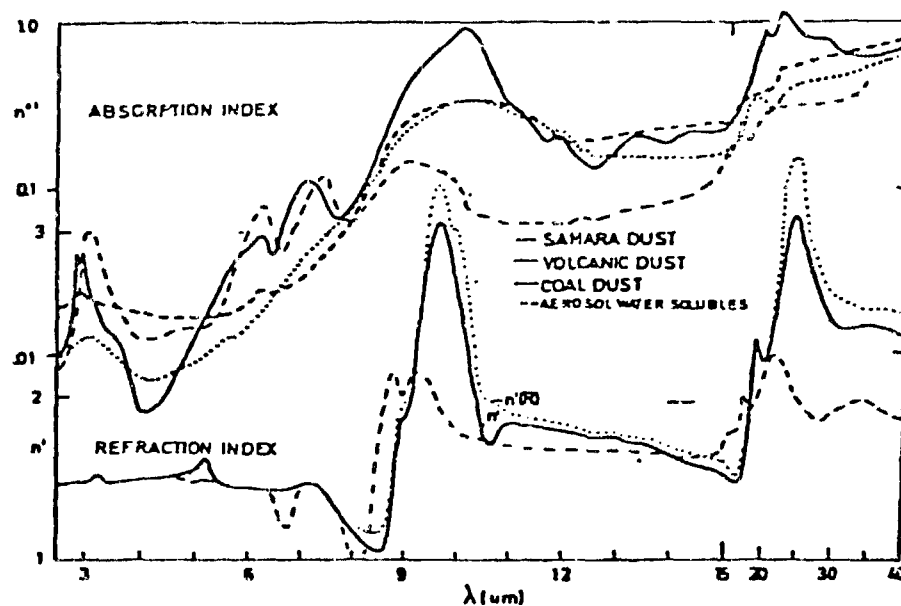
Fig. 5.17 Optical constants n', and n" of Sahara dust as compared with those of aerosol water-solubles and n" of volcanic dust and flyash. The dotted part of the n' curve of Sahara dust refers to observed reflectance [n' = (1 + R)/(1-R)] before correction for n".

5-55

Ebersole [39] compiled data by Volz and Lindberg for the real and imaginary indices for atmospheric dust. These are illustrated in Figs. 5.18 and 5.19. Finally, an excellent analysis of the imaginary refractive index was done by Lindberg, et al. [41] for a variety of locations. These are tabulated in Table 5.12.
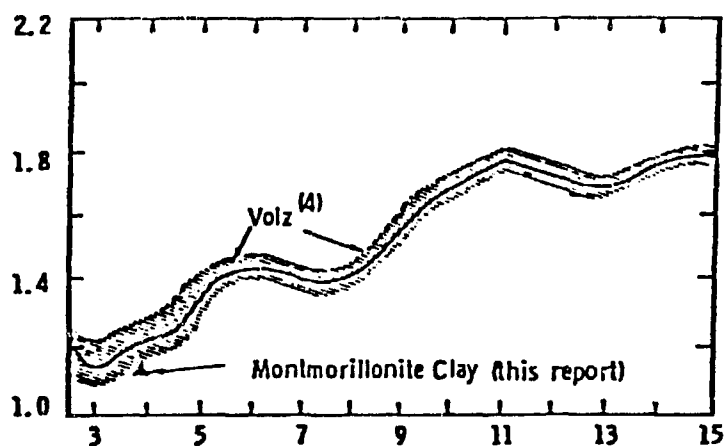
FIGURE 5.18   REAL INDEX OF REFRACTION FOR ATMOSPHERIC DUST
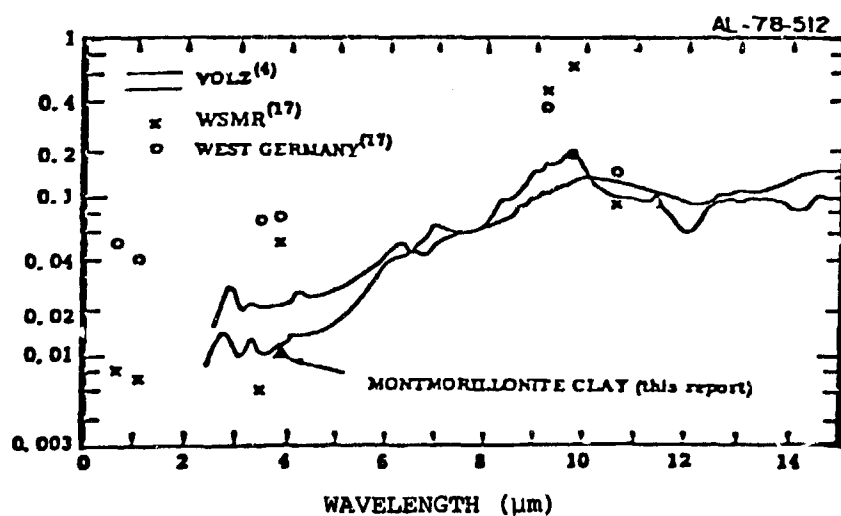
FIGURE 5.19   IMAGINARY REFRACTIVE INDEX VALUES FOR DUST SAMPLES

5-56

TABLE 5.12

IMAGINARY PART OF REFRACTIVE INDEX FOR VARIOUS REGIONS [13]

LOCATION, DATE	COMPLEX INDEX				OBSERVED COMPONENTS*
	0.30μm	0.69μm	1.06μm	1.70μm	
Manchester, G. B., May 76	.0546	.0616	.0713	.0968	AS, C, N
Meppen, W. Ger., May 76	.0436	.0506	.0603	.0803	AS, C, N
Rennes, Fr., Feb 76	.0183	.0222	.0290	.0429	AS, C, S, N
Lolland, Den, May 76	.0130	.0152	.0185	.0323	AS, C, N, S, Q
Garmish.P., W. Ger., May 76	.0077	.0156	.0220	.0264	AS, C, Q
Tel Aviv, Israel, Apr 76	.0363	.0282	.0295	.0396	S, CA, N, C
Aberdeen, M.D., USA May 76	.0152	.0167	.0202	.0341	AS, C, S, Q
Canal Zone, Panama, Apr 76	.0154	.0114	.0119	.0147	S, N
Negev Desert, Israel, May 76	.0103	.0053	.0053	.0068	G, S, CA, N
WSMR, N. Mex., USA, Jun 76	.0112	.0051	.0051	.0066	S, Q, CA, N

*AS - Ammonium Sulfate, C - Free Carbon, S - Silicate Clays, G - Gypsum, Q - Quartz, CA - Calcite,
N - Nitrate (Cation not identified)

5.2.2   GASEOUS AND PARTICULATE EXHAUST EMISSION

In this section we will consider the exhaust products from
military vehicles and the generation of dust by moving vehicles.
The Jeeps, trucks, tanks and other mobile equipment used by the
military will emit gases and particulates from their exhaust
systems in ranging amounts depending upon the type and size of
the engine and power demand. From the available data in the
literature as well as information gathered by personal contacts
we analyzed the critical factors such as gas concentration and the
cumulative mass distribution of the particulates. A more thorough
investigation of this source of gases is contained in the report
by Turner et al. [19].

5.2.2.1   Yield Factor

The major gaseous exhaust products of spart ignition (SI)
engines (gasoline engines) are CO_2, H_2O, CO, NO, and hydrocarbons.
O, H, OH, and H_2 also form during the combustion process, but
these are all highly reactive and have short lifetimes. CO_2 and
H_2O are not generally considered to be pollutants and exhaust
measurements of carbon dioxide and water vapor are rare despite
the fact that substantial amounts are emitted. CO_2 and H_2O are
important absorbers in the infrared, however. Table 5.13 indicates
the various military vehicles and associated emission data.

Table 5.14 lists estimates of engine emissions, in grams per
kilometer, for the three spark ignition engines from Table 5.13.
These estimates were made using the following formula:

$$\text{emission} \left(\frac{gm}{km}\right) = \text{emission} \left(\frac{gm}{cm^3}\right) \times \text{displacement } (cm^3)$$

$$\times 2{,}500 \text{ rpm} \times 1/2 \times 1 \frac{min}{km} \qquad (5.29)$$

TABLE 5.13

MILITARY VEHICLE DATA FOR SIX U.S. VEHICLES
Data compiled from References 43-46.

Vehicle Type	Engine Characteristics		hp/rpm	Manufacturer	Fuel Capacity	Vehicle Weight (loaded)
	Type	Model				
M151 Series Jeep	gas	Continental M151 4 cylinder 141-5 cu.in.	71/4000	AM General Corp.	56 l	1600-2000 kg
M705 Series 4x4 1 1/4 ton truck	gas	OHC 6-230 6 cyl. 230.5 cu. in displ.	132.5/4900	AM General Corp.		3800 kg
M34 Series 6x6 2 1/2 ton truck	gas	OA-331 Reo COA-331 Continental	146/3400	AM General Corp. (earlier, Reo and Studebaker)	189 l	8000-11000 kg
M60 Series Main battle tank	diesel	Continental 12 cyl. AVDS-1790-2 AVDS-1790-2A	750/2400	Chrysler	1457 l 1420 l	46000-52000 kg
M48 Series Main battle tank	diesel	Continental 12 cyl. AV-1790 AV-1790-8 AVDS-1790 AVI-1790-8	810/2800 825/2800 750/2400 810/2100	GM, Ford, Chrysler	757 l to 1420 l depending on model.	45000-49000 kg
M551 Light tank/reconnaissance vehicle	diesel	Detroit Diesel 6V53T 6 cyl.	300/2800	GM	598 l	16000 kg

TABLE 5.14

ESTIMATED EMISSIONS OF VEHICLES WITH SPARK IGNITION ENGINES, AND 1972 FEDERAL STANDARDS FOR PASSENGER CARS

	Jeep (Continental M151)	1 1/4 Ton Truck (OHC 6-230)	2 1/2 Ton Truck (COA-331)	1972 Federal Standards
H_2O	320 gm/km	520 gm/km	750 gm/km	
CO_2	700	1130	1630	
CO	17	27	39	24 gm/km
NO	7.0	11	16	2.5
HC	3.5	5.6	8.2	2.1

The factor of 1/2 is necessary because it takes two turns of
the engine for all the cylinders to fire in a four stroke engine.
A speed of one kilometer per minute is 37 miles per hour. The
federal standards for 1972 United States passenger cars is in-
cluded in Table 7 for comparison. When the federal standards were
changed in 1971 from units of concentration by volume to grams per
mile, conversions were done using a standard formula for exhaust
volume per mile as a function of vehicle weight. Had we used
this formula, our estimates (at least for the Jeep) would have
been lower.

Since 1972 the United States standards have become much more
rigid, leading to widespread use of smaller engines, with operat-
ing parameters modified to reduce emissions, and to measures
such as catalytic removal. These changes are not likely to be
seen on the battlefield.

Diesel engines emit H_2O, CO_2, CO, NO, hydrocarbons, and
aldehydes. Emission of CO, NO, and hydrocarbons is less than for
a comparable spark ignition engine. Diesel particulate emission
is higher than for comparable spark ignition engines, ranging
from 0.1 to 0.5 gm/bhp-hr for light duty engines to 1.0 to
1.5 gm/bhp-hr for large engines. The particulates are composed
primarily of carbon and carbon compounds. The small particles
are spherical and dominate the number distribution. The large
particles are aggregates and agglomerates of smaller particles,
have cluster and chain-like appearance, and dominate the mass
density.

Table 5.15 lists estimates of emission for the six U.S. military
vehicles whose characteristics are listed in Table 5.13. These
values are calculated in grams per minute. The same values may
be interpreted as grams per kilometer by assuming an average speed
of 1 kilometer per minute (37 mph). The values in Table 5.15 for
diesel engines assume the engines operating at two-thirds of their
rated horsepower. The gaseous emissions for diesel engines are

5-61

TABLE 5.15

ESTIMATED EMISSIONS FOR SIX U.S. MILITARY VEHICLES, IN GRAMS PER MINUTE

	Spark Ignition Engines			Diesel Engines		
	Jeep	1 1/4 Ton Truck	2 1/2 Ton Truck	M 551 light tank	M 60 battle tank	M 48 battle tank
H_2O	320	520	750	670	1500	1600
CO_2	700	1130	1630	1800	4000	4300
CO	17	27	39	13	44	47
NO	7	11	16	20	64	68
Aldehydes	–	–	–	1.7	4.2	4.4
Hydrocarbons	3.5	5.6	8.2	6.8	18	19
Particulates	0.1	0.2	0.3	3.3	12.5	13.3

less than for equivalent spark ignition engines, and the greater emission for the diesels in Table 5.15 is due to their much greater size and horsepower.

Although the values in Table 5.15 are not intended as absolute upper bounds, the estimates tend to be high rather than low. When a range of "typical" emission values was known, the high end of the range was used to calculate the values in Table 5.15. Engine emissions are highly variable, and the values in Table 5.15 must only be interpreted as rough estimates.

5.2.2.2   Attenuation Coefficients

Habibi [47] examined auto exhausts with an integrating nephelometer to determine visible scattering coefficients. He reports the following results:

	low aromatic content fuel	high aromatic content fuel
unleaded fuel	0.2 km^{-1}	1.3 km^{-1}
leaded fuel	0.15 km^{-1}	0.36 km^{-1}

Despite lower total emission rates, the unleaded fuel produces an aerosol with somewhat higher scattering coefficient. An earlier study discussed by Habibi [47] included tests for scattering and absorption coefficients in the air in a tunnel after driving a test vehicle inside the tunnel. The results of that study were:

	scattering	absorption
unleaded fuel	0.26 km^{-1}	0.31 km^{-1}
leaded fuel	0.24 km^{-1}	0.09 km^{-1}

5-63

Although this information is not a sufficient basis for any sweeping conclusions, it does seem to indicate that the larger, carbon dominated particles from unleaded fuel combustion cause slightly more scattering and considerably more absorption than particulates from leaded fuel, despite the smaller total mass emission for unleaded fuel.

Smoke is often monitored by smoke meters which measure the extinction of visible light over a fixed path. Vuk, Jones, and Johnson [48] provide a relationship between the smoke density measured by a smoke meter and the particle concentration. This is shown in Figure 5.20. Smoke density is the extinction coefficient in reciprocal meters, and the concentration in Figure 5.20 is the concentration at the sampling temperature. The curve in Figure 5.20 is a straight line with a slope of $0.0082 \text{ m}^{-1}/\text{mg} - \text{m}^{-3}$.
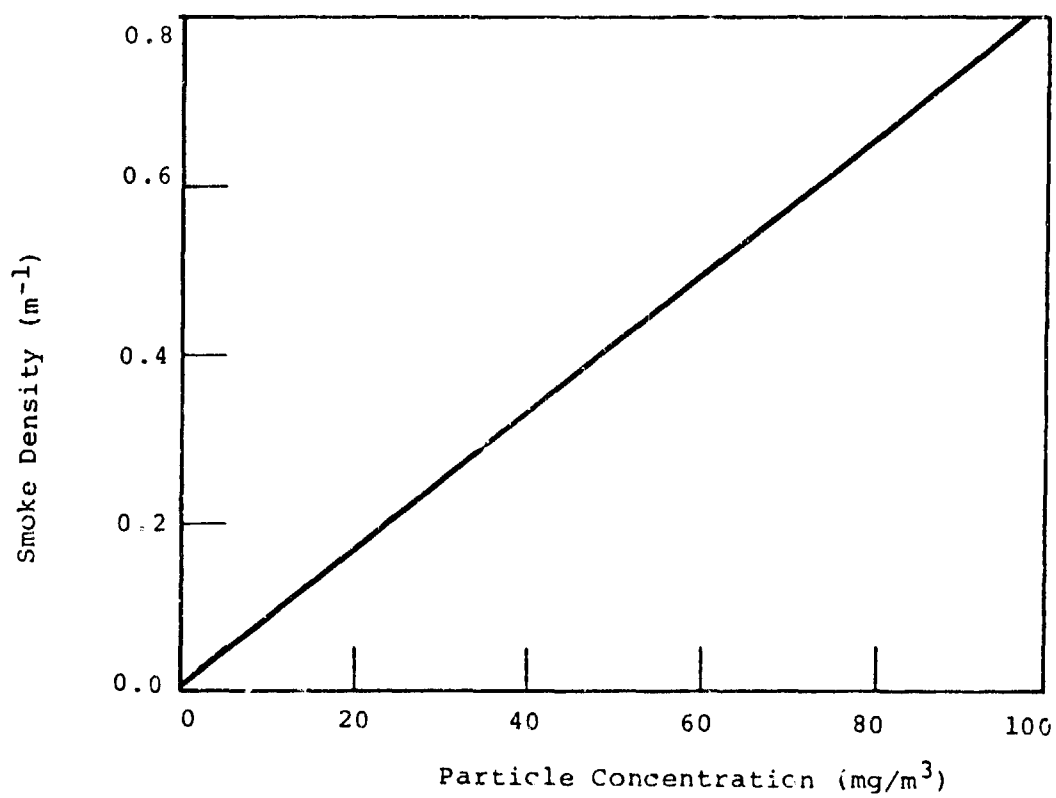
FIGURE 5.20.   RELATIONSHIP OF SMOKE DENSITY AND PARTICLE CONCENTRATION
AT THE EXHAUST TEMPERATURE.   SMOKE DENSITY IS THE VISIBLE
EXTINCTION COEFFICIENT.   FROM VUK, JONES, AND JOHNSON [48].

5.2.2.3 Scattering Parameters

No information has been obtained on the scattering phase functions for gaseous or particulate exhaust emission.

5.2.2.4 Dispersion Parameters

No specific information is available on the dispersion parameters for gases and particles resulting from exhaust emissions. These factors will probably be similar to the dispersion parameters for other gases and particulates with similar compositions.

5.2.2.5   Other Parameters

Among other parameters are the shapes, sizes, rates of emission and composition of exhaust particles.

Size distributions for diesel particulates tend to be bimodal, although this trend is not always as well defined as for particulates from spark ignition engines. Deposition on and reentrainment from the exhaust system walls is not a major source of large particles, as it is for spark ignition engines. The two modes for diesel particulates are small spherical particles formed from combustion related processes and aggregation, and larger agglomerates of these small particles. Figure 5.21 shows a particle size distribution measured by Khatri and Johnson [49]. The various peaks of the multi-mode structure as presumably due to different growth processes. The overall nature of the curve is bimodal, with the left hand portion of the curve expected to rise somewhat higher and then fall off sharply before reaching 0.001 µm (based on the observation of several authors that the smallest precursor particles are around 0.001 µm diameter).

Figure 5.22 is a size distribution by mass from Vuk, Jones, and Johnson [48]. The bimodal nature is not clearly defined here, with only a small peak or simply a long tail at the high mass end of the distribution. Between 50 and 75% of the spark ignition particulate mass is in particles smaller than 1 µm, versus 93% for diesel particulates.

Although the data for Figure 5.21 and 5.22 are from different experiments an important difference between the number density and mass size distributions is apparent. The mass distribution shows that 10% of the mass is contained in particles larger than 0.7 µm, but from the number density distribution only a small fraction of a percent of the particles are larger than 0.7 µm.
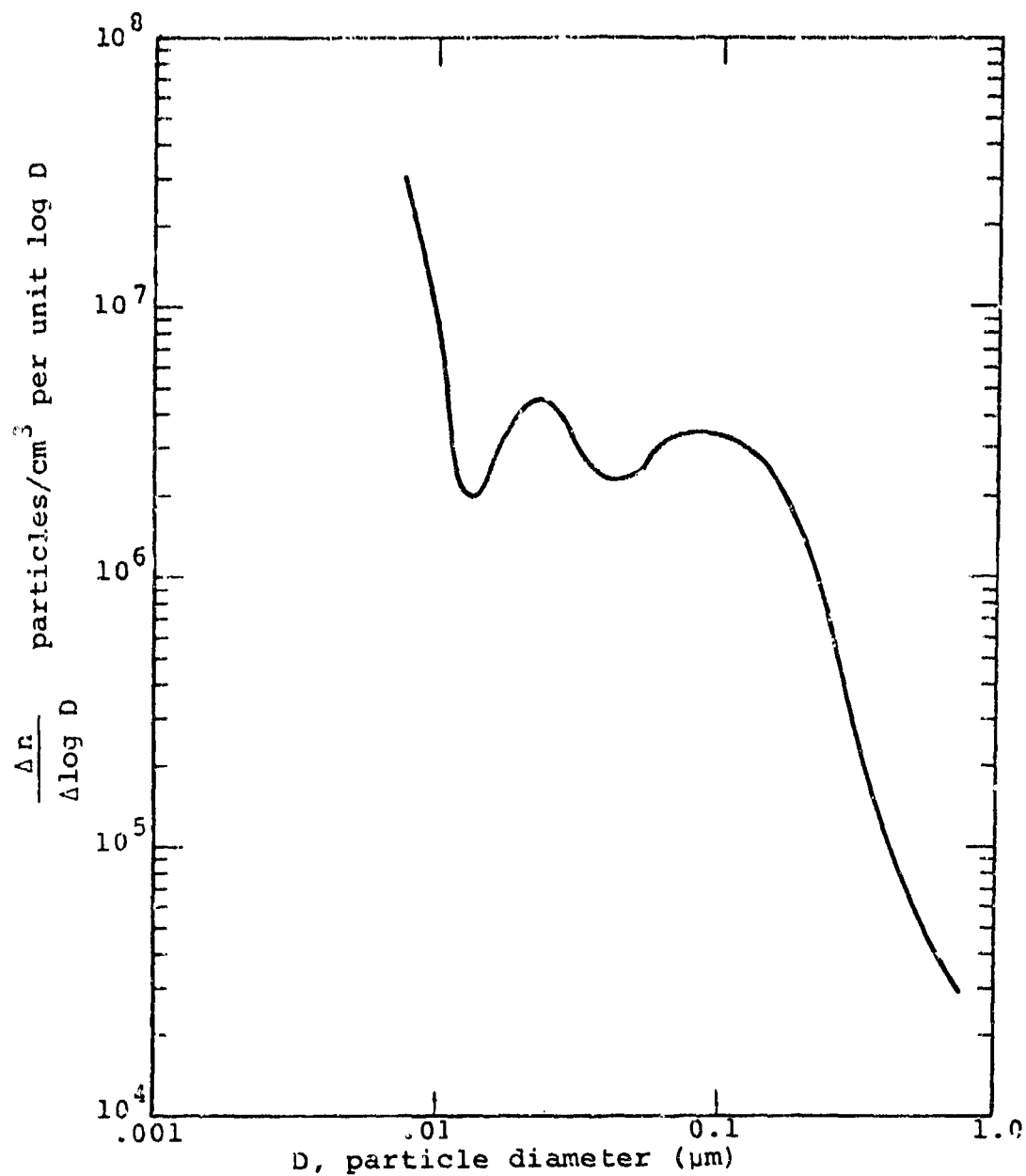
FIGURE 5.21. PARTICLE SIZE DISTRIBUTION FROM A DIESEL ENGINE. THE AREA UNDER THE CURVE BETWEEN TWO VALUES OF D REPRESENTS THE NUMBER PER cm^3 OF PARTICLES IN THAT SIZE RANGE. FROM KHATRI AND JOHNSON [49].
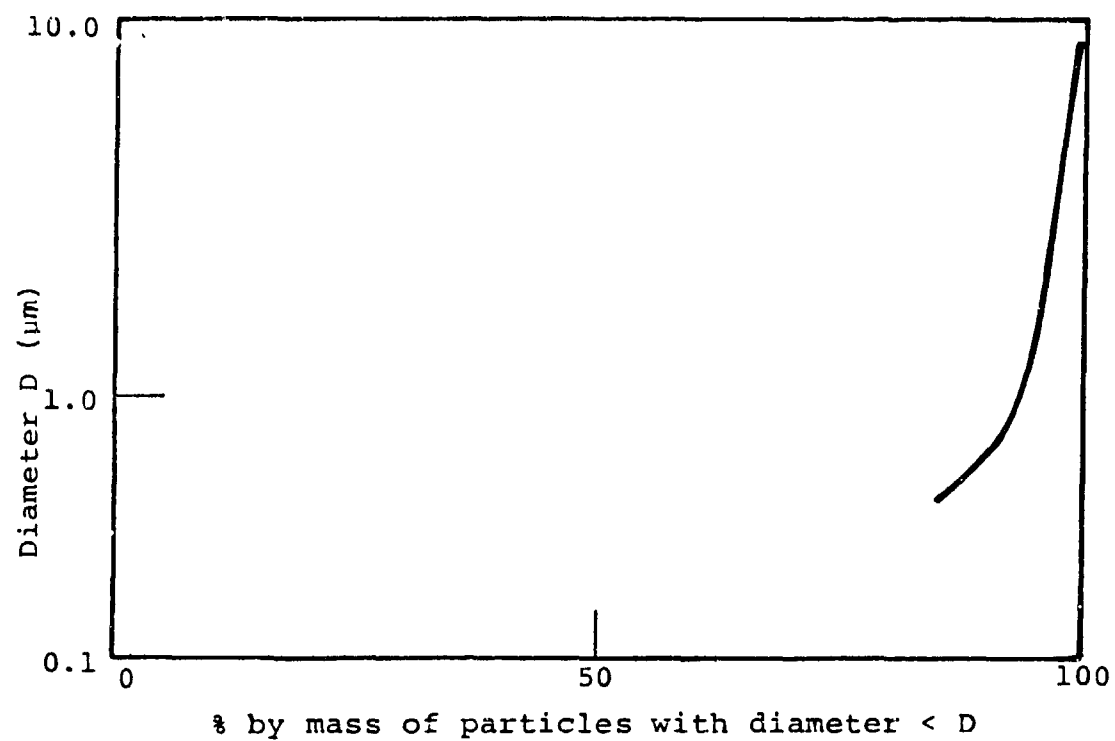
FIGURE 5.22. SIZE DISTRIBUTION BY MASS FOR PARTICULATES FROM A DIESEL ENGINE, FROM VUK, JONES AND JOHNSON [48].

5-70

The total particulate emission from the tests done by Vuk, Jones, and Johnson [48] was 246 mg/bhp-hr, averaged over the SAE 13-Mode Cycle (which consists of different loads and engine speeds). The range was from 82 to 507 mg/bhp-hr. These values are quite low for a large engine. Typical values for diesels range from 0.5 gm/bhp-hr for light duty engines to 1.0 to 1.5 gm/bhp-hr for large, heavy duty engines [50].

The number density from the work of Khatri and Johnson [49] corresponding to Figure 5.21 was 2.2×10^7 particles/cm^3. This was for mode 3 of the 13-mode cycle (1800 rpm, 25% load). The average over all the non-idle cycles was 5×10^7 particles/cm^3.

The composition of particulate matter from diesel engines depends on exhaust temperature. Above 200°C exhaust temperature the carbon to hydrogen molar ratio (atoms of carbon per hydrogen atom) is constant at 7 or higher [48], indicating that the particles are predominantly carbon. Below 200°C exhaust temperature (that is, for low load and low engine speed), the C/H ratio drops sharply, approaching 0.5, which is the approximate ratio for fuel molecules. There is also an increase in the relative number of large particles at exhaust temperatures below 200°C. At these lower exhaust temperatures, hydrocarbon vapors condense, using the existing carbon particles as condensation nuclei, to form hydrocarbon droplets.

5.3 BATTLEFIELD FIRES

5.3.1 FUEL FIRES

In this section we present data and models which describe the burning of fuel in bulk quantities as opposed to the combustion processes which occur in internal combustion engines.

5.3.1.1 Yield Factors

There is no specified yield factor defined for burning fuel. One can define the yield factor for spilled fuel or for burning in a drum or other container as

$$YF = \frac{\text{Mass of fuel burned in time interval } \Delta t}{\text{time interval } \Delta t} \qquad (5.30)$$

One of the authors of this handbook (Turner) had several personal conversations with personnel in the oil business and he was unable to obtain a useful relation for this term.

5.3.1.2   Attenuation Coefficients

Oil fires are composed of carbon or carbon-like material as well as other material which does not burn. No quantitative information exists on attenuation coefficients of fuel fire fumes or smoke.

5.3.1.3 Scattering Parameters

(Data void)

5.3.1.4   Turbulence

(Data void)

5.3.2   VEHICLE FIRES

5.3.2.1   Burning Land Vehicles

There is very little information on burning vehicles insofar as their quantitative attenuation properties are concerned. Some laboratory investigations have been performed on the materials of which vehicles are made.

In order to investigate the products of smoke from burning vehicles one would like to have an inventory of the type of burnable material, its weight or volume, and composition for each vehicle to be considered. Such information is not available. TARCOM in Warren, Michigan has the responsibility for collecting information on these subjects but all they could provide was the reference "Handbook of Ordnance Materials" which is out of print.

Information does exist on the burning of materials which are not necessarily related to military vehicles. A study by Dow Chemical Company [51] describes the laboratory analysis of burning material such as plywood and cotton batting. Samples were used in a chamber exposed to one watt per cm^2 heat flux and a 0.18 kilowatt intensity single point ignition source and the rate release of various components (gms/min-m^2) was measured. Of the plywood, 44 grams was the original mass whereas 13 grams was the mass of the cotton batting. The release rate data for plywood and the cotton batting are illustrated in Figures 5.23-5.30 and Tables 5.16 and 5.17.

Another study [52] was performed using samples of wood, rigid urethane foam, and PVC plastic under non-flaming conditions. The smoke particle size distributions were determined through sampling techniques using a Whitby aerosol analyzer and an Andersen sampler. Figure 5.31 depicts the comparison of size distributions for the three materials.
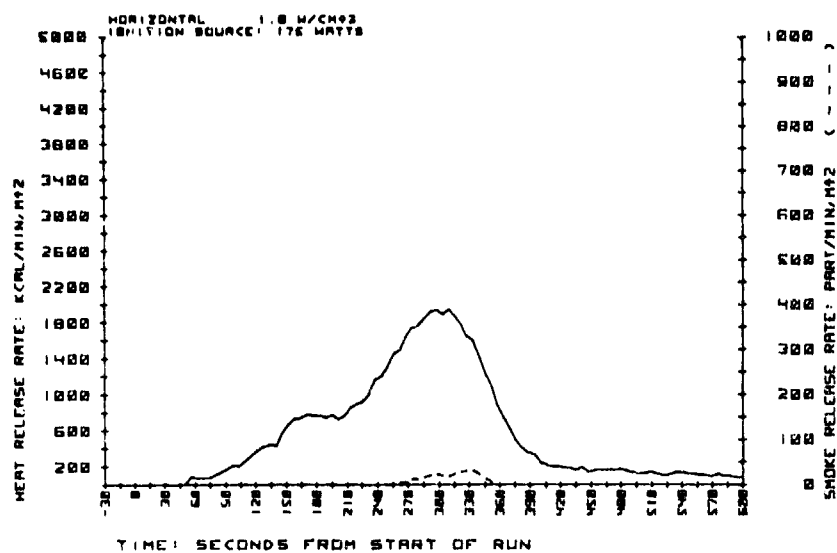
FIGURE 5.23. HEAT AND SMOKE RELEASE FROM PLYWOOD PANELING.
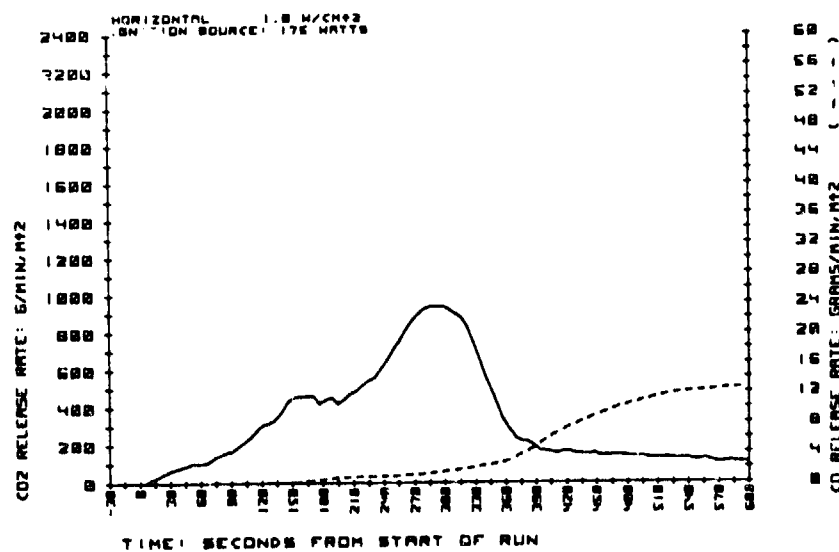
FIGURE 5.24. CO_2 AND CO RELEASE FROM PLYWOOD PANELING.

5-77
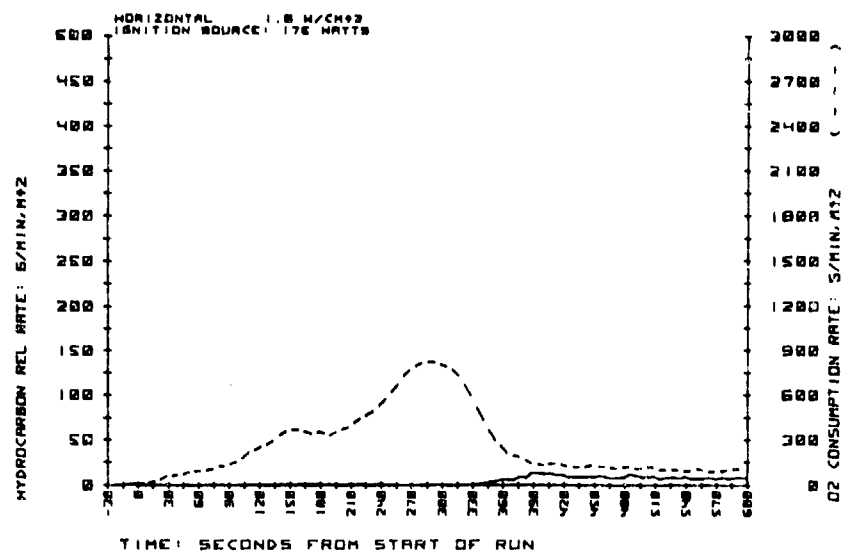
FIGURE 5.25.   HYDROCARBONS RELEASE AND O_2 CONSUMPTION FROM PLYWOOD
PANELING.
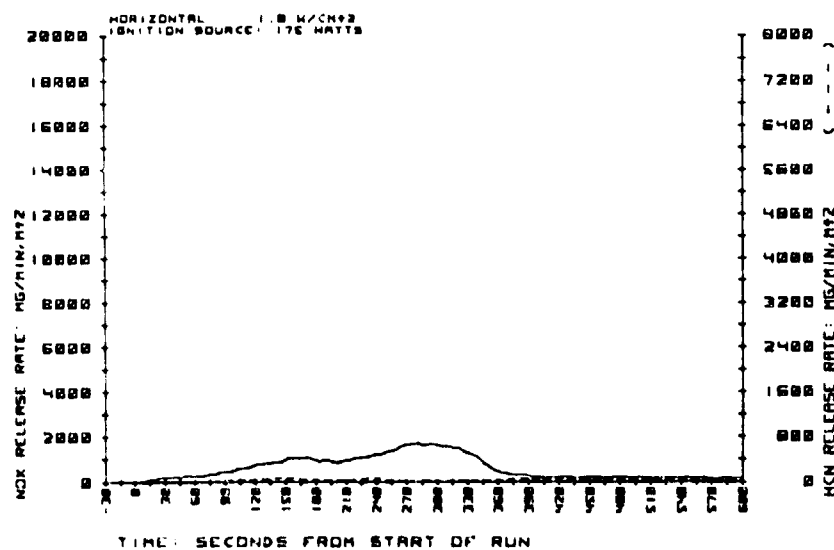
FIGURE 5.26. NO_x AND HCN RELEASE FROM PLYWOOD PANELING.
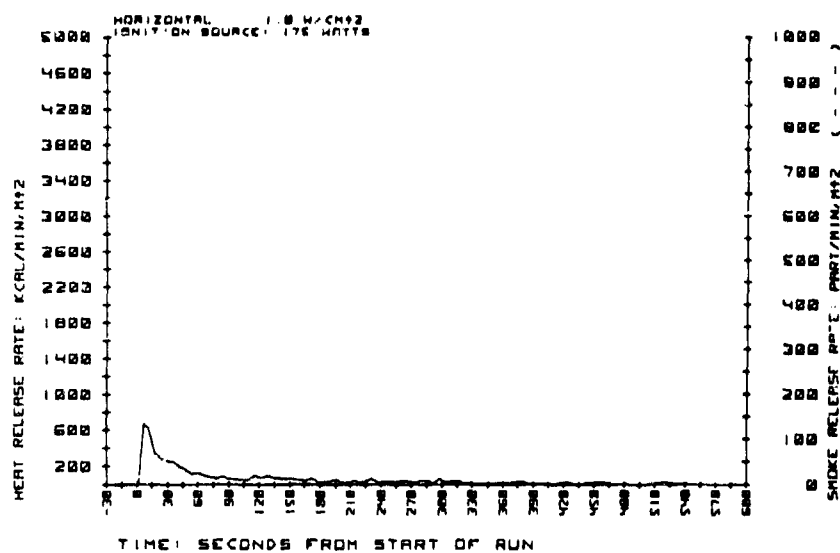
FIGURE 5.27. HEAT AND SMOKE RELEASE FROM COTTON BATTING.
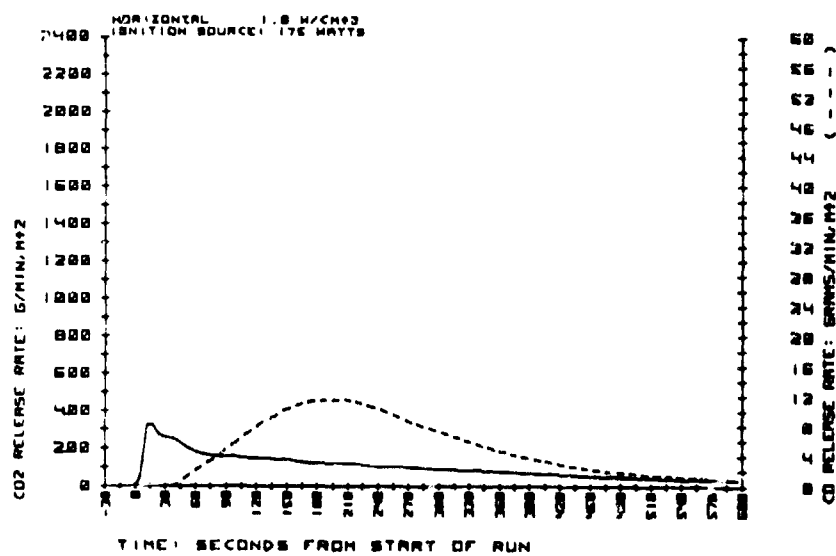
FIGURE 5.28. CO_2 AND CO RELEASE FROM COTTON BATTING.
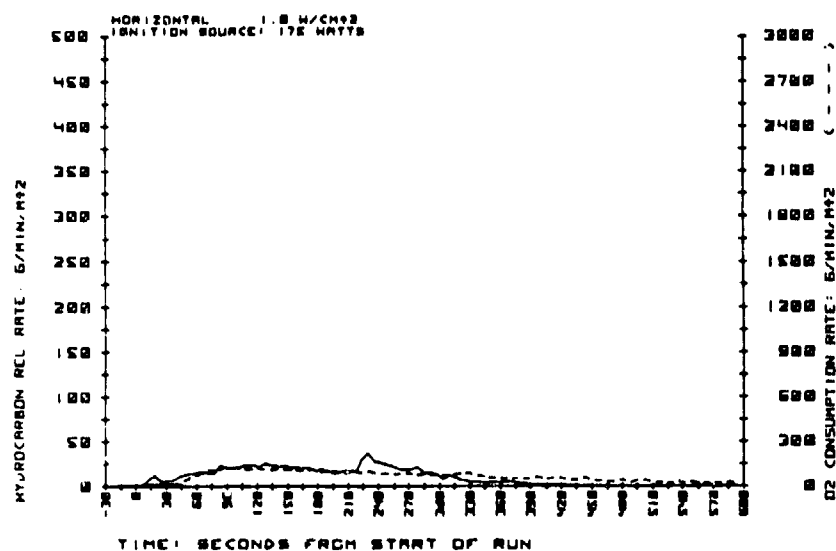
FIGURE 5.29.   HYDROCARBONS RELEASE AND O_2 CONSUMPTION FROM COTTON BATTING.
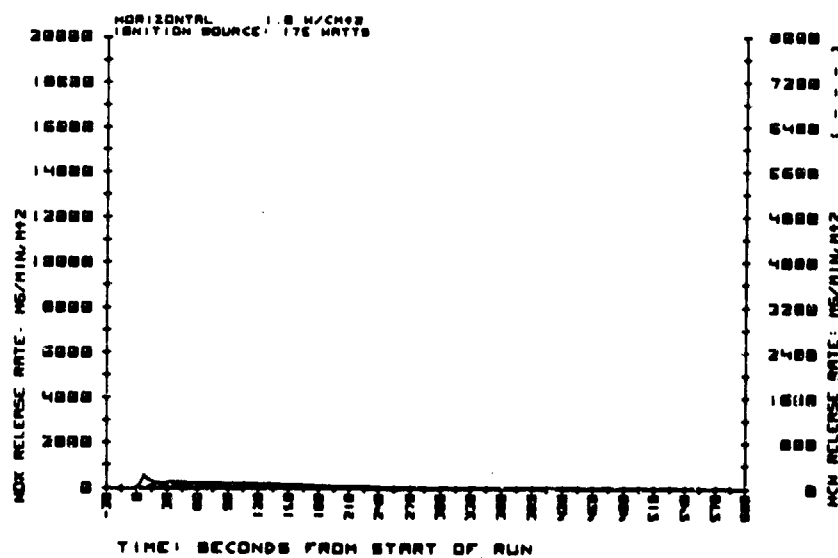
FIGURE 5.30. NO_x AND HCN RELEASE FROM COTTON BATTING.

TABLE 5.16

RELEASE RATE DATA FOR PLYWOOD PANELING AT 1.0 w/cm^2

Data (units)	Total Released per M^2 After			Max Rate Units/min, M^2	Time to Max
	3 min	5 min	10 min		
Heat(KCAL)	820	3390	5630	1950	310
Smoke(Particles)	0	11.3	30.7	32	334
CO(grams)	<1	2.0	41.4	13	600
CO$_2$(grams)	630	1950	3260	940	290
NOx(mg)	1610	4200	6160	1700	280
HCN(mg)	84	150	345	70	146
O$_2$(grams)	522*	1660	2720	825	290
Hydrocarbons(g)	2.3	4.3	40.4	13	390

*oxygen is depleted rather than released

TABLE 5.17

RELEASE RATE DATA FOR COTTON BATTING AT 1.0 w/cm^2

Data(units)	Total Released per M^2 After			Max Rate Units/min, M^2	Time to Max
	3 min	5 min	10 min		
Heat(KCAL)	430	505	555	660	7
Smoke(Particles)	<1	<1	<1	<1	145
CO(grams)	15.9	35.6	49.8	11.5	200
CO$_2$(grams)	520	737	1020	328	22
NOx(mg)	673	849	1040	560	7
HCN(mg)	150	183	220	60	83
O$_2$(grams)	233*	409	637	130	95
Hydrocarbons (grams)	49	90	100	37	235

*oxygen is depleted rather than released

Y-axis: Particle Weight Percent/Δ log D_p

X-axis: Particle Size - Microns

Legend:
—— Wood
— — Urethane
—·— PVC

$6.2 W/cm^2$
Air
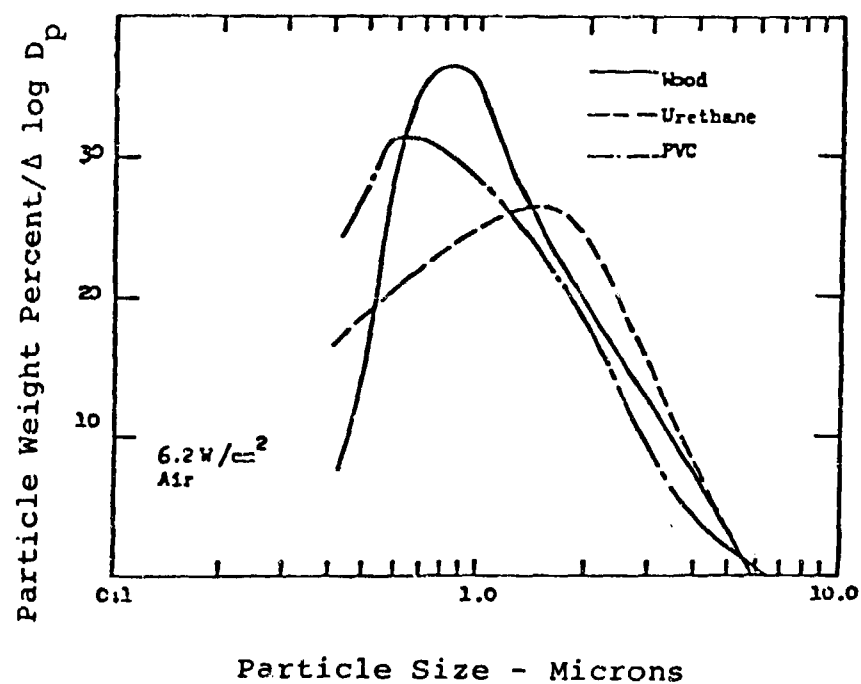
FIGURE 5.31. COMPARISON OF PARTICLE WEIGHT DISTRIBUTIONS
FOR WOOD, URETHANE AND PVC.

5-82

Seader and Ou [53] performed a series of experiments using the NBS Aminco Smoke-density Chamber. They measured the optical depth of various samples of burning (flaming and non-flaming) natural and snythetic polymers assuming a monochromatic light source, a uniform, stable, and monodisperse particulate system of spherical particles, and the single scattering. The results of their experiments are illustrated in Figures 5.32 and 5.33 in which the volume extinction coefficient $\kappa(m^{-1})$ is plotted against the mass concentration or density $\rho(mg/cm^3)$. By definition

$$\kappa(m^{-1}) \equiv \kappa_m(m^2/mg)\, \rho(mg/m^3) \qquad (5.31)$$

where κ_m is the mass extinction coefficient. It should be noted that their particulate optical density (POD) is related to the mass extinction coefficient given throughout this report by the following:

$$\kappa_m(m^{-1}) = 2.304 \text{ POD } (cm^2/gm). \qquad (5.32)$$

Thus, the mass extinction coefficient of the non-flaming mode is 4.38 m^2/gm and for the flaming mode it is 7.60 m^2/gm. The experimental data in Figure 5.32 are for a range of κ_m between 1.84 m^3/gm and 7.37 m^3/gm whereas for Figure 5.33 the range in κ_m is between 5.99 m^3/gm and 9.67 m^2/gm.

DIRT-I TEST

DIRT-I is the acronym given to the Dusty Infrared Test-I which was conducted at White Sands Missile Range in October, 1978. A number of excellent measurements were performed to

5-83
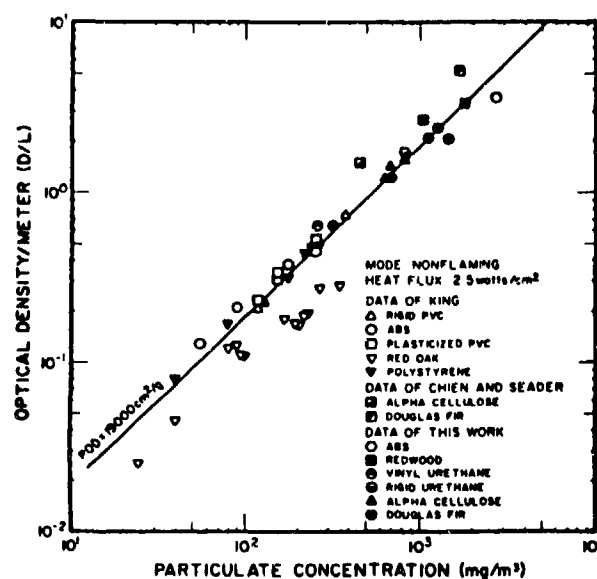
FIGURE 5.32. CORRELATION OF EXPERIMENTAL DATA ON PARTICULATE OPTICAL DENSITY FOR NONFLAMING MODE.
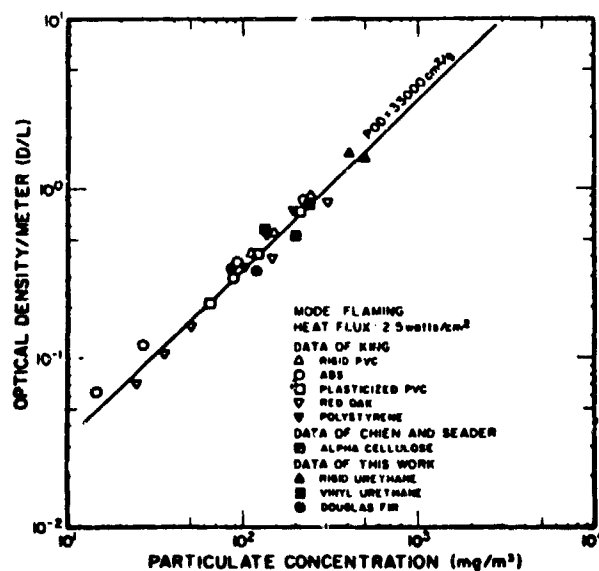
FIGURE 5.33. CORRELATION OF EXPERIMENTAL DATA ON PARTICULATE OPTICAL DENSITY FOR FLAMING MODE.

measure particle size distributions, soil samples, refractive indices, and various other optical parameters of interest. Of particular concern to us here is the so-called "G-Event" which was a fuel fire. Thirty-eight liters of diesel fuel, two liters of motor oil, and one rubber tire were placed into each container. The containers consisted of four 55-gallon steel drums cut in half and laid in a truck. As the entire mixture burned and produced great volumes of black smoke for a period of about 37 minutes a payload of instruments was flown through the cloud eleven times at various altitudes.

The analysis of this fire revealed that, as expected, the smoke contained a high percentage of carbon. The imaginary part of the refractive index is illustrated in Figure 5.34 for the spectral range 0.3 µm to 1.7 µm. The corresponding particle size distribution is depicted in Figure 5.35. It is interesting that there seems to be a bimodal aspect to the curve in a manner similar to that found in the airborne dust studies. More detailed information on DIRT-I is given in Section 7.
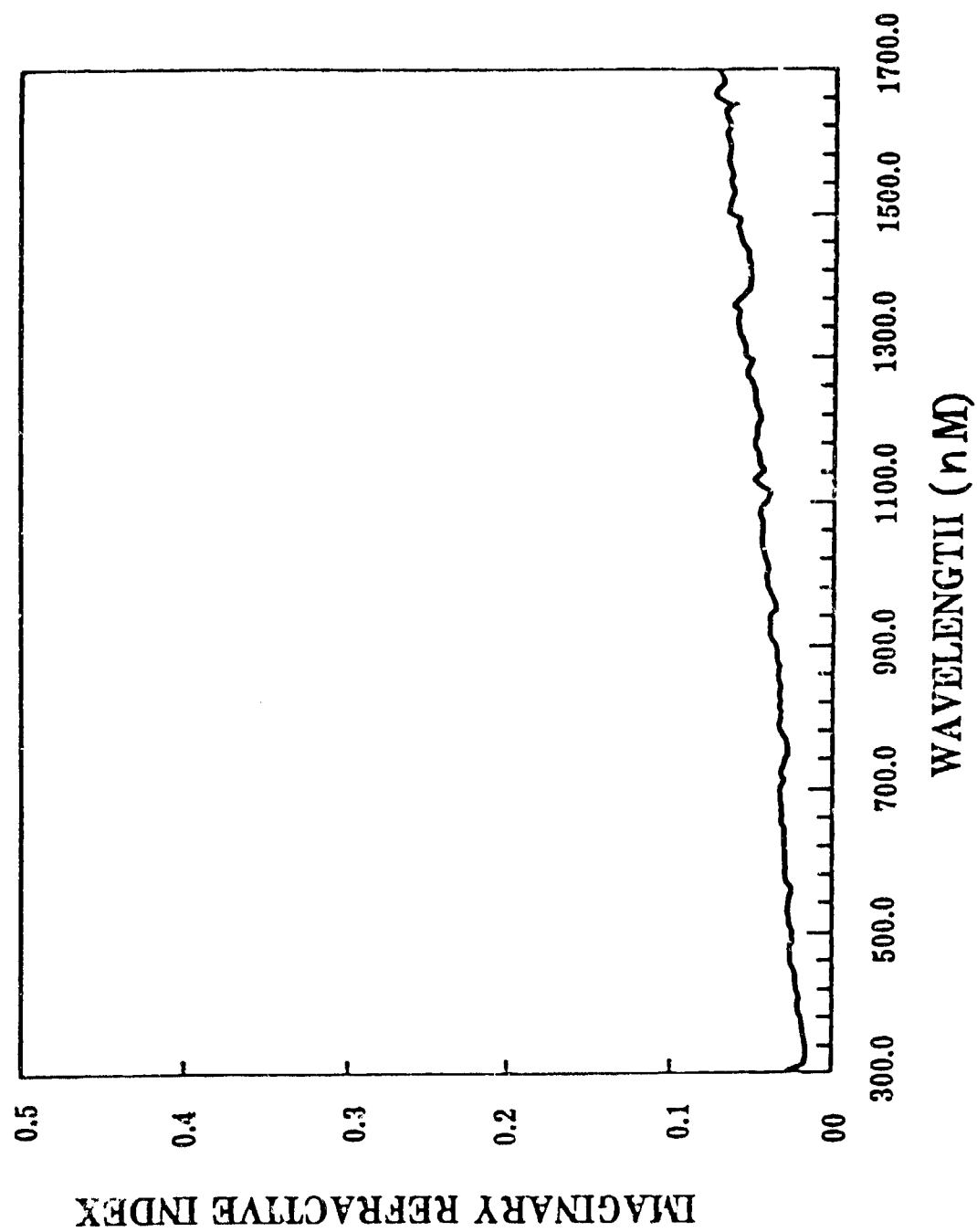
FIGURE 5.34. VISIBLE AND NEAR INFRARED IMAGINARY REFRACTIVE INDEX FOR BURNING RUBBER AND OIL SMOKE PARTICLES COLLECTED BY AIRBORNE PAYLOAD DURING EVENT G-1.
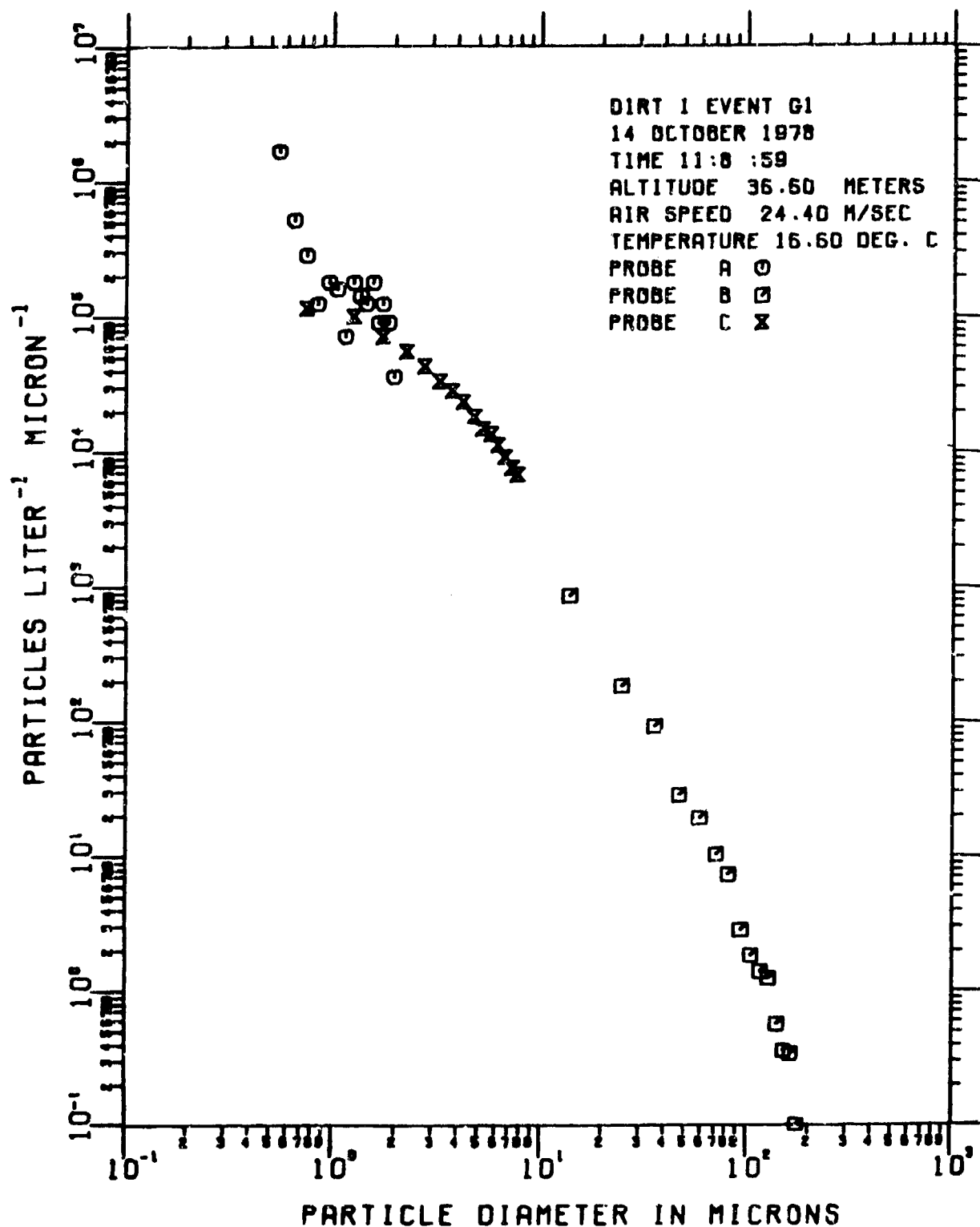
FIGURE 5.35. THIS PARTICLE SIZE DISTRIBUTION WAS RECORDED OVER A 10-SECOND INTERVAL 36.6 METERS ABOVE GROUND LEVEL DURING EVENT G-1. IT IS REPRESENTATIVE OF THE DENSE BLACK SMOKE THAT RESULTED FROM BURNING DIESEL OIL, MOTOR OIL, AND RUBBER.

5.3.2.2   Crashed Airplanes

No data exist on the burning of crashed airplanes. If the composition of airplanes is similiar to that of other military land vehicles then the results presented in Section 5.3.2.1 on burning land vehicles also apply here.

5.4 LAUNCHER INDUCED CONDITIONS

See classified supplement.

REFERENCES FOR SECTION 5

1. L.D. Duncan, R.C. Shirkey, R.A. Sutherland, E.P. Avara, and H.H. Monahan, "The Electro-Optical Systems Atmospheric Effects Library, Volume I: Technical Documentation", Atmospheric Sciences Laboratory Report ASL-TR-0047, December, 1979.

2. J.H. Thompson, "Models for Munition Dust Clouds", Atmospheric Sciences Laboratory Report ASL-CR-79-0005-2, June, 1979.

3. R. Zirkind, "A Battlefield Obscuration Model (Smoke and Dust)", General Research Corporation Report 524-02-79-CR, 1979.

4. C.H. Hayes, "High Explosive Dust Model for Battlefield Environment Laser Designator Weapon System Simulation (BELDWSS)" Lockheed Report LMSC-HREC-TM-D568393, August, 1978.

5. "Cratering from High Explosive Charges: Compendium of Crater Data", U.S. Army Engineer Waterways Experiment Station Technical Report 2-547, Report 1, May, 1960.

6. "Cratering from High Explosive Charges: Analysis of Crater Data", U.S. Army Engineer Waterways Experiment Station Technical Report 2-547, Report 2, June, 1961.

7. C.A. Miller, "Terrain Characteristics at DIRT-I Test Site, White Sands Missile Range, New Mexico", U.S. Army Engineer Waterways Experiment Station Paper EL-79-1, April, 1979.

8. U.S. Army Materiel Command Engineering Design Handbook, Principles of Explosive Behavior, AD900 260, April, 1972.

9. C.A. Miller, "Terrain Characteristics at DIRT-I Test Site, White Sands Missile Range, New Mexico", U.S. Army Engineer Waterways Experiment Station Paper EL-79-1, April, 1979.

10. Mary Ann Seagraves and Louis D. Duncan, "An Analysis of Transmittances Measured Through Battlefield Dust Clouds", U.S. Army Electronics Research and Development Command, Atmospheric Sciences Laboratory, White Sands Missile Range, NM 88002, dated February, 1980, Report ASL-TR-0050.

11. R.W. McMillan, R. Rodgers, R. Platt, D. Guillory, and J.J. Gallagher, "Millimeter Wave Propagation Through Battle-field Dust", Atmospheric Sciences Laboratory Report ASL-CR-79-0026-1, June, 1979.

12. J.F. Ebersole, R. Vaglio-Laurin, D.S. Dvore, and M. Martinez-Sanchez, "Obscuration Effects of Artillery-Produced Dust Clouds on Infrared Electro-Optical Systems", SPIE Proceedings Vol. 197, August, 1979.

13. F.E. Volz, Applied Optics 11 (4), 1972.

14. F.D. Lindberg, "Measured Effects of Battlefield Dust and Smoke on Visible, Infrared, and Millimeter Wavelength Propagation: A preliminary Report on Dusty Infrared Test-I (DIRT-I)", Atmospheric Sciences Laboratory Report ASL-TR-0021, January, 1979.

15. C.W. Wilson, "Air Blast Generated Battlefield Gases", SAI Internal Report, 1978.

16. Army Materiel Command Pamphlet AMCP 706-180, "Principles of Explosive Behavior", 1972.

17. M.A. Cook, "The Science of High Explosives", Reinhold Publishing Co., 1959.

18. D.H. Leslie, P.G Eitner, J.L. Manning, and S.M. Singer, "Infrared Electro-Optic System Performance Effects Due to Absorption by Battlefield Gases", SAI Report: SAI-78-010-AA-I, 1979.

19. R.E. Turner, P.G. Eitner, and J.L. Manning, "Analysis of Battlefield-Induced Contaminants for E-O SAEL", Vol. 1, SAI Report: SAI-79-005-AA-I, 1979.

20. B.R. Morton, G. Taylor, J.S. Turner, "Turbulent Gravitational Convection From Maintained and Instantaneous Sources", Proc. Roy. Soc., London, 234 (A), 1956.

21. J.S. Turner, :The Dynamics of Spheroidal Masses of Buoyant Fluid", Journal of Fluid Mechanics 19, 1965.

22. R.K. Dumbauld, "Smoke Diffusion Model Computer Program", H.E. Cramer Company, Inc., Report, Contract: DAEA-77-C-0060, Fall, 1977.

23. "AFGL Trace Gas Molecular Line Compilation", 1979.

24. J.H. Seinfeld, "Air Pollution: Physical and Chemical Fundamentals", McGraw-Hill, 1975.

25. F.R. Faxvog and D.M. Roessler, Applied Optics 17 (16), 1978.

26. D.M. Roessler and F.R. Faxvog, Applied Optics 18 (9), 1979.

27. D.M. Roessler and F.R. Faxvog: JOSA 70(2)(1980).

28. A.W. Casey and A.H. Biermann, "Characterizing High-Energy-Formed Particulates with the Scanning Electron Microscope/Energy Dispersive Spectrometer System", Progress Report UCID-17652, Lawrence Livermore Laboratories (1977).

29. A. LaRocca and R.E. Turner, "Atmospheric Transmittance and Radiance: Methods of Calculation", Environmental Research Institute of Michigan Report, June 1975.

30. J.W. Roberts, et al., "Cost and Benefits of Road Dust Control in Seattle's Industrial Valley," JAPCA, Vol. 25, No. 9, September, 1975.

31. C. Anderson, "Air Pollution from Dusty Roads," as presented at the 17th Annual Highway Engineering Conference, 1 April 1971.

32. J.M. Hoover, "Surface Improvement and Dust Palliation of Unpaved Secondary Roads and Streets," Final Report, by Engineering Research Institute, Iowa State University, ERI Project 856-S, submitted to the Iowa State Highway Commission, July, 1973.

33. "Air Pollution from Unpaved Roads," a research paper by the School of Engineering, University of New Mexico, January 12, 1971.

34. PEDCo Environmental Specialists, Inc., "Investigation of Fugitive Dust, Volume I - Sources, Emissions and Control," prepared for the Environmental Protection Agency, Office of Air Quality Planning and Standards, Research Triangle Park, North Carolina, June, 1974.

35. Midwest Research Institute, "Development of Emission Factors for Fugitive Dust Sources," prepared for the Environmental Protection Agency, Office of Air Quality Planning and Standards, Research Triangle Park, North Carolina, June, 1974.

36. An Implementation Plan for Suspended Particulate Matter in the Phoenix Area, Vol. I, II, and III., U.S. Environmental Protection Agency, Research Triangle Park, North Carolina 27711.

37. F.E. Volz, "Infrared Optical Constants of Ammonium Sulfate, Sahara Dust, Volcanic Pumice, and Flyash", Appl. Optics 12, 564-569, 1973.

38. F.E. Volz, "Infrared Refractive Index of Atmospheric Aerosol Substances", Appl. Optics 11, 755-759, 1971.

39. J.F. Ebersole, Experimental Investigation of Battlefield Aerosols Pertinent to High Energy Laser Propagation, Final Technical Report, ARI-RR-115, Aerodyne Research, Inc., 1977.

40. J.D. Lindberg, "The Composition and Optical Absorption Coefficient of Atmospheric Particulate Matter", Optical and Quantum Electronics 7, 131-139, 1975.

41. J.D. Lindberg, J.B. Gillespie, B. Hines, Measurement of Imaginary Refractive Indices of Atmospheric Particulate Matter from a Variety of Geographic Locations, Radiation in the Atmosphere, Ed., H.J. Bolle, Science Press, Princeton, 1977.

42. G.W. Grams, I.H. Blifford, Jr., D.A. Gillette, and P.B. Russell "Complex Index of Refraction of Airborne Soil Particles", J. Appl. Met 13, 459-471, 1974.

43. C.F. Foss, Jane's World Armoured Fighting Vehicles, St. Martin's, New York, 1976.

44. C.F. Foss, Military Vehicles of The World, Charles Scribner's Sons, New York, 1976.

45. B.H. Vanderveen, The Observer's Military Vehicles Directory from 1945, Frederick Warne & Co., Inc., New York, 1972.

46. W. Bryzik, U.S. Army Tank Command, private communication.

47. K. Habibi, "Characterization of Particulate Matter in Vehicle Exhaust", Environ. Sci. Tech. 7, 223-234, 1973.

48. C.T. Vuk, M.A. Jones, and J.H. Johnson, The Measurement and Analysis of The Physical Character of Diesel Particulate Emissions, SAE Technical Paper 760131, 1976.

49. N.J. Khatri and J.H. Johnson, The Physical Size Distribution of Diesel Particulate Matter and The Study of The Coagulation Process, SAE Technical Paper 760788, 1978.

50. J. Alson, U.S. Environmental Protection Agency, Ann Arbor, Michigan, private communication.

51. R.M. Herrington, B.A. Story, "The Release Rate of Heat, Smoke and Primary Toxicants from Burning Materials", J. Fire and Flammability 9, 284-306, 1978.

52. C.P. Bankston, R.A. Cassanova, E.A. Powell, B.T. Zinn, "Initial Data on the Physical Properties of Smoke Produced by Burning Materials Under Different Conditions", J. Fire and Flammability 7, 165-180, 1976.

53. J.D. Seader and S.S. Ou, Correlation of the Smoking Tendancy of Materials, Fire Research 1, 3-9, 1977.

6.1 NATURAL BATTLEFIELD ENVIRONMENTAL MODELS

In this section are described various models which deal with sources of environmental degradation. These models include natural and induced extinction, i.e. models which describe the attenuation and/or scattering of radiation in the natural environment in which there is human activity. A basic description of the models is given along with the typical input and output parameters.

6.1.1   LINE OF SIGHT OBSCURATION MODELS

In this section are described these models which allow one to calculate the attenuation of electromagnetic radiation along a specific line of sight from one point to another in a scattering, absorbing, or emitting medium. The obscuring medium may be com-posed of natural aerosols , fog particles, hydrometeors (pre-cipitation), gases, smoke, and dust particles. Some models treat the problem in a complete and practical way, i.e. they allow one to compute the line-of-sight transmittance directly from specific input data. Other models are less direct, i.e. they may allow one to calculate the particulate size distribution or mass extinction coefficient, given certain input parameters. It is then left to the user to implement these model outputs in a manner which is compatible with his problem. The interrelationships among the various parameters were described in Section 2.

6.1.1.1   Aerosol Extinction Models

Here are described extinction models for the natural aerosol component of the atmosphere. Thus, these models are used for hazes characterized generally by visual ranges greater than about 1 km.

6.1.1.1.1 Lockheed Model

Wells, Gal, and Munn [1] of the Lockheed Palo Alto Research Laboratory developed a model for the calculation of volume extinction coefficients in terms of relative humidity, altitude, visual range at sea level, and wind speed. They used Deirmendjian's size distribution, i.e.,

$$n_D(r) = ar^\alpha \exp[-br^\gamma] \tag{6.1}$$

where the parameters a and γ are given as a power law in wind speed v. Fitting the equations to actual data for aerosol distributions over the Pacific Ocean they determined the form of the parameters a and γ. Also, using the change in aerosol density with altitude they determined a new size distribution formula given by

$$n(r´) = \beta[vr^{-4}S_c + \alpha ar´ \exp(-br´^\gamma)S_M] \tag{6.2}$$

where

$r´ = r/F´$

$F´ = F(f)/F(0.8)$; for $f \geq 0.4$ (f = relative humidity fraction)

and S_c and S_M are the continental and maritime aerosol scale heights, α and β are visual range factors, and v is a normalization parameter for the total number density of particles under low wind conditions. Equation 6.2 takes into consideration the aerosol growth law

6-2

$$F(f) = 1 - 0.9 \ln[1 - f]. \qquad\qquad (6.3)$$

An example of the volume extinction coefficient as a function of wind speed and visual range is illustrated in Figure 6.1 for a continental maritime mixing ratio of 1:2.5 at a wavelength of 3.8 µm.

It should be noted that in the Lockheed model quantities which depend on wind speed were derived using data over sea surfaces. It is far more difficult to obtain data over land areas in terms of wind speed and undoubtedly there would be greater variability due to the heterogeneous nature of land surfaces.

A diagram of the input and output parameters of the Lockheed model is given in Figure 6.2.
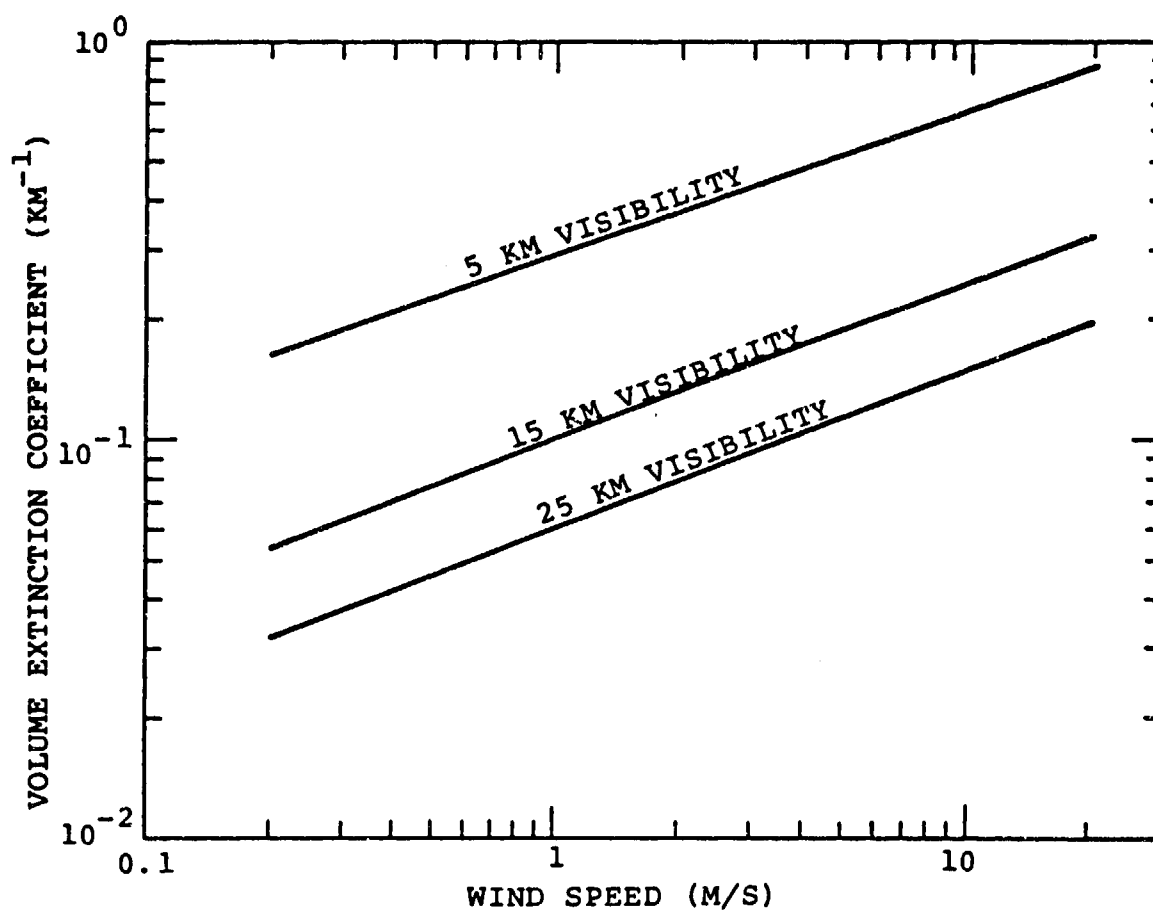
FIGURE 6.1   VOLUME EXTINCTION COEFFICIENT ACCORDING TO TH
WELLS-GAL-MUNN MODEL.   WAVELENGTH = 3.8 μm.

6-4

LOCKHEED MODEL

```
┌──────────────────────────────────────────────┐
│                    INPUT                       │
├──────────────────────────────────────────────┤
│                                                │
│   WAVELENGTH                                   │
│                                                │
│   WIND SPEED (M/SEC)                           │
│                                                │
│   VISIBILITY (SEA LEVEL) (KM)                  │
│                                                │
│   ALTITUDE (KM)  <   5 KM                      │
│                                                │
│   RELATIVE HUMIDITY                            │
│                                                │
└──────────────────────────────────────────────┘
                        │
                        ▼
┌──────────────────────────────────────────────┐
│                   OUTPUT                       │
├──────────────────────────────────────────────┤
│                                                │
│   PARTICLE SIZE DISTRIBUTION                   │
│                                                │
│   VOLUME EXTINCTION COEFFICIENT                │
│                                                │
└──────────────────────────────────────────────┘
```
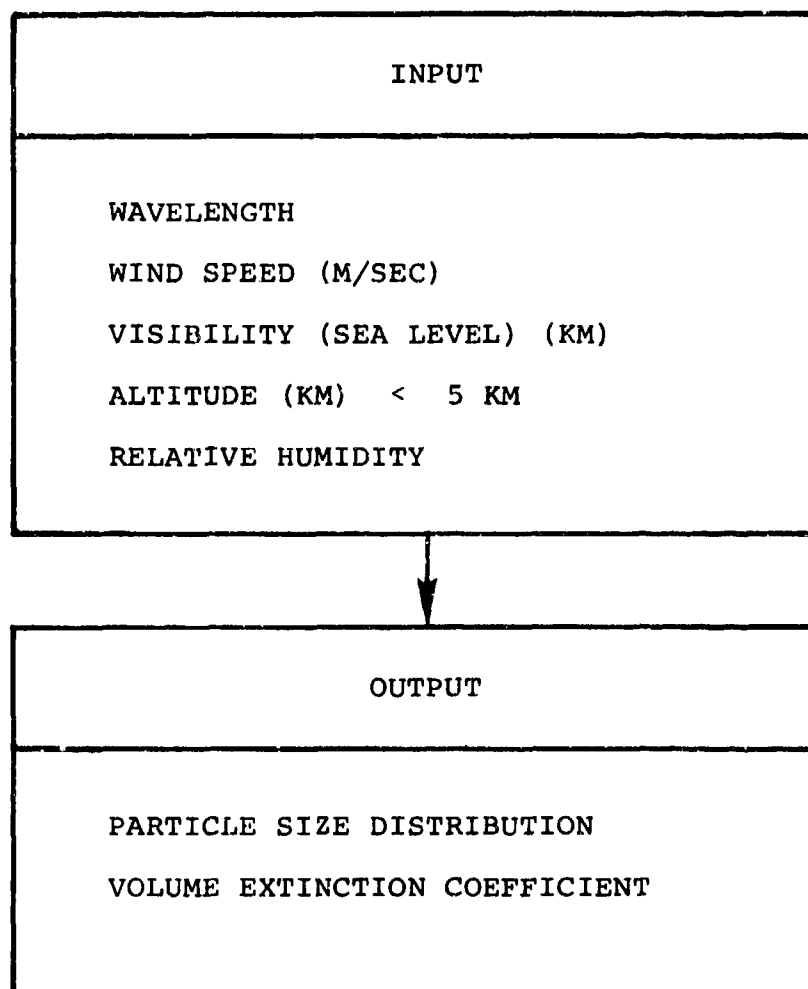
FIGURE 6.2   INPUT AND OUTPUT PARAMETERS FOR THE LOCKHEED
              MODEL.

6.1.1.1.2 Laops Model

Barnhardt and Streete [2] of the Laboratory of Atmospheric and Optical Physics, Southwestern (LAOPS) developed a model for aerosol scattering coefficients in the infrared in terms of relative humidity. The constant factor growth law which they used is

$$F_{BS}(f) = 1 - 0.36 \ln(1 - f) \qquad (6.4)$$

and the mixed particle distribution factor is

$$n(r) = Mn_m(r) + Cn_c(r) \qquad (6.5)$$

where M and C are the relative weights of the maritime and continental distributions. They also considered the relative humidity dependence of the complex index of refraction, i.e

$$m(f) = 1.54 + 0.030 \ln(1 - f) \qquad (6.6)$$

for the condensation nucleus.

Using these equations Barnhardt and Streete calculated the volume scattering coefficients for various wavelengths from 0.5 to 10.5 μm and for various relative humidities and continental maritime mixing ratios. These results are illustrated in Figures 6.3 through 6.4. The results are good for a relative analysis of the effect of changes in relative humidity and air mass mixings but do not illustrate the absolute value in terms of visual range.

6-6
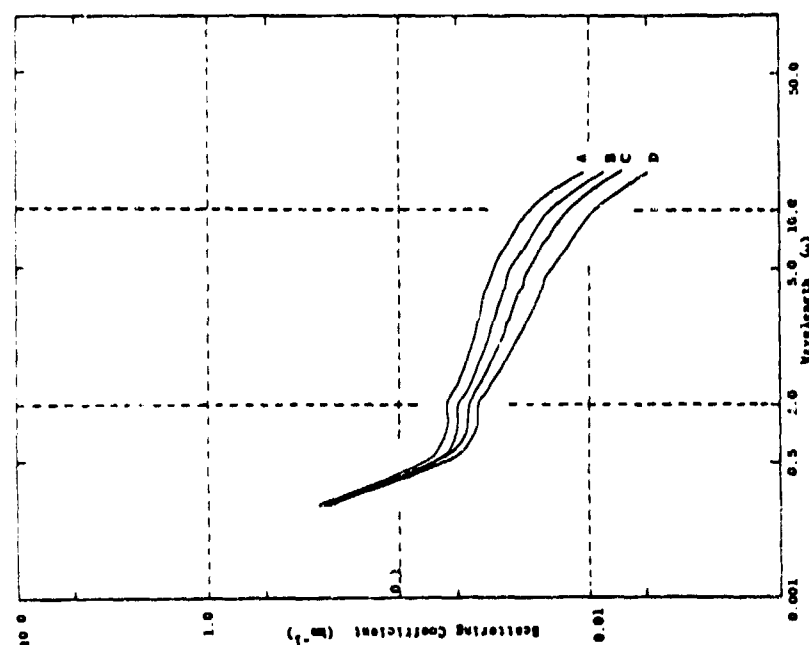
FIGURE 6.3   CALCULATED SCATTERING COEFFI-
CIENTS AT 50% RELATIVE HUMIDITY
FOR SEVERAL MIXINGS, CONTINENTAL:
MARITIME; (A) 1.0:2.5; (B) 1.0:2.0;
(C) 1.0:1.5; and (D) 1.0:1.0.
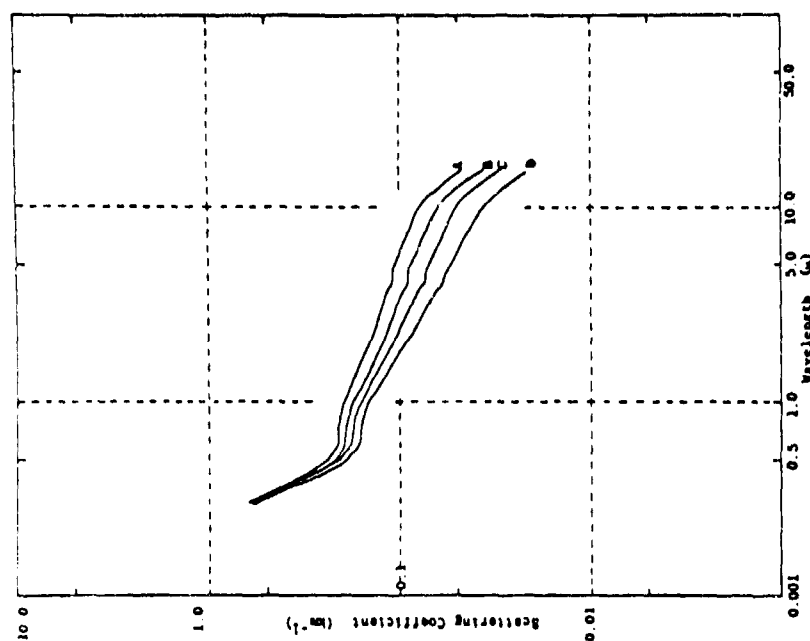
FIGURE 6.4   CALCULATED SCATTERING COEFFI-
CIENTS AT 90% RELATIVE HUMIDITY
FOR SEVERAL MIXINGS, CONTINENTAL:
MARITIME; (A) 1.0:2.5; (B) 1.0:2.0;
(C) 1.0:1.5; and (D) 1.0:1.0.

6-7

Figures 6.5 and 6.6 clearly indicate the effect of the large
growth in particle size with increasing relative humidity. It
seems to be important at all wavelengths but especially between 1
and 10 μm. There is no wind speed, altitude, or visual range de-
pendence in this model as in the Lockheed model but the relative
humidity dependence seems to be valid at least for the data for
which the model calculations have been compared.

The general range of validity of the model by Barnhardt and
Streete is for the 1.0 - 15.0 μm wavelength region. An indication
of the input and output parameters is given in Figure 6.7.

FIGURE 6.6. CALCULATED SCATTERING COEFFI-
CIENTS FOR A 1.0:2.5 CONTIN-
ENTAL:MARITIME MIXING RATIO
FOR SEVERAL VALUES OF RELATIVE
HUMIDITY; (A) 98.8%; (B) 95%;
(C) 90%; (D) 80%; (E) 70%;
(F) 60%, AND (G) 50%.

FIGURE 6.5. COMPARISON OF CALCULATED AND
MEASURED SCATTERING COEFFI-
CIENTS. ALL CALCULATED CURVES
ARE FOR A 1.0:1.0 CONTINENTAL:
MARITIME MIXING; (A) CALCULATED,
98.8% R.H.; (B) MEASURED, 97%
R.H.; (C) CALCULATED, 95% R.H.;
(D) CALCULATED, 60% R.H.;
(E) MEASURED, 57% R.H., and
(F) CALCULATED, 50% R.H.

LAOPS MODEL

```
┌─────────────────────────────────────────────────┐
│                                                 │
│                     INPUT                       │
│                                                 │
├─────────────────────────────────────────────────┤
│                                                 │
│  WAVELENGTH                                     │
│                                                 │
│  RELATIVE HUMIDITY                              │
│                                                 │
│  AEROSOL MIX (CONTINENTAL/MARITIME)             │
│                                                 │
└─────────────────────────────────────────────────┘
                          │
                          │
                          ▼
┌─────────────────────────────────────────────────┐
│                                                 │
│                    OUTPUT                       │
│                                                 │
├─────────────────────────────────────────────────┤
│                                                 │
│  PARTICLE SIZE DISTRIBUTION                     │
│                                                 │
│  VOLUME SCATTERING COEFFICIENT                  │
│                                                 │
└─────────────────────────────────────────────────┘
```

FIGURE 6.7   INPUT AND OUTPUT PARAMETERS FOR THE LAOPS MODEL

6.1.1.1.3 AFGL Model

The various computer codes under the general name LOWTRAN developed by the Air Force Geophysics Laboratory are well known [3]. The original emphasis in these codes was on the transmittance along a horizontal, vertical, or short path for molecular absorption. More recently, aerosol attenuation and thermal emission have been added to the analysis. Here we are primarily interested in the aerosol part of the programs. The volume extinction and absorption coefficients are given for several atmospheres (maritime, urban, rural, tropospheric average continental) and for wavelengths between 0.20 and 30 um for a visual range of 23 km and 5 km. The extinction and scattering coefficients for any wavelength and visual range are given by a simple interpolation, i.e.

$$\frac{\kappa(z,\lambda,V) - \kappa(z,\lambda,V_1)}{\kappa(z,\lambda,V_1) - \kappa(z,\lambda,V_2)} = \frac{\frac{1}{V} - \frac{1}{V_1}}{\frac{1}{V_1} - \frac{1}{V_2}} \qquad (6.7)$$

where $\kappa(z,\lambda,V)$ is the volume extinction coefficient at altitude z, wavelength λ, and visual range V. The altitude dependence is given by a table of number density as a function of altitude for 23 and 5 km visual range models. Thus, knowing $\kappa(0,\lambda,V_1)$ and $\kappa(0,\lambda,V_2)$, the surface values, one can solve Eq. 6.7 for $\kappa(z,\lambda,V)$. This is however, a limited method because it necessarily assumes that all atmospheres have the same aerosol profiles independent of the visual range V. There is no dependence of aerosol properties on wind speed or relative humidity.

It should be pointed out that LOWTRAN is probably a good code to use for gaseous transmittance and for thermal radiance but one should use caution in accepting the aerosol transmittance values.

Also, there is no radiance calculated in LOWTRAN for scattered
radiation. The only radiance is that arising from radiation which
is emitted and attenuated along a path. A specification of the
input and output parameters for the AFGL model is given in
Figure 6.8.

AFGL MODEL

```
┌─────────────────────────────────────────────────┐
│                     INPUT                         │
├─────────────────────────────────────────────────┤
│                                                   │
│   WAVELENGTH                                       │
│                                                   │
│   ALTITUDE                                         │
│                                                   │
│   VISUAL RANGE ,  RELATIVE HUMIDITY                │
│                                                   │
└─────────────────────────────────────────────────┘
                         │
                         ▼
┌─────────────────────────────────────────────────┐
│                     OUTPUT                        │
├─────────────────────────────────────────────────┤
│                                                   │
│   VOLUME EXTINCTION COEFFICIENT                    │
│                                                   │
│   TRANSMITTANCE                                    │
│                                                   │
└─────────────────────────────────────────────────┘
```
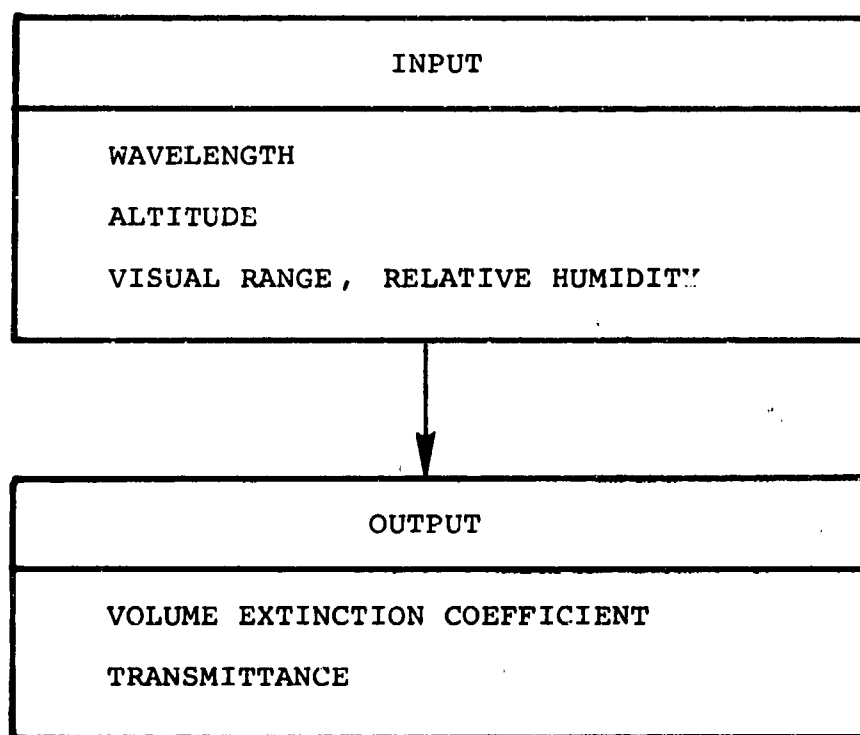
FIGURE 6.8   INPUT AND OUTPUT PARAMETERS FOR THE AFGL MODEL

6-12

6.1.1.1.4 SAI Water-Haze Model

Most attenuation models depend upon visual range or particle number density at the Earth's surface. This is not realistic however, because although the visual range might be the same at the surface for some atmospheres, the vertical profiles of density would be quite different. Hence, the slant path and vertical path transmittances would be quite different. A model to account for these differences using actual measured data in West Germany was devised by one of the authors (Turner) and is presented in detail in an Air Force Report [4]. The basic idea is as follows: from the measured particle size distributions one calculates the volume extinction coefficient at $\lambda = \lambda_0 (= 0.55 \ \mu m)$ and the liquid water content. These functions were calculated for nine size distributions which represent data for haze and light haze conditions. The data points were plotted and a straight line in log-log space was fit through the points. It is represented in Figure 6.9 and is given by

$$\ln \kappa_{A,p} \ (\lambda,z,V) = S(\lambda) \ \ln W_p(z,V) + \ln I(\lambda) \qquad (6.8)$$

where A refers to aerosol and p is the profile parameter, κ is the extinction coefficient, W is the liquid water content (gm/cm^3) and $S(\lambda)$ and $I(\lambda)$ are the slope and intercept. Using a simple scaling law the extinction coefficient for any wavelength and visual range at the surface is given by

$$\kappa_{A,p}(\lambda,0,V) = I(\lambda) \left[\frac{\frac{C}{V} - \kappa_R(\lambda,0) - \kappa_G(\lambda_0,0)}{I(\lambda_0)} \right]^{S(\lambda)/S(\lambda_0)} \qquad (6.9)$$
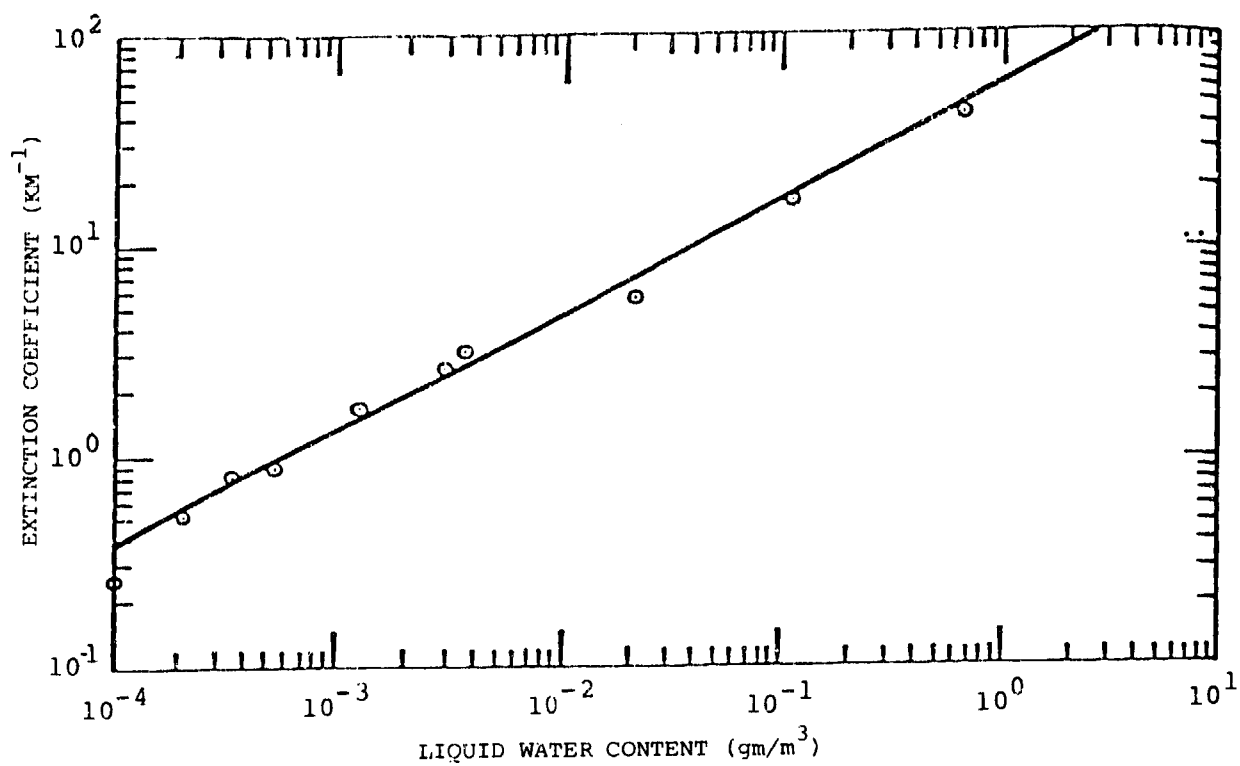
FIGURE 6.9   DEPENDENCE OF VOLUME EXTINCTION COEFFICIENT ON LIQUID
WATER CONTENT FOR A WATER HAZE AT A WAVELENGTH OF 0.55 μm.

Thus, knowing V and $I(\lambda)$ and $S(\lambda)$ one can calculate the surface volume extinction coefficient.

The liquid water content at the surface is given by

$$W_p(0,V) = \left[\frac{0.07184615}{V} - 0.0002181408\right]^{1.8639} \quad (6.10)$$

for $V \le 329.36$ km. which is illustrated in Figure 6.10. The liquid water volume density, i.e.

$$U_p(V) = \int_0^\infty W_p(z,V)\,dz \quad (6.11)$$

$$= W_p(0,V)J_p \quad (6.12)$$

is then specified as an independent quantity. Hence, the integral J_p can be evaluated for a profile p from Equation (6.12). Having determined the profile parameter p the atmosphere is completely determined in terms of surface visual range V and the integrated water content U_p.
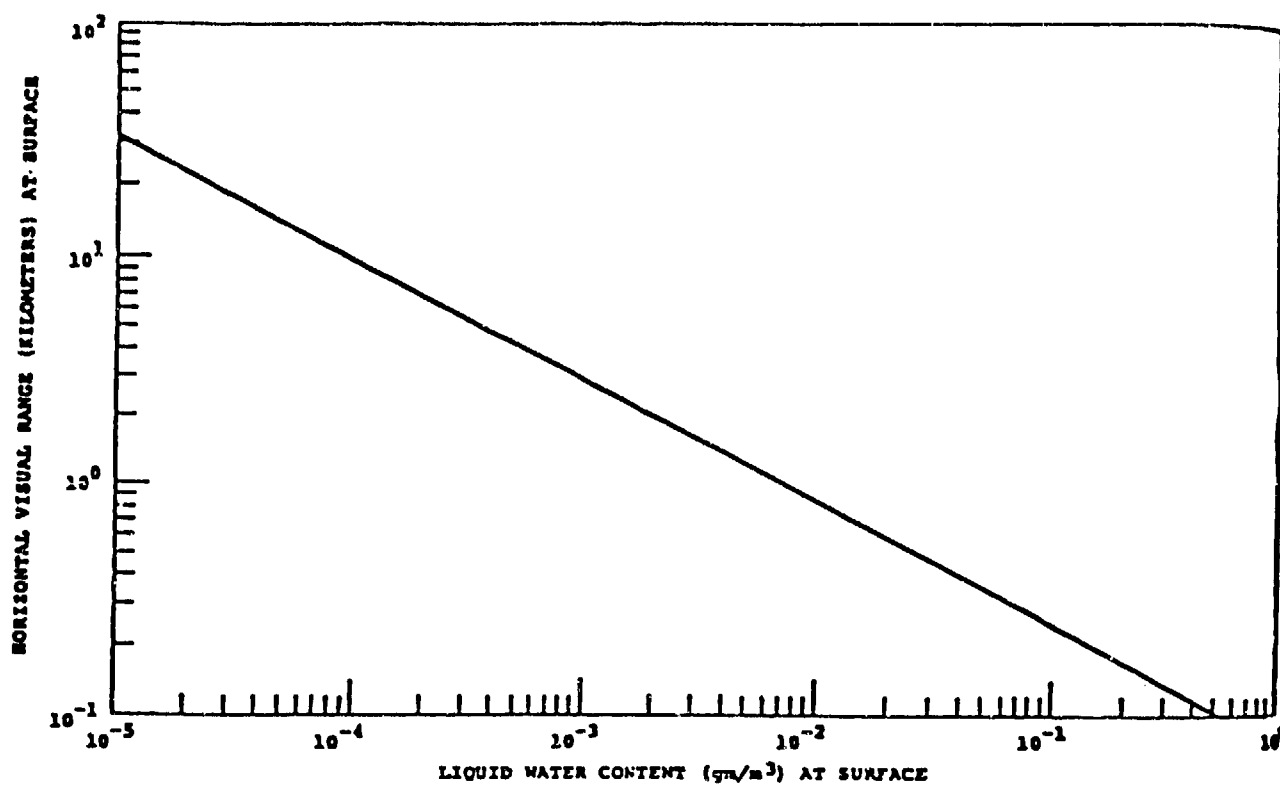
FIGURE 6.10   VARIATION OF HORIZONTAL VISUAL RANGE AT THE SURFACE
                VS. LIQUID WATER CONTENT AT SURFACE FOR WATER HAZE.

6-16

A description of the input and output parameters is given in Figure 6.11.

SAI WATER HAZE MODEL

```
┌─────────────────────────────────────────────┐
│                    INPUT                      │
├─────────────────────────────────────────────┤
│                                               │
│   WAVELENGTH                                  │
│                                               │
│   VISUAL RANGE                                │
│                                               │
│   LIQUID WATER CONTENT                        │
│                                               │
└─────────────────────────────────────────────┘
                       │
                       ▼
┌─────────────────────────────────────────────┐
│                   OUTPUT                      │
├─────────────────────────────────────────────┤
│                                               │
│   VOLUME EXTINCTION COEFFICIENTS              │
│                                               │
└─────────────────────────────────────────────┘
```
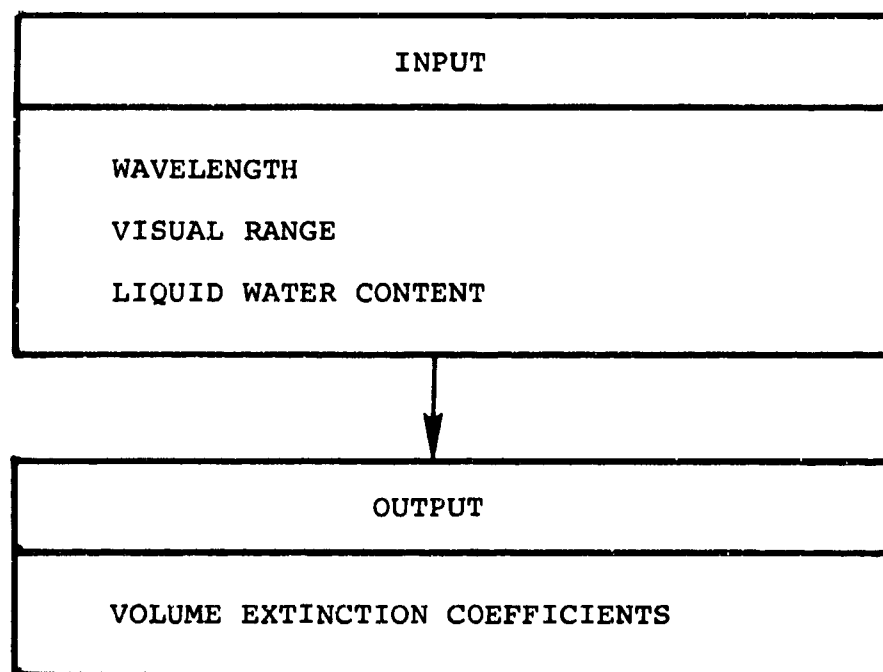
FIGURE 6.11   INPUT AND OUTPUT PARAMETERS FOR THE SAI-WATER
               HAZE MODEL.

6.1.1.1.5 RAND Model

A model for calculating beam transmittance and contrast transmittance was developed by Huschke [5] at the RAND Corporation. We have already described in detail the contrast transmittance algorithms for this model in another section of this report. For the complete model Huschke has an elaborate procedure for using weather data to calculate such quantities as

6-17

the probability of a cloud-free line of sight, extinction
coefficients for the visible and 8-12 μm region, water vapor
absorption coefficients, and beam transmittance. The basic
input and output requirements are listed in Figure 6.12 and 6.13
respectively. It is, of course, almost impossible to compare
calculations of the complete model with other models since other
models do not contain provisions for the details which the RAND
model contains.

HUSCHKE MODEL

INPUT	
SOLAR ELEVATION ANGLE	$(0^o - 90^o)$
RECEIVER DEPRESSION ANGLE	$(0^o - 90^o)$
VISUAL RANGE	(NO LIMITS SPECIFIED)
SURFACE ALBEDO	$(0 \leqslant \bar{\rho} < 1.0)$
CLOUD COVER	(EIGHTS)
DEWPOINT TEMPERATURE AT SURFACE	(^oC)
TEMPERATURE AT SURFACE	(^oC)
SENSOR ALTITUDE	(KM)
WIND SPEED AT SURFACE	(KNOTS)
CEILING HEIGHT	(KM)
CLOUD LAYER ALTITUDES	(KM)
DATE, LOCATION, TIME OF DAY	

FIGURE 6.12   INPUT PARAMETERS FOR THE HUSCHKE MODEL.

6-18

OUTPUT	
TOTAL EXTINCTION COEFFICIENT	(VISIBLE, 8 - 12 ʜʍ)
AEROSOL EXTINCTION COEFFICIENT	(VISIBLE, 8 - 12 ʜʍ)
WATER VAPOR CONTINUUM ABSORPTION COEFFICIENT	
WATER VAPOR MOLECULAR ABSORPTION COEFFICIENT	
SKY-GROUND RATIO	
CONTRAST TRANSMITTANCE	(VISIBLE, 8 - 12 ʜʍ)
BEAM TRANSMITTANCE	(VISIBLE, 8 - 12 ʜʍ)
PROBABILITY OF A CLOUD-FREE LINE OF SIGHT	

FIGURE 6.13   OUTPUT PARAMETERS FOR THE HUSCHKE MODEL.

6.1.1.1.6 SAI (Aerosol Growth) Attenuation Model

A simplified extinction model is needed for the estimation
or determination of aerosol extinction coefficients in terms of
meteorological variables such as temperature, relative humidity,
wind speed, wind direction, visibility, etc. At the current level
of our technology and science it may only be possible to arrive
at an average or a statistical connection among the pertinent
variables due to the complexity of the atmospheric aerosol. It
is believed by many investigators however, that at least more
deterministic submodels can be developed to deal with more restricted
data bases. To this end Turner [6] has performed calculations which
illustrate the general trends in aerosol extinction coefficients
for the spectral region 1.06 μm, visible (0 45 - 0.65 μm), and
the two infrared bands 3-5 μm, and 8-12 μm.

The basic algorithm is a simple one. One relates the volume extinction coefficient at wavelength λ' to the coefficient in the visible, i.e.

$$\kappa(\lambda',f) = \left[\frac{3.912}{V} - 0.011978\right] \frac{\overline{\sigma}(\lambda',f)}{\overline{\sigma}(\lambda_0,f)} \qquad (6.13)$$

where the quantity in brackets is just the aerosol volume extinction coefficient at 0.55 ($= \lambda_0$) and $\overline{\sigma}(\lambda,f)$ is the aerosol total cross section at wavelength λ and relative humidity f averaged over the particle size. Thus, one has a simple model which determines the volume extinction coefficient in any spectral region as a function of two meteorological parameters, visibility V, and relative humidity f. Examples of how the model can be used are illustrated in Figures 6.14 and 6.15. These figures indicate that if one has the volume extinction coefficient at a wavelength of 0.55 μm (or equivalently, the visual range) and a knowledge of the relative humidity, then the volume extinction coefficient is known in other spectral bands. A description of the input and output parameters of this model is given in Figure 6.16.
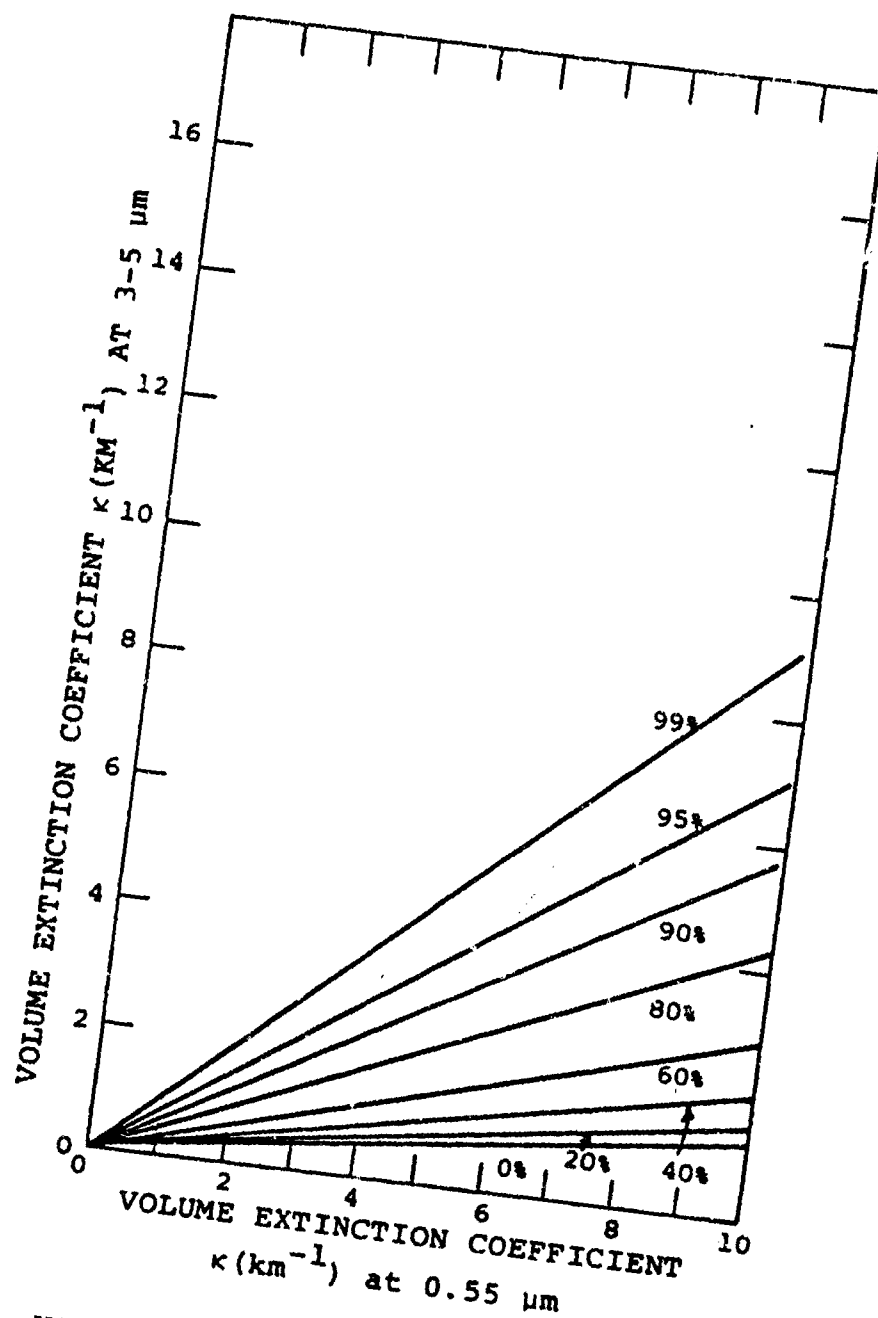
FIGURE 6.14 VOLUME EXTINCTION COEFFICIENTS AT 3-5 μm AND 0.55 μm FOR A SERIES OF RELATIVE HUMIDITIES BETWEEN 0% AND 99%. DERIVED USING DEIRMENDJIAN'S HAZE L MODEL. THE NUMBER DENSITY N (PARTICLE/UNIT VOLUME) VARIES ALONG EACH LINE OF CONSTANT RELATIVE HUMIDITY.

$$\kappa(3-5) = \kappa(0.55)\left(\frac{\overline{\sigma}(3-5)}{\overline{\sigma}(0.55)}\right)$$

6-21
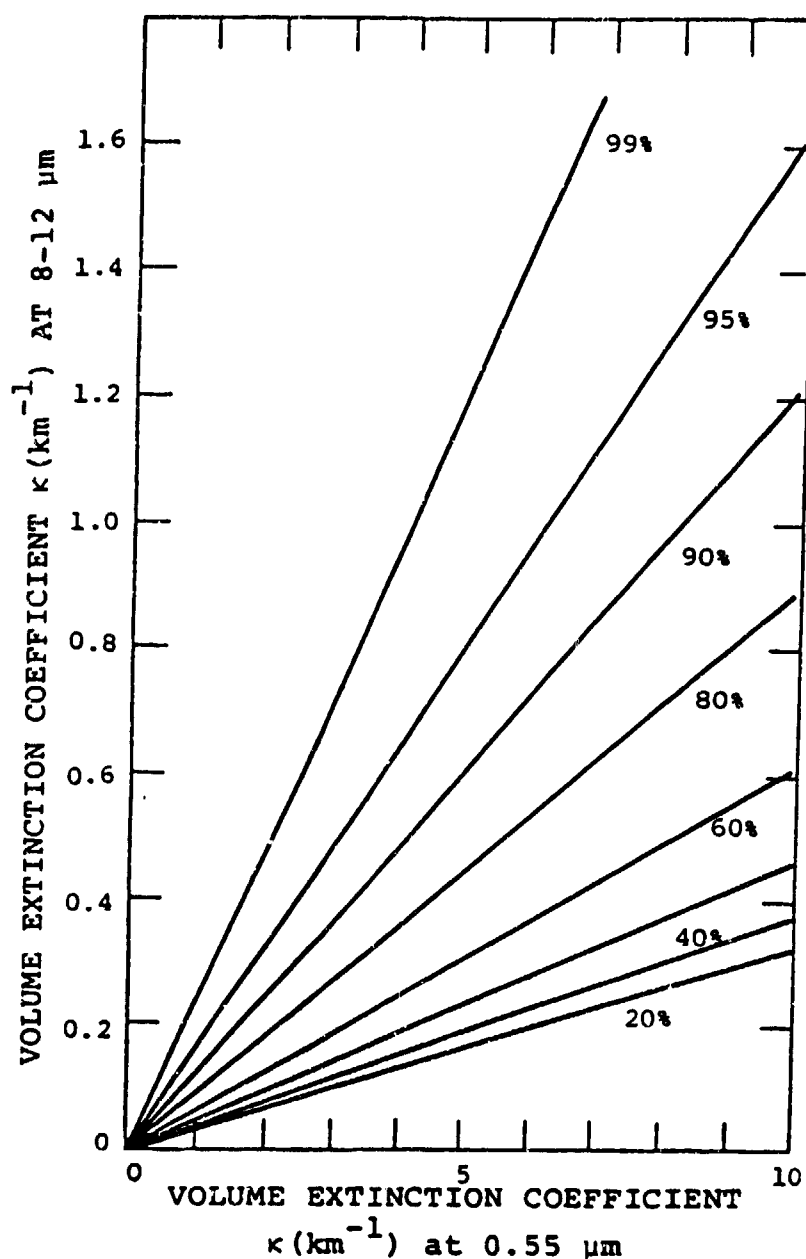
FIGURE 6.15   VOLUME EXTINCTION COEFFICIENTS AT 8-12 μm AND 0.55 μm
FOR A SERIES OF RELATIVE HUMIDITIES BETWEEN 0% AND
99%.   DERIVED USING DEIRMENDJIAN'S HAZE L MODEL.   THE
NUMBER DENSITY N (PARTICLE/UNIT VOLUME) VARIES ALONG
EACH LINE OF CONSTANT RELATIVE HUMIDITY.

$$\kappa(8-12) = \kappa(0.55) \left(\frac{\overline{\sigma}(8-12)}{\overline{\sigma}(0.55)}\right)$$

6-22

```
+--------------------------------------------------+
|                     INPUT                        |
+--------------------------------------------------+
|                                                  |
|   WAVELENGTH                                      |
|                                                  |
|   VISUAL RANGE                                    |
|                                                  |
|   RELATIVE HUMIDITY                               |
|                                                  |
+--------------------------------------------------+
                         |
                         |
                         v
+--------------------------------------------------+
|                    OUTPUT                         |
+--------------------------------------------------+
|                                                  |
|   SPECTRAL OR BAND VOLUME -                       |
|                                                  |
|   EXTINCTION COEFFICIENT                          |
|                                                  |
+--------------------------------------------------+
```
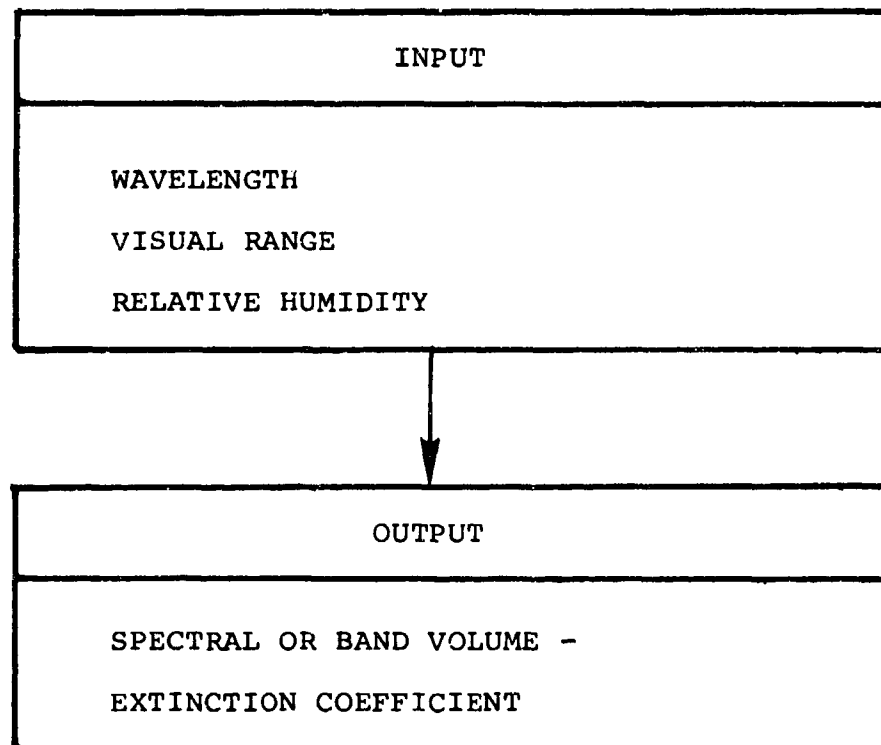
FIGURE 6.16   INPUT AND OUTPUT PARAMETERS FOR THE SAI (AEROSOL
               GROWTH) ATTENUATION MODEL

6-23

6.1.1.2 Fog Extinction Models

6.1.1.2.1. SAI Water-Haze Model

This model, described in Section 6.1.1.1.4 can also be used to calculate the volume extinction coefficient for the visible and infrared spectral regions for a fog. In fact, the model was originally developed based on experimentally measured vertical profiles of fog data from Grafenwöhr, West Germany.

6.1.1.2.2 IDA Model

A simple phenomenological model was developed by Roberts [7] at the Institute of Defense Analyses based upon field measurements conducted at Grafenwöhr, F.R.G. He assumes that the extinction cross section in the small particle range is given by

$$\sigma_e \propto r^3 , \qquad (6.14)$$

an approximation which holds true only for long wavelength IR ($\lambda = 10 \ \mu m$) and for light fogs and for moderate absorption. The volume extinction coefficient for this case is then

$$\kappa(\text{large } \lambda) \sim \int_{r_m}^{r_M} n(r) r^3 dr \sim V(\text{Volume}). \qquad (6.15)$$

On the other hand, for particles which are large compared to the wavelength we have the geometric cross section limit, or

$$\sigma_g = 2\pi r^2 \qquad (6.16)$$

and

$$\kappa(\text{small } \lambda) \sim \int_{r_m}^{r_M} n(r) r^2 dr \sim A(\text{Area}), \qquad (6.17)$$

6-25

an approximation which should hold for fogs and precipitation. Thus, from Eqs. (6.15) and (6.17) we would expect

$$\kappa \text{ (large } \lambda) = C_\lambda \kappa^{3/2} \text{ (small } \lambda) . \qquad (6.18)$$

Equation (6.18) represents the Rayleigh scattering region for absorbing particles. For non-absorbing particles the law should be

$$\kappa \text{ (large } \lambda) = C_\lambda \kappa^{3} \text{ (small } \lambda) . \qquad (6.19)$$

because the Rayleigh scattering cross section is proportional to r^6. The critical assumption which Roberts makes is that for a particular aerosol and spectral region, the attenuation or extinction is most critically dependent upon the volume of particulates in the atmosphere path and not so much upon the detailed description of the distribution function. In analyzing the Grafenwöhr data Roberts found a relationship

$$\kappa \text{ (10 } \mu m) \sim \kappa^{1.47} \text{ (0.7 } \mu m) \qquad (6.20)$$

with an exponent quite close to 1.50 as required by Eq. 6.18.

Thus, the IDA model agrees with the SAI-Water Haze model and also allows one to determine the volume extinction coefficient in one spectral region relative to another. A description of the input and output parameters is given in Figure 6.17.

IDA MODEL

```
┌─────────────────────────────────────────────┐
│                    INPUT                      │
├─────────────────────────────────────────────┤
│        VISIBLE EXTINCTION COEFFICIENT         │
└─────────────────────────────────────────────┘
                       │
                       ▼
┌─────────────────────────────────────────────┐
│                   OUTPUT                      │
├─────────────────────────────────────────────┤
│          IR EXTINCTION COEFFICIENTS           │
└─────────────────────────────────────────────┘
```
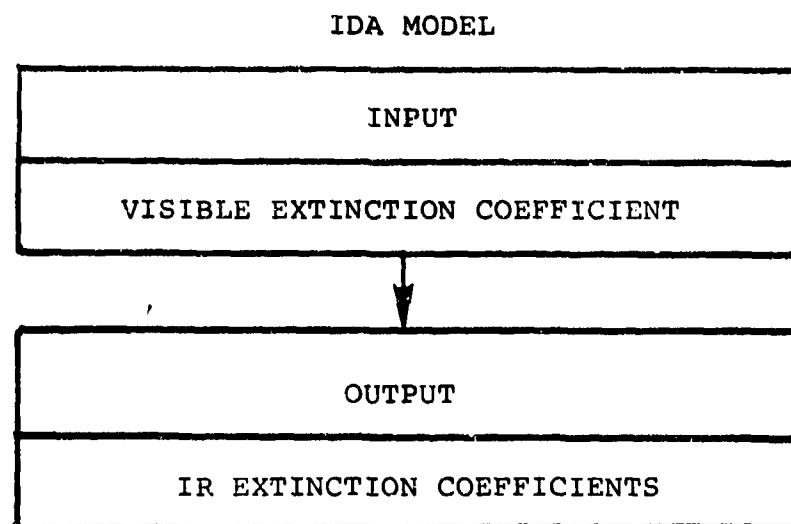
FIGURE 6.17   INPUT AND OUTPUT PARAMETERS FOR THE IDA MODEL

6.1.1.2.3. ASL Model

Pinnick et al. [8] have analyzed 341 particle size
distribution measurements made at different geographic locales
and under a variety of meteorological conditions. They found
a strong linear relationship between the volume extinction
coefficient at a wavelength of 11 μm and the liquid water
content of a fog. This relationship is given by

$$\kappa \ (\lambda = 11\mu m) = 128 \ w \tag{6.21}$$

where κ is the volume extinction coefficient in units of
km^{-1} and w is the fog liquid water content (g/m^3). Other
approximate relationships are given for various wavelengths.
The input and output parameters for this fog model are given
in Figure 6.18.

ASL MODEL

```
┌─────────────────────────────────────────┐
│                 INPUT                    │
├─────────────────────────────────────────┤
│                                          │
│              WAVELENGTH                  │
│                                          │
│          LIQUID WATER CONTENT            │
│                                          │
└─────────────────────────────────────────┘
                     │
                     ▼
┌─────────────────────────────────────────┐
│                OUTPUT                    │
├─────────────────────────────────────────┤
│                                          │
│      VOLUME EXTINCTION COEFFICIENTS      │
│                                          │
└─────────────────────────────────────────┘
```
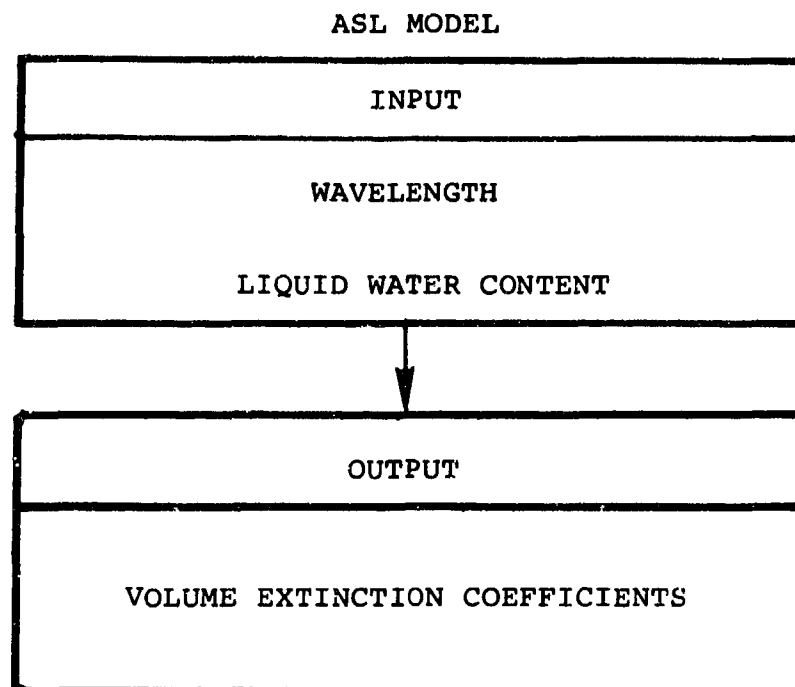
FIGURE 6.18   INPUT AND OUTPUT PARAMETERS FOR ASL FOG MODEL

6.1.1.2.4   G/AP Aerosol Model

Data were collected on fogs at Ft. A.P. Hill, Virginia
and at Grafenwöhr, Germany. The model which resulted from
this data analysis is called the G/AP Aerosol Model. Portions
of these data have been previously reported [9] but Figures
6.19 and 6.20 illustrate the present data in their entirety.

Figure 6.19 shows curve fits to the data relating visible
and 3-5µm extinction through fog. The wet and dry curves
are fits to data subsets defined by observed meteorological
conditions. The "wet" condition is indicative of a high
aerosol moisture content. Each day of data was classified as
wet or dry by its predominant optical character when an on-site
determination of the fog's nature was not made. The middle
curve, as noted, is a fit to all of the data. The relation-
ship between visible extinction and that in the 8-12µm band-
pass is shown in Figure 6.20.
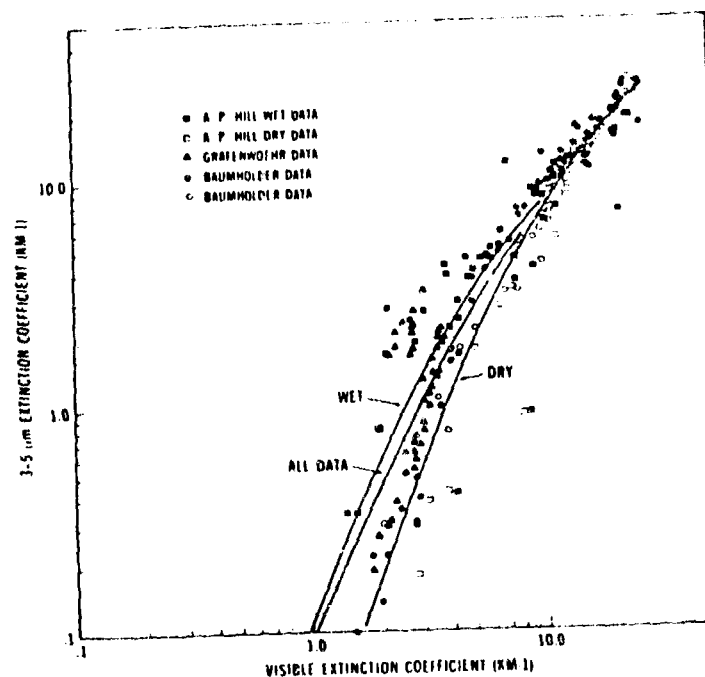
FIGURE 6.19   3-5 μm G/AP AEROSOL MODEL.   LOW VISIBILITY AEROSOL
ATTENUATION DATA AND DERIVED EMPIRICAL FITS FOR
LOCATIONS IN VIRGINIA AND GERMANY.

FIGURE 6.20   8-12 μm G/AP AEROSOL MODEL.   LOW VISIBILITY AEROSOL
ATTENUATION DATA AND DERIVED EMPIRICAL FITS FOR
LOCATIONS IN VIRGINIA AND GERMANY.

6-29
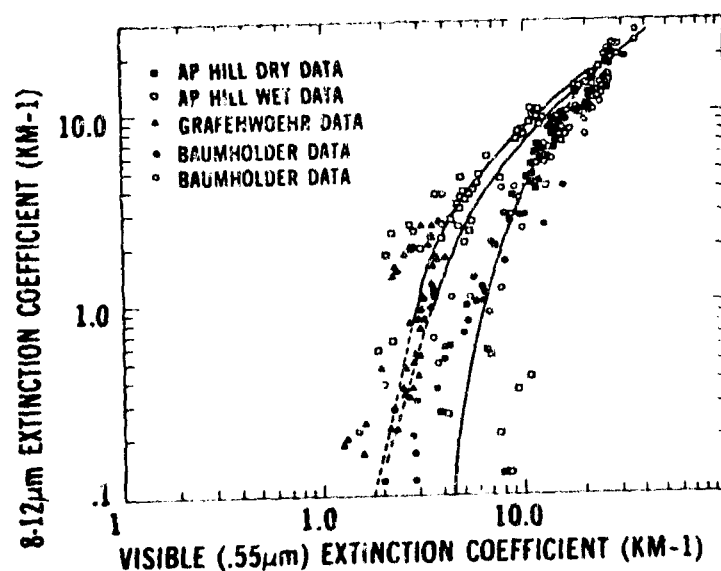
The equations which result from the data analysis for wet and
dry fog are the following:

WET FOG:
$$\sigma_{3-5} = 10^{-.917+2.595 \log \sigma_{.55}-.782 (\log \sigma_{.55})^2}$$

$$\sigma_{8-12} = 10^{-1.144+2.871 \log \sigma_{.55}-.895 (\log \sigma_{.55})^2} \tag{6.22}$$

DRY FOG:
$$\sigma_{3-5} = 10^{-1.667+3.398 \log \sigma_{.55}-.863 (\log \sigma_{.55})^2} \tag{6.23}$$

$$\sigma_{8-12} = 10^{-1.712+2.565 \log \sigma_{.55}-.328 (\log \sigma_{.55})^2}$$

and, for the combined cases of wet and dry fogs the equations
are:

COMBINED:
$$\sigma_{3-5} = 10^{-1.0+2.404 \log \sigma_{.55}-.511 (\log \sigma_{.55})^2}$$

$$\sigma_{8-12} = 10^{-.98+1.851 \log \sigma_{.55}-.212 (\log \sigma_{.55})^2} \tag{6.24}$$

$$\sigma_{.55} = 10^{.239+.751 \log \sigma_{1.06}-.281 (\log \sigma_{1.06})^2}$$

Additional data gathered at $1.06\mu m$ have resulted in the scaling
law that is also shown above. These formulations are currently
being used to evaluate E-O systems performance under limited
visibility conditions. The σ's in Equations (6.22, 6.23, and
6.24) represent the extinction coefficients in units of km^{-1}.
The input and output parameters for the G/AP Aerosol Model are
indicated in Figure 6.21

G/AP AEROSOL MODEL

INPUT
VISUAL RANGE, OR VOLUME EXTINCTION COEFFICIENT IN THE VISIBLE REGION FOG TYPE (DRY OR WET)

OUTPUT
VOLUME EXTINCTION COEFFICIENTS IN SPECTRAL REGIONS 3-5μm, 8-12μm, AND 1.06μm
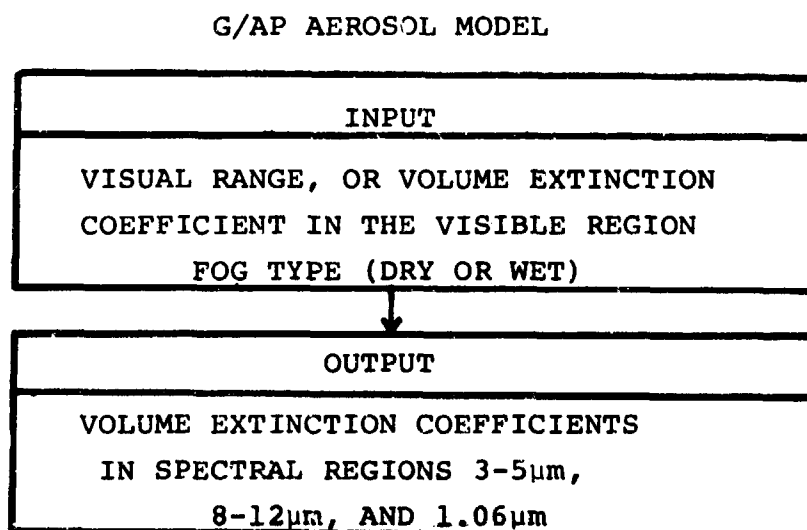
FIGURE 6.21   INPUT AND OUTPUT PARAMETERS FOR THE G/AP
AEROSOL MODEL

6-30

6.1.1.3 Precipitation Extinction Models

In this section we describe the extinction models for various forms of precipitation.

6.1.1.3.1 Chu-Hogg Model

In 1968, Chu and Hogg [10] considered the attenuation of 0.63, 3.5, and 10.6 µm radiation through rain and snow. They performed calculations and compared the results with measurements over a 2.6 km path. Taking into consideration forward scattering, it was found that the attenuation by rain could be calculated to good accuracy from the average path rain rates. The measured rain attenuation coefficients for a wavelength of 0.63 µm is illustrated in Figure 6.22. It is found that the attenuation coefficient can be given in terms of the rain rate, p (mm/hr) by the following:

$$\alpha\left(\frac{dB}{km}\right) = 0.155 \ p \left(\frac{mm}{hr}\right) + 2.66. \qquad (6.25)$$

Equation (6.25) is generally valid for rain rates above 12.5 mm/hr. The relationship between the attenuation at other wavelengths and the rain rate is illustrated in Figure 6.23. The input and output parameters for this rain model are given in Figure 6.24.
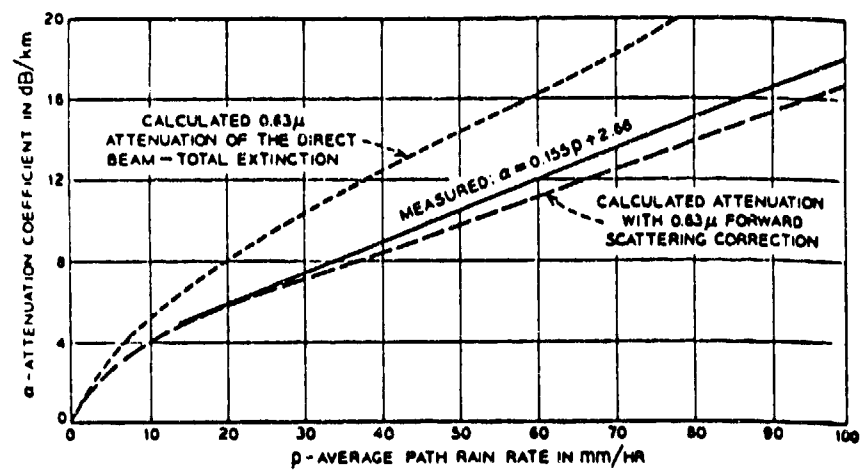
FIGURE 6.22 MEASURED RAIN ATTENUATION COEFFICIENTS OF
0.63 μ FOR A 2.6 KM PATH: STANDARD DEVIATION
IS ±2.8 dB PER KM AT A RAIN RATE OF 50 MM/HR.
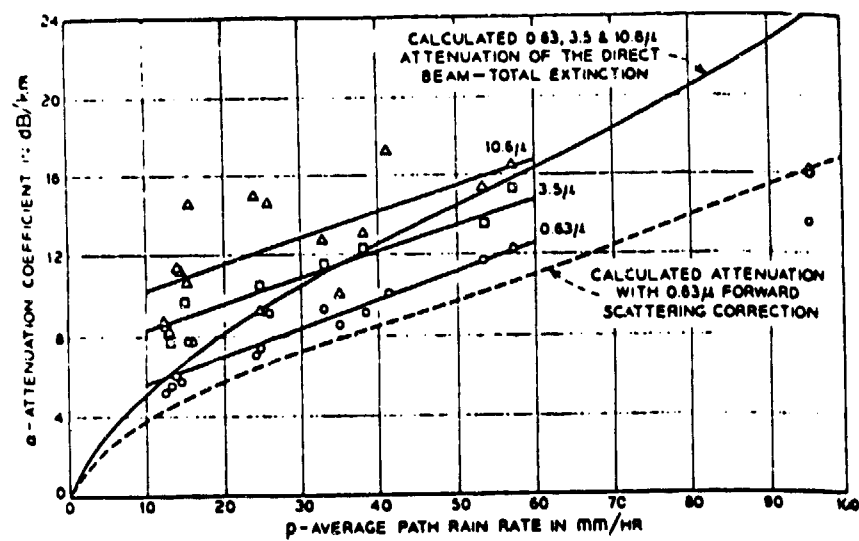
FIGURE 6.23 MEASURED ATTENUATION COEFFICIENTS OF A RAIN
STORM FOR A 2.6 KM PATH.

CHU-HOGG MODEL

INPUT
WAVELENGTH
RAIN RATE

OUTPUT
ATTENUATION COEFFICIENT AT 0.63 μM, 3.5 μM, 10.6 μM
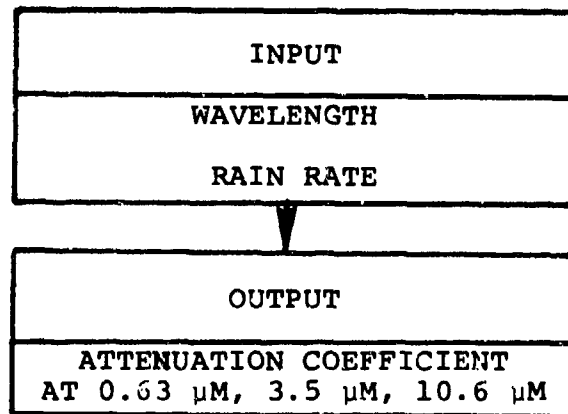
FIGURE 6.24 INPUT AND OUTPUT PARAMETERS FOR THE CHU-HOGG
MODEL.

6.1.1.3.2 Polyakova Model

In 1957 Polyakova [11] demonstrated that the volume extinction coefficient for rain, α_{rain} in the 0.4 μm to 15 μm can be expressed in terms of the rainfall intensity, J, by the following:

$$\alpha_{rain} = 0.21 \; J^{0.74} \tag{6.26}$$

where α_{rain} has units of km^{-1} and J has units of mm/hr. The input and output parameters of this model are given in Figure 6.25.

POLYAKOVA MODEL

INPUT
SPECTRAL REGION
RAIN RATE

OUTPUT
VOLUME EXTINCTION COEFFICIENT
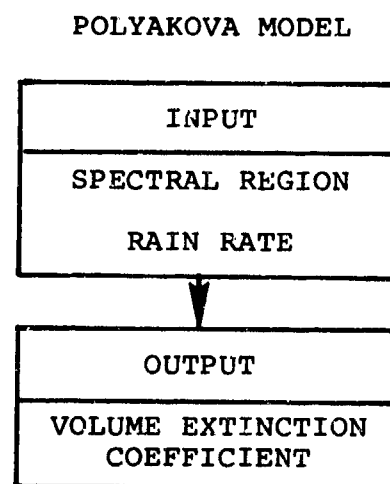
FIGURE 6.25 INPUTS AND OUTPUT PARAMETERS FOR THE POLYAKOVA MODEL.

6.1.1.3.3 Selzer Model

For millimeter wavelengths, attenuation by rain is the most dominant form of atmospheric attenuation. In Figure 6.26 are data by Goldstein [12] of the volume attenuation coefficient of rain in the millimeter wavelength region. The curves are values calculated by Selzer [13]. As one can see from the figure, the calculated values agree with the data quite well. According to the model, the extinction coefficient depends upon the refractive index of water which is temperature dependent. The model can account for this effect.

Figure 6.27 indicates the input and output parameters for the Selzer model.
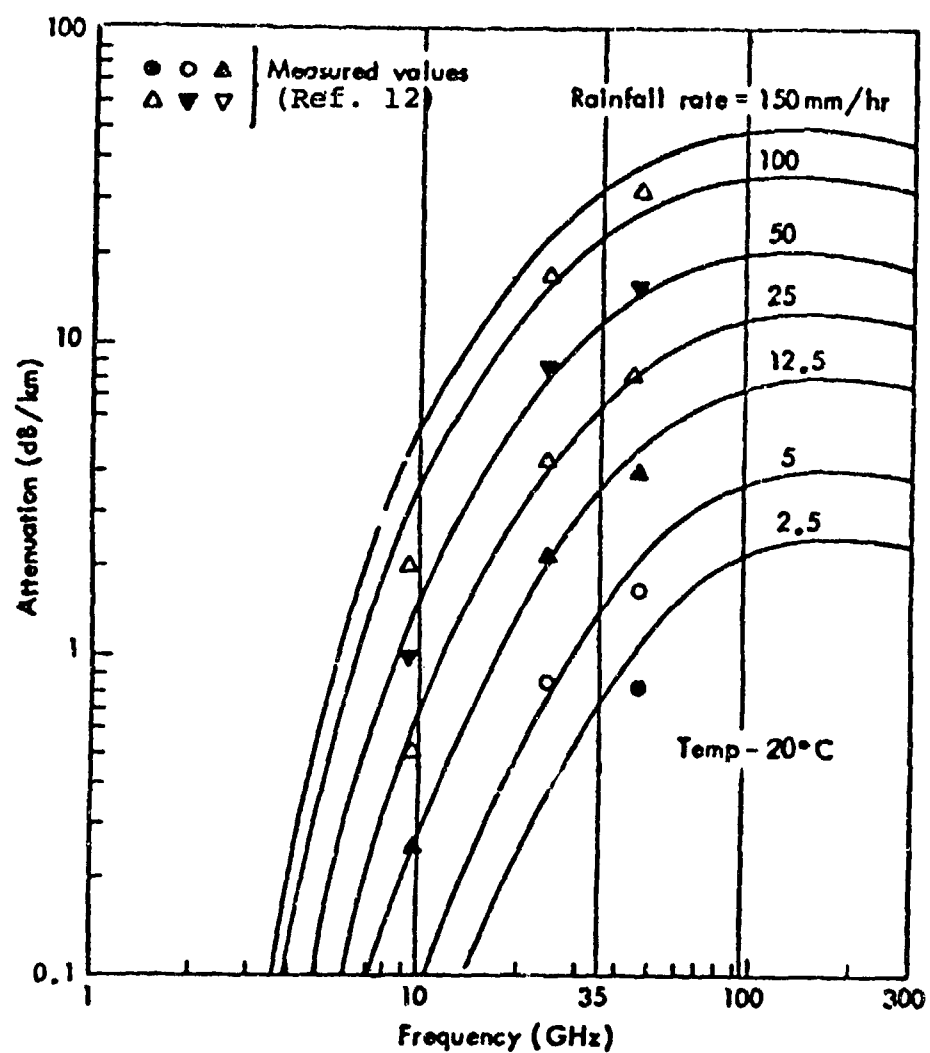
FIGURE 6.26 LOGARITHMIC PLOT OF CALCULATED VALUES OF
ATTENUATION BY RAIN IN dB/KM.

SELZER MODEL

INPUT
WAVELENGTH
TEMPERATURE
RAIN FALL RATE

OUTPUT
VOLUME ATTENUATION COEFFICIENT
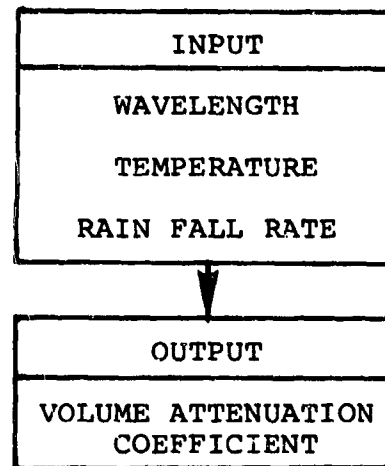
FIGURE 6.27 INPUT AND OUTPUT PARAMETERS FOR THE SELZER MODEL.

6.1.1.3.4 G/AP Snow Model

Data collected at Grafenwöhr, Germany and at Ft. A. P. Hill, Virginia were reported by Sola and Bergemann[14]. Regression lines were generated from the data and are illustrated in Figures 6.28 and 6.29 for the 3-5 µm and 8-12 µm spectral regions respectively. The equations for the volume extinction coefficients in these regions as a function of the visible coefficient are:

$$\sigma_{3-5} = -0.139 + 1.176\ \sigma_{0.55} \qquad (6.27)$$

$$\sigma_{8-12} = 0.022 + 1.279\ \sigma_{0.55} \qquad (6.28)$$

where the extinction coefficients have units of km^{-1}. It should be realized that snow is complicated by the presence of fog and the wide variety of snowflakes. Mason [15] reports on the same data. He provides figures on the volume extinction coefficient at 3.5 µm and 10.6 µm as a function of the visual range. These results are depicted in Figures 6.28 and 6.29 respectively. Mason gives the following mathematical relationships between the volume extinction coefficients and the visual range:

$$\alpha_{0.63} = 3V^{-1} \qquad (6.29)$$

$$\alpha_{3.5} = 3V^{-1.1} \qquad (6.30)$$

$$\alpha_{10.6} = 3.8V^{-0.95} \qquad (6.31)$$

The input and output parameters for the G/AP snow model are indicated in Figure 6.32.

FIGURE6.28 3-5 µM SNOW SCATTERING MODEL. EXTINCTION DATA TAKEN THROUGH SNOW AT A. P. HILL, VIRGINA SHOWING THE RELATIONSHIP BETWEEN THE VISIBLE-NEAR IR AND 3.918 µM.
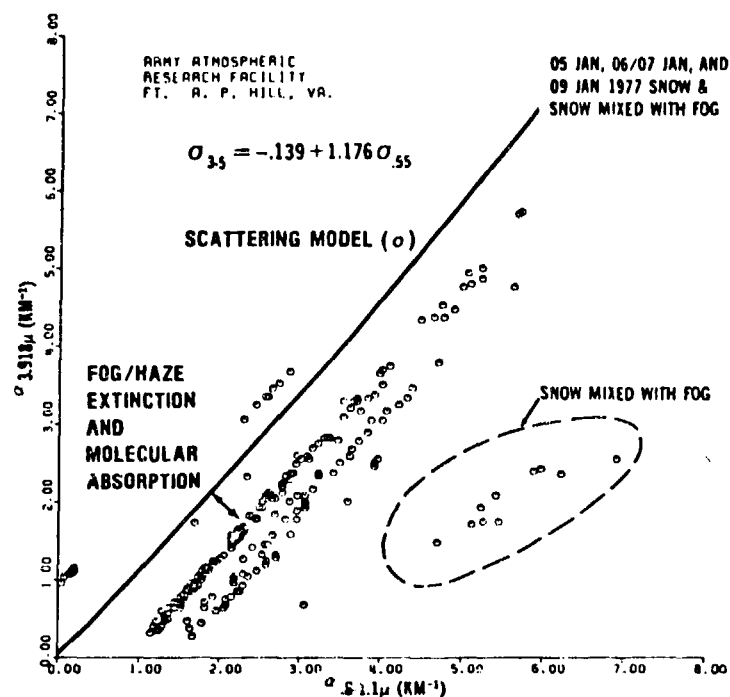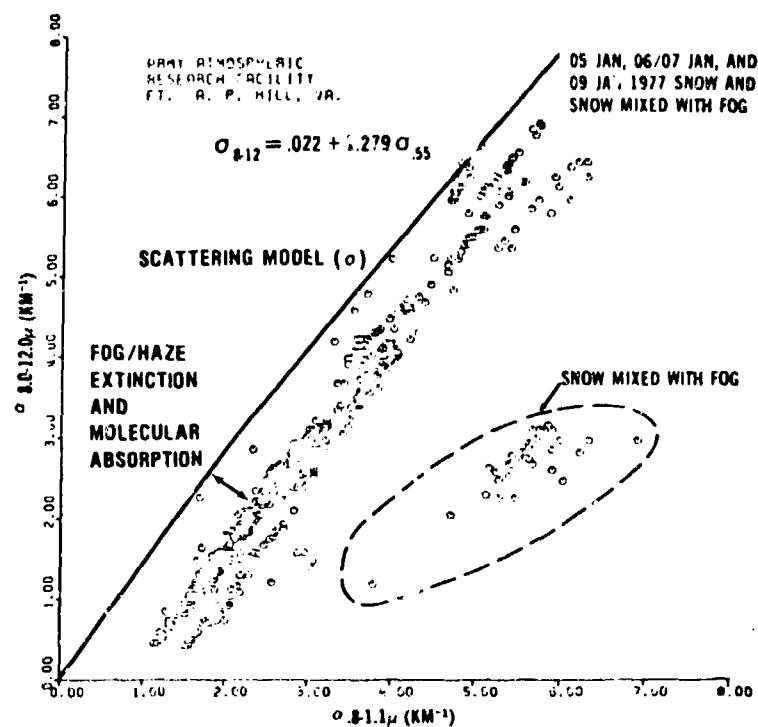
FIGURE 6.29 8-12 μM SNOW SCATTERING MODEL. EXTINCTION
DATA TAKEN THROUGH SNOW AT A. P. HILL, VIRGINIA
SHOWING THE RELATIONSHIP BETWEEN THE VISIBLE-
NEAR IR AND 8-12 μM.
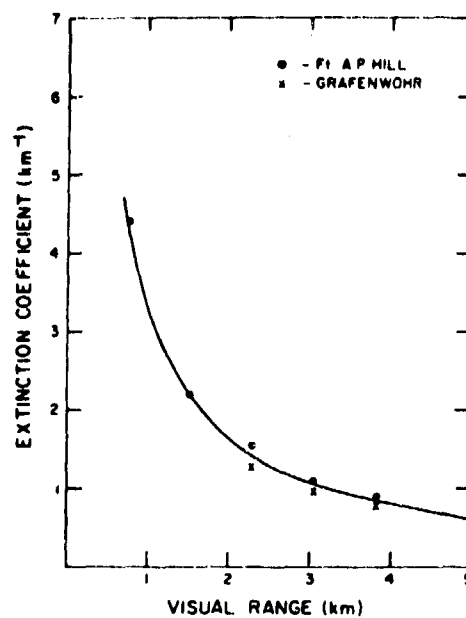
FIGURE 6.30   EXTINCTION AT 3.5 μm VERSUS
              VISUAL RANGE FROM SOLA AND
              BERGEMANN.   CORRECTED ACCORDING
              TO POLYAKOVA'S RESULTS.
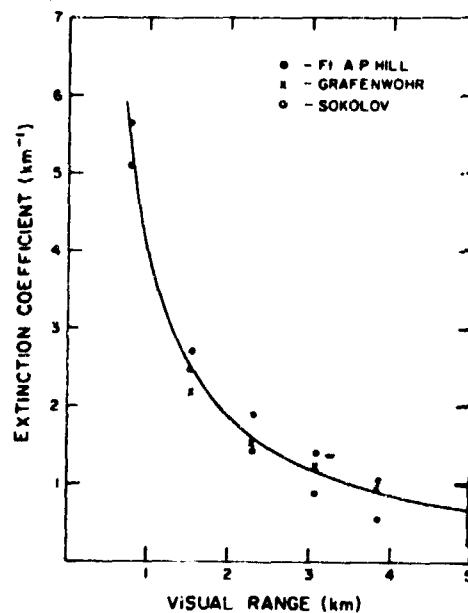
FIGURE 6.31   EXTINCTION AT 10.6 μm VERSUS
              VISUAL RANGE FROM SOLA AND
              BERGEMANN.   CORRECTED ACCORDING
              TO POLYAKOVA'S RESULTS.

6-41

G/AP SNOW MODEL

```
┌─────────────────────────────┐
│           INPUT             │
├─────────────────────────────┤
│         WAVELENGTH          │
│                             │
│        VISUAL RANGE         │
│                             │
│     VISIBLE EXTINCTION      │
│        COEFFICIENT          │
└─────────────────────────────┘
              │
              ▼
┌─────────────────────────────┐
│          OUTPUT             │
├─────────────────────────────┤
│     VOLUME EXTINCTION       │
│        COEFFICIENT          │
└─────────────────────────────┘
```
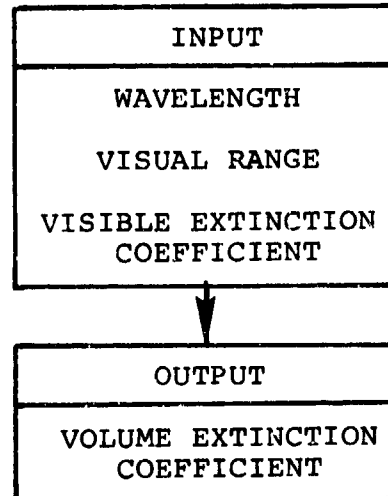
FIGURE 6.32   INPUT AND OUTPUT PARAMETERS FOR THE G/AP
SNOW MODEL.

6.1.1.4 Molecular Extinction Models

Depending on the wavelength, molecular absorption and
scattering can have a significant attenuating effect on
electromagnetic radiation. Figures 6.33 - 6.36 show band-averaged
molecular transmission spectra for three standard atmospheres,
over a 1 km. path, in four important wavelength bands (these
calculations were done with the LOWTRAN IV computer program,
to be described below). It can be seen that the molecular
scattering component, which accounts for most of the extinction
in Figure 6.33 for wavelengths less than 0.69 μm, is slight over a
1 km. path. By far, the predominant extinction mechanism in
the near, middle, and far IR, and for millimeter wavelengths,
is molecular absorption. However, scattering increases dramati-
cally in the ultraviolet, and over longer paths has familiar
effects in the visible wavelength region, as it accounts for
the blueness of the sky.

Molecular extinction models can be categorized based on
two important restrictions on their applicability. The first
is whether they are designed to give predictions for broad
wavelength bands or for precise single wavelengths. In the
first case the appropriate models are called band models, and
output from these models are applicable when used properly for
performance studies of sensors whose response is nonzero over
a band of frequencies. The second class of models are
appropriate for laser extinction predictions. They give results
often referred to as monochromatic, and also occasionally are
used for broadband studies if extreme precision is required,
since all band models are approximate.

Another fundamental distinction for molecular attenuation
models is based on their ability to handle inhomogeneous
atmospheric slant paths. All models which allow inhomogeneous
path calculations approximate the continuous variation of

6-43
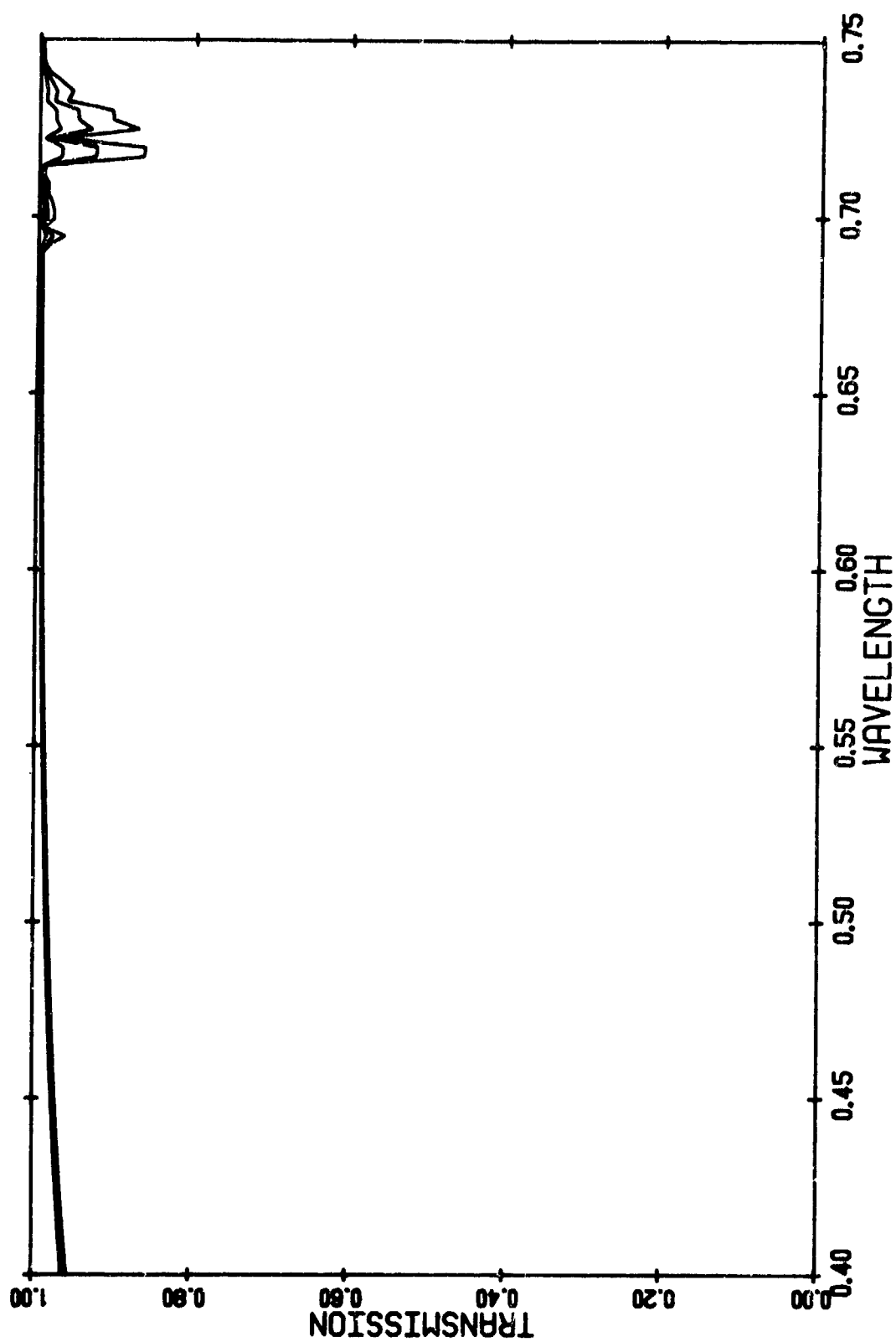
FIGURE 6.33 LOWTRAN IV CALCULATION OF VISIBLE WAVELENGTH MOLECULAR TRANSMISSION
FOR 1 km. SEA LEVEL PATH. MODEL ATMOSPHERES:
top curve - Subarctic Winter
middle curve - 1962 U.S. Standard
bottom curve - Tropical
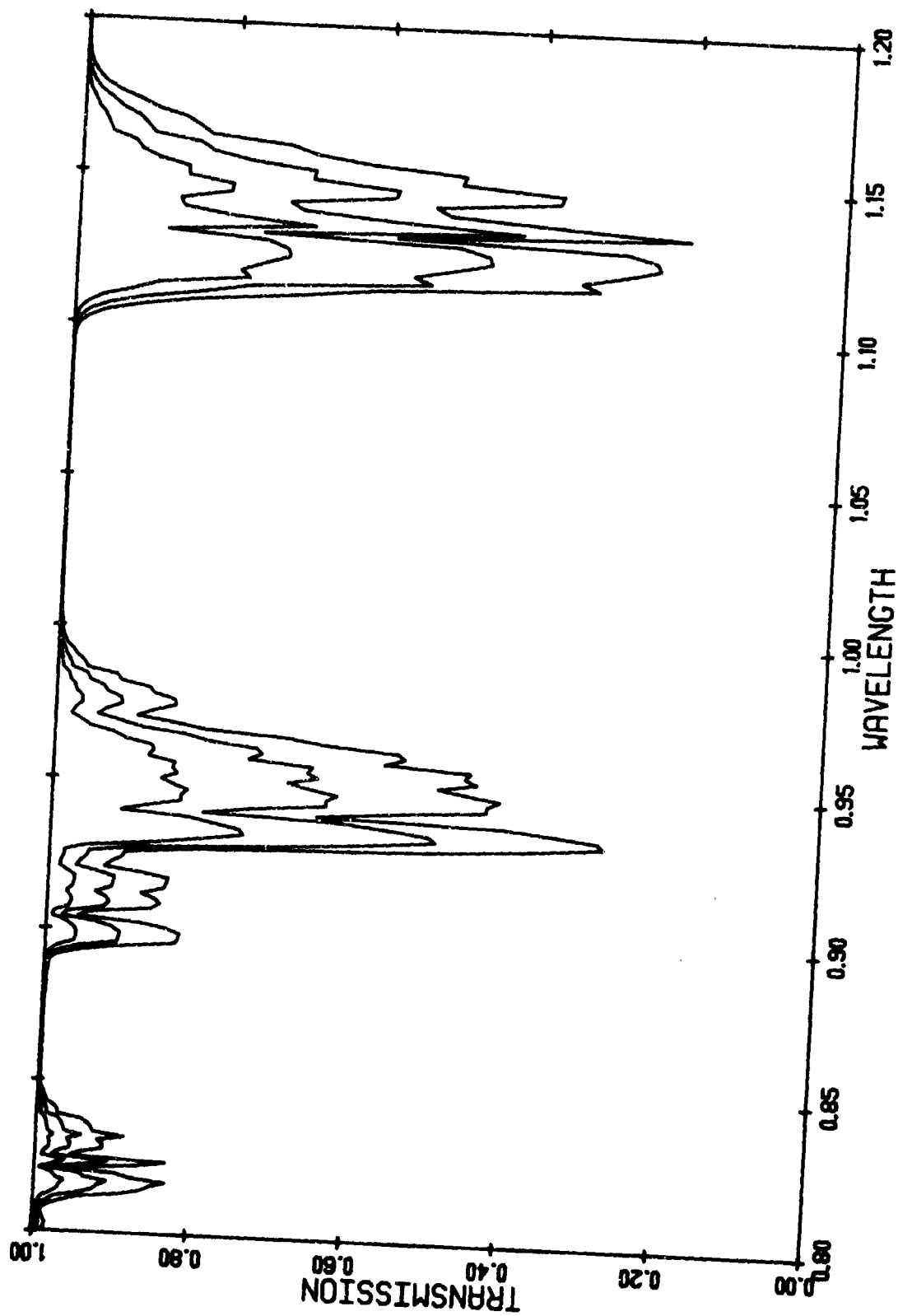
FIGURE 6.34 MOLECULAR TRANSMISSION AS COMPUTED BY LOWTRAN IV, FOR THE SAME CONDITIONS AS IN FIGURE 13, IN THE REGION OF THE GaAs (0.9 μm) and Nd:YAG (1.064 μm) LASERS.
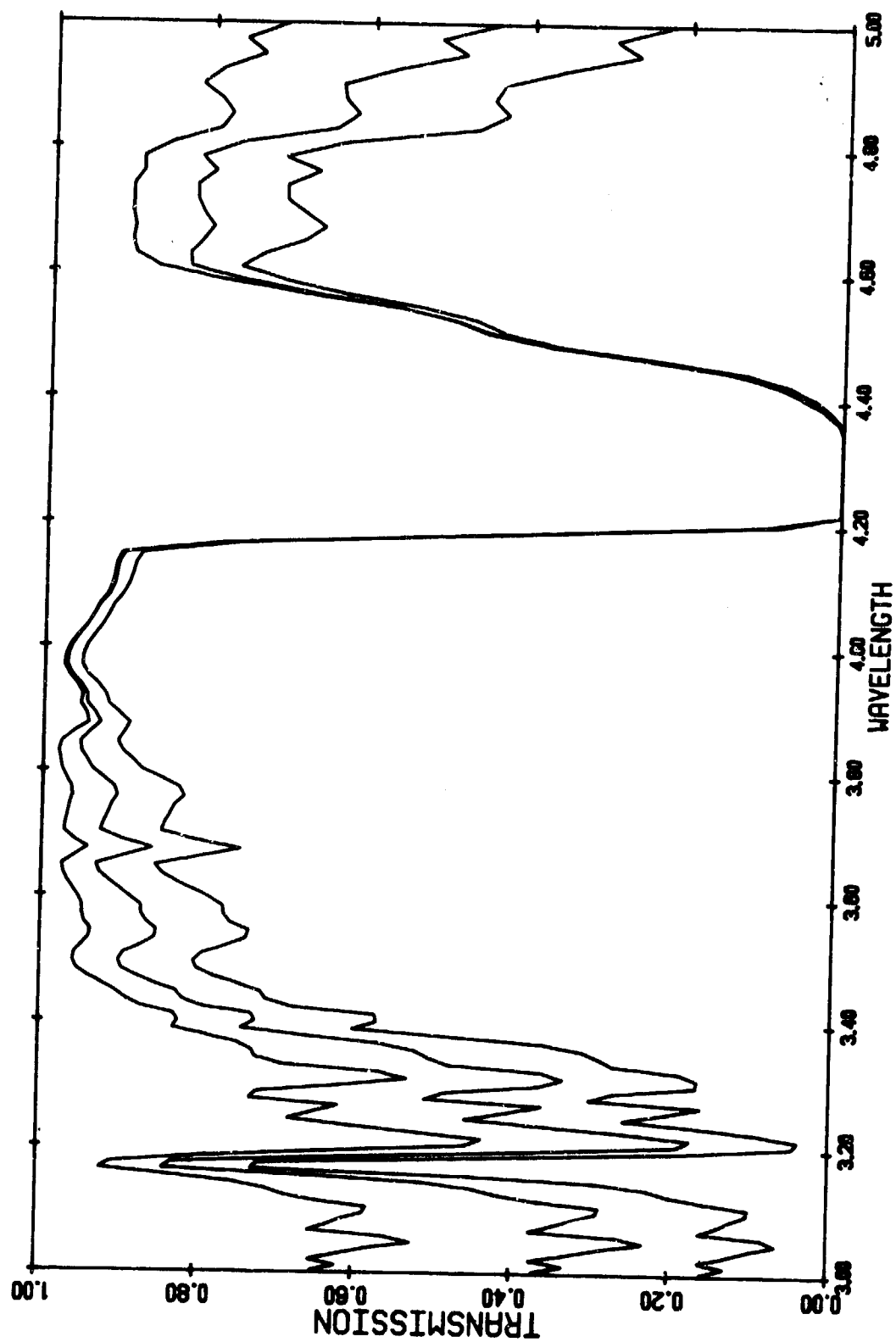
FIGURE 6.35 LOWTRAN IV CALCULATION OF 3.0-5.0 μm MOLECULAR TRANSMISSION, FOR SAME CONDITIONS AS IN FIGURE 13. MAIN WAVELENGTH FOR THE DF LASER IS 3.8 μm.
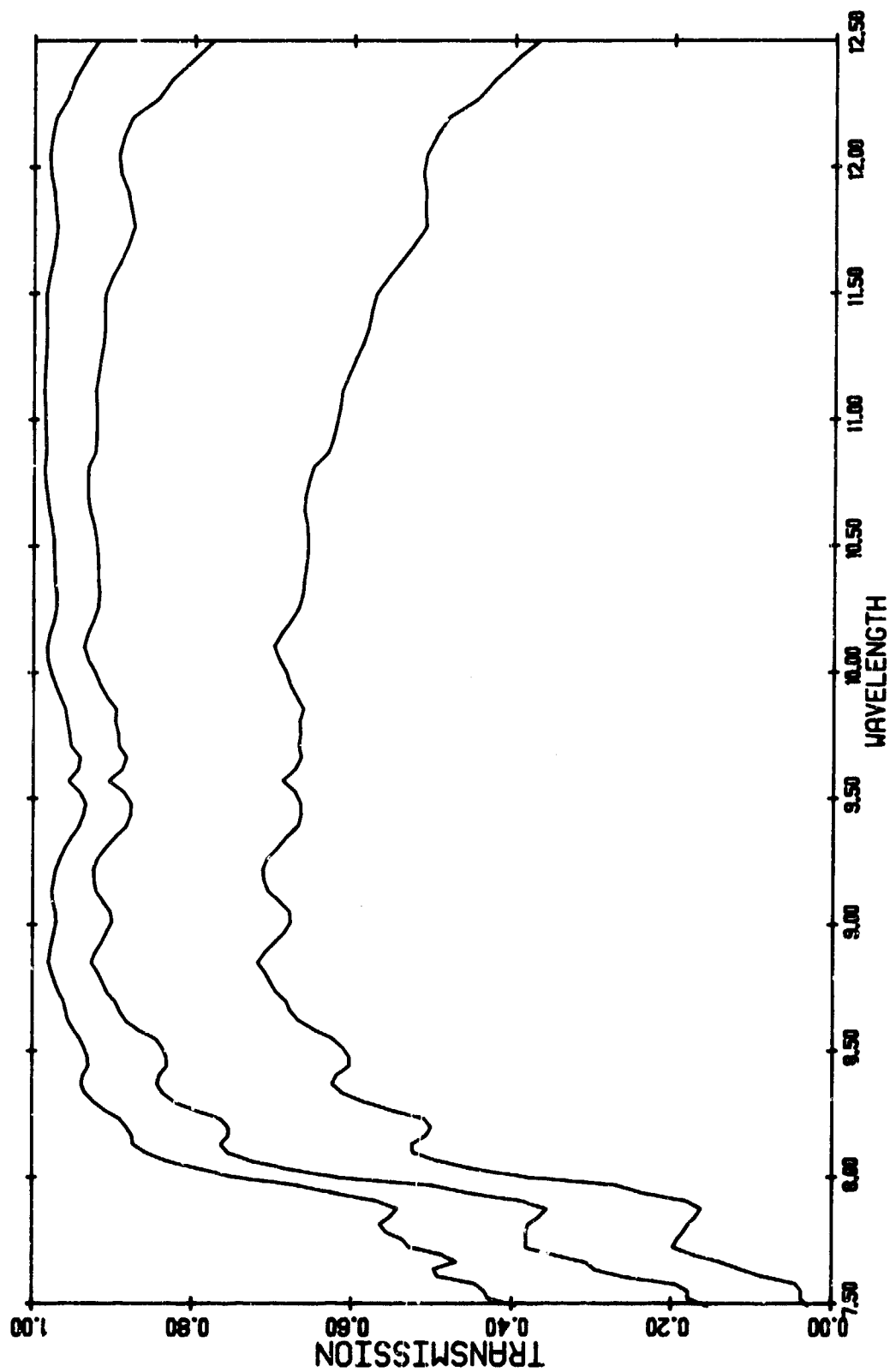
FIGURE 6.36   LOWTRAN IV CALCULATION OF MOLECULAR TRANSMISSION IN THE 7.5-12.5 μm REGION FOR THE SAME CONDITIONS AS IN FIGURE 13.   NOTE THE STRONG ABSORPTION OF THE CO_2 LASER (AT 10.6 μm) BY WATER VAPOR.

pressure, temperature, and humidity found in the real atmosphere with narrow, discrete homogeneous layers. The layers chosen have a significant effect on the accuracy of the calculations. For the LOWTRAN IV approach it was found that the atmosphere can be well approximated with 34 layers, the thickness of the layers initially being 1 km. and then decreasing with height.

The following subsections describe some of the most important molecular attenuation models, as to their applicability and use.

6.1.1.4.1 The LOWTRAN IV Band Model

LOWTRAN IV is a band model designed at AFGL [16] to predict broadband atmospheric transmission and path radiance over arbitrary, possibly inhomogeneous, paths. It is applicable for wavelengths ranging from 0.25 to 28.5 μm and includes scattering and absorption. It contains a single band model for all the uniformly mixed gases, i.e. those gases whose relative abundance does not depend on altitude. The uniformly mixed gases, and their assumed concentrations, are shown in Table 6.1. Representation of these gases by a single band model means that the code cannot handle atmospheres with enhanced concentrations of these molecules, such as CO, which is a common pollutant. The relative concentrations of these gases is fixed once and for all to the values in Table 6.1 because of the choice of a single band model to represent them.

TABLE 6.1

CONCENTRATION OF UNIFORMLY MIXED
GASES IN DRY AIR (PPM BY VOLUME)

CO_2	330
N_2O	0.28
CO	0.075
CH_4	1.6
O_2	2.1×10^5

6-48

The user of LOWTRAN IV has six standard model atmospheres to choose from, or he can specify on his own the altitude dependence of temperature, pressure, relative humidity, and ozone concentration. The model atmospheres available with the code are:

1) midlatitude summer
2) midlatitude winter
3) tropical
4) subarctic summer
5) subarctic winter
6) 1962 U.S. standard.

These model atmospheres specify the height dependence of pressure, temperature, relative humidity, and ozone concentration, as above.

6.1.1.4.2 The ATLES Band Model

The Atles computer program was developed for DARPA by S. J. Young of the Aerospace Corporation [17]. It provides additional capabilities over LOWTRAN in two directions. First, it is designed to model molecular emission at high temperatures, which LOWTRAN cannot do. This gives ATLES the capability to model aircraft plumes, and additionally the code has been used to spectrally model gunflash [22]. Second, ATLES separates the uniformly mixing gases, so that it is possible to study the effect of, say, varying CO concentrations on atmospheric transmission. However ATLES band model coverage is not as good as LOWTRAN'S since only H_2O, CO_2, N_2O, CO, HCl, and HF are included. ATLES therefore neglects the naturally occurring gases CH_4, O_3 and HNO_3.

Input options for ATLES are quite similar to LOWTRAN'S, with the same model atmospheres available, or the option to specify P,T,C data directly. In addition, in order to compute an

aircraft signature it is necessary to have an external computation of the plume flowfield in order to provide plume P,T,C data for ATLES computations. Program outputs are source and sensor radiance values, path radiance, and atmospheric transmittance for a user-specified range of wavelengths.

6.1.1.4.3 LASER Monochromatic Absorption Calculations

The LASER computer program was developed at AFGL to perform exact calculations of monochromatic absorption and scattering at laser frequencies [18] . It computes the effect of molecular absorption lines individually (the "line-by-line" method) and therefore requires the AFGL molecular absorption line compilation [19] , or some other source of spectral data on molecules. It uses model atmospheres similar to LOWTRAN's. LASER does not perform inhomogeneous path transmittance calculations, but instead returns the absorption coefficient at a user-specified altitude. In order to perform calculations for slant paths, therefore, it is necessary to compute attenuation coefficients at several altitudes and add them, to get the effective slant-path attenuation coefficient.

6.1.1.4.4 Polynomial Fits to Laser Absorption Coefficients

The SAI model for laser molecular absorption coefficients is described in reference 20. This model gives the laser absorption at standard pressure as a polynomial expression in temperature T and water vapor pressure P. The most general model is of the form

$$\alpha = A_o + A_1 T + A_2 P + A_3 TP + A_4 P^2 + A_5 TP^2 + A_6 T^2$$
$$+ A_7 T^2 P + A_8 T^2 P^2, \qquad (6.32)$$

where T is in °K and P is in torr of water vapor. This model does not include aerosol absorption and is intended for

6-50

homogeneous paths. Coefficients in this polynomial for the Nd:YAG, CO_2, DF, CO, and GaAs lasers may be found in [20].

6.1.1.4.5 The FASCODE Algorithm

FASCODE, also developed at AFGL, is designed to provide results of monochromatic precision over broad wavelength bands [21]. Since repeated line-by-line calculations are expensive, FASCODE uses a spectral lineshape decomposition method to approximate the exact line shape. As such, its calculations are not strictly exact, though the worst-case error is on the order of three percent. FASCODE as documented above does not include model atmospheres; the user must specify P,T,C data along the optical path, which can be inhomogeneous. Again spectral data for atmospheric gases are provided by the AFGL molecular line compilation.

6.1.1.5 Terrain Blockage Models

Four reports were available on the blockage by the terrain (i.e., by hills, trees). In a report by Dale, et al. [23], we include a brief analysis of terrain blockage [24].

6.1.1.5.1 Foliage and Structure

In order to "see" a target in the visible or infrared spectral region, there obviously must be a direct unobscured LOS between the sensor and the target. This direct LOS may be blocked or degraded by a number of natural or manmade structures, such as hills, rocks, foliage, buildings, etc. The length of time this LOS may be blocked is a direct function of the topography of the land and the location and movement of either, or both, the target and observing sensor. A number of analyses have been conducted to determine the frequency and length of time a target may be obscured from the observer for various topographies of potential battlefields. One of the most commonly analyzed potential battlefield areas is West Germany. The German land areas are considered to be similar to the Piedmont area of Virginia and the countryside of New England.

Over these land areas, the topography is not suited for long, clear range fields of fire for either tanks or Antitank Guided Missiles (ATGM). Figure 6.37 (from Reference 23) shows the probability that an intervisible segment is at least as long as a particular length. Due to land structure (hills and valleys), foliage, and manmade structures, the LOS is interrupted as shown in Table 6.2. Table 6.2 provides the average percentage of loss of intervisibility by cause.
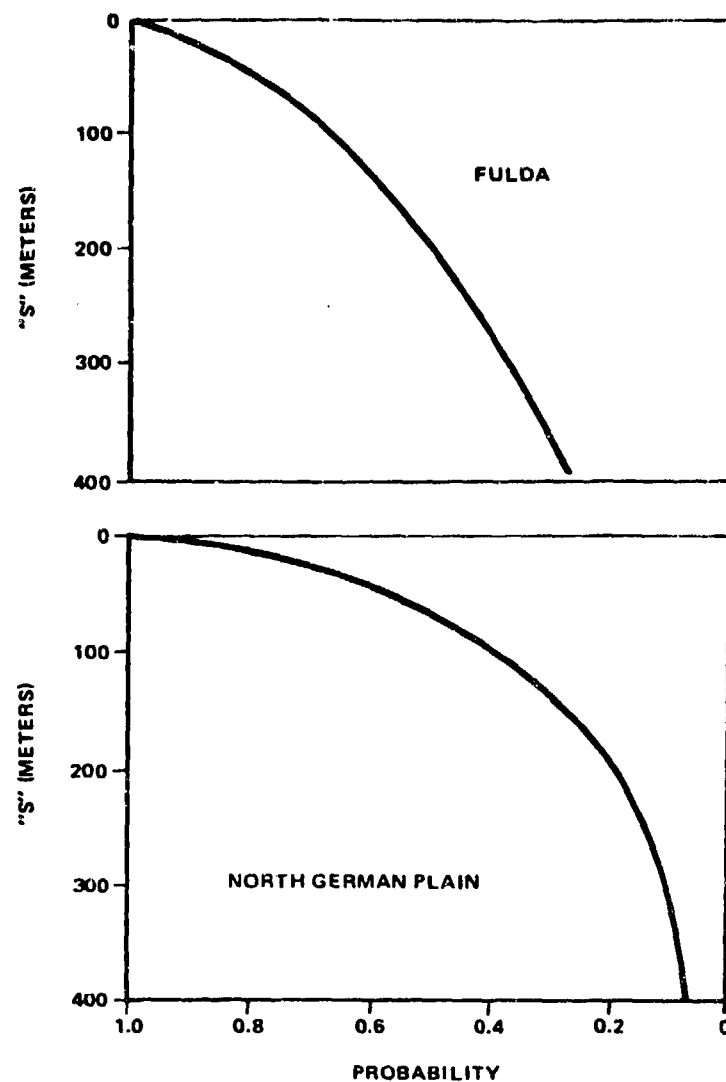
NOTE: THESE CURVES SHOW THAT THE HILLS AND FORESTS IN THE
AMERICAN SECTOR PROVIDE MORE EXPOSURE FOR ATTACKING
TANKS THAN THE FLAT LAND OF THE NORTH GERMAN PLAIN
WHERE ATTACKING TANKS ARE MORE OFTEN SCREENED FROM
VIEW BY VEGETATION.

FIGURE 6.37 PROBABILITY THAT AN INTERVISIBLE SEGMENT IS
AT LEAST AS LONG AS "S".

6-53

TABLE 6.2

AVERAGE PERCENT OF LOSS OF INTERVISIBILITY
BY CAUSE

Area	Landform	Vegetation	Manmade Features
Fulda Gap	58	25	17
North German Plain	21	78	1

6.1.1.6   Smoke Extinction Models

There are a number of models which allow one to calculate
the concentration and/or diffusion of smoke in space and time.
However, there are very few models which allow one to calculate
the extinction or transmission loss through smoke.   In this
section, we present some of these models.

6.1.1.6.1   GRC Smoke Model

R. Zirkind [25] has developed an Obscuring Aerosol Dispersion
Model from which one can calculate the transmission, contrast,
and thermal radiation.   The input data and computational details
are somewhat involved but the general input and output parameters
are given in Figure 6.38.

INPUT

A. SCENARIO

LOCAL TARGET AND OBSERVER LOCATIONS

MUNITION DEPLOYMENT PLAN

MUNITION RATE

SENSOR TYPE AND OPERATIONAL WAVELENGTH BAND

B. SMOKE MUNITIONS

TYPE (MK NO., CALIBER, ETC.)

FILL WEIGHT (GM)

FILL MATERIAL (WP, RP, HC, OIL, ETC.)

BURN TIME AND RATE

C. METEOROLOGICAL CONDITIONS

TIME OF DAY

CLOUD COVER

MEAN WIND SPEED (M/SEC) - SURFACE TO 10 M.

TEMPERATURE, $T(^\circ C)$ - @ 10 M AND 0.5 M ABOVE GROUND LEVEL

WIND DIRECTION

RELATIVE HUMIDITY (RH%)

D. OPTICAL PROPERTIES

SCATTERING, ABSORPTION AND EXTINCTION COEFFICIENTS

VISIBILITY

OUTPUT

TRANSMISSION

VISUAL AND NEAR INFRARED CONTRAST (DAYTIME)

MID-IR (3-5 μM) RADIANCE (DAYTIME)

FIGURE 6.38 INPUT AND OUTPUT PARAMETERS FOR THE GRC SMOKE MODEL.

6-56

6.1.1.6.2 AMSAA Transport and Diffusion Model

In a report by Marchetti [26], the AMSAA (Army Materiel Systems Analysis Activity) Transport and Diffusion Model for Smoke Munitions is described. It is referred to as the Smoke Effectiveness Manual Model (SEMM) and is derived from the original JTCG Smoke Obscuration Model No. 1 (SOM-1). It considers the delivery of white phosphorus (WP) or hexachlorethane (HC) munitions by indirect fire weapons to selected aimpoints located at a given range from the delivery weapons. Single or multiple volleys may be fired. After impact, the computer program determines the amount of obscurant at various time intervals along numerous lines of sight. The obscuring screen is transported and diffused as a function of local meteorological conditions during which time a criterion is applied to determine if target detection can be achieved with the particular visual aid employed. The model is adaptable to a number of spectral ranges and visual aids depending on the input data used. The following distinctive features are noteworthy:

- The smoke model is a transport and diffusion model and requires transmission data.

- The model assumes an uncorrelated Gaussian trivariate distribution for each obscuring burst.

- The model produces "holes" or discontinuities in the smoke screen due to the aiming and precision errors of indirect firing weapons.

- The model is used for detection but with the proper data can be used for recognition and identification.

The basic input and output parameters for the model are indicated in Figure 6.39.

6-57

AMSAA MODEL

```
┌─────────────────────────────────────┐
│                INPUT                 │
├─────────────────────────────────────┤
│       METEOROLOGICAL CONDITIONS      │
│                                      │
│            WIND DIRECTION            │
│                                      │
│             MUNITION TYPE            │
│                                      │
│              VOLLEY SIZE             │
│                                      │
│            SPECTRAL BANDS            │
│                                      │
│             YIELD FACTORS            │
│                                      │
│         DIFFUSION PARAMETERS         │
│                                      │
│         MUNITION FILL WEIGHT         │
│                                      │
│       ATTENUATION COEFFICIENTS       │
│                                      │
│      MUNITION DELIVERY ACCURACY      │
│                                      │
│               AIMPOINTS              │
│                                      │
│              RELIABILITY             │
│                                      │
│               BURN TIME              │
└─────────────────────────────────────┘
                    │
                    ▼
┌─────────────────────────────────────┐
│               OUTPUT                 │
├─────────────────────────────────────┤
│    OBSCURANT AMOUNT AS FUNCTION      │
│       OF TIME AND LOCATION           │
└─────────────────────────────────────┘
```
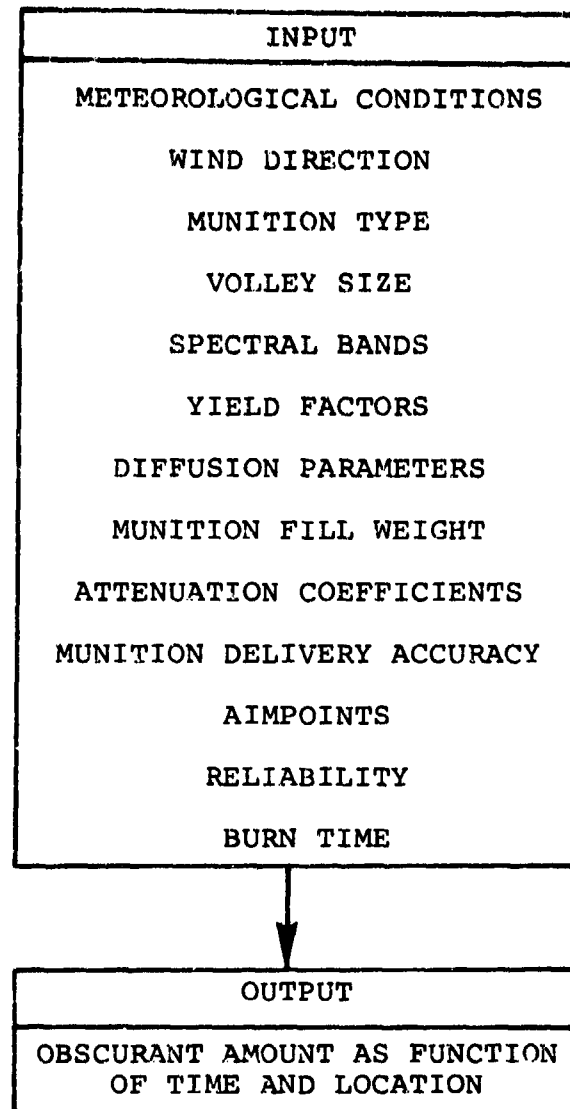
FIGURE 6.39 INPUT AND OUTPUT PARAMETERS FOR THE AMSAA
          MODEL.

6-58

6.1.1.7 Dust Extinction Models

There are several dust extinction models in existence based upon tactical military situations.

6.1.1.7.1 GE-TEMPO Dust Model

Thompson [27] describes in detail the ASL dust model. It is a simplified model which will allow the user to calculate attenuation and other optical effects, given specific environmental and munition characteristics. The general flow chart for this model is given in Figure 6.40.
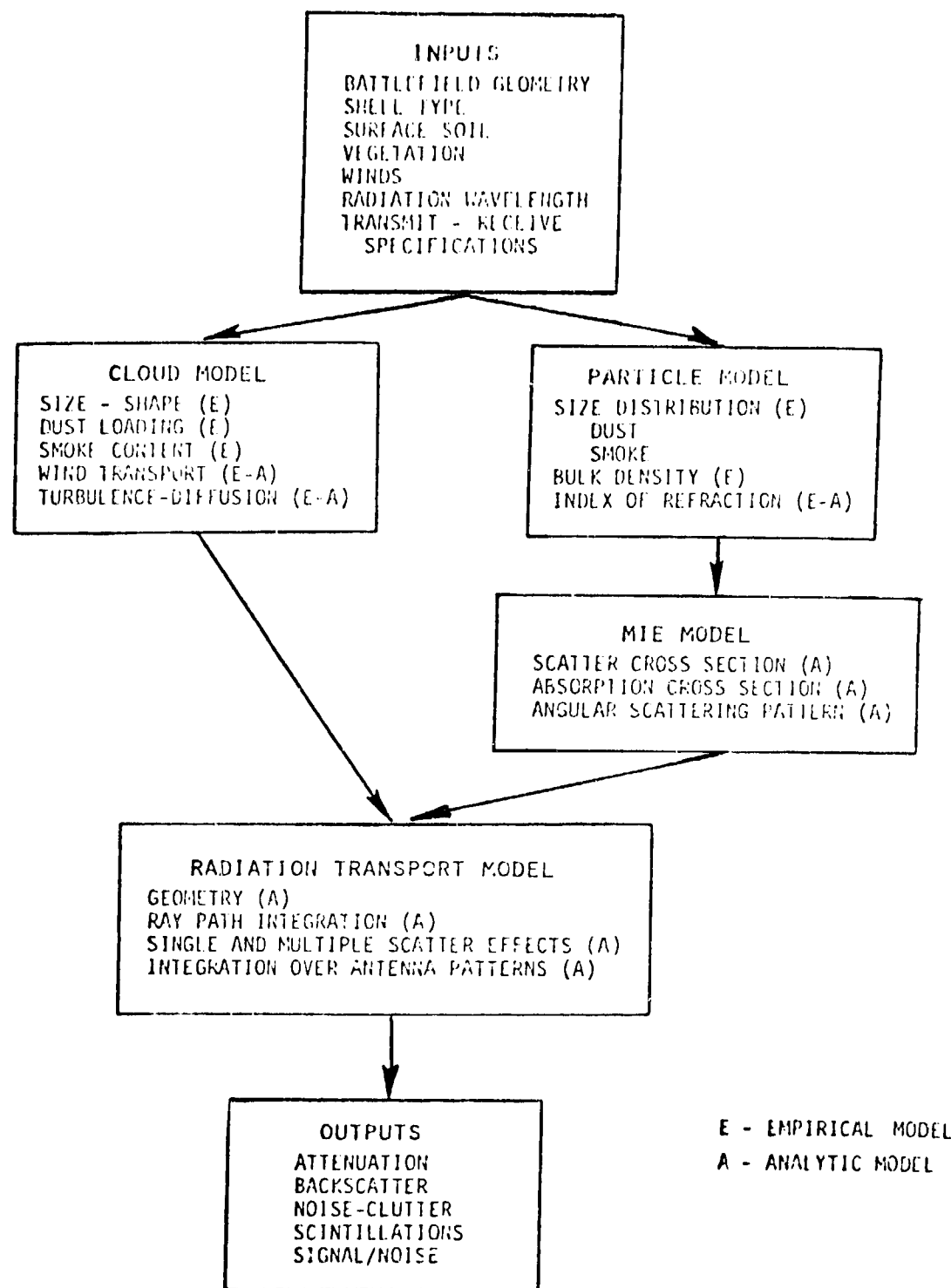
FIGURE 6.40   FLOW CHART FOR ASL DUST MODEL.

6.1.1.7.2 DIRTRAN

DIRTRAN is a dust model produced by Aerodyne Research, Inc. and described by Dvore [28]. The DIRTRAN-I Code is a computer-implemented model for predicting the optical effects of an explosion-produced dust cloud as it disperses in the lower atmosphere. This model is based on first principles of fluid dynamics, atmospherics, and optics. The model has been validated using cloud dimension and line-of-sight optical transmission data from the DIRT I and Graf II-Winter Army dust obscuration field trials. The DIRTRAN-I Code exploits information available about crater sizes produced by explosions in conjunction with distinct models for coupling of energy to the ground for artillery projectiles versus bare charges. The model recognizes that dust ejecta are partitioned into a buoyantly rising fireball and a non-buoyant "dust skirt" which is subject to diffusion in the vertically sheared wind field.

DIRTRAN-I solves separately for these two clouds. The solutions are based on atmospheric diffusion theory and take into account the effects of wind and temperature profiles in the constant shear stress layer of the lower atmosphere for different atmospheric stability categories. Separate treatment is given to particles of different sizes, the larger ones being allowed to settle out. Outputs of the code include dust cloud displacement and dimensions for both the non-buoyant wind-dominated skirt and the initial buoyant fireball as it is wind blown and eventually also becomes subject to wind diffusion. Line-of-sight transmittances at several wavelength bands (visible: 0.4-0.7 μm; infrared: 0.8-1.1, 3.5-4.0, and 8.5-12 μm; mm wave: 94-140 GHz) are also output options.

6.1.1.7.3 SAI Dust Model

R. E. Turner [29] at Science Applications, Inc. analyzed vehicular dust from Ft. Sill, Oklahoma and developed simple scaling relations for the transmission through dust. The relationship between the transmittance at two IR wavelengths is illustrated in Figure 6.41. The mathematical relationships connecting the spectral regions is given by the following:

$$T(9.75 \ \mu m) = T(3.443 \ \mu m)^{0.686} \quad \text{(Complete Range)} \quad (6.33)$$

and

$$T(9.75 \ \mu m) = T(3.443 \ \mu m)^{0.855} \quad \text{(Low Transmittance)}. \quad (6.34)$$
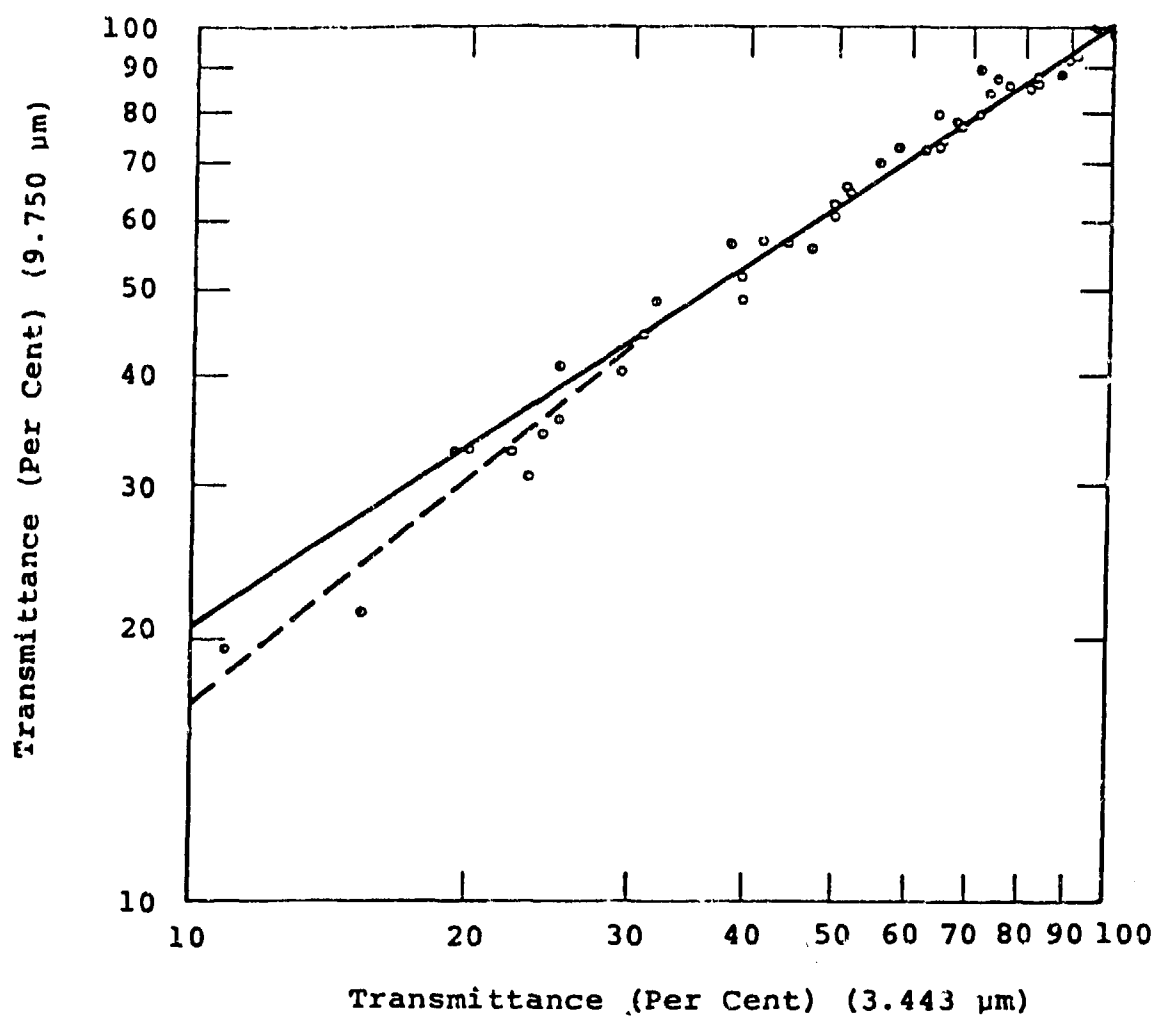
FIGURE 6.41 TRANSMITTANCE AT 9.750 μM VS. TRANSMITTANCE
AT 3.443 μM FOR VEHICULAR DUST FORT SILL,
OKLAHOMA TRIAL DPI-005-P1, 14 MAY 1978.

—— SLOPE = 0.686

--- SLOPE = 0.855

6.1.2 BACKGROUND MODELS

In this section we present models which allow one to calculate the radiation which arises from the background. This may include the sky, terrain, clouds, fires, etc.

6.1.2.1 Terrain Radiation Models

The terrain can reflect solar, lunar, sky, clouds, and other sources of radiation in the visible and near infrared parts of the spectrum and it can emit thermal radiation, the amount of which is determined by the temperature and emissive properties of the surface.

6.1.2.1.1 RADTAU-2

The model RADTAU-2 developed by Turner [30, 31, 32] is a model which calculates the spectral radiance at any point in the atmosphere for a target illuminated by solar, sky, and reflected radiation in the visible and near infrared spectrum and by thermal radiation from the Earth's surface and atmosphere. Examples of the results of radiance calculations using the model are illustrated in Figures 6.42 and 6.43 for a Rayleigh atmosphere (i.e., one which contains no aerosols). The model was specifically developed for hazy atmospheres and can be used to calculate the radiation in conditions ranging from no haze to a fog. The input and output parameters are indicated in Figures 6.44 and 6.45. The model can also be used to calculate the radiation at night for the moon in any phase.
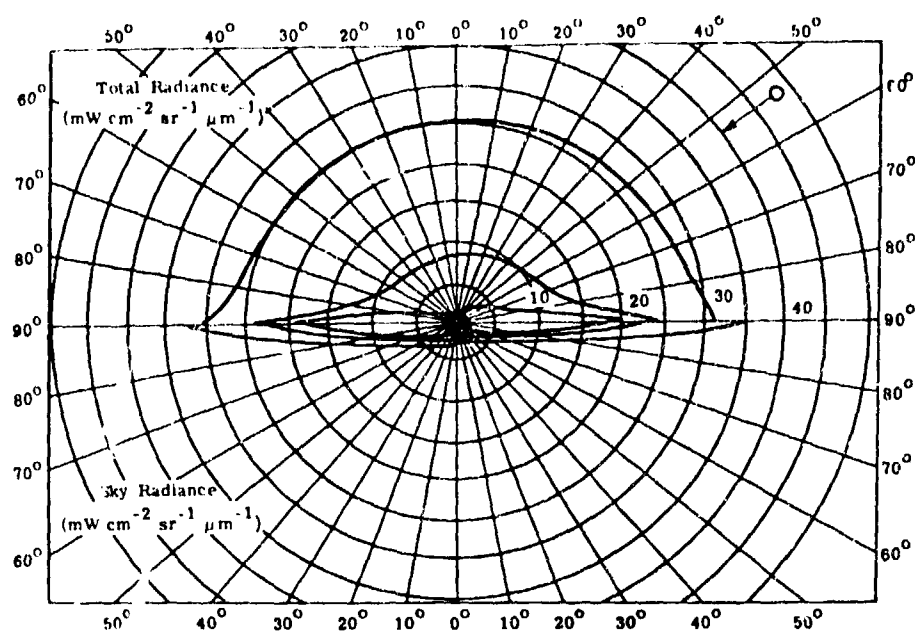
FIGURE 6.42 TOTAL RADIANCE AND SKY RADIANCE AS A
FUNCTION OF VIEW ANGLE IN THE SOLAR
PLANE FOR A RAYLEIGH ATMOSPHERE AND
THREE REFLECTANCES.
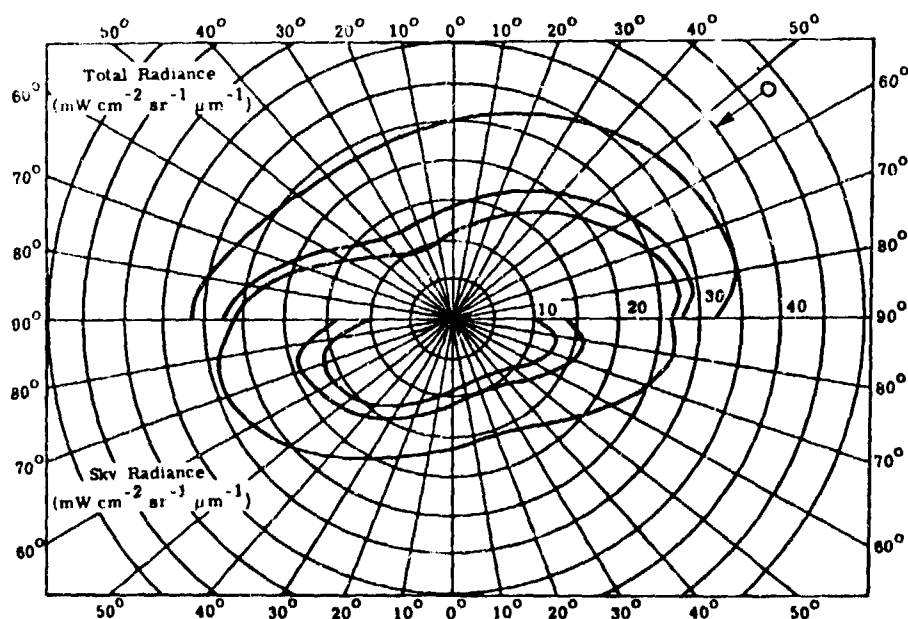
FIGURE 6.43 TOTAL RADIANCE AND SKY RADIANCE AS A
FUNCTION OF VIEW ANGLE IN THE SOLAR PLANE
FOR A RAYLEIGH ATMOSPHERE AND THREE
REFLECTANCES. τ_o IS 53°8'; THE DAY IS JUNE
21.

6-65

INPUT	
SOLAR ZENITH ANGLE	$(0^o - 89^o)$
ZENITH VIEW ANGLE	$(0^o - 89^o)$
NADIR VIEW ANGLE	$(0^o - 89^o)$
RELATIVE AZIMUTH ANGLE	$(0^o - 180^o)$
WAVELENGTH	(μM)
OPTICAL THICKNESS	$(0 - \infty)$
OPTICAL DEPTH OF SENSOR	$(0 - \infty)$
SURFACE ALBEDO	$(0 \leq \bar{\rho} \leq 1.0)$
TARGET REFLECTANCE	$(0 \leq \rho \leq 1.0)$
SURFACE TEMPERATURE	(^oK)
ATMOSPHERIC TEMPERATURE	(^oK)
AEROSOL ABSORPTION	
DATE, LOCATION, TIME OF DAY	

FIGURE 6.44 INPUT PARAMETERS OF TURNER'S
MODEL.

TURNER RADIATION MODEL
(CONTINUED)

OUTPUT	
TRANSMITTANCE (SPECTRAL)	(0.3 - 2.2 μM) THERMAL)
DIRECT TRANSMITTANCE (SPECTRAL)	"
DIFFUSE TRANSMITTANCE (SPECTRAL)	"
PATH RADIANCE (SPECTRAL)	"
SKY RADIANCE (SPECTRAL)	"
BEAM RADIANCE (SPECTRAL)	"
TOTAL RADIANCE (SPECTRAL)	"
THERMAL RADIANCE (SPECTRAL)	"

FIGURE 6.45 OUTPUT PARAMETERS OF TURNER'S
MODEL.

6-66

6.1.2.2 Sky Radiation Models

A number of models can be used to calculate the radiation from the sky. For multiple scattering, the analysis is usually complicated and requires considerable knowledge on the part of the user. Many of the details on the various computational techniques are treated in Reference 32. Here are presented more "practical" models which can more easily be implemented by users.

6.1.2.2.1 RADTAU-2

RADTAU-2, as described in Section 6.1.2.1.1, is a multiple scattering radiative transfer model from which one can calculate the sky radiation for spatially homogeneous conditions. The model will not allow one to calculate the sky radiation for discrete clouds or horizontal haze inhomogeneities. The basic input and output parameters are given in Figures 6.44 and 6.45.

6.1.2.3 Cloud Radiation Models

In the literature surveyed, there were few specific models which treat the radiation from discrete clouds. The model, RADTAU-2, will allow one to calculate the radiation from an overcast sky.

6.1.2.3.1 CLORAD

A cloud radiance model (CLORAD) was developed by Turner [33] for calculating the thermal radiance from clouds in the infrared spectrum. The cloud is assumed to be plane-parallel and of homogeneous composition. The basic input and output parameters are given in Figure 6.46.

CLORAD

INPUT
VIEW ANGLES
WAVELENGTH
SCATTERING PHASE FUNCTION
CLOUD TEMPERATURE
CLOUD OPTICAL THICKNESS
SINGLE SCATTERING ALBEDO

OUTPUT
ANGULAR EMITTANCE
ANGULAR REFLECTANCE
ANGULAR TRANSMITTANCE
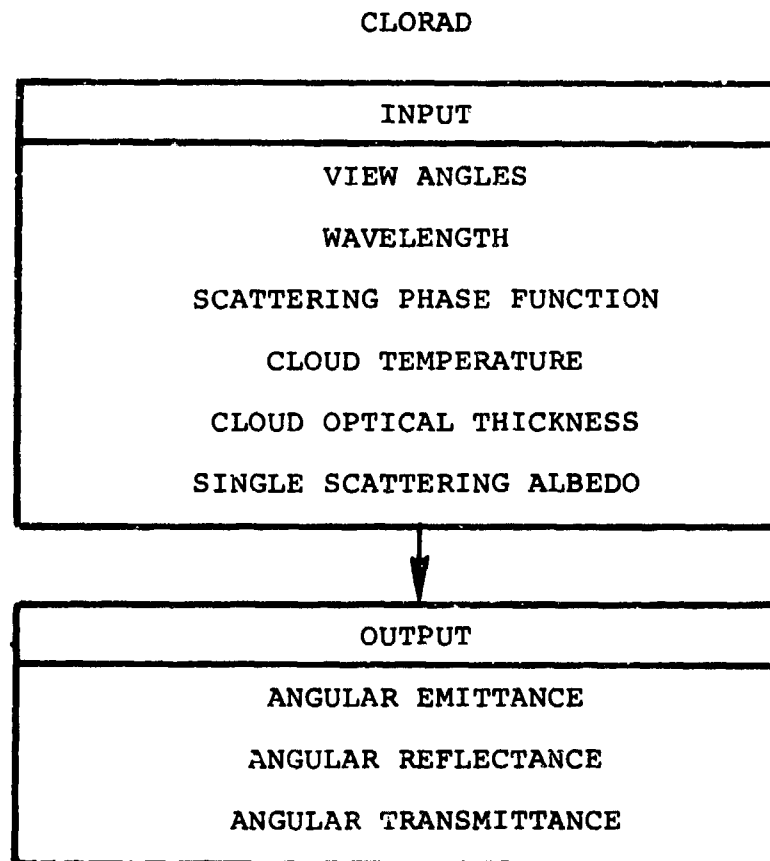
FIGURE 6.46 INPUT AND OUTPUT PARAMETERS FOR CLORAD MODEL.

6.1.2.3.2 Monte Carlo Model

Monte Carlo models have been used for the calculation of radiation in media with complicated geometries. One which has been used extensively is that of Kattawar and Plass [34]. By specifying the model inputs (i.e., the physical, optical and geometric properties of clouds), one can use the model to calculate the spectral radiance as a function of view angle, sun angle, and temperature. As in most Monte Carlo computer programs, however, the run time can be quite large because one is essentially counting photons as they propagate through the cloud. The basic input and output parameters are given in Figure 6.47.

MONTE CARLO METHOD

```
┌──────────────────────────────────┐
│             INPUT                │
├──────────────────────────────────┤
│          WAVELENGTH              │
│                                  │
│           GEOMETRY               │
│                                  │
│       OPTICAL THICKNESS          │
│                                  │
│    SINGLE SCATTERING ALBEDO      │
│                                  │
│          SOLAR ANGLE             │
│                                  │
│          TEMPERATURE             │
└──────────────────────────────────┘
                  │
                  ▼
┌──────────────────────────────────┐
│            OUTPUT                │
├──────────────────────────────────┤
│        SPECTRAL RADIANCE         │
│                                  │
│          CLOUD ALBEDO            │
│                                  │
│             FLUX                 │
└──────────────────────────────────┘
```
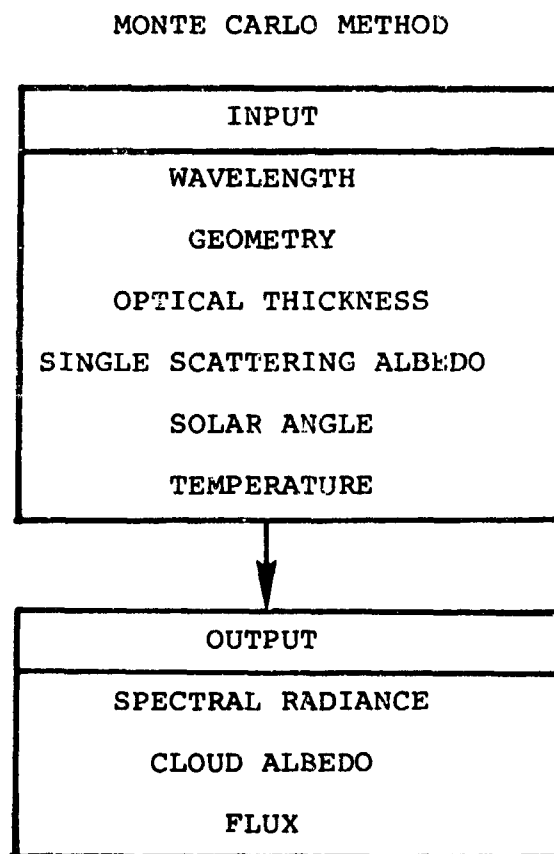
FIGURE 6.47 INPUT AND OUTPUT PARAMETERS FOR THE MONTE CARLO MODEL.

6-69

6.1.2.4 Other Background Radiation Models

(Models not found in literature survey.)

6.1 3   ILLUMINATION SOURCE MODELS

In this section are models which describe the illumination conditions in the battlefield for various sources.

6.1.3.1   Sun Illumination Models

The solar irradiance at any point in the atmosphere is given by:

$$E[\lambda,\tau(\lambda,z)] = \mu_o E_o(\lambda) \exp[-\tau(\lambda,z)/\mu_o] \qquad (6.35)$$

where: λ = Wavelength of the radiation

$\tau(z)$ = Spectral optical depth at altitude z

$E_o(\lambda)$ = Spectral solar extraterrestrial irradiance at the top of the atmosphere

μ_o = Cosine of the solar zenith angle.

For the irradiance at the ground, Equation (1) becomes:

$$E[\lambda,\tau_o(\lambda)] = \mu_o E_o(\lambda) \exp[-\tau_o(\lambda)/\mu_o] \qquad (6.36)$$

where $\tau_o(\lambda)$ is the spectral optical thickness of the atmosphere.

6.1.3.1.1   Turner Solar Model

One model for the solar spectral irradiance in the visible and near infrared spectrum is that used by Turner [35] in the RADTAU-2 model. The extraterrestrial solar spectrum, $E_o(\lambda)$ used is illustrated in Figure 6.48 and the relationship between the optical depth and horizontal visual range is given in Figure 6.49. The base input and output parameters are indicated in Figure 6.50.
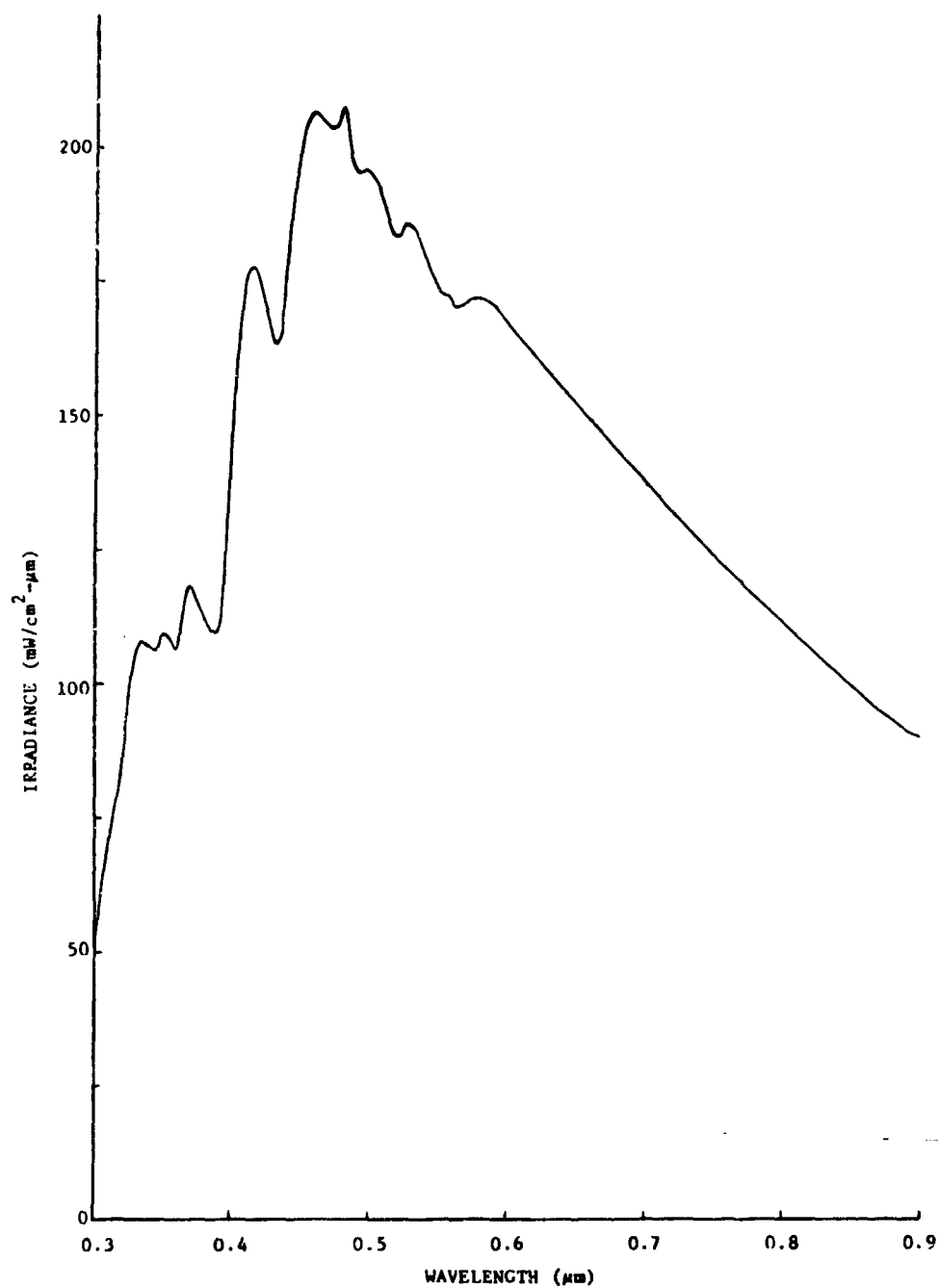
FIGURE 6.48   NASA STANDARD EXTRATERRESTRIAL SOLAR SPECTRUM.
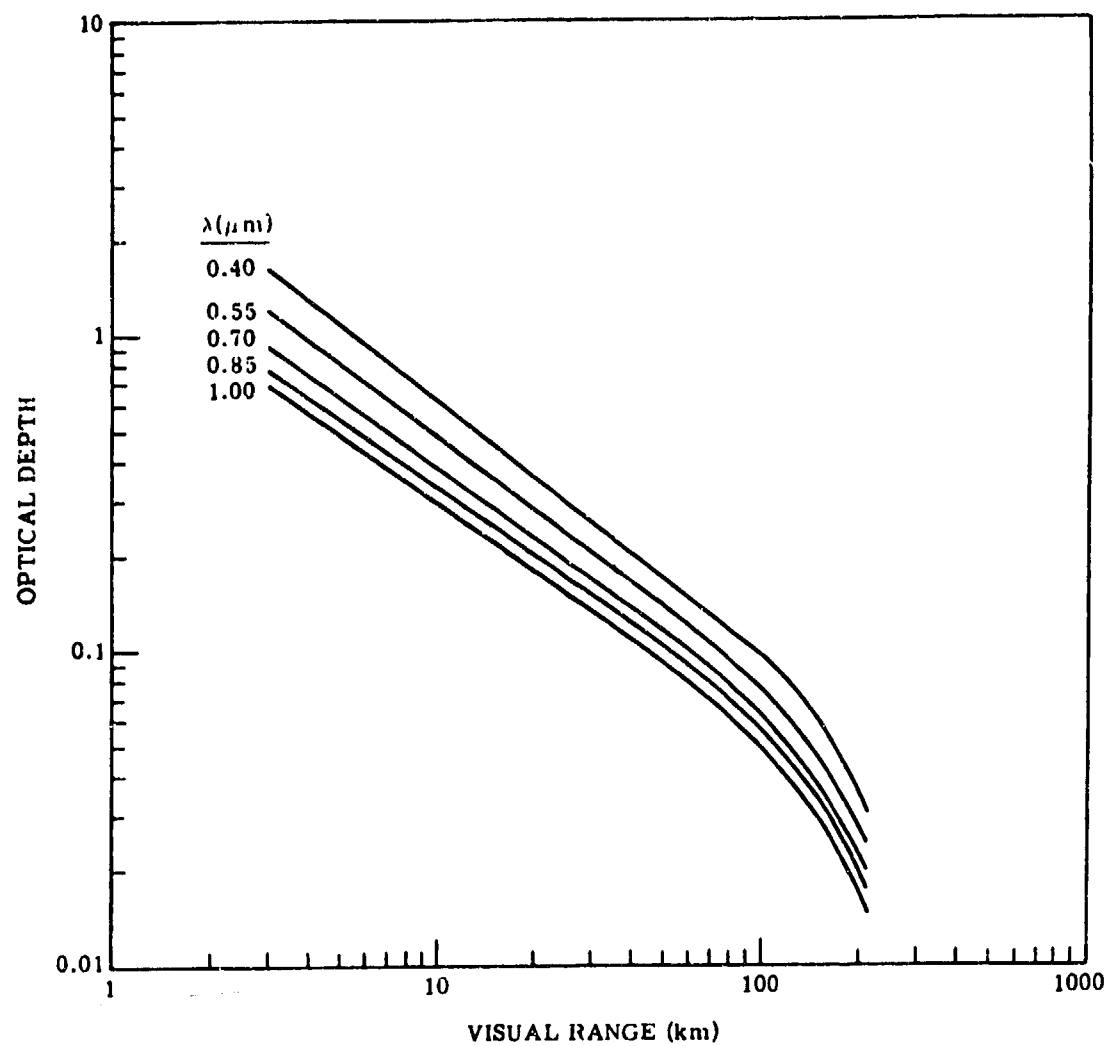
FIGURE 6.49 AEROSOL OPTICAL DEPTH τ_A VERSUS RANGE V.
PARAMETER IS SPECTRAL WAVELENGTH, λ.

6-73

TURNER SOLAR MODEL

```
┌─────────────────────────────────────────┐
│                 INPUT                    │
├─────────────────────────────────────────┤
│              WAVELENGTH                  │
│                                          │
│    SPECTRAL OPTICAL THICKNESS OR         │
│            VISUAL RANGE                  │
│                                          │
│          SOLAR ZENITH ANGLE              │
└─────────────────────────────────────────┘
                     │
                     ▼
┌─────────────────────────────────────────┐
│                OUTPUT                    │
├─────────────────────────────────────────┤
│           SPECTRAL IRRADIANCE            │
└─────────────────────────────────────────┘
```
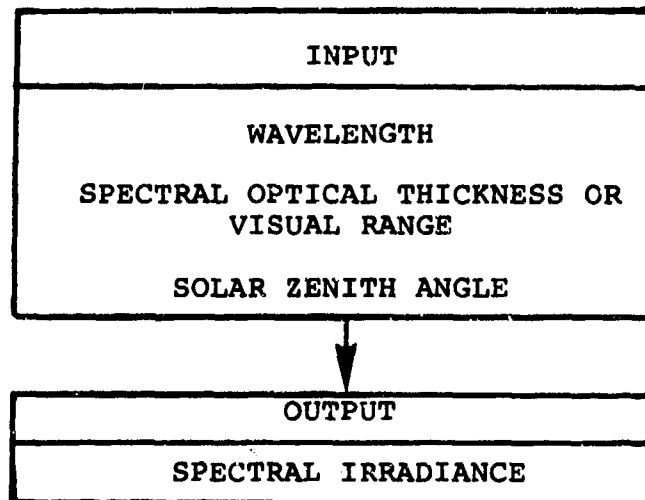
FIGURE 6.50 INPUT AND OUTPUT PARAMETERS
          FOR THE TURNER SOLAR MODEL

6.1.3.2 Moon Illumination Models

As in the case of the sun, there are models of the spectral irradiance due to the moon. It is more complicated however, because of the spectral albedo of the lunar surface and the phase of the moon.

6.1.3.2.1 Brown's Model

Here are included the results of measurements of solar and lunar irradiance by Brown [36]. In a sense, it is a model in that one can use input parameters and obtain the lunar irradiance. The input and output parameters for Brown's model are indicated in Figure 6.51. Figure 6.52 illustrates the illuminance as measured by Brown. It should be noted that this model does <u>not</u> provide the spectral irradiance.

BROWN'S MODEL

INPUT
ALTITUDE (ANGLE) OF MOON
LUNAR PHASE (IN QUARTERS)

OUTPUT
LUMINOUS INCIDENCE
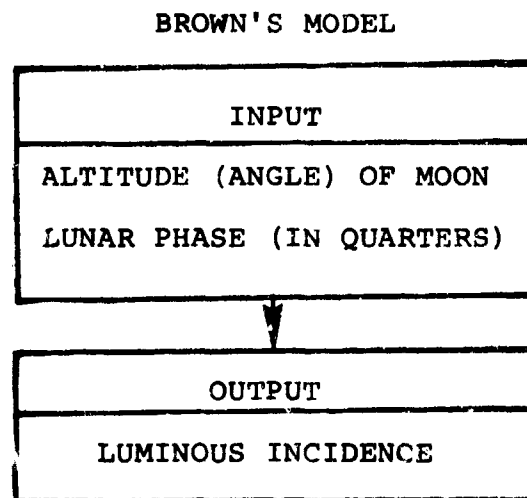
FIGURE 6.51   INPUT AND OUTPUT PARAMETERS FOR BROWN'S MODEL.
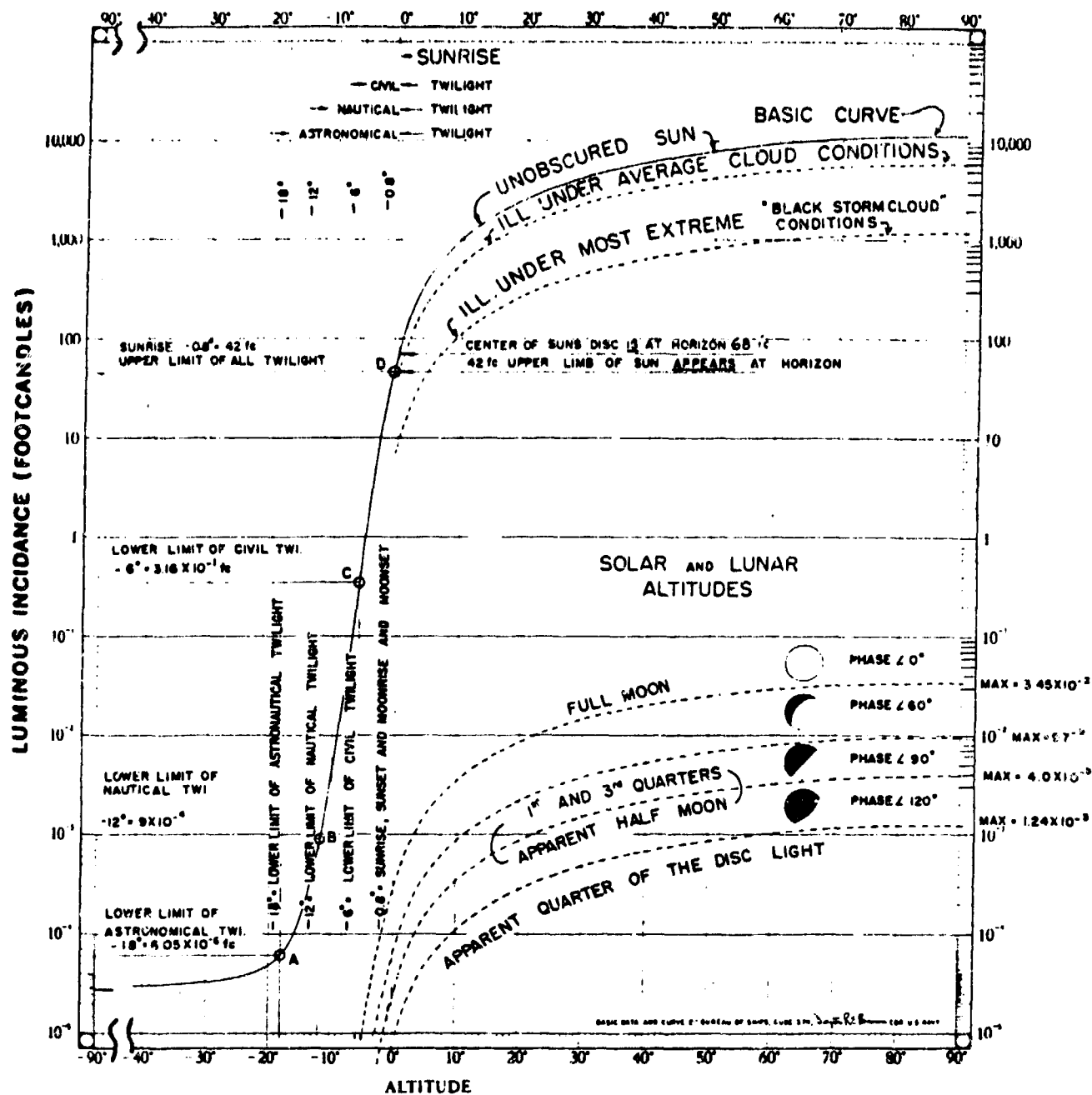
FIGURE 6.52   NATURAL LUMINOUS INCIDENCE (ILLUMINANCE) AS A
FUNCTION OF SOLAR AND LUNAR ALTITUDE AND FOR
VARIOUS PHASES OF THE MOON AS MEASURED BY BROWN.

6.1.3.2.2 Nighttime Model

A series of measurements were performed by Pleiter and Morley [37] and by Vatsia, et al [38]. The measurements were done under various conditions of cloud cover, moon altitude, and time. This we call simply, the Nighttime Model. The spectral radiance is illustrated in Figure 6.53. The input and output parameters for the Nighttime Model are given in Figure 6.54. It should be noted that this model is approximate insofar as the moon altitude and cloud cover are concerned. One can interpolate for intermediate conditions.

	DATE	TIME (E.D.T.)	MOON ALT.	MOON FRAC ILLUM.	CLOUD COVER	TEMP. (°C)	R.H.%	HORIZ. ILLUM. (Lux)
①	OCT. 13, 68	2000	−11.8°	−	0.06	5.0	80	1.966×10^{-3}
②	OCT. 13, 68	2035	−9.3°	−	0.06	5.0	80	2.106×10^{-3}
③	OCT. 13, 68	2300	5.8°	0.65	0.00	2.0	93	3.124×10^{-3}
④	OCT. 14, 68	0030	19.0°	0.56	0.25	1.0	95	7.568×10^{-3}
⑤	OCT. 14, 68	0330	48.4°	0.56	0.87	−0.5	96	1.334×10^{-2}
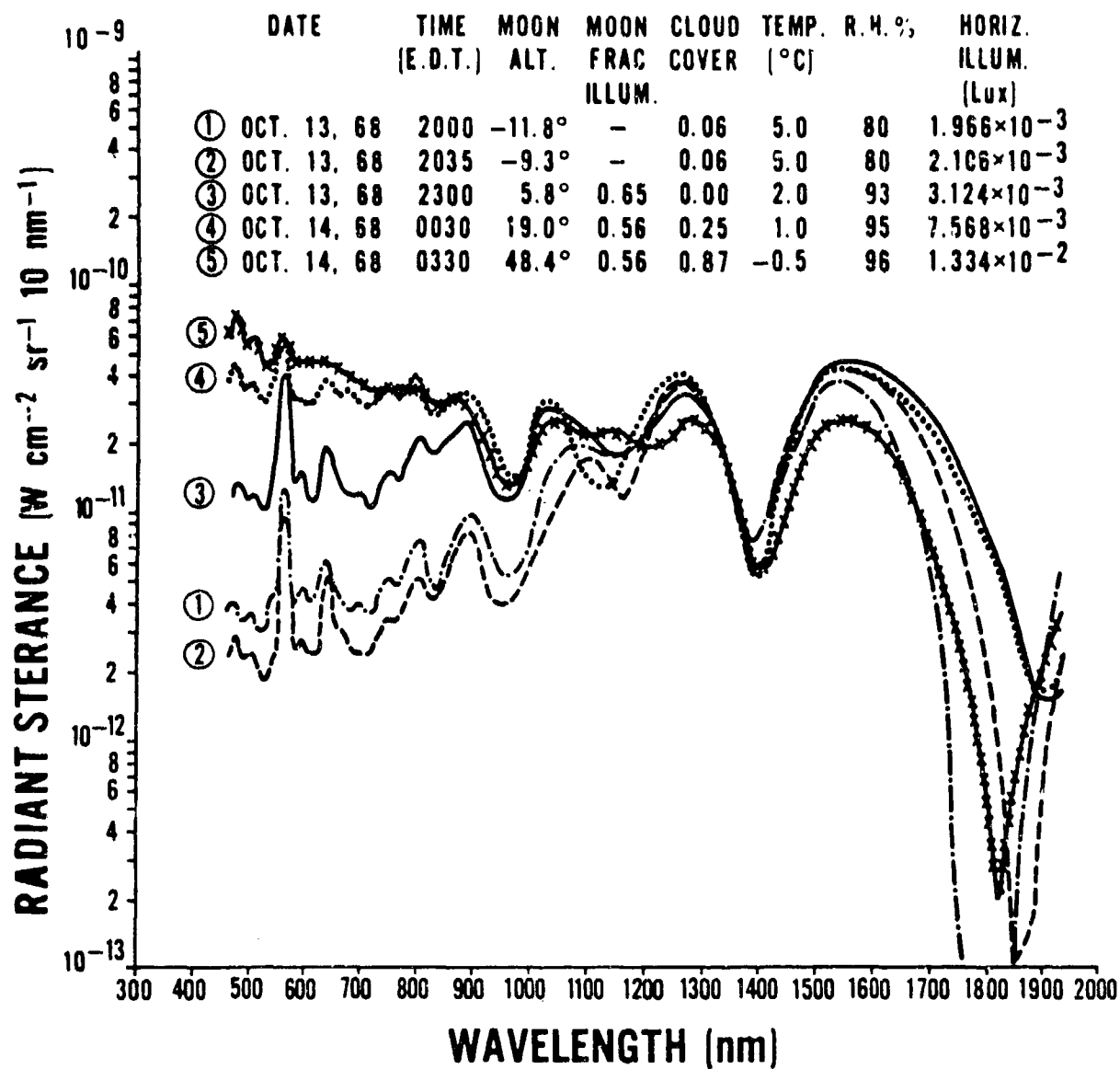
FIGURE 6.53   NIGHT SKY RADIANT STERANCE SPECTRA FOR VARIOUS ALTITUDES OF THE MOON AS MEASURED BY VATSIA, STICH AND DUNLAP [38].

NIGHTTIME MODEL
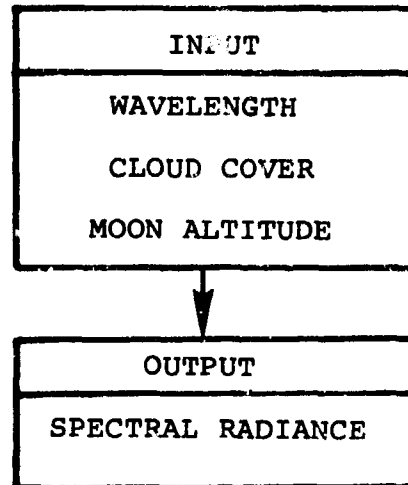
FIGURE 6.54   INPUT AND OUTPUT PARAMETERS
             FOR THE NIGHTTIME MODEL

6.1.3.2.3 The Turner-Lunar Model

Another model developed by Turner and Lambeck [39] is a spectral lunar irradiance model which applies to the spectral region 0.3-2.0 μm. The lunar spectral irradiance at the Earth's surface is given by Equation (6.37), i.e.

$$E_m[\lambda, \chi, \tau_o(\lambda)] = \mu_o E_{om}(\lambda, \chi) \exp [-\tau_o(\lambda)/\mu_o] \qquad (6.37)$$

which is the same as for the solar model except for the extraterrestrial irradiance $E_{om}(\lambda, \chi)$. The symbol χ is the lunar phase. The values of $E_{om}(\lambda, \chi)$ and the solar spectrum, $E_o(\lambda)$ are given in Figure 6.55. The lunar extraterrestrial irradiance in Figure 6.55 is for a phase of 0° (i.e., a full moon). For other phases, one must multiply the values in Figure 6.55 by the phase function in Figure 6.56. An example of the total (direct and diffuse) lunar irradiance as provided by the Turner-Lunar model is illustrated in Figure 6.57 The input and output for the direct lunar irradiance from the Turner-Lunar model is given in Figure 6.58.
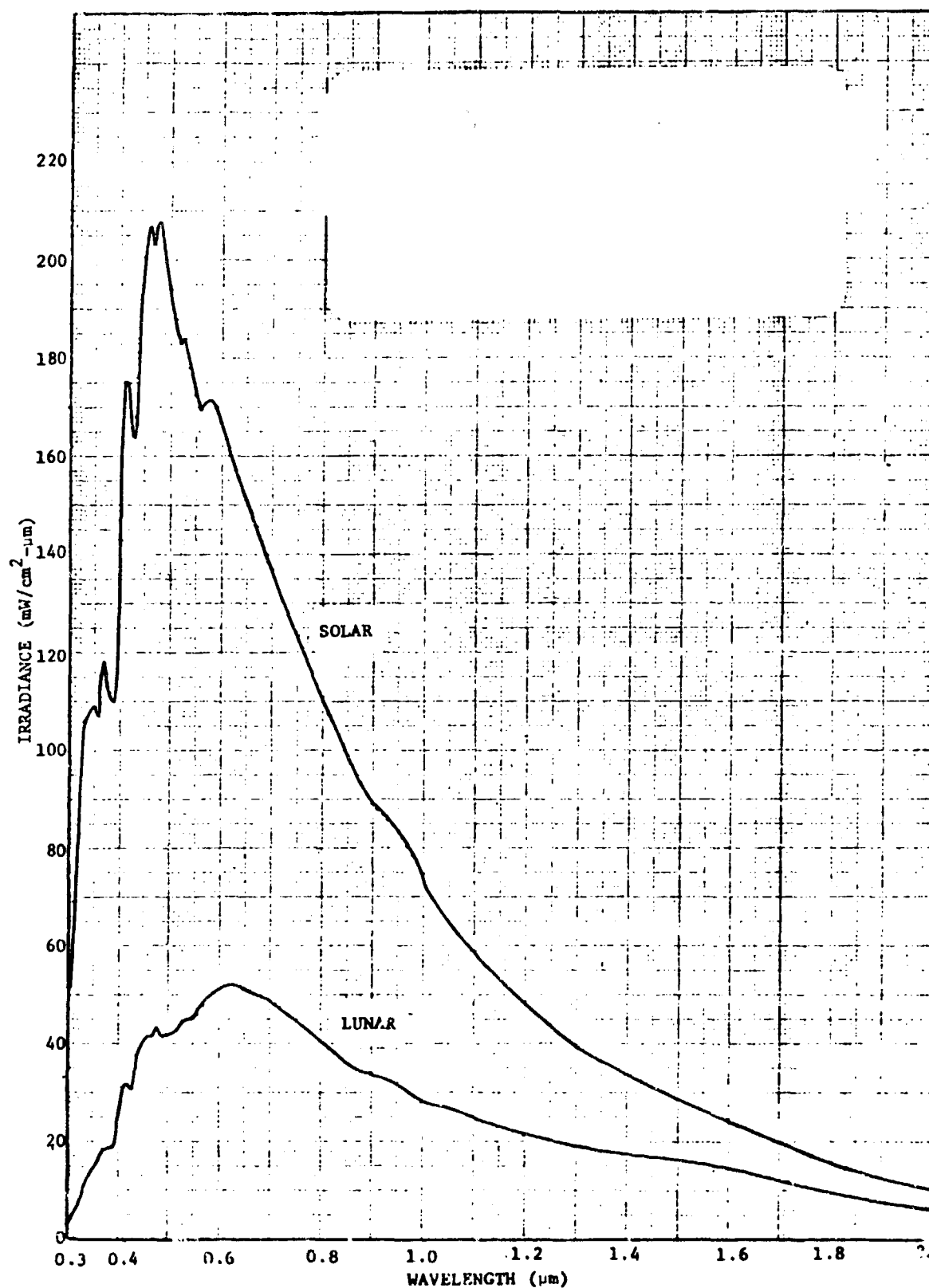
FIGURE 6.55 SOLAR AND LUNAR SPECTRAL IRRADIANCE AT THE TOP
OF EARTH'S ATMOSPHERE. LUNAR VALUES SHOULD BE
MULTIPLIED BY 10^{-5}.

6-91
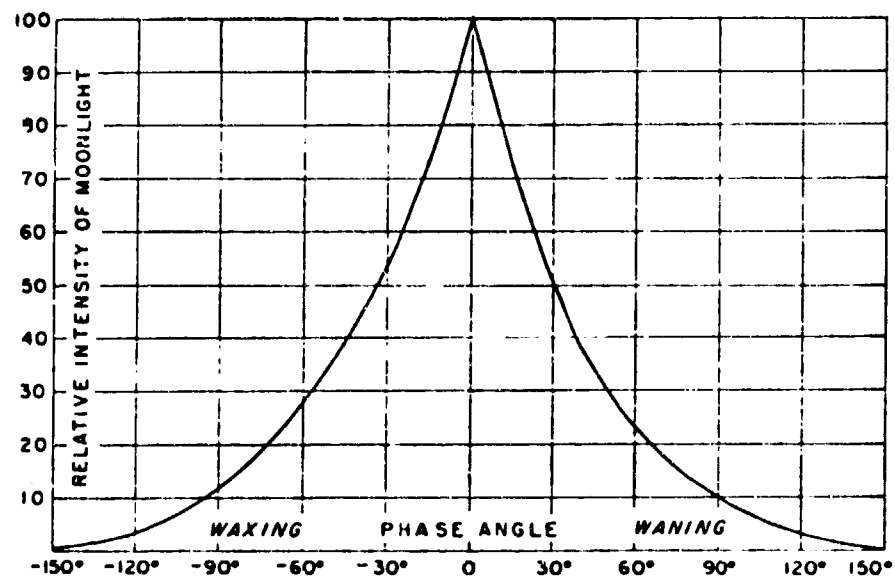
FIGURE 6.56 VARIATION IN A LUNATION
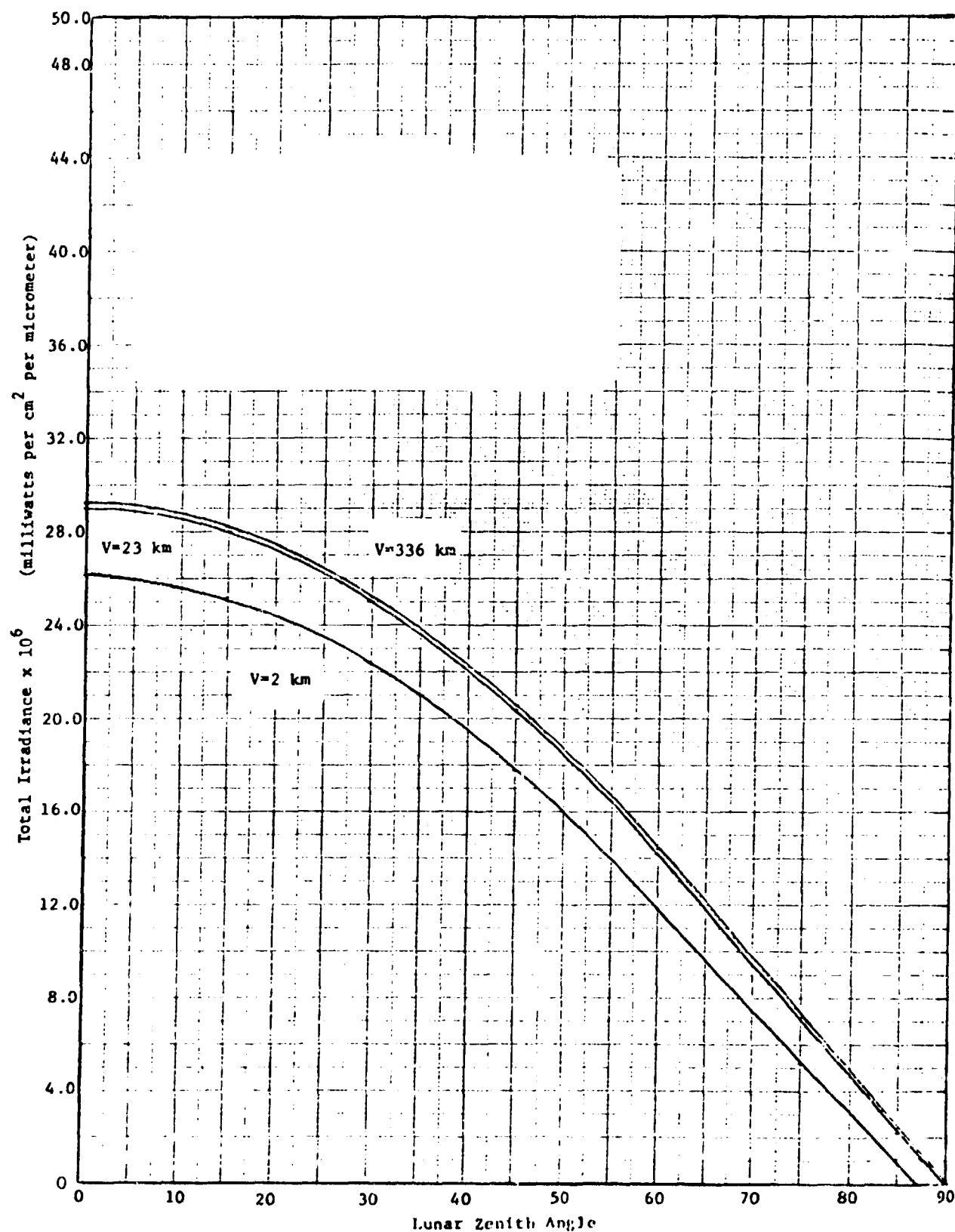
FIGURE 6.57   TOTAL IRRADIANCE AT THE EARTH'S SURFACE VS.
LUNAR ZENITH ANGLE.   V=VISIBILITY.   WAVELENGTH
=.55 MICROMETERS.   HAZY ATMOSPHERE.   BACKGROUND
REFLECTANCE=0.0.   LUNAR PHASE ANGLE=90°

6-83

TURNER LUNAR MODEL

INPUT
WAVELENGTH
MOON ANGLE (ZENITH)
PHASE ANGLE
SPECTRAL OPTICAL THICKNESS OR VISUAL RANGE

OUTPUT
SPECTRAL IRRADIANCE
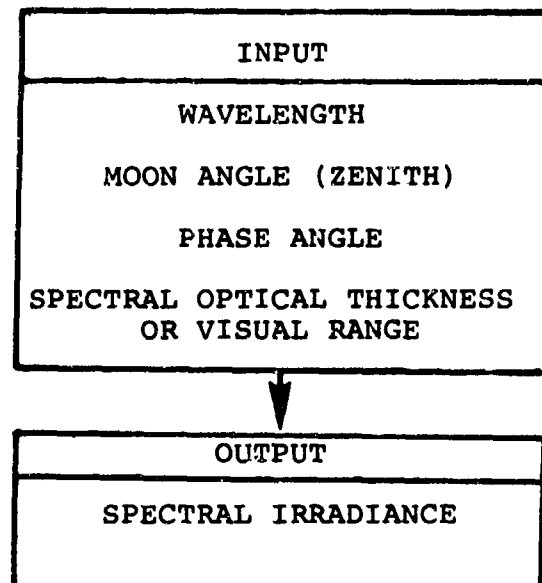
FIGURE 6.58   INPUT AND OUTPUT PARAMETERS
FOR THE TURNER LUNAR MODEL.

6.1.3.3 Artificial Source Illumination Models

In this section, we present models on the illumination of a battlefield by artificial sources (i.e., flares, fires).

6.1.3.3.1 Multiple Flare Model

An investigation of natural and artificial illumination sources was performed by Turner and Lambeck [39]. This model allows one to place a number of point sources in any position in three-dimensional space and the spectral irradiance is calculated at any point on the ground. A typical output of the model is illustrated in Figure 6.59. A flow chart of the combined artificial and natural illumination model is in Figure 6.60.

Wavelength = .55 micrometers
Hazy Atmosphere
Visibility = 2 km

Altitude of Flares =

.2 km

.1 km   .4 km
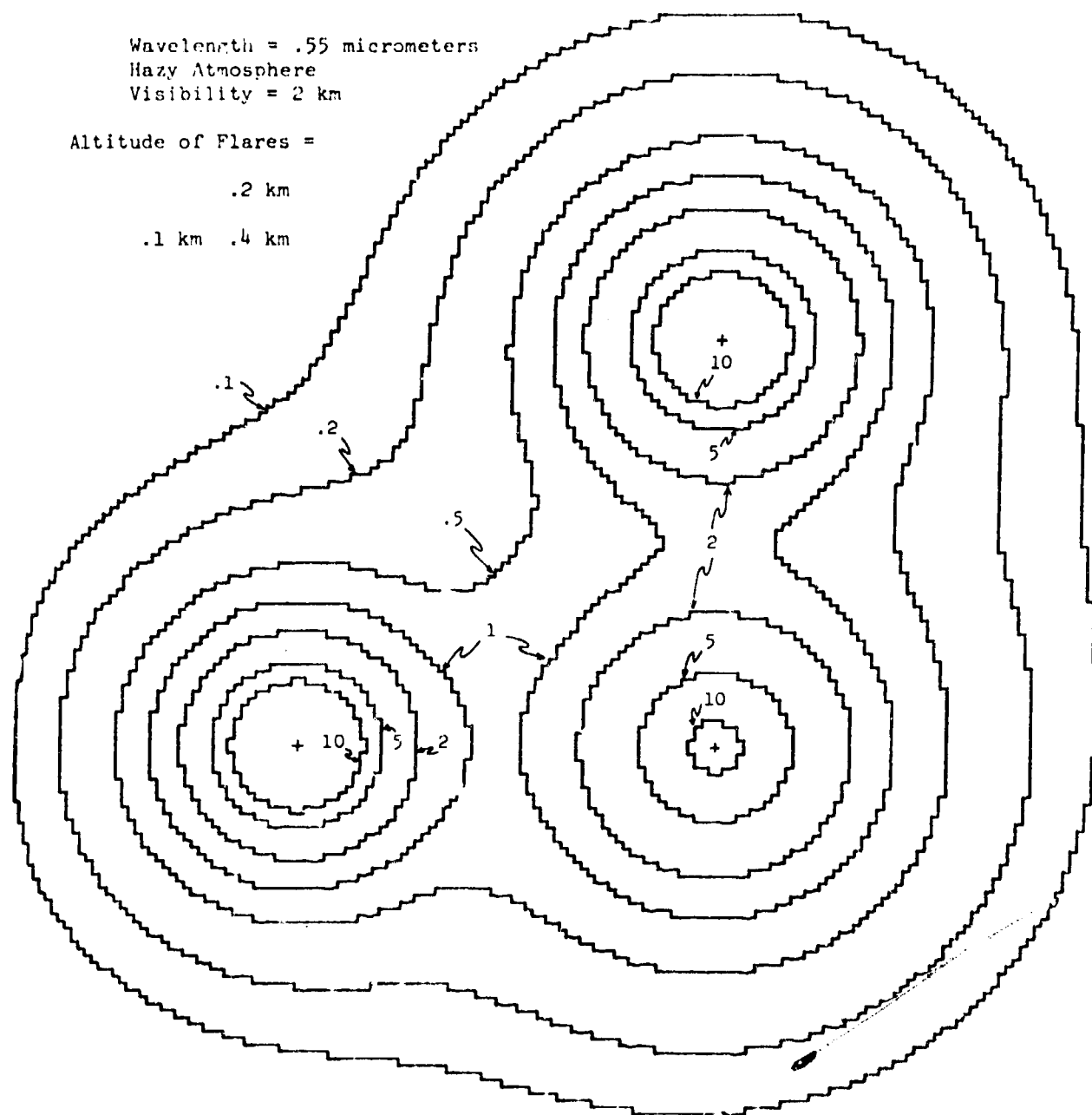
Contour levels are in units of 10^{-3} milliwatts per cm^2 per micrometer

Scale = .5 km per inch

FIGURE 6.59   CONTOURS OF CONSTANT DIRECT PLUS SIMPLY SCATTERED
IRRADIANCE GENERATED BY THREE MARK 45 FLARES.

6-86

ILLUMINATION MODEL

```
┌─────────────────────┐  ┌─────────────────────┐  ┌─────────────────┐
│ SCENE DEFINITION    │  │ METEOROLOGICAL DATA │  │ DATE, TIME      │
│ POINT SOURCES       │  │ HUMIDITY,PRESSURE   │  └─────────────────┘
│ DISTR. SOURCES      │  │ TEMP., VISIBILITY,  │  ┌─────────────────┐
│ TERRAIN CONDITIONS  │  │ TRANSMITTANCE,      │  │ LUNAR PHASE,    │
│                     │  │ CLOUD COVER,        │  │ LUNAR ZENITH    │
│                     │  │ FOG HEIGHT          │  │ ANGLE           │
└─────────────────────┘  └─────────────────────┘  └─────────────────┘

    ┌──────────────┐         ┌──────────────────┐
    │ REFLECTANCE  │         │ ATTENUATION      │
    └──────────────┘         │ COEFFICIENTS,    │
                             │ OPTICAL DEPTH    │
                             └──────────────────┘

   ┌─────────────────────┐              ┌─────────────────────┐
   │ ARTIFICIAL SOURCE   │              │ NATURAL SOURCE      │
   │ MODEL               │              │ MODEL               │
   └─────────────────────┘              └─────────────────────┘

        ┌────────────────────────────────────────────────┐
        │ NATURAL AND ARTIFICIAL RADIATION FIELDS:       │
        │        SPECTRAL TRANSMITTANCE                  │
        │        SPECTRAL IRRADIANCE                     │
        │        SPECTRAL SKY RADIANCE                   │
        │        SPECTRAL BEAM RADIANCE                  │
        │        SPECTRAL PATH RADIANCE                  │
        │        TOTAL SPECTRAL RADIANCE                 │
        └────────────────────────────────────────────────┘
```

FIGURE 6.60   ILLUMINATION MODEL FOR NATURAL AND
              ARTIFICIAL SOURCES.

6-87

6.1.3.4 Combat Illumination Models

In this section are various illumination models which can be used to calculate the illumination in a battlefield.

6.1.3.4.1 COIL

COIL is a Combat Illumination Model developed by Stathacopoulos, et al. [40] in 1975 to calculate the incident radiation due to artificial sources at specified points in the battlefield. These points are called "targets" and are described by giving their location and the direction of the normal to the surface. Target illumination in any spectral band of interest from 0.3 to 30 μm is calculated, taking into account the temporal and spectral characteristics of both the source and sensor, the effects of the terrain in obscuring and scattering radiation, the scattering of illumination by overhead cloud layers, and the absorption and scattering of radiation by the atmosphere. Targets may be sensor apertures, in which case COIL gives aperture irradiance for calculating the response of the sensor to the source itself.

COIL is an event-based program; that is, the illumination of the targets is calculated at definite times specified by the user. Thus, inherent in COIL is the concept of a scenario describing the motions of sources and the times when they turn on and turn off. Such an organization allows COIL to be run as a self-contained program, or to be inserted into larger event-based computer simulations of tactical warfare or reconnaissance missions. The basic input and output parameters for COIL are indicated in Figure 6.61.

COIL

INPUT	
HVEG	Height of vegetation
POBS	Probability of seeing through vegetation
TERMOD	One if terrain is considered, zero if not
XTC YTC	Origin of terrain grid
DEL	Grid mesh size
ZTER	Terrain data
NSRC	Number of sources
NTRG	Number of targets
NSNS	Number of sensors
TGISO	One if targets isotropic, zero if target orientation considered
TDELTA	Time increment
TIMEL	Time limit
ALPHAB	Absorption coefficient
ALPHAT	Scattering coefficient
ALAER	Altitude of clouds above zero level
VSBLTY	Visibility
H_2O	Precipitable water in the atmosphere
RLAER	Reflectance of clouds
SRC	Source type, motion tag, time on, time off
REF	Source initial coordinates and optical axis
CTRG	Target coordinates
VTRG	Target orientation
SNCD	Sensor location or target-sensor range
SENS	Sensor number, sensor type
REARTH	Reflectivity of the earth

OUTPUT	
T	Time
TG	Target number
SR	Sensor number
SRC	Source number
RADAMP	Direct illumination
SCAT	Scattered illumination
TOTAMP	Total of RADAMP for particular target
TOT SCATT	Total of SCAT for particular target

FIGURE 6.61 INPUT AND OUTPUT PARAMETERS FOR COIL

6-89

6.2 SENSOR MODELS

In this section we present information on models which are components of sensor systems.

6.2.1 NVL STATIC PERFORMANCE THERMAL MODEL

This model considers infrared imaging sensors in the 3-5 μm and the 8-14 μm bands in terms of detection and recognition performance [41]. By static, the model implies there is no search involved in finding the location of the target. The model predicts system performance by the following parameters:

- Minimum resolvable temperature
- Minimum detectable temperature
- Modulation transfer function
- Noise equivalent temperature difference.

The first two parameters characterize the display-observer interaction, while the last two parameters characterize the electro-optical sensor itself.

6.2.1.1 NVL Performance Model: Minimum Resolvable Temperature

This device-observer parameter is defined as the minimum temperature difference above 300°K required to resolve a four bar pattern of 7:1 aspect ratio. The MRT is a function of spatial (bar target) frequency f_B. The expression for MRT (f_B) is:

$$MRT(f_B) = \left(\frac{\pi^2}{4\sqrt{14}}\right)\left(\frac{S}{N}\right) \cdot \left(\frac{NET}{H_{TOT}(f_B)}\right)\left(\frac{Vf_B Q(f_B)\Delta Y}{\Delta f_n F_R \eta_{ov} t_e}\right)^{1/2} \qquad (6.38)$$

where: S/N = 2.25, the threshold for single bar

$H_{TOT}(f_B)$ = MTF for combined sensor and eyeball

t_e = 0.2 sec., eye integration time

$$\text{NET} = \text{Noise Equivalent Temperature (6.2.1.4)}$$

$$F_R = \text{Frame rate (sec}^{-1})$$

$$\eta_{ov} = \text{Overscan ratio (vertical instantaneous field-of-view [IFOV] to scan line spacing)}$$

$$\Delta Y = \text{Object space angular subtense (vertical) (unit: mrad), vertical IFOV}$$

$$\Delta f_n = \text{Noise bandwidth (6.2.1.4)}$$

$$V = \text{Scan velocity (mr/sec.)}$$

$$Q(f_B) = \text{Effect of noise with integration by the eye:}$$

$$Q(f_B) = \int_0^\infty S(f_x) H_N^2(f_x) H_{WB}^2(f_x) H_{EYE}^2(f_x) df_x \qquad (6.39)$$

where: H_N = MTF of the components after the detector

H_{WB} = Fourier transform of the bar width, a sine function

H_{EYE} = Eyeball MTF

f_x = Possible frequency components.

As the target frequency approaches zero, the quantity $f_B Q(f_B)$ approaches one.

6.2.1.2 NVL Performance Model: Minimum Detectable Temperature

This device-observer parameter is defined as the minimum temperature difference above 300°K, for a target of given dimension W, required to just detect the target. The difference between the MDT and the MRT is the target: a bar target for MRT and a square or circular target for the MDT. The result is:

$$MDT(W) = \left(\frac{S}{N}\right)' \left(\frac{NET}{A_T \int H_W^2 \, H_{TOT}^2 \, d^2 f}\right) \left(\frac{V \Delta y \; P(w)}{\Delta f_n t_e F_R \eta_{ov}}\right)^{1/2} \qquad (6.40)$$

where: $(S/N)'$ = Threshold signal-to-noise ratio required for detection

A_T = Target area in radians

H_W = Two dimensional target Fourier transform

H_{TOT} = Two dimensional sensor and eyeball transform.

Other quantities have been defined in Section 6.2.1.1. $P(W)$ is as $Q(f_B)$ with H_{WB} replaced by $H_W H_{TOT}$, and also is integrated in both directions.

6.2.1.3 NVL Performance Model: Modulation Transfer Function

The electro-optical sensor parameter, the MTF, is defined as the absolute value of the Fourier Transform of the spread function. The total MTF is approximated by the product of component MTF's, given below.

Optical Diffraction Limit:

$$H_{OPT} = \frac{2}{\pi} \left\{ \cos^{-1} A - A(1-A^2)^{1/2} \right\} \qquad (6.41)$$

where:

$A = \lambda F f_x / d$

λ = Wavelength

F = F/number

d = Focal length

f_x = Spatial frequency.

For optical geometric blur, CRT display, and vibration:

$$H = \exp(-K_1 f_x^2) \qquad (6.42)$$

where K_1 is the parameter for the respective quantities, with units of $mrad^2$. For the detector spatial filter and the LED display:

$$H = \sin(\pi f_x K_2) / \pi f_x K_2 \qquad (6.43)$$

with K_2 the respective angular subtense (units: mrad). For the detector and electronics temporal roll-off:

$$H = \left(1 + (f/K_3)^2 \right)^{-1/2} \qquad (6.44)$$

where F is the temporal frequency ($f_x V$), and K_3 is the respective 3 db roll-off frequencies.

6-93

Finally, the eyeball MTF is given by:

$$H = \exp(-Gf_x/M) \qquad (6.45)$$

where M is the system magnification and G is the gamma parameter given below:

LIGHT LEVEL, LOG (fL)	GAMMA
3	0.8133
2	0.9598
1	1.0980
0	1.4650
-1	1.8300
-2	2.2773
-3	2.7653
-4	3.3347
-5	3.9040

6.2.1.4 NVL Performance Model: Noise Equivalent Temperature

The electro-optical sensor parameter, the NET, is defined as the temperature difference above 300° K of an extended source which gives a peak SNR of one in the electronic channel between the detector and display. This is given as:

$$NET = \frac{4F^2 \sqrt{\Delta f_n}}{\pi A_d^{1/2} N^{1/2} T_o \int_{\Delta \lambda} D_\lambda^*(f_1) L_\lambda' d\lambda} \qquad (6.46)$$

where:

Δf_n = Noise bandwidth (Hz)

A_d = Detector area (cm^2)

T_o = Average optical transmission

$D_\lambda^*(f_1)$ = Specific detectivity in cm $Hz^{-1/2}$ W^{-1} at a specific measuring frequency f_1, given as a function of wavelength

L_λ = Temperature derivative of Planck radiation at 300 K (w cm^{-2} sr^{-1} K^{-1})

$\Delta \lambda$ = Spectral bandpass

N = Number of detectors scanned and summed in series

F = F/number of system optics.

$$\Delta f_n = \int_0^\infty S(f) \, H_{ELECT}^2 \, H_{MD}^2 \, df \qquad (6.47)$$

where $S(f)$ is the normalized noise power spectrum from the detector, with H_{ELECT} and H_{MD} the electronic and measuring device MTF, respectively.

$$H_{MD}(f) = \left[1-(f/f_o)^2\right]^{-1/2} \qquad (6.48)$$

with $f_o = (2T_d)^{-1}$, where T_d is the detector dwell time.

6-95

For white noise, $H_{ELECT} \simeq 1$ and $f < f_o$,

$$\Delta f_n \approx \left(\frac{\pi}{2}\right)\left(\frac{1}{2T_d}\right). \qquad (6.49)$$

The dwell time is:

$$T_d = \frac{\Delta x \cdot n \cdot \Delta Y \cdot \eta_{sc}}{\alpha \cdot \beta \cdot \eta_{ov} \cdot F_R} \qquad (6.50)$$

where: α, β = Fields of views for horizontal and vertical direction

Δx = Object space angular subtense (horizontal) (i.e., instantaneous field-of-view)

ΔY = Like Δx, but vertical

n = Number of parallel detectors

F_R = Frame rate

η_{sc} = Scan efficiency

η_{ov} = Overscan ratio.

6.2.1.5 NVL Target Submodel

The target submodel of the thermal model is based on target size. The model target is a rectangle with the smaller dimension called the real target critical dimension. The length of the rectangle is then whatever length gives an area equal to the real world target. In general, the infrared signature pattern is referenced with respect to a large ensemble of experimental results and not a specific one.

6.2.1.6 NVL Background Submodel

The background submodel of the thermal model operates on the general feature of the average temperature difference from the background. The temperature difference of a target is an area-weighted average over the entire signature. From this average temperature is subtracted the average background temperature. However, the submodel uses a more basic quantity of power difference, so the temperature difference is converted to a power signal using the appropriate form of the radiation law of Planck. The background submodel does not account for background clutter so that predictions may be invalid if clutter is high.

6.2.1.7 NVL Atmospheric Submodel

The atmospheric submodel of the thermal model considers visibility degradations due to atmospheric absorption and scattering of gases and aerosols. Two ranges are considered:

Non-severe (5 km or more)

    LOWTRAN version of the AFGL is used

Severe (less than 5 km)

    Empirical scattering coefficients are used according
    to spectral regions (based on measurements in Germany
    and at Ft. A. P. Hill, Virginia).

6-97

6.2.2 MARSAM PHOTOGRAPHIC MODEL

In this section are presented the MARSAM Photographic Model and its various submodels [42].

6.2.2.1 MARSAM Atmospheric Submodel

This submodel includes several subsections.

· Sun's Spectral Illumination given

    - As a function of wavelength bands

    - As measured at the top of the atmosphere

· Direct Ground Illumination given

    - As attenuated by various atmospheric layers for dust, smoke, water vapor, haze, fog, clouds, rain, snow, or gaseous molecules

    - Basic equation is:

$$I_{grd}(\lambda) = I_{sun}(\lambda) \, \exp \left[-\sum_{i=1}^{N} \beta_i(\lambda) t_i \csc \zeta \right] \tag{6.51}$$

where: $I_{grd}(\lambda)$ = Ground illumination

         $I_{sun}(\lambda)$ = Illumination above atmosphere

            $\beta(\lambda)$ = Coefficient of extinction per unit distance

            t = Vertical thickness of layer

            ζ = Solar elevation

            i = Individual layer.

    - Diffuse Sky Brightness Ground Illumination contribution to ground illumination as a function of wavelength.

    - Target, Background and Shadow Intrinsic Brightness Equation

$$B(\lambda) = \frac{I(\lambda) \ r(\lambda)}{\pi} \tag{6.52}$$

6-98

where: $B(\lambda)$ = Surface Brightness

   $I(\lambda)$ = Total direct and diffuse illumination

   $r(\lambda)$ = Surface reflectance.

- Brightness of these five scene components is
  calculated:

  · The area of interest

  · Shadow area of the area of interest

  · Average background noise

  · Ambient background, of immediately
    surrounding area

  · Shadow area of the ambient background.

6.2.2.2 MARSAM Exposure Submodel

Components considered:

- Camera exposure with film
- Large scene exposure
- Dynamic limits and gamma of film
- Output of atmospheric model.

6.2.2.3 MARSAM Decision Submodel

Components considered:

- Resolution limit calculation
- Target detection and/or identification criterion
- Contrast comparison.

6.2.2.4 MARSAM Display Submodel

Components considered:

- Image position display
- Errors of image position
- Dimensions of image on display.

6-100

6.2.3 REALISTIC EUROPEAN BATTLEFIELD TARGET ACQUISITION MODEL (REBTAM)

The Realistic European Battlefield Target Acquisition Model (REBTAM) relates tactical and meteorological parameters directly to sensor performance [43]. The basic inputs to the model are the tactical scenario, implying geographic location (such as the nation), threat force structure (threat target and vehicles of that region), and munition types. The model gives performance profiles of electro-optical sensors in terms of effectiveness using historic weather data. Submodels include:

1. the target signature subroutine;
2. the atmospheric propagation subroutine; and
3. the terrain subroutine.

These submodels pass information to the sensor model which generates performance parameters for the particular system under study.

6.2.3.1 The REBTAM Target Signature Submodel

The REBTAM target signature subroutine consists of a matrix of most probable signatures in each spectral region for each important target, such as the M-60, XM-1, ZSU-23, etc. This model will eventually be replaced by a first-principle, empirically based model E-O SIGMO, which will have the ability to predict signatures as a function of environmental variables.

6.2.3.2 REBTAM Atmospheric Propagation Submodel

The atmospheric propagation submodel consists of a set of laws relating transmission in each spectral band to meteorological inputs, smoke concentration, and dust quantity resulting from high explosive artillery munitions. This atmospheric routine is eventually scheduled to be replaced by the analytical model E-O SAEL (Electro-Optical Sensor Atmospheric Effects Library) being developed at ASL.

6.2.3.3 REBTAM Terrain Submodel

This subroutine will consist of data bases of line-of-sight
distributions identified at the various locations. These
distributions are still in the process of being identified.

6.2.3.4 REBTAM Sensor Model

The outputs from the three environmental submodels are target-
to-background signal strength, atmospheric transmission, and
probability of a line-of-sight. The sensor submodel uses these
to generate target acquisition probabilities as a function of
range or time. The sensor model can be run iteratively for a
distribution of signature, atmospheric, and terrain valves based
on the climatology distribution for the desired geographic
location. Such a distribution of performance is called a sensor
performance profile, as illustrated in Figure 6.62. Currently
available performance models include those for visual, image
intensifier, TV, and thermal imaging systems. Plans are to
extend this to include laser active systems and mm wave radar.

GRAF/0600-1200/SEP-NOV
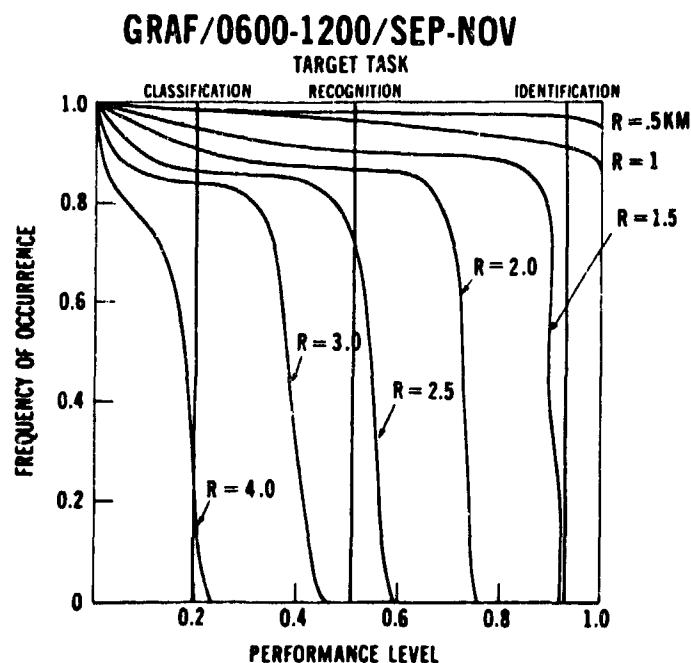
FIGURE 6.62 AN EXAMPLE OF A SENSOR PERFORMANCE PROFILE FOR A
HYPOTHETICAL INFRARED NIGHT SIGHT. R IS THE RANGE
(km) BETWEEN TARGET AND OBSERVER.

6.2.4 SYSTEM ASSESSMENT MODEL

No reference material presently available in this category.

6.2.5 ADDITIONAL SENSOR MODELS

This space is left for expansion.

6.3 COMBAT MODELS

Combat models or war "game" models have the highest level
of complexity in that they generally include a large number of
sensor models, and they include details of combat activity.
Effects of the battlefield environmental contion may or may not
be included in a given combat model.

6.3.1 CARMONETTE MODEL

The Carmonette Model gives a stochastic, battalion level simulation of ground combat [44]. This model was designed to simulate small unit battles emphasizing unit movement, target detection, weapon firing, effects of different weapon mixes, effects of tactics, effects of sensors and detection devices, and to provide assessment of results.

The Carmonette model uses preplanned scenarios and force postures. It simulates the battle area with a maximum 60x63 grid representation of terrain. Terrain data are input by grid square and include elevation, height of vegetation, indices of cover and concealment, and indices of trafficability. Grid sizes overlaying terrain are usually run at 100 meter squares.

Detailed orders are given that control the actions of each unit. No provision is made for causing groups of units to act in any coordinated manner. Individual units in the model are used to represent individual soldiers or individual vehicles up to units of platoon size. The model can have up to 70 units per side and up to 63 killable elements per unit. There can be up to 56 weapon types and up to 36 sensors used in the model. Combat can include land forces and armed helicopters.

Simulated infantry can be mounted or dismounted. Dismounted infantry and armored vehicles can be pinned down. Heavy armored units cannot be pinned down. Heavy and light armored vehicles can be caused to button up. Artillery, including mortars, can provide scheduled and on-call fires, but adjustments in artillery fire are not simulated. Resupply, evacuation, and maintenance functions are not simulated, and forces cannot fire upon others on the same side in CARMONETTE.

CARMONETTE MODEL SUMMARY

INPUT DATA	COMBAT PROCESSES	OUTPUT INFORMATION
(for weapons, sensors mobility and units)	Terrain and LOS calculations	(on total force or by units; cumulative, or chronological)
effective ranges	Unit movement	
rates of fire	Target acquisition	casualties
terrain LOS	Target selection	target kill
measurement rates	Weapon firing and impact	operational statistics
geometry	Communications	
probability of gain/ loss of target information	Assessment of results	ammunition expenditure
Lethal areas		
suppression		
tactical decisions		

6-107

Certain accumulated data can be obtained by weapon or target class and specified range intervals, and the average and variance of ammunition expenditure by weapon type is available.

The major functions of the Carmonette model and their interrelations are shown in Figure 6.63.
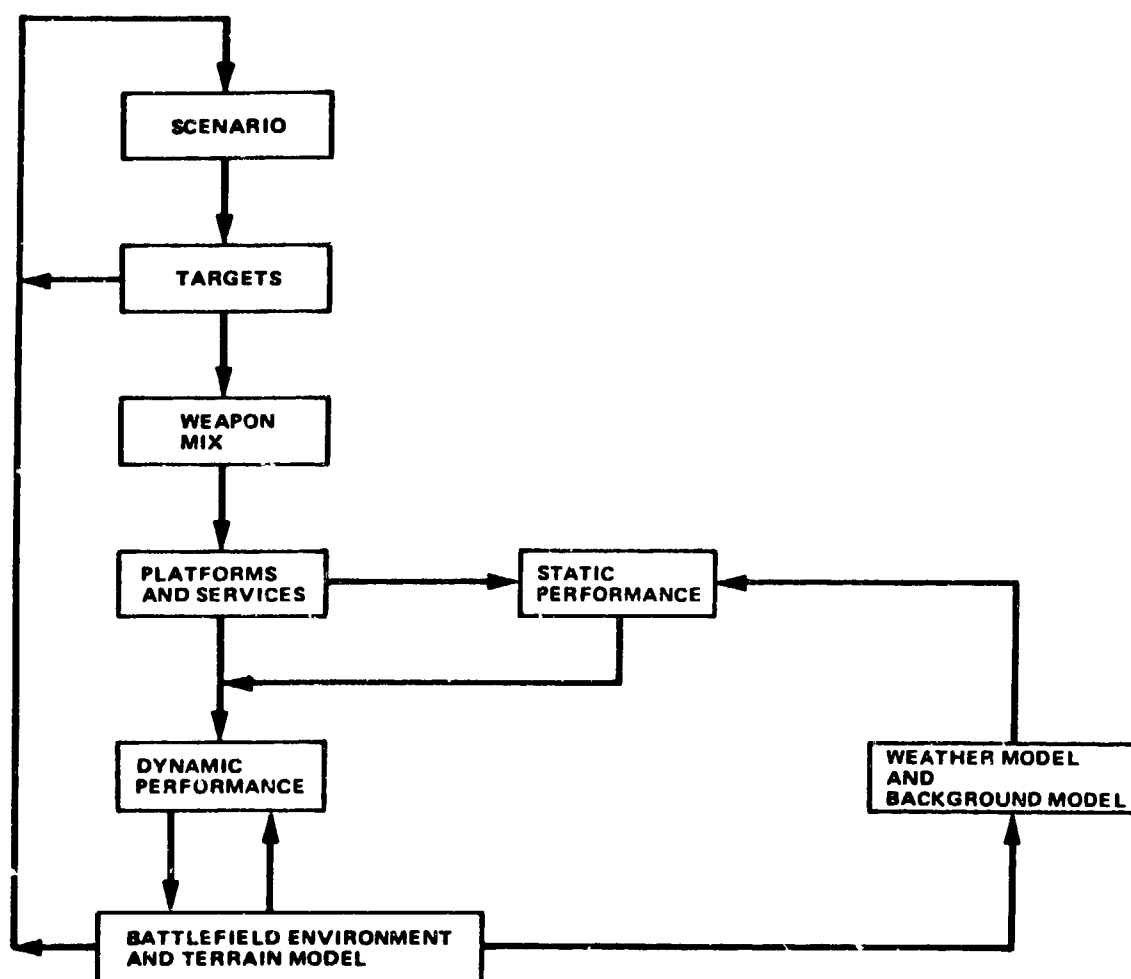
FIGURE 6.63 CARMONETTE MODEL WITH MAJOR FUNCTIONS SHOWN.

6.3.1.1 Carmonette Search Submodel

The Carmonette search submodel is the target detection and acquisition process. This submodel is the means by which visibility degradation mechanisms are included in the model.

During a simulation run, detection of a single element implies detection of the entire unit. Detection of a unit by one element implies detection by all elements of the associated unit. The visible area of the largest element of a unit is used for detection calculations. The electro-optical sensors that currently can be represented are: the unaided eye, binoculars, and in Section 6.3.1.2, passive night vision devices. The calculations used to determine probability of detection for the unaided eye and binoculars require inputs as given in Table 6.3 below.

TABLE 6.3

VISUAL DETECTION INPUTS

Symbol	Definition
σ_s	Scattering cross section
σ_s	Absorption cross section
$R_{B(\lambda)}$	Background reflectance
$R_{T(\lambda)}$	Target reflectance
MD	Minimum dimension of target (meters)

The inputs are then calculated as shown in Tables 6.4 through 6.6 with the relationship connecting the visual angle and liminal contrast given in Figure 6.64.

6-109

TABLE 6.4

VISUAL DETECTION CALCULATIONS

Symbol	Definition	Computation
	Computed in Preprocessor Program	
M_3	Visual background reflectance	$M_3 = \int R_B(\lambda)B(\lambda)K(\lambda)d\lambda$
M_4	Visual target reflectance	$M_4 = \int R_T(\lambda)B(\lambda)K(\lambda)d\lambda$
P_1	Integral of night sky brightness	$P_1 = \int B(\lambda)K(\lambda)d\lambda$
LL	Light level	$LL = \pi\alpha(6850)(9.3 \times 10^4)P_1$
	Computed in Battle Model Program	
R	Observer-target range	(Normal program calculation)
T	Transmittance	$T = e^{-(\sigma_s + \sigma_s)R}$
K_3	Computational variable	$K_3 = 1 - e^{-\sigma_s R}$
C_o	Intrinsic contrast	$C_o = \dfrac{|M_4 - M_3|}{M_3}$
C	Perceived contrast	$C = \dfrac{C_o}{1 + \dfrac{K_3 \cdot P_1}{C_G \cdot T \cdot M_3}}$
N_f	Computational variable	$N_f = \dfrac{MD \cdot MAG}{R}(57)(60)\dfrac{1}{\beta}$
P_D	Probability of detection	$P_D = 1 - e^{(-N_1 \cdot N_f{}^2)}$

TABLE 6.5

VALUES INCLUDED IN PROGRAM AS CONSTANTS

Symbol	Definition	Value
$B(\lambda)$	Night sky spectral radiance	
	Moonlight	$B(\lambda) = 10^{(-0.237\lambda - 7.87)} \times 10^{-2}$
	Part Moon	$B(\lambda) = 10^{(+0.480\lambda - 8.76)} \times 10^{-2}$
	Starlight	$B(\lambda) = 10^{(+1.45\lambda - 9.95)} \times 10^{-2}$
β	Angular size of a minimal visual target	Figure 7-1
$K(\lambda)$	Relative sensitivity of the eye	Table 7-4
MAG	Magnification	1.0 unaided eye 7.0 7X50 binoculars
C_G	Constant	0.75
α	Constant	0.5 unaided eye 33.0 7X50 binoculars
N_1	Constant	1.5 unaided eye 0.01 7X50 binoculars

TABLE 6.6

DATA BASE FOR RELATIVE SENSITIVITY OF THE EYE

Wavelength (microns)	K_λ
0.4	4.37×10^{-3}
0.5	2.69×10^{-1}
0.6	7.47×10^{-1}
0.7	3.55×10^{-3}
0.8	3.89×10^{-6}
0.9	1.70×10^{-8}
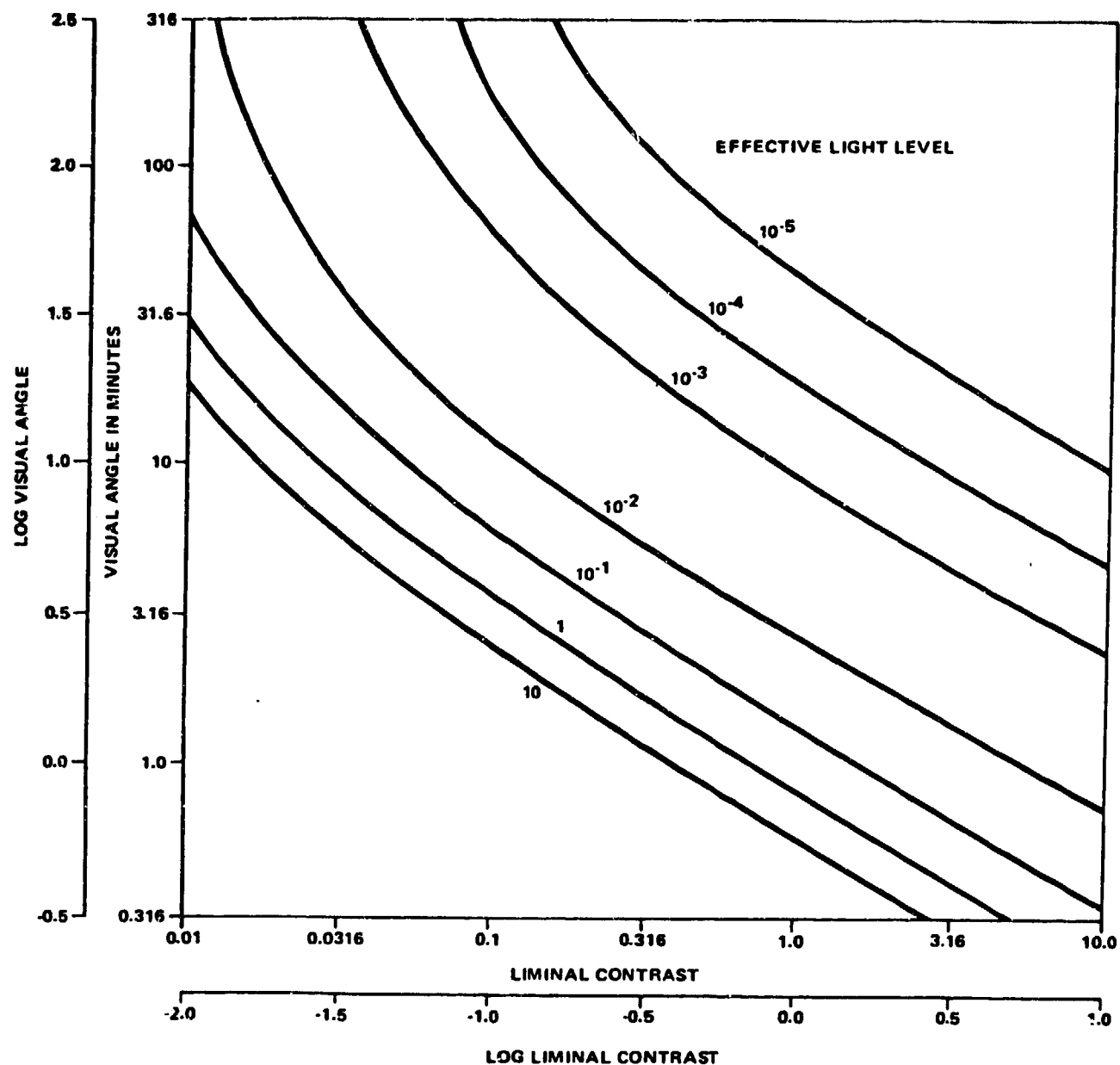
FIGURE 6.64 BLACKWELL'S CURVES SHOWING THE DATA USED
TO RELATE THE VISUAL ANGLE TO THE LIMINAL
CONTRAST FOR VALUES OF THE EFFECTIVE LIGHT
LEVEL FOR A BARELY DETECTABLE TARGET.

REFERENCES FOR SECTION 6

1. W.C. Wells, G. Gal, and M.W. Munn, Aerosol Distributions in Maritime Air and Predicted Scattering Coefficients in the Infrared, Appl. Optics, 16, No. 3, 1977.

2. E.A. Barnhardt and J.L. Streete, A Method for Predicting Atmospheric Aerosol Scattering Coefficients in the Infrared, Appl. Optics, 9, No. 6, 1970.

3. J.E.A. Selby, F.X. Kneizys, J.H. Chetwynd, Jr., and R.A. McClatchey, Atmospheric Transmittance/Radiance: Computer Code LOWTRAN 4, AFGL-TR-78-0053, Air Force Geophysics Laboratory, February 1978.

4. F.G. Smith, R.E. Turner, R.E. Meredith, A Study of Current and Future Technology FLIR Performance in the European Environment, AFAL-TR-78-159, October 1978.

5. R.E. Huschke, Atmospheric Visual and Infrared Transmission Deduced from Surface Weather Observations: Weather and Warplanes VI, R-2016-PR, October 1976.

6. R.E. Turner, Contaminated Atmospheres and Remote Sensing, Remote Sensing of Earth Resources, Vol. III, F. Shahrokhi, Ed., 1974.

7. R.E. Roberts, Atmospheric Transmission Modeling: Proposed Aerosol Methodology with Application to the Grafenwohr Atmospheric Optics Data Base, IDA Paper P-1223, 1976.

8. R.G. Pinnick, S.G. Jennings, P. Chylek, H.J. Auvermann, Relationships Between IR Extinction, Absorption, and Liquid Water Content of Fogs, ASL-TR-0037, Atmospheric Sciences Laboratory, White Sands Missile Range, NM 88002, August, 1979.

9. J.R. Moulton, R.J. Bergemann, and M.C. Sola, (U) "European Winter Atmospheric Environment" (U), IRIS Proceedings, August 1976, (Secret).

10. T.S. Chu and D.C. Hogg, Effects of Precipitation on Propagation at 0.63, 3.5, and 10.6 Microns, The Bell System Technical Journal, May-June, 1968.

11. E.A. Polyakova, 1957: "An Experimental Test of the Formula for the Coefficient of Light Attenuation in Rain," Trans. (Trudy); Main Geophysical Observatory, 68. (See also pp. 126-127 Zuev, V.E., "Atmospheric Transparency in the Visible and the Infrared:, Soviet Radio Press, 1966, Translated from Russian by Z. Lerman, available from the US Dept. of Commerce, Clearinghouse for Federal Scientific and Technical Information, Springfield, VA 22151).

12. H. Goldstein, Attenuation by Condensed Matter; _Propagation of Short Radio Waves_, McGraw-Hill Book Co., Inc., D.E. Kerr, (Ed.) New York, 1951.

13. D.E. Selzer, Computed Transmission Through Rain at Microwave and Visible Frequences, Bell System Tech. J., Vol. 49, No. 8, October, 1970.

14. M. Sola and R. Bergemann, Multispectral Propagation Measurements Through Snow, Tech. Digest of the Top. Meeting in Opt. Prop. through Turb., Rain and Fog, OSA, Aug., 1977.

15. J.B. Mason, Light Attenuation in Falling Snow, ASL-TR-0013, Atmospheric Sciences Laboratory, August, 1978.

16. J.E. Selby, F. Kneizys, R. Chetwynd, and R.A. McClatchey, Atmospheric Transmittance/Radiance: Computer Code LOWTRAN IV, AFGL-TR-78-0053 (1978).

17. S.J. Young, Description and Use of the Plume Radiation Code ATLES, Interim Report, Aerospace Report SAMSO-TR-77-100, May 1977.

18. R.A. McClatchey and A.P. d'Agati, Atmospheric Transmission of Laser Radiation: Computer Code LASER, AFGL-TR-78-0029 (1978).

19. R.A. McClatchey, et al., AFCRL Atmospheric Absorption Line Parameters Compilation, AD-762 904, January 1973.

20. L.D. Duncan et al., The Electro-Optical Systems Atmospheric Effects Library, Volume I-Technical Documentation, ASL-TR-0047, December 1979.

21. H.J. Smith, D.J. Dube, M.E. Gardner, S.A. Clough, F.X. Kneizys, and L.S. Rothman, FASCODE – Fast Atmospheric Signature Code (Spectral Transmittance and Radiance), AFGL Report AFGL-TR-78-0081, January 1978.

22. V. Yousefian, Parametric Analysis of Muzzle Flash (U), Aerodyne Report E SD-TR-76-376, August 1976.

23. H.A. Dale, R.T. Ferrenz, S.H. Gordon, M.J. Lun, R.A. Rollin, M.P. Tracy, T.A. Wild, M.B. Williams, A Survey on the Inclusion of Battlefield Visibility Degradation in Selected Army Models, The Johns Hopkins University Applied Physics Laboratory, FS-77-069, July 1977.

24. Operations Manual FM-100-5 How to fight, Department of the Army, 1 July 1976.

25. R. Zirkind, A Battlefield Obscuration Model (Smoke and Dust), General Research Corporation Report 524-02-79-CR, October 1979.

26. R.M. Marchetti, A Transport and Diffusion Model for Smoke Munitions, U.S. Army Materiel Systems Analysis Activity, Technical Report No. 272, August 1979.

27. J.H. Thompson, "ASL-DUST: A Tactical Battlefield Dust Cloud and Propagation Code," Volume I-Model Formulations, ASL-CR-80-0143-1, and Volume II-User's Manual, ASL-CR-80-0143-2.

28. D. Dvore, DIRTRAN-I User's Manual, ASL-CR-80-0043-1, January 1980.

29. R.E. Turner, Analysis of Battlefield-Induced Contaminants for E-O SAEL, SAI-79-005-AA(1), Final Report for 1979, Science Applications, Inc., December 1979.

30. R.E. Turner, Atmospheric Effects in Remote Sensing, Remote Sensing of Earth Resources, Vol. II, F. Shahrokhi, Ed. 1973.

31. R.E. Turner, Signature Variations Due to Atmospheric Effects, Proceedings of the Tenth International Symposium on Remote Sensing of Environment, Center for Remote Sensing Information and Analysis, Environmental Research Institute of Michigan, Ann Arobr, Michigan, 1975.

32. B. Herman and R.E. Turner, The Infrared Handbook, "Atmospheric Scattering," Chapter IV, USGPO, 1978.

33. D. Anding, R. Kauth and R.E. Turner, Atmospheric Effects on Infrared Multispectral Sensing of the Sea Temperature from Space, Final Report No. 2676-6-F, The University of Michigan, 1970.

34. G.W. Kattawar and G.N. Plass, Infrared Cloud Radiance, Applied Optics, Vol. 8, No. 6, June 1969.

35. R.E. Turner, Investigation of Earth's Albedo Using Skylab Data, Final Report, ERIM 102200-20-F, Environmental Research Institute of Michigan, Ann Arbor, Michigan, 1976.

36. D.R.E. Brown, Natural Illumination Charts, Report No. 374-1, Department of the Navy, Bureau of Ships, Washington, D.C. 1952.

37. D. Pleiter and G.A. Morley, Night Radiation Measurements, Defense Documentation Center, AD 865 252.

38. M.L. Vatsia, U.K. Stich and D. Dunlap, J. Opt. Soc. Amer., Vol. 59, p. 483, 1969.

39. R.E. Turner and P.F. Lambeck, Natural and Artificial Illumination in Optically Thick Atmospheres, Environmental Research Institute of Michigan, Final Report 108300-4-F, April 1975.

40. A.D. Stathacopoulos, H.F. Gilmore, A.Z. Czipott, C.N. Gordon and G. Rohringer, Combat Illumination Model (COIL), General Research Corporation, CR-2-548, March 1975.

41. Night Vision Laboratory Static Performance Model for Thermal Viewing Systems, Research and Development Technical Report ECOM-7043, April 1975.

42. Mathematical Model Reconnaissance and Penetration Study, Volume I: Systems Analysis, USAF Systems Command, WPAFB, Ohio, Report SEG-TR-65-40, May 1965.

43. J.A. Ratches, Realistic European Battlefield Target Acquisition Model (REBTAM), Report DELNV-TR-0008, U.S. Army Night Vision and Electro-Optics Laboratories, July 1979.

44. G.S. Colonna et al., Carmonette, Vol. I: General Description, General Research Corporation Report dated November 1974.

SECTION 7

TESTS AND STUDIES

7.0 INTRODUCTION

Tests are defined as those projects or activities which involve field measurements, be they at the "battlefield environment only", sensor, or combat level. Studies are loosely defined as those projects which are analytical in nature, or simulations on "paper", rather than in the field. We include laboratory data as studies, since such must generally be extrapolated or modeled to be applied to real field conditions.

7.1 TESTS

This section has three subsections:
1. tests which address environmental conditions only,
2. tests which address sensors in environment, and
3. tests which address combat (i.e., outcome of a battle).

7.1.1 TESTS THAT INVOLVE BATTLEFIELD ENVIRONMENT ONLY

7.1.1.1 Optical Properties of Atmospheric Quantities in Europe (OPAQUE) Tests

No description was provided of this test series.

7.1.1.2 Dusty Infrared Transmission (DIRT)

Reports on DIRT-I and DIRT-II are available as well as reports on various aspects of the data analysis. However, much of the data remains to be analyzed. DIRT-III is of course too recent to have been included in a report. We have used a test plan for its discussion.

We would like to point out that the introduction to the DIRT-I report includes an insightful discussion of the problems encountered in trying to relate tests of E-O performance to outcome of battle conclusions.

7.1.1.2.1 DIRT-I, October 1978

The DIRT-I (Dusty Infrared Test-I) was conducted at the U.S. Army's White Sands Missile Range, New Mexico in October. 1978 under the cooperative efforts of the Atmospheric Sciences Laboratory (ASL) and the Waterways Experiment Station. A thorough description of the test along with preliminary results are presented in a report by Lindberg [1].

The primary objectives of DIRT-I were as follows:

1. Provide a developmental test of some of the technology which must be brought to bear on the problems associated with specifying the extreme complexities of the natural atmosphere, differing soil properties, seasonal and meteorological variations, different types and different applications of military munitions, and the engineering details of the E-O systems themselves. This developmental test was to provide, in a coordinated program, information of direct use to E-O sensor and obscuration modeling communities. Specifically addressed were lidars, soil analyses, FLIR images, aerosol samples, transmissometers and others.

2. Characterization of the dust cloud produced by various amounts of high energy explosives.

3. Acquisition of data for the development of scaling laws for various sizes of high energy explosives.

The test was conducted by ASL between 2 and 14 October 1978 in the extreme southeast corner of White Sands Missile Range, New Mexico. The test site was approximately 5 kilometers from the Jarilla Mountains, near Orogrande, New Mexico. The test area was graded to remove all vegetation.

The tests included static detonation of various sized TNT charges arranged in various patterns and the detonation of both static and artillery-delivered 155 millimeter howitzer rounds.

7-2

An additional test was of the smoke produced by a fuel fire made to simulate burning wreckage on the battlefield. For this test four 55-gallon steel drums were cut in half and laid in a trench in the center of the test area, perpendicular to the optic axis. Each drum contained 38 liters of diesel fuel, two liters of motor oil, and one rubber tire.

Figure 7.1 shows the orientation of the test area and locations of the test area and the major instrumentation and support sites. Figure 7.2 shows the detailed layout of the DIRT-I site and location of experiments and equipment. Figure 7.3 shows vertical and horizontal projections of the measurement beams traversing the explosion test area. In addition to the E-O instrumentation and the meteorological monitoring equipment, a payload was flown, suspended from a helicopter, through the explosion dust cloud in an effort to characterize the dust cloud.

DIRT I INSTRUMENTATION SITE
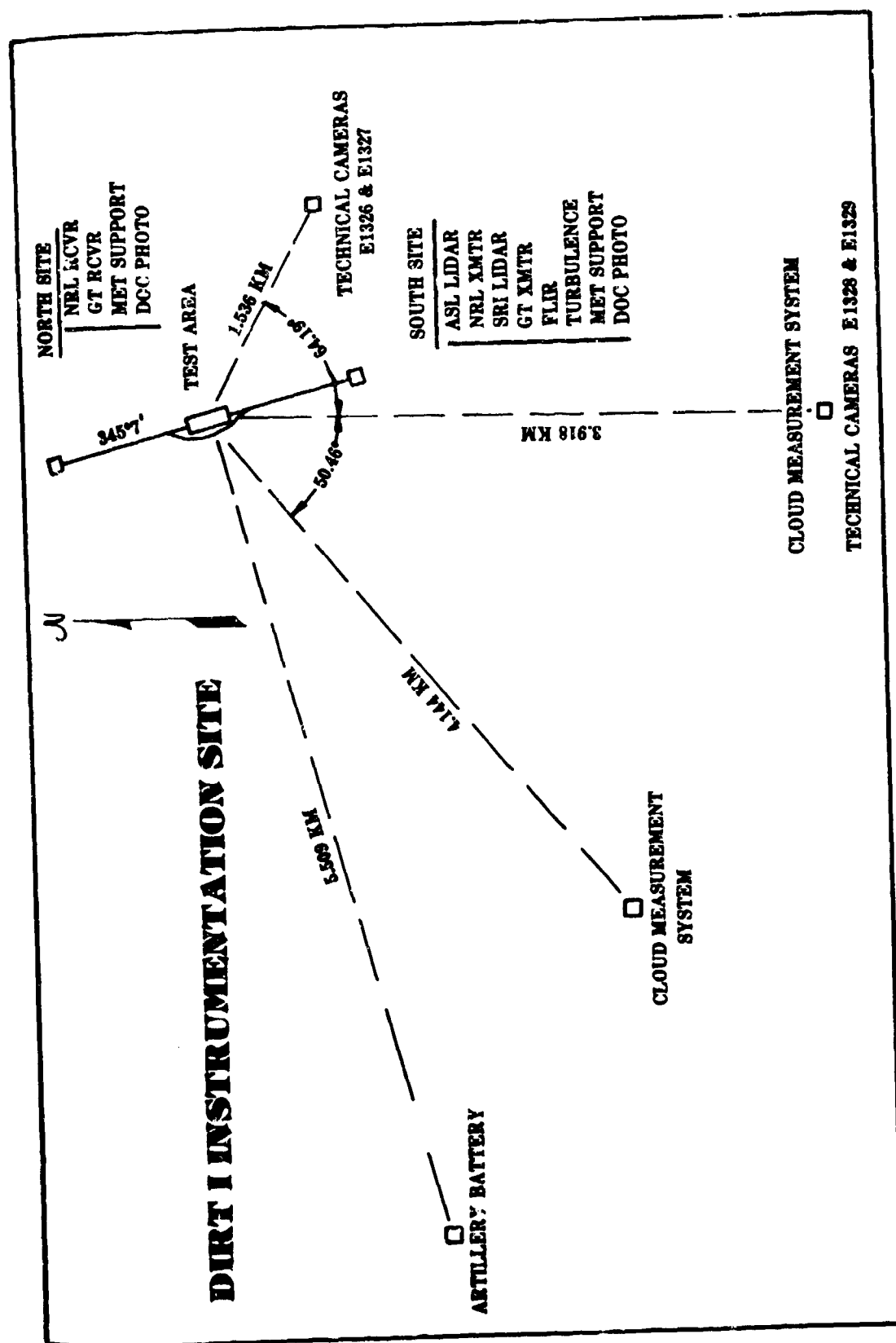
FIGURE 7.1   PLANE VIEW OF DIRT-I SITE SHOWING REMOTELY LOCATED INSTRUMENTATION
AND SUPPORT ELEMENTS. GENERAL LOCATION IS IN EXTREME SOUTHEAST
CORNER OF WHITE SANDS MISSILE RANGE, NEW MEXICO. REFERENCE [1].

FIGURE 7.2 DETAILED LAYOUT OF DIRT-I SITE SHOWING LOCATIONS OF VANS
AND EXPERIMENTS AT EACH END. PATH LENGTH FROM NORTH TO
SOUTH IS 2 km. TEST AREA, WHERE EXPLOSIVES WERE DETONATED
AND ARTILLERY SHELLS IMPACTED, IS 100 by 300 m.
REFERENCE [1].

7-5
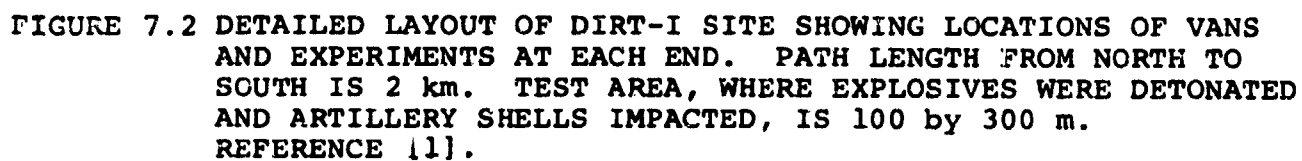
DIRT I
HORIZONTAL BEAM PATH
IN
TEST AREA
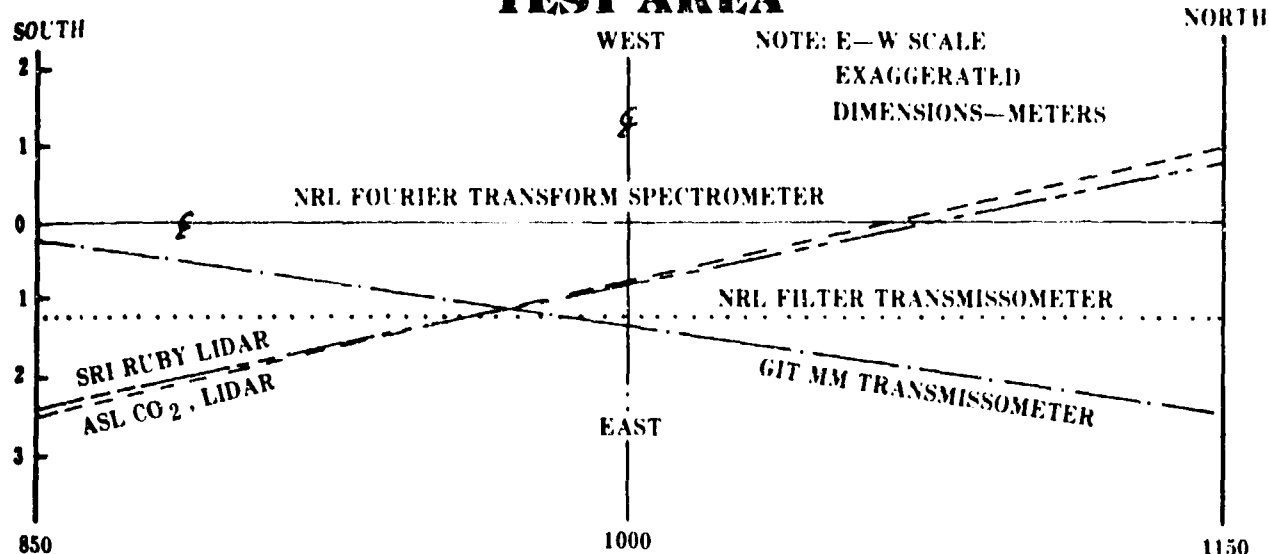
DIRT I
HEIGHT ABOVE GROUND
OF
MEASUREMENT BEAMS

IN TEST AREA
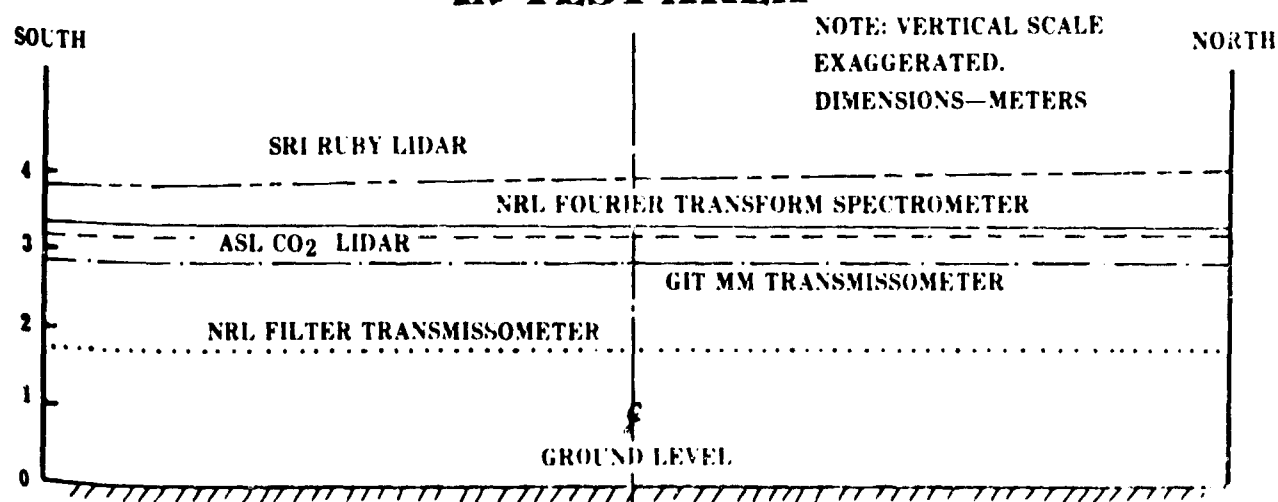
FIGURE 7.3   HORIZONTAL AND VERTICAL CROSS SECTIONS OF VARIOUS
MEASUREMENT BEAMS AS THEY TRAVERSE THE EXPLOSIVE
TEST AREA.   THE EAST-WEST AND VERTICAL SCALES ARE
EXAGGERATED. [1]

7-6

The following measurements/monitoring were done during the tests:

Propagation

1. A Fourier transform spectrometer was operated from 2 to 14 μm wavelengths by NRL. A resolution of 2 cm^{-1} was used.

2. Filter transmissometer data were taken by NRL at 0.546 μm, 1.06 μm and 10.25 μm.

3. Lidar measurements were made at 0.694 μm and 10.6 μm (ruby and CO_2 respectively). The ruby lidar (SRI MARK IX) was from Stanford Research Institute and the CO_2 lidar was ASL's.

4. Millimeter wavelength transmission measurements were made at 94 and 140 GHz by Georgia Tech.

Imagery

1. A FLIR (Forward Looking Infrared) imagery test was conducted by ASL using a tank thermal sight, AN/VSG-2, to obtain both visible and infrared wavelength photography.

2. Multispectral raster scan images were recorded by ASL in the spectral regions 0.5 - 0.7 μm, 1.06 - 0.2 μm, 3.0 - 5.0 μm, and 8.0 - 14 μm.

3. Photographic coverage of DIRT-I included both technical and documentary functions. Technical photography covered only the detonations and provided for time history correlation. Documentary photographs covered all aspects of the tests, from detonations to support functions.

Characterization

1. Particle size distribution measurements were made using a payload suspended from a CH54 "Skycrane" helicopter. This payload was flown through the dust cloud and also included vertical and forward anemometers, a temperature sensor, and a radar altimeter. Particle size distributions

were measured by three particle size spectrometers over the range 0.3 to 180 μm.

2. Electro-Optical Meteorological parameters were measured. A Cambridge system was used to measure ambient temperature and dew point. Wind direction and speed were measured at 1, 2 and 4 meters above the ground. A temperature profile was measured using copper - constantan thermocouples at 1, 2 and 4 meters above the ground. These measurements were made at both sites except that the 2 meter wind speed was not measured at the transmitter (south) site. Optical turbulence ($C_n{}^2$) was measured with a white light scintillometer which was operated along a 200 meter path, 2 meters above the ground at the south site, looking north towards the test area. An acoustic sounder was used to measure qualitatively the strength of vertical variations in atmospheric density ($C_T{}^2$).

3. Suspended particulate matter and soil samples were collected during the tests. Soil samples were collected from the general impact area and from explosion craters. The samples of suspended particulate matter were collected at a site about 50 meters east of the impact area and from the airborne payload. The fixed site consisted of two particulate sampler collectors mounted 3 meters from the ground. This site, in addition, contained an 8-state Anderson Air Sampler. The airborne payload included two membrane filter air samplers. The samples were analyzed for imaginary refractive index in the 0.3 to 1.7 μm spectral region, composition, size, and shape.

4. Soil characterization and crater measurements were done during the test. The objectives of the soil characterization were to obtain a correlative set of data concerning ambient soil characteristics (with depth), explosive forces. The crater geometry data were to provide an estimate of the volume of material injected into the

atmosphere and to judge the effect of soil variations within the site on the volume of material injected into the atmosphere.

5. A last minute attempt was made to obtain gas sampling in the area of the explosions. A gas analyzer capable of detecting either carbon monoxide or ammonia gas was used. Due to the last minute nature of this effort few conclusive data were obtained. One test indicated the presence enhanced levels of carbon monoxide. No ammonia was found.

7.1.1.2.2 DIRT-II, July 1979

The DIRT-II test report [2] was received at the time this Handbook was being written. Therefore this summary is brief. Due to the similarity between DIRT-I and DIRT-II this brevity should not pose too difficult a problem.

The objectives of DIRT-II were as follows:

1. Determine the transmission and backscatter of electromagnetic radiation through dust clouds at selected visible, infrared, and near millimeter wavelengths.

2. Compare craters formed by the detonation of artillery munitions with those formed by high-explosive material.

3. Measure dust cloud growth, movement, and diffusion for explosions.

4. Characterize soil in the area.

5. Measure pertinent meteorological parameters during the test.

The DIRT-II test was conducted in the north-central portion of White Sands Missile Range, New Mexico, during the period 18 through 28 July 1979, and was conducted by the Atmospheric Sciences Laboratory in conjunction with the U.S. Army Engineer Waterways Experiment Station. DIRT-II was a logical extension of DIRT-I. The soil in the DIRT-II area was different (higher water content and predominantely silt and clay rather than being sandy).

As stated earlier DIRT-II was quite similar to DIRT-I. One difference was that, instead of using the airborne payload suspended from a "Skycrane" helicopter, a remotely piloted aircraft was used. Unfortunately this aircraft crashed on the second day of tests, but its short life proved that it could be valuable in such a test. Other differences in the tests mainly involved E-O measurement. In DIRT-II the following measurements were not made: a) FTS measurements, b) Lidar measurements, and c) FLIR tests.

7.1.1.2.3 DIRT-III, April 1980

A) DIRT-III A

The objectives of DIRT-III A were as follows:

1. Compare craters formed by detonation of artillery including 105 mm, 155 mm, 122 mm USSR and 152 mm USSR with those formed by high explosive material in soil conditions which are much different from DIRT-I and DIRT-II, in this case Ft. Polk, Louisiana.

2. Measure dust cloud growth, movement and diffusion.

3. Soil characterization

4. Measurement of mesoscale meteorology during the test period.

5. Determination of electro-optical transmission properties through dust clouds.

6. Determination of particle size distribution in the dust clouds

The Munitions Effective Bare Charge Equivalence portion of the test was done in order to assemble and develop data on effects of cased munitions and to permit reliable simulation of their effects by use of bare charges in tests against buried target facilities.

B) DIRT-III B

Bare charge detraction of tailored soils. Measurements similar to DIRT-III A will be made (excluding those related to artillery ammunition). Test batches of sand, soil and clay and mixtures will be tested.

7.1.1.3 MIRADCOM Near-Millimeter Wave Transmission Measurements

No description was provided of this test series.

7.1.1.4 NRL5 km Path and Fourier Transform Spectrometer Measurements

No description was provided of this test series.

7.1.1.5   Optical Signatures Program (OSP)

These measurements were done at San Nicolas Island and managed by the Naval Weapons Center (NWC), China Lake, California. Since a vital component of target signature is the atmospheric extinction of the signature, an atmospheric transmission measurements program was formulated to obtain the transmission required to develop an observed signatures predictive modeling capability.

The optical path and facility layout for the OSP measurements are shown in Figure 7.4. The optical path extends over the ocean. Transmission data were obtained with a Barnes Transmissometer, Model 11-201T. This instrument is equipped to obtain data in at least fourteen bands from the visible through the infrared regions of the spectrum. The bands used in this program were: 0.5 to 0.61 μm, 1.0648 ± 0.02 μm, 4.8 to 5.0 μm, 3.4 to 4.1 μm, 2.9 to 3.1 μm, 3.4 to 3.6 μm, 3.7 to 3.9 μm, 3.8 to 4.2 μm, 4.0 to 4.2 μm, 4.4 to 4.7 μm, 8.0 to 12.0 μm, 9.0 to 11.5 μm, and 10.6 ± 0.15 μm.

Meteorological information collected during each measurement included the following:

- General sky condition
- Visibility
- Air Temperature
- Dew point temperature
- Relative humidity
- Barometric pressure
- Wind speed
- Wind direction.

7-13

SAN NICOLAS ISLAND TEST FACILITY
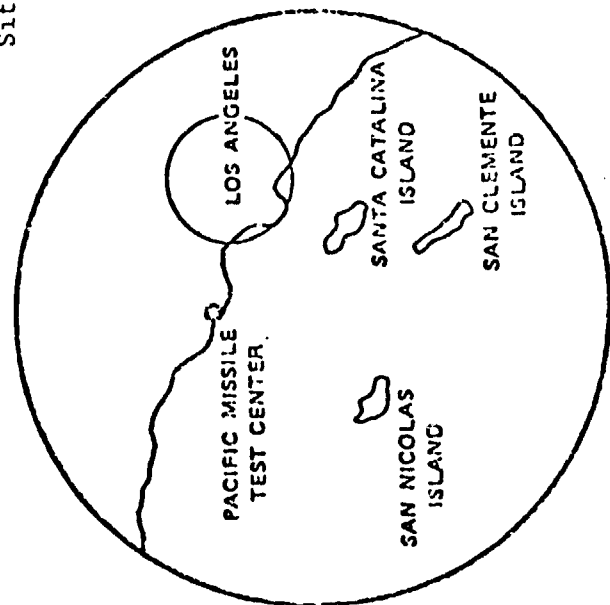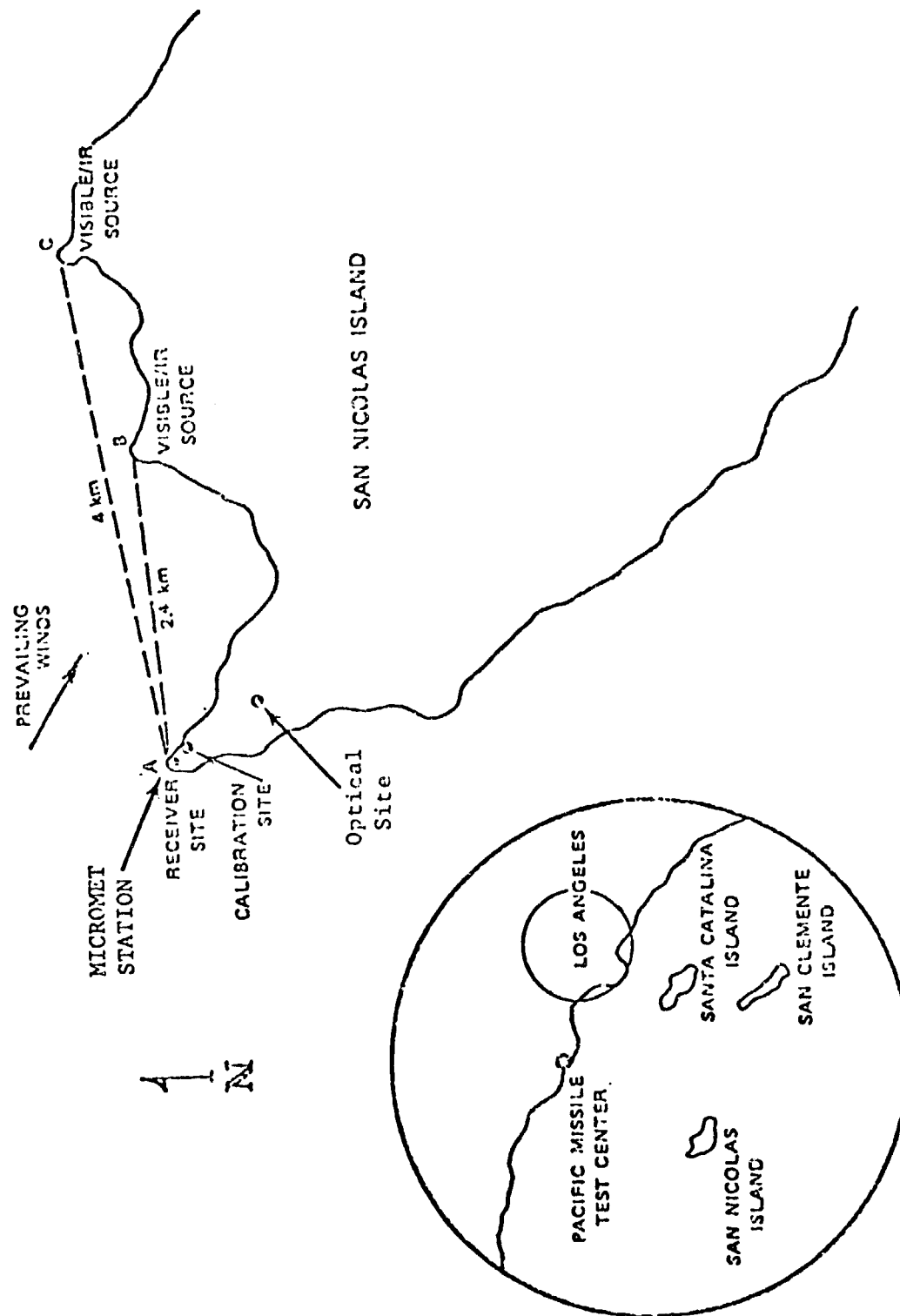
FIGURE 7.4   OSP LAYOUT

7.1.1.6 Dust/Debris Test at Ft. Sill, May 1978

The Dust/Debris Test was conducted at Ft. Sill, Oklahoma by Dugway Proving Ground at the request of PM Smoke. These tests were conducted during May 1978. Information presented here is from Reference [3]. The purpose of the test was to characterize clouds resulting from battlefield dust and debris.

The test layout is shown in Figure 7.5. A total of 24 trials were staged. In four of these, vehicles were used to produce the dust cloud. In the other twenty tests, exploding munitions were used.

Transmittance was measured in the visible (0.4 to 0.7 µm, color corrected) and in the infrared (1.06, 3.4 and 9.75 µm). Other quantities measured were dust sampler dosages, particle size distributions, extinction coefficients, cloud growth dimensions, cloud luminance (1.06 µm), integrated concentration along line of sight, soil moisture content assays, and weapons data. Cloud size was judged from the west and east cameras, and also from the TV monitor at the Command Post. Dust samples were not collected in some of the trials. The cloud luminance data are not too useful since they are dependent upon solar and sky brightness, and these were not measured.
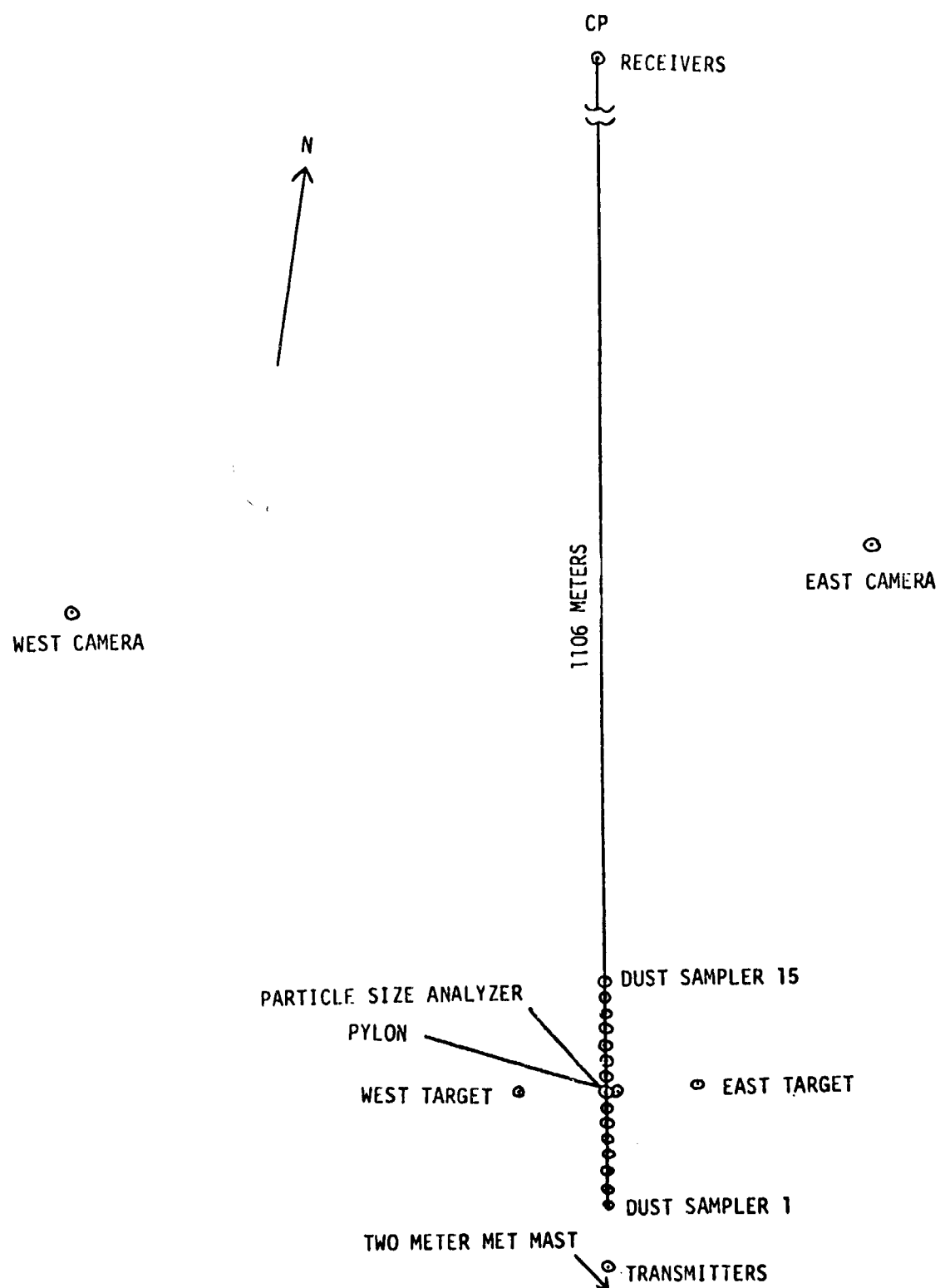
FIGURE 7.5. LOCATION OF GRID INSTRUMENTATION

7.1.1.7 A.P. Hill Tests

These tests were conducted at Ft. A.P. Hill, Virginia, by the U.S. Army's Night Vision Laboratory (NVL). The overall objective of this program was to measure the atmospheric attenuation in spectral regions of prime interest to E-O systems under conditions that severely degrade performance capability in association with a quantification of the meteorological state of the atmosphere for the purpose of understanding and modeling these conditions. A continuous effort was made over the course of a year to obtain a statistical sample of atmospheric transmission in a continental environment. NVL has combined these data with data obtained at Grafenwöhr, FRG to form a continental Grafenwöhr/A.P. Hill (GAP) model.

These transmission measurements were made with one common receiver site and three source sites, at 230 meters, 2 kilometers, or 5 kilometers from the receiver. Transmission measurements were made at the receiver site at each of the wavelengths 0.5 μm, 1.06 μm, 3 to 5 μm and 8 to 12 μm.

The following quantities were monitored at the receiver site.

- Dry bulb and dew point temperature

- Wind speed and direction

- Pressure

- Precipitation rate and amount

- Visibility

- Aerosol size distributions (ASL supported)

7-17

At the 330 meter source site the following were monitored.

- Temperature

- Relative humidity

- Amount of precipitation.

At the 2 kilometer source site the following were monitored.

- Temperature

- Relative humidity

- Amount of precipitation.

At the 5 kilometer source site the following were monitored.

- Pressure

- Temperature

- Relative humidity.

In additions to these quantities the data are further characterized as to whether they were obtained during "wet" or "dry" fog.

7.1.2 TESTS INCLUDING SENSOR PERFORMANCE IN A BATTLEFIELD ENVIRONMENT

7.1.2.1 Smoke Week Tests

7.1.2.1.1 Smoke Week I, November 1977

Smoke Week I was conducted late in November of 1977 at Dugway Proving Grounds, Utah, under the direction of PM Smoke. This test was carried out to measure the effect of various smoke producing devices upon electro-optical (E-O) devices, under controlled and/or well monitored conditions. The E-O measurements consisted of both a) transmission measurements at wavelengths of interest and b) direct tests of E-O systems themselves.

The summary given here is from Reference [4] which should of course be consulted if more detail is desired.

The test was conducted on the Horizontal Grid located approximately 13 miles west of Ditto Technical Center, Dugway Proving Ground (DPG). Figure 7.6 shows the test grid and DPG instrumentation. There is a discrepancy in the report as to which wavelengths were monitored at points 1, 4, 3, and 7. Figure 7.6 lists 3.38 μm and 3.443 μm, but at two other places it is claimed that the 9 - 11 μm range was observed. Location 5 is at the Command Post (CP). Figure 7.7 shows a more detailed view of the sampling line including showing the placement of the various samplers. The CI's measure total dosage for an event, the AP's measure smoke concentration versus time and the PSA's measure particle size distribution. The sampling line consisted of the following aerosol samplers; 100 CI's, 20 AP's and three PSA's. Figure 7.8 shows the detonation points. The outside points are located along lines L and R (from Figure 7.6) for detonation points S (south) and N (north) respectively. The inside points lie midway between lines L and M, and Q and R for points S and N respectively.

Table 7.1 gives a summary of the test events occurring during Smoke Week I. WP is white phosphorus, RP is red phosphorus, PWP is plasticized white phosphorus and HC is hexacloroethane.

7-19

(1) 3.383 chopped source

(2) 9.750μm, 3.443μm chopped source, black, white and OD targets and chopped visual sources

(3) 3.443μm source

(4) 3.383(±0.098)μm receiver

(5) Two 0.4–C.7μm receivers
    Two 1.06(±0.008)μm receivers

(6) 3.443(±0.079)μm, 9.750(±2.121)μm receiver

(7) 3.443(±0.079)μm receiver

(8) Rotating black, white and open target

(9) 32 meter meteorological tower

(10) 300 meter sampling line (100 CI samplers, 20 AP samplers, and 3 PSA samplers)

(11) 18.3 meter vertical sampling tower

(12) Slant 1.06(±.0173)μm receiver

FIGURE 7.6 TEST GRID CONFIGURATION SHOWING DPG INSTRUMENTATION [4].

7-20

Sampling data recording cables

110 & 220V power cables to operate sampling equipment

100

90

80

70

60

NOTE: Munition(s) should be functioned a minimum of 100 meters upwind of Line 2 to allow sufficient mixing. In all cases, distance selected must permit adequate mixing.

50

40

30

20

• CI Sampler Position
⊙ AP and CI Positions
▷ PSA Positions

10

1

!...?0m...!
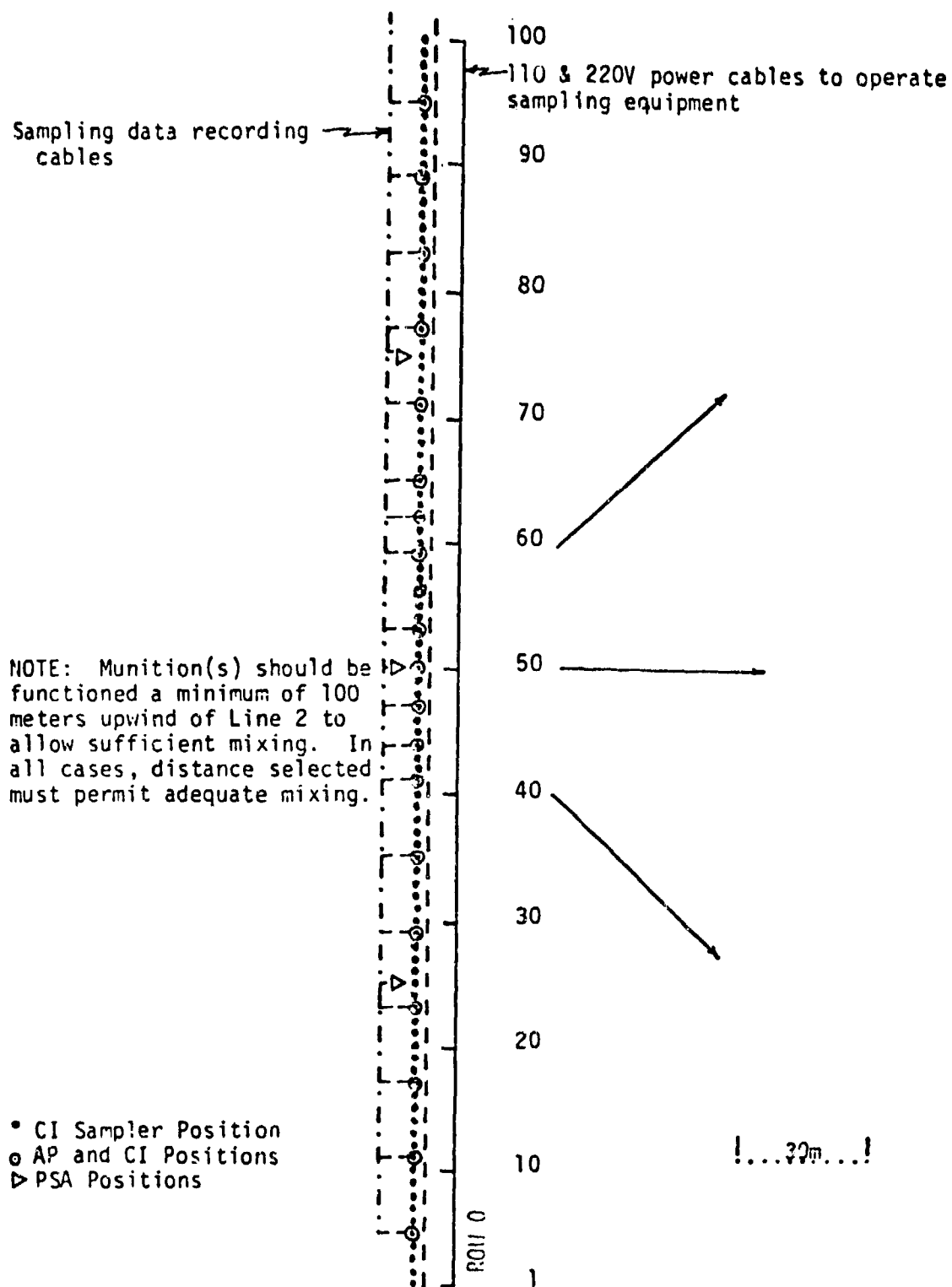
FIGURE 7.7   SAMPLING LINE (REF [4]).

7-21

30.5m
H——H

DP1-002-T33
 Between S1.5 and S3.5
 on inside line
DP1-003-TID
 At S4 on outside line
 on 295° Azimuth
DP1-003-T2D
 At S2 on outside line
 on Azimuth toward S3
DP1-002-T12
 Centered at N1.5 on
 inside line
DP1-005-T4
 Centered at N3 on
 inside line
DP1-005-T12
 Centered at N3.5 on
 inside line
DP1-005-T16
 Centered at N3 on
 inside line
DP1-002-T16
 Between N2 and N3
 on inside line
DP1-005-T3
 Start at N3 along
 Azimuth line towards S2
DP1-002-T24
 Start at N4 along
 Azimuth line towards N3
DP1-002-T34
 Start at N2 along
 Azimuth line towards N3
DP1-002-T4
 Centered at N2.5 on inside
 line

S5 • •
S4 • •
S3 • •
S2 • •
S1 • •

• • N5
• • N4
• • N3
• • N2
• • N1

Sampling Line

North

CP

Munitions were spaced at 3.7 meter intervals with the exception of the L8A1 grenades that were dynamically fired.

South Detonation Points			North Detonation Points	
Inside	Outside		Inside	Outside
S1(-273.8, -76.2)	(-273.8, -91.4)	N1	(-273.8, 76.2)	(-273.8, 91.4)
S2(-318.4, -76.2)	(-318.4, -91.4)	N2	(-318.4, 76.2)	(-318.4, 91.4)
S3(-350.0, -76.2)	(-350.0, -91.4)	N3	(-350.0, 76.2)	(-350.0, 91.4)
S4(-381.6, -76.2)	(-381.6, -91.4)	N4	(-381.6, 76.2)	(-381.6, 91.4)
S5(-426.2, -76.2)	(-426.2, -91.4)	N5	(-426.2, 76.2)	(-426.2, 91.4)

FIGURE 7.8. DETONATION POINT LOCATIONS
(REF.[4]).

7-22

TABLE 7.1.

SUMMARY OF SMOKE WEEK TEST TRIALS (REF.[4])

Trial Identification	Trial Date	Fire Time(MST)	Type of Smoke	Caliber of Munition	Type of Munitions	Number of Munitions
DPI-002 T33	15 Nov 77	1201:00	HC	105mm	M84A1 Canister	9 18^2
DPI-002 TID	17 Nov 77	1256:59	RP	NA	L8A1 Grenade	8
DPI-002 T2D	17 Nov 77	1411:00	RP	NA	L8A1 Grenade	12
DPI-002 T12	18 Nov 77	1337:00	PWP	4.2 in.	M328A1	12
DPI-005 T4	18 Nov 77	1448:00	WP	82mm	Foreign[1]	11
DPI-005 T12	18 Nov 77	1542:00	WP	122mm	Foreign	6
DPI-005 T16	18 Nov 77	1733:00	WP	130mm	Foreign	6
DPI-002 T16	18 Nov 77	1845:00	WP	4.2 in.	M328A1	11
DPI-005 T8	18 Nov 77	2019:50	WP	120	Foreign	11
DPI-002 T24	19 Nov 77	1026:00	WP	155mm	M110E2	12
DPI-002 T34	19 Nov 77	1149:00	WP	155mm	M110E2	6
DPI-002 T4	19 Nov 77	1258:00	HC	105mm	M84A1 Canister	36^2

[1]Additional specifications of the foreign munitions may be obtained from PM Smel
[2]Number of submunitions or canisters.

7-23

The following conditions were monitored/controlled during the tests:

Meteorological Measurements

The following meteorological conditions were monitored, (ranges of allowed values are indicated in brackets where applicable): wind direction (between +45° and -45° from the normal to the sample line), mean wind speed (between 2.5 and 5.5 m/sec), std. dev. in azimuthal wind angle, std. dev. in elevation wind angle, temperature gradient between 0.5 and 8 meter heights, power law exponent of vertical profile of mean wind speed, Pasquill stability category, relative humidity, solar azimuth, solar altitude, air density, solar radiation, barometric pressure, and the visibility [>10 miles].

Aerosol Characterization

Aerosol characterization included chemical impinger measurements and the recording of aerosol cloud particle size distribution, particle number density, and mass concentration.

Photographic Coverage

Cloud dimensions measurements versus time were provided by motion picture coverage. Sequential still photographs were taken at time intervals of 30 and 60 seconds for projectiles and smoke pots respectively. Photographic coverage also supplied information about the distance from the cloud to the target. Color television recordings were made of the screening operations.

Electro-Optical Measurements

Transmission measurements were made at the following wavelength ranges; 9 - 11 μm, 0.4 - 0.7 μm, 1.06 μm and 3.39 μm.

The luminance of the targets was measured. These were, a white target (diffuse white reflector), a black target (matted black absorber), and an olive drab (OD) target.

7-24

The E-O systems tested can be grouped as follows: a) night-sights and trackers, b) beam riders, c) designators and seekers, d) non-prototype measurement set-ups, and e) millimeter wave radars.

The nightsight and trackers tested were as follows:
a) the Hughes multi-element tracker which is designed to replace the current TOW tracker, b) the production TOW launcher and the AN/TAS-4 night sight. Video tape recordings were taken of both the FLIR (AN/TAS-4) and the visual scene to allow a subjective deter-mination of the point at which the scene is no longer useful. c) the TOW missile beacon, which had output intensities of 1, 10 and 300 times the standard source so as to evaluate performance of improved systems, etc. d) the Texas Instruments video thermal tracker (VTT).

The beam rider systems tested were as follows: a) the Northrop Corporation CO_2 laser beamrider systems, using either the Northrop HgCdTe detector or a Saunder Associates HgCdTe detector, b) the Raytheon CO_2 heterodyne laser system which used both continuous wave and pulsed CO_2 lasers, providing for 50 dB of dynamic range, c) the Saunders Associates GaAs beam rider system known as the Saunders Gray Code Beamrider Guidance Link, d) the Northrop GaAs laser beamrider system, and e) the Ford Aerospace and Communica-tions Corporation system using a GaAs laser.

Various non prototype systems were tested: a) Texas Instru-ments fielded a CO_2 laser system to measure beam attenuation, beam spreading, and scintillation in the presence of various smoke and or dust conditions. This test setup used a detector to monitor the output of the McDonnell Douglas CO_2 beamrider (which isn't described with the other beamriders). This laser was used as a source to minimize the number of lasers involved in testing. b) MIRADCOM conducted experiments aimed at inferring performance of Laser Guidance Systems (LDS) in a smoke environment. c) Harry Diamond Laboratories tested two systems. One was a dual channel

nephelometer and the other was an optical-backscatter system (also called a short pulse system), which used a GaAs laser.

The laser designator tested was the Copperhead Designator, also called the Ground Laser Locator Designator (GLLD). During tests this was aimed at a stationary M-48 tank which was running.

The Ballistic Research Laboratory set up radar sets operating at the millimeter frequencies of 35, 95 and 140 GHz.

REFERENCES FOR SECTION 7

1. J.D. Lindberg, "Measured Effects of Battlefield Dust and Smoke on Visible, Infrared and Millimeter Wavelength Propagation: A Preliminary Report on Dusty Infrared Test-I (DIRT-I)", ASL-TR-0021, January, 1979.

2. Bruce C. Kennedy, "Dusty Infrared Test-II (DIRT-II) Program", ASL-TR-0058, May, 1980.

3. "Dust/Debris Test Conducted at Ft. Sill Oklahoma by Dugway Proving Ground" Final Test Report, Volumes 1 and 2, DPG-FR-78-313, September, 1978.

4. Eugene Bowman and Joseph Steedman, "Smoke Week I Electro-Optical (E-O) Systems Performance in Characterized Smoke Environment at Dugway Proving Ground, Utah, November, 1977", PMSMK-T-002-78, April, 1978.

DISTRIBUTION LIST

No. of Copies	Organization	No. of Copies	Organization
2	Office of Secretary of Defense ATTN: ODDR&E (E&PS) Washington, DC 20310	1	Commander US Army Materiel Development & Readiness Command ATTN: DRCPA-S 5001 Eisenhower Avenue Alexandria, VA 22333
1	Office of Secretary of Defense ATTN: CSDDRE-DDT&E Washington, DC 20310	1	Commander US Army Materiel Development & Readiness Command ATTN: DRCRE 5001 Eisenhower Avenue Alexandria, VA 22333
1	HQDA (DAMO-RQA) WASH DC 20310		
1	HQDA (SAUS-OR) WASH DC 20310		
1	HQDA (DAMA-WSM) WASH DC 20310	1	Commander US Army Materiel Development & Readiness Command ATTN: DRCDE-R 5001 Eisenhower Avenue Alexandria, VA 22333
1	HQDA (SARDA) WASH DC 20310		
1	HQDA (DAMA-CSS) WASH DC 20310		
1	HQDA (DAMI-ISP - Mr. Beck) WASH DC 20310	1	Commander US Army Materiel Development & Readiness Command ATTN: DRCDE-DM 5001 Eisenhower Avenue Alexandria, VA 22333
1	Commander US Army Materiel Development & Readiness Command ATTN: DRCLDC 5001 Eisenhower Avenue Alexandria, VA 22333	1	Commander US Army Armament Research & Development Command ATTN: DRCPM-CAWS Dover, NJ 07801
1	Commander US Army Materiel Development & Readiness Command ATTN: DRCNC 5001 Eisenhower Avenue Alexandria, VA 22333	1	Commander US Army Armament Research & Development Command ATTN: DRCPM-ADC Dover, NJ 07801
1	Commander US Army Materiel Development & Readiness Command ATTN: DRCPM 5001 Eisenhower Avenue Alexandria, VA 22333	1	Commander US Army Armament Research & Development Command ATTN: DRDAR-LCS Dover, NJ 07801

No. of Copies	Organization	No. of Copies	Organization

1	Commander
	US Army Armament Research
	   & Development Command
	ATTN: DRDAR-LCW
	Dover, NJ 07801
		1	Commander
			US Army Communications
			   R&D Command
			ATTN: DRCPM-TDS-TF
			FT Monmouth, NJ 07703

1	Commander
	US Army Armament Research
	   & Development Command
	ATTN: DRDAR-LCA
	Dover, NJ 07801
		1	Commander
			US Army Electronics
			   R&D Command
			ATTN: DRDEL-SA
			FT Monmouth, NJ 07703

1	Commander
	US Army Armament Research
	   & Development Command
	ATTN: DRDAR-AS
	Dover, NJ 07801
		2	Commander
			US Army Electronics R&D Command
			ATTN: DRDEL-CCM (COL Murrary/
			       Dr. W. Pepper)(Mr. Walter
			       Pathshall/Mr. Harrelson)
			2800 Powder Mill Road
			Adelphi, MD 20783

1	Commander US Army Armament Research & Development Command ATTN: DRDAR-RA Dover, NJ 07801	1	Commander Harry Diamond Laboratories ATTN: DELHD-RAF (Mr. D. Giglio) 2800 Powder Mill Road Adelphi, MD 20783
1	Commander US Army Aviation R&D Command ATTN: DRCPM-AAH PO Box 209 St. Louis, MO 63166	1	Commander Harry Diamond Laboratories ATTN: DELHD-SAB 2800 Powder Mill Road Adelphi, MD 20783
1	Project Manager BLACK HAWK US Army Aviation R&D Command ATTN: DRCPM-BH PO Box 209 St. Louis, MO 63166	1	Commander US Army Engineer Center & FT Belvoir ATTN: ATSE-CDC (Mr. Minnick) FT Belvoir, VA 22060
1	Project Manager Target Acquisition Designation Systems/Pilot Night Vision System ATTN: DRCPM-AAH-TP PO Box 209 St. Louis, MO 63120	1	Commander US Army Mobility Equipment R&D Command ATTN: DRXFB-RCT (Mr. F. Kezer) FT Belvoir, VA 22060

No. of Copies	Organization
1	Commander US Army Mobility Equipment R&D Command ATTN: DRDME-ZT FT Belvoir, VA 22060
1	Director Night Vision & Electro- Optics Laboratory FT Belvoir, VA 22060

3	Director
	Night Vision & Electro-
	  Optics Laboratory
	ATTN: DELNV-VI
	      (Mr. R. Bergemann)
	      (Mr. T. Cassidy)
	      (Ms. L. Obert)
	FT Belvoir, VA 220460

1	Commander Dugway Proving Ground Dugway, UT 84022
1	Commander US Army Missile Command ATTN: DRCPM-TO Redstone Arsenal, AL 35898
1	Commander US Army Missile Command ATTN: DRCPM-HD Redstone Arsenal, AL 35898
1	Commander US Army Missile Command ATTN: DRCPM-RS Redstone Arsenal, AL 35898
1	Commander US Army Missile Command ATTN: DRSMI-O Redstone Arsenal, AL 35898

No. of Copies	Organization
1	Commander US Army Missile Command ATTN: DRSMI-D Redstone Arsenal, AL 35898
1	Commander US Army Missile Command ATTN: DRSMI-R Redstone Arsenal, AL 35898
1	Commander US Army Missile Command ATTN: DRSMI-CGA (Dr. B. Fowler) Redstone Arsenal, AL 35898
1	Commander US Army Missile Command ATTN: DRSMI-RHA Redstone Arsenal, AL 35898
1	Commander US Army Tank-Automotive R&D Command ATTN: DRSTA-RPL Warren, MI 48090
1	Commander US Army Tank-Automotive R&D Command ATTN: DRCPM-ITV (COL C. Adsit) Warren, MI 48090
1	Program Manager XM1 Tank System ATTN: DRCPM-GCM 38111 Van Dyke Avenue Warren, MI 48090
1	Program Manager Fighting Vehicle Systems ATTN: DRCPM-FVS Warren, MI 48090

No. of Copies	Organization	No. of Copies	Organization

1	Commander
	US Army Armament Materiel
	   Readiness Command
	ATTN: DRSAR
	        (Mr. Herman Michels)
	Rock Island, IL 61201
		1	Commander
			US Army Combined Arms Combat
			   Developments Activity
			ATTN: Library
			FT Leavenworth, KS 66027

1	Director
	Eustis Directorate
	US Army Air Mobility
	   R&D Command
	ATTN: SADL-EU-MOS
	        (Mr. E. Gilbert)
	FT Eustis, VA 23604
		1	Commander
			US Army Combined Arms Training
			   Developments Activity
			ATTN: ATZL-TDA
			FT Leavenworth, KS 66027

1	Commander
	US Army Foreign Science
	   & Technology Center
	220 7th Street, NE
	Charlottesville, VA 22901
		1	Commander
			US Army Combined Arms Training
			   Developments Activity
			ATTN: ATZL-TDA-DS (LTC McGurk)
			FT Leavenworth, KS 66027

1	Commander/Director
	US Army Cold Region Research
	   Engineering Laboratory
	ATTN: CRREL-RG (G. Aitken)
	Hanover, NH 03755
		1	Commander
			US Army Combined Arms Studies
			   & Analysis Activity
			ATTN: ATZL-CAC-A (COL Reed)
			FT Leavenworth, KS 66027

1	Commander US Army Training & Doctrine Comd ATTN: ATCD-CF FT Monroe, VA 23651	1	Commander US Army Combined Arms Center ATTN: ATZL-CAT-MK (LTC D. Bacon) FT Leavenworth, KS 66027

1	Commander
	US Army Combined Arms Combat
	   Developments Activity
	ATTN: ATCA-CFP
	FT Leavenworth, KS 66027
		1	Commander
			US Army Combat Developments
			   Experimentation Command
			ATTN: ATEC-CG
			FT Ord, CA 93941

1	Commander
	US Army Combined Arms Combat
	   Developments Activity
	ATTN: ATCA-CAM-V
	FT Leavenworth, KS 66027
		1	Commander
			US Army Combat Developments
			   Experimentation Command
			ATTN: ATEC-PL-M (Dr. Love)
			FT Ord, CA 93941

		1	Commander US Army Combat Developments Experimentation Command ATTN: ATEC-PL-TL FT Ord, CA 93941

DISTRIBUTION LIST - Continued

No. of Copies	Organization	No. of Copies	Organization
1	Commander TRADOC Combine Arms Test Activity ATTN: ATCAT-TL FT Hood, TX 76544	1	Director US Army Materiel Test & Evaluation Command ATTN: STEWS-TE-AG (Mr. Southworth) White Sands Msl Rg, NM 88002
1	Commander TRADOC Combined Arms Test Activity ATTN: ATCAT-SA (Dr. D. Collier) FT Hood, TX 76544	1	Director US Army Materiel Test & Evaluation Command ATTN: STEWS-TE-PC (Mr. Doyle Rexrode) White Sands Msl Rg, NM 88002
1	Director US Army TRADOC Systems Analysis Activity ATTN: ATAA (Hugh McCoy) White Sands Msl Rg, NM 88002	1	Director Atmospheric Science Laboratory ATTN: DRSEL-BL-SY (Mr. F. Horning) White Sands Msl Rg, NM 88002
1	Director US Army TRADOC Systems Analysis Activity ATTN: ATAA-TDB (Mr. Luis Dominquez) White Sands Msl Rg, NM 88002	1	Director Atmospheric Science Laboratory ATTN: DELAS-D White Sands Msl Rg, NM 88002
1	Director US Army TRADOC Systems Analysis Activity ATTN: ATAA-TGA (Mr. Stadtlander) White Sands Msl Rg, NM 88002	1	Commander Office of Missile Electronic Warfare ATTN: DELEW-WLM-SE White Sands Msl Rg, NM 88002
1	Director US Army TRADOC Systems Analysis Activity ATTN: ATAA-TGP White Sands Msl Rg, NM 88002	1	Commandant US Army Field Artillery School ATTN: ATSF-CD FT Sill, OK 73503
1	Director US Army Materiel Test & Evaluation Command ATTN: STEWS-TE-LD White Sands Msl Rg, NM 88002	1	Commandant US Army Field Artillery School ATTN: ATSF-TSM-C FT Sill, OK 73503
		1	Commandant US Army Field Artillery School ATTN: ATSF-WD FT Sill, OK 73503
		6	Director Atmospheric Science Laboratory ATTN: DELAS-EO-MO (Dr. R.B. Gomez) White Sands Msl Rg, NM 88002

DISTRIBUTION LIST - Continued

No. of Copies	Organization	No. of Copies	Organization
1	Commandant US Army Field Artillery School ATTN: ATZR-TC FT Sill, OK 73503	1	Commander US Army Concepts Analysis Agcy ATTN: CSCA-SMG (Mr. Hock) 8120 Woodmont Avenue Bethesda, MD 20014
1	Commandant US Army Field Artillery School ATTN: AFVI-CG FT Sill, OK 73503	2	Commander US Army Concepts Analysis Agcy ATTN: CSCA-SMS (Mr. John Clark) (Mr. Martin Dwarkin)
1	Commandant US Army Field Artillery School ATTN: ATSF-CD-DA (Mr. Millspaugh) FT Sill, OK 73503		8120 Woodmont Avenue Bethesda, MD 20014
1	Commandant US Army Air Defense School ATTN: ATSA-CDM-W (CPT Braeden) FT Bliss, TX 79916	1	Commander US Army Concepts Analysis Agcy ATTN: CSCA-MCM (Mr. W. Chandler) 8120 Woodmont Avenue Bethesda, MD 20014
1	Commandant US Army Infantry School ATTN: ATSH-CD-CF (Mrs. Jody Shirley) FT Benning, GA 31905	1	Commander US Army Operational Test & Evaluation Agency ATTN: CSTE-TM-FA 5600 Columbia Pike Falls Church, VA 22041
1	Commandant US Army Infantry School ATTN: ATSH-CD-CS FT Benning, GA 31905	1	Commander US Army Logistics Eval Agcy ATTN: DALO-LEI New Cumberland Army Depot New Cumberland, PA 17070
3	Commander US Army Concepts Analysis Agcy ATTN: CSCA-RQN (Mr. Van Albert) (MAJ Rinehart) 8120 Woodmont Avenue Bethesda, MD 20014	1	Director Defense Advanced Research Projects Agency ATTN: TTO 1400 Wilson Boulevard Arlington, VA 22209
1	Commander US Army Concepts Analysis Agcy ATTN: Library 8120 Woodmont Avenue Bethesda, MD 20014	1	Commander US Army Intelligence Anal Ctr ATTN: IAX-OT-P Arlington Hall Station Arlington, VA 22212

No. of Copies	Organization	No. of Copies	Organization

1	Chief
	Defense Logistics Studies
	    Information Exchange
	US Army Logistics Management
	    Center
	ATTN: DRXMC-D
	FT Lee, VA 23801
		1	Commander
			US Army Aviation Center
			    & FT Rucker
			ATTN: ATZQ-D (Mr. McCabe)
			FT Rucker, AL 36362

2	Commander
	The Defense Technical
	    Information Center
	ATTN: TCA
	Cameron Station
	Alexandria, VA 22314
		1	Commander
			US Army Armor Center
			    & FT Knox
			ATTN: ATZK-CD-SD (MAJ Brinkley)
			FT Knox, KY 40121

1	Commander US Army Research Office Research Triangle Park Durham, NC 27709	1	Commander US Army Forces Command ATTN: AFOB-FS FT McPherson, GA 30330
1	Commandant US Army Chemical School FT McClellan, AL 36201	1	Commander US Army Forces Command ATTN: AFLG-RE FT McPherson, GA 30330
1	Commander US Army Electronic Proving Gd FT Huachuca, AZ 85613	1	Commander US Army Forces Command ATTN: AFOP-TAS FT McPherson, GA 30330

1	Commander
	US Army Military Police &
	    Chemical School/Trng Ctr
	    & Ft McClellan
	ATTN: ATZN-CM-CDC
	FT McClellan, AL 36205
		1	Commander
			Naval Weapons Center
			ATTN: Dr. Swinford
			China Lake, CA 93555

1	Commander US Army Signal Center & FT Gordon ATTN: ATZH-CD (COL David) FT Gordon, GA 30905	1	Commander Naval Weapons Center ATTN: Code 40701 China Lake, CA 93555

1	Commander
	US Army Signal Center &
	    FT Gordon
	ATTN: ATZH-CD-CS (LTC Bratcher)
	FT Gordon, GA 30905
		2	Commander
			Naval Weapons Center
			ATTN: Code 385
			        (Mr. R. Reed Jr.)
			        (Mr. R. Bird)
			China Lake, CA 93555

No. of Copies	Organization	No. of Copies	Organization

1	Commander
	Naval Surface Weapons Systems
	ATTN: Code G-31
	       (Mr. G. Seidl)
	Dahlgren, VA 22448
		1	Center for Naval Analysis
			Marine Corps Operations
			  Analysis Group
			ATTN: Document Center
			1401 Wiscn Boulevard
			Arlington, VA 22209

1	Commander Naval Support Weapons Center ATTN: Code DG-302 (Ms. D. Shamblin) Dahlgren, VA 22448	1	Commander-In-Chief, Pacific Research & Analysis Office Box 13, J77 ATTN: Mike Mulhern Camp H.M. Smith, Hawaii 96861
1	Commanding Officer Naval Intelligence Support Ctr ATTN: NISC Code 4330 (Mr. H. St. Aubin) 4300 Suitland Road Suitland, MD 20390	1	Commander Wright-Patterson Air Force Base ATTN: AFLC Wright-Patterson AFB, OH 45433
1	Director Naval Research Laboratory ATTN: Code 5709 (Mr. W. Howell) Washington, DC 20375	1	Commander Readiness Command MacDill Air Force Base Tampa, FL 33608
1	Chief Naval Materiel Command ATTN: MAT-0315 (Mr. K. Takle) Washington, DC 20360	1	Headquarters TAC-DRA ATTN: MAJ R. Summerville Langley AFB, VA 23365
1	Commander Naval Suport Support Ctr ATTN: Mr. D. Johnson Crane, ID 47522	1	Director Marine Corps Development Ctr ATTN: Mr. M. Fulmer Quantico, VA 22134

1	Commander
	US Navy Amphibious Base
	  Surface War Development Gp
	ATTN: Mr. R. Daily
	Little Creek
	Norfolk, VA 23521
		1	HQ, US Army Europe &
			    Seventh Army
			Office of the Deputy Chief
			  of Staff, Intelligence
			ATTN: AEAGB-PDN(S&E)
			       (Mr. Stan Stenrod)
			APO, NY 09403

No. of Copies	Organization	No. of Copies	Organization
1	HQ, US Army Europe & Seventh Army ATTN: AEAGC/COL Cook APO NY 09403	1	Director, HEL ATTN: DRXHE Bldg. 520
1	HQ, JUSMAG-Korea ATTN: Document Center APO San Francisco 96302	3	Commander, Ordnance Chemical Ctr & School ATTN: ATSL-DAC-L (Mrs. Weston) ATSL-CD-TA ATSL-CLC-C
1	Office of Strategic Research/ Strategic Evaluation Center CIA Headquarters Building Washington, DC 20205	5	Director, BRL ATTN: DRDAR-BLW (A. Finnergy) DRDAR-PD (N. Gerri) DRDAR-BLU DRDAR-BL DRDAR-DLV (Saccenti) Bldg. 328
1	Director Institute for Defense Analysis Systems Evaluation Division ATTN: Mr. R. Roberts 400 Army-Navy Drive Arlington, VA 22202	1	Director, BRL ATTN: DRDAR-PSB-S Bldg. 305
1	Director Institute for Defense Analysis ATTN: Documents Library 400 Army-Navy Drive Arlington, VA 22202	2	Director, CSL ATTN: DRDAB-CLY-A DRDAB-CLN-S
	Aberdeen Proving Ground	2	Commander, APG/EA ATTN: SAREA-CL-PF SAREA-DE-MS
11	PM, Smoke/Obscurants ATTN: DRCPM-SMK-M DRCPM-SMK-T (LTC J. Bulger) Bldg. 324		
2	Commander, TECOM ATTN: DRSTE-ME (Mr. W. Baity) DRSTE-CM-F Bldg. 314		